

Thick Perovskite Solar Cells over Micrometer-Sized Textured Surfaces

Zur Erlangung des akademischen Grades eines

**DOKTORS DER INGENIEURWISSENSCHAFTEN
(Dr.-Ing.)**

von der KIT-Fakultät für
Elektrotechnik und Informationstechnik des
Karlsruher Instituts für Technologie (KIT)

angenommene

Dissertation

von

M. Sc. Ahmed Hassan Ramadan Ahmed Farag
geb. in Kairo, Ägypten

Tag der mündlichen Prüfung: 24.04.2023

Hauptreferent: Tenure-Track-Prof. Dr. Ulrich W. Paetzold

Korreferent: Prof. Dr. Jan Philipp Hofmann



This document is licensed under a Creative Commons Attribution-ShareAlike 4.0 International License (CC BY-SA 4.0):
<https://creativecommons.org/licenses/by-sa/4.0/deed.en>

Kurzfassung

Angesichts des raschen Anstiegs des weltweiten Energiebedarfs und der Tatsache, dass ein großer Teil der Energieerzeugung auf der Nutzung umweltschädlicher Ressourcen beruht, ist die Entwicklung umweltfreundlicher erneuerbarer Energiequellen von zentraler Bedeutung. In diesem Zusammenhang spielt die Photovoltaik (PV) eine Schlüsselrolle bei der Erzeugung von Elektrizität ohne CO₂-Ausstoß. Derzeit liegt der Anteil der Solarenergie an der gesamten Stromerzeugung bei 3,6% (für 2050 wird er auf 40% geschätzt), wobei 95% des PV-Marktes von Silizium (Si)-Solarzellen beherrscht werden. In den letzten zehn Jahren haben sich Perowskit-Solarzellen (PSZs) mit einem derzeitigen Rekordwirkungsgrad von 25,7% als aussichtsreicher Kandidat für die PV-Technologie der nächsten Generation erwiesen. Darüber hinaus wurde durch die Integration von PSZs in einer monolithischen Perowskit/Si-Tandem-Architektur bereits ein Rekordwirkungsgrad von 32,5% erzielt. Dies deutet darauf hin, dass diese Konfiguration in der Lage ist, die theoretische Wirkungsgradgrenze einer Einfachsolarzelle (~33,7 %) zu übertreffen. Da niedrige Kosten und Kompatibilität mit Industriestandards notwendig sind, um die Tandemtechnologie auf den Markt zu bringen, ist die Verarbeitung von Perowskit-Dünnschichten auf texturierten Si-Bottomzellen im Vergleich zum Einsatz planarer polierter Gegenstücke vorteilhaft. Darüber hinaus ermöglichen texturierte Oberflächen eine effizientere Lichtsammlung durch die Minimierung von Reflexionsverlusten und führen folglich zu einer höheren Kurzschlussstromdichte (J_{sc}).

Die Verarbeitung von Perowskit-Dünnschichten auf texturierten Substraten ist jedoch mit mehreren Herausforderungen verbunden, welche die positiven Auswirkungen der besseren optischen Eigenschaften limitieren. Erstens führt die Herstellung herkömmlicher Perowskit-Dünnschichten mit einer Dicke von ~350-500 nm mittels Drehbeschichtung auf mikrometergroßen Texturen dazu, dass einige der Pyramidenspitzen durch die Oberfläche ragen was Kurzschlüsse hervorrufen kann. Dies geht mit einem schlechten Füllfaktor (FF) und einer niedrigen Leerlaufspannung (V_{oc}) der entsprechenden PSZs einher und limitiert daher den Wirkungsgrad solcher PSZs. Zweitens können PSZs mit zu dicken Perowskit-Absorbern eine geringere Ladungsträgerextraktion aufweisen, was die Wirkungsgrade der Bauelemente einschränkt. Drittens ist die Abscheidung von konformen Lochtransportschichten (HTLs) auf texturierten Oberflächen mit herkömmlichen Lösungsmittel-basierten Abscheidungsmethoden schwierig, was zu einer ineffizienten Lochextraktion führen kann. Im gleichen Zusammenhang ist die nicht-strahlende Rekombination an der HTL/Perowskit-Grenzfläche aufgrund der großen Oberfläche, die eine texturierte Oberfläche im Vergleich zu einer planaren Oberfläche aufweist, verstärkt. Berücksichtigt man schließlich die komplexe Geometrie einer mikrometergroßen, pyramidenförmigen, texturierten Oberfläche (die aus Wandseiten, Spitzen und Tälern besteht), so neigt der resultierende Perowskit-Film dazu, eine hohe Oberflächenrauigkeit zusammen mit spannungsbedingten Unebenheiten aufzuweisen, was zu einer schlechten Grenzfläche zwischen Perowskit und Elektronentransportschicht führen kann. Darüber hinaus beeinträchtigt das Vorhandensein von Hohlräumen in den Tälern der pyramidenförmigen Texturen, aufgrund der verzögerten Lösungsmittelextraktion, den Kontakt zwischen Perowskit und der angrenzenden HTL, was zu einem hohen Serienwiderstand und damit zu einem geringen FF führt.

Ziel dieser Arbeit ist es, die oben genannten Herausforderungen zu überwinden, indem dicke, effiziente Perowskit-Absorber sowie HTLs entwickelt werden, die mit texturierten Oberflächen kompatibel sind, und die mit der Verarbeitung von PSZs auf mikrometergroßen texturierten Oberflächen einhergehenden Spannungsverluste zu verringern. Zunächst wird ein dicker Perowskit-Absorber ($\sim 1 \mu\text{m}$) entwickelt, der eine vollständige Oberflächenbedeckung auf texturierten Oberflächen gewährleistet. Da die Absorberdicke im Bereich der Ladungsträgerdiffusionslänge liegt, wird in der Perowskit-Präkursorlösung ein Lewis-Basen-Zusatz verwendet, der die Kristallisationsdynamik verbessert und die optoelektronische Qualität des Films erhöht, um eine gute Ladungsträgerextraktion zu gewährleisten. Als nächstes wird eine HTL mittels Vakuumabscheidungsverfahren entwickelt, um eine konforme Beschichtung von texturierten Oberflächen zu ermöglichen und gleichzeitig nicht-strahlende Rekombinationsverluste an der HTL/Perowskit-Grenzfläche zu unterdrücken. Halbstapel, bei denen aufgedampfte selbstorganisierte Monoschichten (SAM)-HTLs zum Einsatz kommen, zeigen eine von 1,145 V auf 1,213 V verbesserte implizierte V_{OC} im Vergleich zu den weit verbreiteten NiOx-Schichten. Dies zeigt die Überlegenheit aufgedampfter SAMs im Vergleich zu konventionellen vakuumabgeschiedenen HTLs und macht sie zu einem starken Kandidaten für die Weiterentwicklung der Perowskit-Technologie.

Weiterhin werden die Spannungsverluste im Bulk und an den Grenzflächen von Perowskit-Dünnschichten, die auf texturierten Oberflächen hergestellt wurden, quantifiziert und die Gründe für diese Verluste durch eingehende morphologische, kompositorische und mikrostrukturelle Analysen untersucht. Darüber hinaus wird eine systematische Anleitung für die Anwendung von Strategien zur Verringerung von Spannungsverlusten gegeben, die Folgendes umfasst: Grenzflächenoptimierung, Oberflächenpassivierung, Optimierung von Prozessierungs-Parametern sowie Lösungsmittel-, Molaritäts- und Stöchiometrieoptimierung der Präkursorlösung. In dieser Hinsicht führte die Anwendung der angesprochenen Strategien für PSZs, die auf mikrometergroßen texturierten Substraten hergestellt wurden, zu einem höheren Wirkungsgrad im Vergleich zu Referenz Bauelementen. Die entsprechenden durchschnittlichen Verbesserungen bei V_{OC} , J_{SC} , FF und PCE betragen 74 mV, 1,7 mA/cm², 6% bzw. 3,5%, und gingen mit einer verbesserten Kurzzeitstabilität und einer wesentlich geringeren Hysterese einher. Darüber hinaus wiesen PSZs, die auf der texturierten Oberfläche hergestellt wurden, eine vergleichbare V_{OC} auf wie die auf planaren Gegenstücken hergestellten, was auf die positiven Auswirkungen der eingesetzten Strategien zur Verringerung von Spannungsverlusten hinweist. Schließlich wurden PSZs auf replizierten mikrometergroßen Texturen hergestellt, um die optischen Gewinne zu untersuchen. Dies führte zu einer bemerkenswerten Verringerung der Reflexionsverluste im Vergleich zu den planaren Gegenstücken, mit einem gewichteten AM1,5G-Reflexionsgrad von 5,2% bzw. 9,9%. Der texturierte Stapel wies eine Netto J_{SC} -Erhöhung von 1,6 mA/cm² und damit 87,3% des maximal erreichbaren J_{SC} für die verwendete Bandlücke auf, was einen der höchsten in der Literatur berichteten Werte darstellt. Darüber hinaus zeigten PSZs, die über replizierten Texturen hergestellt wurden, unter realistischen Bestrahlungsbedingungen eine anhaltend bessere Leistung.

Abstract

Given the fast increase in global energy demand and the fact that a large part of energy production relies on environmentally harmful resources, the development of eco-friendly renewable energy resources is pivotal. In this regard, photovoltaics (PV) play a key role in generating electricity without producing CO₂. Currently, the contribution of solar energy in electricity generation is ~3.6% (estimated to be ~40% in 2050), whereas 95% of the PV market is dominated by silicon (Si) solar cells. During the last decade, perovskite solar cells (PSCs) have presented themselves as strong candidate for the next generation PV technology with a current record power conversion efficiency (PCE) of 25.7%. Furthermore, integrating PSCs into a monolithic perovskite/Si tandem architecture already enabled a record PCE of 32.5%, which indicates the ability of this configuration to beat the theoretical limit of a single-junction solar cell (~33.7%). As low costs and compatibility with industrial standards are necessary for bringing the tandem technology to the market, processing perovskite thin films over textured Si sub-cells is favorable compared to employing planar polished counterparts. Furthermore, textured surfaces enable more efficient light harvesting by minimizing reflection losses and consequently result in short-circuit current density (J_{sc}) gains.

However, there are multiple challenges related to processing perovskite thin films on top of textured substrates that hamper the positive impact of optical gains. First, spin-coating conventional perovskite thin films, with a thickness of ~350-500 nm, over micrometer-sized textures, implies that some of the pyramidal tips will reach out to the surface and consequently induce detrimental shunting paths. This is accompanied by poor fill factor (FF) and open-circuit voltage (V_{oc}) in respective PSCs and, therefore, limits their device performance. Second, PSCs employing too thick perovskite absorbers can exhibit reduced charge carrier extraction that limits device performance. Third, depositing a conformal hole transport layer (HTL) over a textured surface using conventional solution-processed deposition methods is quite challenging, which might lead to inefficient hole extraction. In the same context, given the large surface area that a textured surface exhibits compared to a planar, non-radiative recombination at the HTL/perovskite interface is enhanced. Finally, considering the complex geometry of a micrometer-sized pyramidal textured surface (which consists of wall sides, tips, and valleys), the resultant perovskite film tends to exhibit high surface roughness, together with strain-related surface wrinkles that may result in a poor perovskite/electron transport layer interface. Furthermore, the presence of voids in the valleys of pyramidal textures, due to delayed solvent extraction, affect the contact between perovskite and the adjacent HTL, resulting in high series resistance and thereby low FF.

The aim of this thesis is to overcome the above-mentioned challenges by developing thick efficient perovskite absorbers as well as HTLs compatible with the textured surface, and mitigate the voltage losses associated with processing PSCs over micrometer-sized textured surfaces. First, a thick perovskite absorber (~1 μm) that assures full surface coverage over textured surfaces is developed. As the absorber thickness is in the range of the charge carrier diffusion length, a Lewis base additive is employed in the perovskite precursor solution that improves the crystallization dynamics and enhances the film's optoelectronic quality to ensure good charge carrier extraction. Next, an HTL is developed *via* vacuum-deposition method to enable conformal coating of textured surfaces while simultaneously suppressing

non-radiative recombination losses at the HTL/perovskite interface. Half-stacks employing evaporated self-assembled monolayer (SAM)-HTLs exhibited an improved implied V_{OC} from 1.145 V to 1.213 V compared to the widely used NiO_x layers. This indicates the superiority of evaporated SAMs as compared to conventional vacuum-deposited HTLs, making them a strong candidate in pushing the perovskite technology further.

Further, voltage losses in the bulk as well as at interfaces of perovskite thin films processed over textured surfaces are quantified and the reasons behind these losses are investigated *via* in-depth morphological, compositional, and microstructural analysis. In addition, a systematic guidance for employing voltage loss mitigation strategies is provided that includes: Interfacial engineering, surface passivation, processing parameters optimization, solvent engineering as well as precursor molarity and stoichiometry optimization. In this regard, employing the addressed strategies for PSCs processed over micrometer-sized textured substrates resulted in superior PV performance compared to reference devices. The corresponding average gains in V_{OC} , J_{SC} , FF, and PCE were 74 mV, 1.7 mA/cm², 6%, and 3.5%, respectively, and came along with improved short-term stability and much lower hysteresis. What is more, PSCs processed over the textured surface exhibited a comparable V_{OC} to those processed on planar counterparts, indicating the positive impact of employed voltage losses mitigation strategies. Finally, PSCs were processed over replicated micrometer-sized textures to investigate the optical gains. This resulted in a remarkable reduction in reflection losses compared to their planar counterparts, with AM1.5G weighted reflectance of 5.2% and 9.9%, respectively. The textured stack exhibited a net J_{SC} gain of 1.6 mA/cm² and a corresponding 87.3% of the maximum attainable J_{SC} for the employed bandgap, which makes it among one of the highest reported values in literature. Furthermore, PSCs processed over replicated textures exhibited a continued outperformance under realistic irradiation conditions.

Table of Contents

Kurzfassung	i
Abstract	iii
1. Introduction	1
2. Fundamentals.....	7
2.1 Hybrid organic-inorganic metal halide perovskites	7
2.2 Working principle of perovskite solar cells	9
2.3 Electrical representation and characteristics of a solar cell	10
2.4 Theoretical limit of a single-junction solar cell	14
2.5 Recombination mechanisms and voltage losses	15
2.6 The relation between recombination and V_{OC}	18
2.7 Light management	20
3. Fabrication and characterization.....	25
3.1 Fabrication methods.....	25
3.2 Characterization	31
4. Thick absorber perovskite solar cells	43
4.1 Introduction.....	44
4.2 Thickness optimization, surface coverage, and PV performance	45
4.3 Urea additive and its impact on morphology and photophysical properties.....	49
4.4 Comparison of the PV performance	52
4.5 Summary	54
5. Hole transport layers with nearly lossless interface.....	57
5.1 Introduction.....	58
5.2 Thermally evaporated SAMs and their chemical environment	59
5.3 Wettability and surface coverage.....	64
5.4 Surface morphology and crystal structure	69
5.5 Photophysical properties.....	70
5.6 Photovoltaic performance	74
5.7 Washing the evaporated SAM-HTLs.....	78
5.8 Compatibility with other perovskite absorbers	80
5.9 Compatibility with textured surfaces	82
5.10 Summary	84
6. Voltage losses mitigation and efficient light harvesting in PSCs processed over textured surfaces.....	87

Table of Contents

6.1	Introduction	89
6.2	Anti-solvent quenching and the presence of voids	90
6.3	Surface coverage, micro cracks, and voltage losses	93
6.4	Precursor stoichiometry, excess PbI_2 , and voltage losses	94
6.5	Solvent engineering, surface morphology, and voltage losses	101
6.6	Solution-processed and evaporated passivation schemes for higher V_{oc}	104
6.7	Device performance.....	106
6.8	Efficient light harvesting (textured vs planar PSCs)	111
6.9	Summary.....	118
7.	Conclusion and Outlook	121
	Appendix	127
	References	137
	List of publications and conference contributions	155
	Acknowledgments.....	159

1. Introduction

Despite the considerable effort to make human life on earth energy efficient, emission of carbon dioxide (CO₂) is still increasing.¹ Burning natural resources such as coal, natural gas, and oil for generating electricity results in detrimental by-products such as methane, CO₂, in addition to other greenhouse gasses.¹ Releasing such greenhouse gasses to the atmosphere traps the reflected solar irradiation, resulting in increased temperature of the earth's surface. This temperature increase has already shown a small portion of its negative impact such as melted Antarctic and Arctic ice caps, ocean acidity, increased sea level, etc.^{2,3} Such big challenge, that threatens the whole planet, requires fundamental change in technological trends, human behavior, and current policies. In this regard, the Paris Agreement highlighted that countries have committed themselves to reduce the carbon footprint in order to control the average temperature increase on earth.⁴ Although the addressed commitment is not impossible to achieve, it is quite challenging considering the current circumstances as well as the expected increase in future energy demands. The global energy consumption is expected to increase by ~30% in 2040 due to the corresponding world population increase and considering the future economic growth.⁵ Such expected increase in future energy demand, with the large portion of it dominated by environmentally harmful resources, will have serious consequences on human life on planet earth. Thus, the development of eco-friendly renewable energy resources such as wind and solar is pivotal.

Although nowadays solar energy contribution in generating electricity is quite low (~3.6%), the growth of photovoltaic (PV) technology sheds light on potential increase in the upcoming decades. In recent years, a considerable reduction in PV modules fabrication cost has taken place, which thereby made PV technology one of the strong candidates to increase its share in energy production. In this regard, PV technology is expected to grow further, with the potential to produce ~40% of the global energy by 2050.⁶ Although prices of generating electricity employing a rooftop-PV system has dropped drastically since 1990, leveled cost of electricity (LCOE) makes PV still lagging behind, compared to other electricity generation sources.⁷ In addition to automated mass production, increasing power conversion efficiency (PCE) plays a key role in reducing the LCOE further. On the other hand, the currently well-established silicon (Si) PV is too close to its fundamental limits (current certified record is 26.7%, where the theoretical limit is ~29.4%).⁸ A promising approach to beat the theoretical limit of a single-junction solar cell (~33.7%) and thereby reduce the LCOE is multi-junction solar cells.⁹ A typical multi-junction solar cell employs two (or more) absorber layers with different band gaps, which benefits from broad-band light absorption of the solar spectrum. A PCE of 32.8% under one Sun illumination is reported

for a gallium arsenide/Si tandem, which indicates the potential of multi-junction solar cells in beating the theoretical limit.⁸ However, typical high cost of the III-V materials (to which gallium arsenide belongs) in addition to their sensitive and complex manufacturing process is not favorable regarding LCOE. Emerging PV technologies, particularly perovskite solar cells (PSCs) have presented themselves as a strong candidate for single and multi-junction solar cells.¹⁰

Since they have been introduced to the PV community in 2009 with 3% PCE, PSCs have exhibited a remarkable progress in their PCE within the last few years, with a current certified record of 25.7%.⁸ In addition to high efficiency that PSCs exhibit, the perovskite absorber layer can be fabricated *via* various deposition techniques such as spin-coating, blade-coating, inkjet printing, and slot-die coating, employing one or hybrid two-step process.^{11–14} Furthermore, perovskite thin films can be thermally evaporated *via* co-evaporation of precursor materials or sequential layer deposition.^{15–18} Such variety of deposition techniques provides process flexibility and versatility compared to other well-established PV technologies. In addition, organic-inorganic metal halide perovskite absorbers enable band gap tunability in a range from 1.2 to 2.3 eV by optimizing the perovskite precursor stoichiometry, which makes PSCs attractive for tandem applications.^{19,20} A prominent examples is integrating PSCs in Perovskite/CIGS tandems with a current record of 24.2%.²¹ Furthermore, employing top perovskite sub-cell in perovskite/Si monolithic tandems enabled a recent record of 32.5%, which exceeds the record PCE of single-junction Si solar cells substantially and highlights the high potential of this configuration.⁸

Although the exceptionally high PCE that monolithic perovskite/Si tandems exhibit, their PV performance suffers inferior light harvesting.^{22–26} Chen *et al.* estimated current density losses of ~ 7 mA/cm² in high efficiency perovskite/Si tandem solar cells, which stem from reflection and parasitic absorption losses.²² Therefore, employing light management strategies that mitigate transmission and reflection losses is necessary for efficient light harvesting and thereby increasing PCE further.^{22–26} Antireflection coatings (ARCs) such as MgF₂ and LiF are typically used at the air/transparent conductive oxide (TCO) interface of monolithic tandems, which have been shown to reduce reflection losses due to the reduction in refractive indices contrast at this particular interface,^{27–32} however, efficient light incoupling can be obtained only if ARCs are combined with textures.^{23,33}

Researchers were inspired by nature's evolutions such as the unique texture of flowers' petals and replicated these textures onto solar cells, seeking efficient light harvesting.^{34–40} For example, Schmager *et al.* used nanoimprint lithography to replicate the texture of viola petals, which possess micro and nanotextures, onto crystalline Si solar cells with a remarkable success ($\sim 6\%$ improvement in PCE).⁴¹ In the same context, Hünig *et al.* replicated the texture of Rosa 'El Toro' petals as light harvesting elements in organic solar cells, which increased the short-circuit current density (J_{sc}) by ~ 2 mA/cm².⁴² For single-junction PSCs, Tockhorn *et al.* processed their devices onto replicated periodic nanostructures with different shapes, height, width, and periodicity. Their approach enabled efficient light incoupling and thereby obtained the record J_{sc}/J_{sq} reported so far (93.6%), where J_{sq} is the maximum attainable current density for a certain band gap.³⁷ The remarkable enhancement in J_{sc} motivated them to implement a similar approach on perovskite/Si monolithic tandems by nanotexturing the Si sub-cell, which enabled 29.8% PCE (the world record as of 24th of May, 2022).⁴³

Although employing replicated nanotextures have demonstrated exceptional reflection losses mitigation and consequently efficient light harvesting, it is more compatible with the laboratory scale rather than the industrial standards due to the high cost (which contradicts LCOE) and mass production challenges (which doesn't meet the industrial standards).^{44,45} In this regard, random pyramidal textures, employed in commercial Si PV *via* inexpensive anisotropic wet chemical etching is a better alternative. Instead of the refractive index grading that nanotextures provide, such micrometer-sized textures minimize reflection losses as they increase light incoupling probability.⁴⁶⁻⁴⁹ Furthermore, these textures induce light trapping effect and therefore, a considerable increase in optical path length that enhances the absorption probability near the band gap of the absorber is obtained.⁴⁶⁻⁴⁹ Superior light management in commercial Si PV is achieved by employing random pyramidal textures with a size of $\sim 5 \mu\text{m}$ (a typical peak to valley distance is also in the same range).^{13,50-52} Such large size textures fit perfectly with Si single-junction solar cells, however, employing such textured Si sub-cell in a monolithic perovskite/Si tandem is quite challenging. Furthermore, it constrains the process flexibility, as most of the common and efficient perovskite top cell deposition methods (mainly, solution processing) will be excluded.

Optimizing the pyramidal textures size down to $\sim 1-2 \mu\text{m}$ has been shown to maintain efficient light harvesting compared to that of the large size textures, while reducing the texture size further comes at the expense of increased reflection losses due to imperfect texturing.⁵³⁻⁵⁶ Meanwhile, optimal surface coverage over these textures requires thick perovskite absorbers to prevent detrimental shunting paths.⁵³⁻⁵⁷ On the other hand, PSCs employing thick perovskite absorbers exhibit inferior PV performance due to inefficient charge carrier extraction as a consequence of increased absorber thickness. Furthermore, thicker absorbers tend to exhibit poor optoelectronic properties, which consequently increase non-radiative recombination, resulting in an open-circuit voltage (V_{oc}) deficit. Hence, developing a thick enough perovskite absorber layer that assures optimal surface coverage over such intermediate sized pyramidal textures ($\sim 1-2 \mu\text{m}$) and simultaneously possess high optoelectronic quality is pivotal.^{53,54,58,59}

In addition to the surface coverage challenge, textured surfaces exhibit large surface area compared to their planar counterparts. Therefore, non-radiative recombination losses at the hole transport layer (HTL)/perovskite interface are expected to be much higher.^{60,61} Hence, identifying a proper HTL is crucial to mitigate the corresponding voltage losses at the HTL/perovskite interface. Furthermore, as the micrometer-sized pyramidal texture exhibits different types of surfaces in a micrometer scale (i.e. tips, valleys, and wall sides), conformal coverage of the HTL on such texture becomes crucial. Nickel oxide (NiO_x) is widely employed HTL in the inverted *p-i-n* PSCs architecture. As NiO_x can be deposited *via* vacuum-deposition methods such as electron beam evaporation and sputtering,⁶²⁻⁶⁶ it provides conformal coating on planar as well as textured surfaces, however, several studies indicated that PSCs employing NiO_x suffer relatively high hysteresis and voltage losses due to chemical interactions between NiO_x and the perovskite film.⁶⁷⁻⁷¹ Although various solution-processed HTLs such as Poly-TPD, PTAA, and self-assembled monolayers (SAMs) indicated high quality HTL/perovskite interface,⁷²⁻⁷⁴ conformal coverage of solution-processed HTLs over micrometer-sized textures remains challenging and results in low fabrication yield.^{61,75} In this regard, developing a compatible HTL with textured surfaces that provides conformal coverage and suppresses non-radiative recombination at the HTL/perovskite interface is necessary to push the PV technology further.

In the same context, various voltage losses mitigation strategies should be considered when processing perovskite films over textured surfaces. For example, introducing a surface passivation layer in between the perovskite absorber and electron transport layer (ETL), mitigates voltage losses at this interface.^{73,74,76–80} Such passivation strategies are applicable in planar single-junction PSCs and planar perovskite/Si tandems, however, the voltage gains are more pronounced when processing over textured surface due to the resultant surface roughness of the perovskite films compared to a planar counterpart. In addition to surface passivation, solvent engineering strategies enable controlling the formation of surface wrinkles and thereby enhance the perovskite/ETL interface quality.^{81–83} Furthermore, optimizing the deposition parameters prevents the formation of voids in the valleys of pyramidal textures and consequently enables higher fill factor and V_{OC} .⁶¹

To raise up for the challenges accompanied with processing PSCs over micrometer-sized pyramidal textures discussed above, we focus in this thesis on developing a thick perovskite absorber that enables optimal surface coverage over $\sim 1\text{-}2\ \mu\text{m}$ sized pyramidal textures. In the same context, we investigate the reasons behind the poor PV performance of PSCs employing such thick absorber ($\sim 1\ \mu\text{m}$ when processed over planar surface) compared to the baseline perovskite absorber counterparts ($\sim 350\ \text{nm}$). Furthermore, we adopt a bulk passivation strategy by introducing a Lewis base additive into the perovskite precursor solution, which controls the crystallization dynamics, resulting in thick perovskite films with remarkably large grains and superior optoelectronic quality. After developing a thick efficient perovskite absorber, we develop a compatible HTL with the textured surface that provides conformal coverage and suppress non-radiative recombination at the HTL/perovskite interface. Furthermore, we investigate the various voltage losses mechanisms that comes along with processing perovskites over textured surfaces and provide a systematic guidance on how to mitigate these voltage losses by employing one or more of the following strategies: solvent engineering, perovskite precursor stoichiometry and molarity optimization, interfacial engineering, processing parameters optimization, and surface passivation. The investigations, discussions, and guideline approached in this thesis provides a deeper understanding on this timely research topic and will be beneficial for scientists processing perovskites over randomly textured surfaces.

The scope of this thesis is outlined as follows:

Chapter 2: In this chapter, we discuss the fundamentals and theoretical principles that correlate to the following results chapters such as: working principle of solar cells and their theoretical limit, crystallography and optical properties of metal halide perovskites, recombination mechanisms and the accompanied voltage losses in solar cells, in addition to fundamentals of light management strategies.

Chapter 3: This chapter introduces the fabrication methods and characterization tools employed in this thesis.

Chapter 4: In this chapter, we discuss the development of a thick perovskite absorber that assures optimal surface coverage over micrometer-sized pyramidal textures, followed by the discussion of implementing additives to enhance the optoelectronic properties of the resultant thick films.

Chapter 5: This chapter introduces the development of an HTL that enables conformal coverage of the textured surface and suppresses non-radiative recombination at the

HTL/perovskite interface.

Chapter 6: Having developed a thick efficient perovskite absorber together with a compatible HTL, this chapter provides further investigations on voltage losses mitigation strategies in PSCs processed over textured surfaces. Applying these strategies enabled comparable V_{oc} to that of planar references, thus, we further discuss the impact of processing perovskites over textured surfaces on the optical gains and consequently PCE.

Chapter 7: This chapter summarizes the key results in this thesis and provides an outlook.

2. Fundamentals

In this chapter, we discuss some of the theoretical principles which will reinforce understanding of the results in subsequent chapters. First, we introduce the metal halide perovskites, explaining their crystallography and outstanding optoelectronic properties, which made them attractive materials for photovoltaic (PV) applications. Afterwards, we discuss solar cell basic principles, electrical representation, and characteristics. Finally, we recall the theoretical limits of solar cells as introduced by Shockley and Queisser and shed some light on why the PV parameters of solar cells are generally failing to achieve these theoretical limits.

2.1 Hybrid organic-inorganic metal halide perovskites

Perovskites are named after Count Lev Alekseyevich von Perovski, the mineralogist who first discovered them. They are typically compounds represented by the general formula ABX_3 , where X is an anion, A and B are large- and middle-sized cations, respectively.⁸⁴ In principle the physical, chemical, and optoelectronic properties of perovskites can be modified by controlling the type and ratio of the components thereof, which makes perovskites attractive semiconductors. In this section, we discuss some of the important properties of organic-inorganic metal-halide perovskites.

2.1.1 Crystallography of ABX_3 perovskites

The structural properties of ABX_3 perovskites are typically described by A-site cations in the center of a cuboctahedral, while the B-site cation and the X anion are sharing the corners with BX_6 octhedra as shown in Figure 2.1. For organic-inorganic perovskite crystals designed for PV applications, the X anion is typically iodine (I⁻), bromide (Br⁻), or chloride (Cl⁻).^{85,86} A composition of two or more anions with some certain ratios is also valid and considered to be one of the valuable advantages that perovskites possess.^{85,86} Common B-site cations are lead (Pb⁺²) and tin (Sn⁺²), while the A-site cation is represented by one or a mixture of organic [such as formamidinium (FA⁺) and methylammonium (MA⁺)] and inorganic [such as cesium (Cs⁺) and rubidium (Rb⁺)] cations.⁸⁷ Prominent examples would be $FAPbI_3$ for single-cation perovskite composition,⁸⁸ $Cs_{0.17}FA_{0.83}PbI_{2.75}Br_{0.25}$ for double-cation and double-anion (which we will report in Chapter 4 and Chapter 6),⁶¹ and $Cs_{0.05}MA_{0.22}FA_{0.73}Pb(I_{0.77}Br_{0.23})_3$ for triple-cation and double-anion (which we will report in Chapter 5).⁶⁰

The perovskite crystal structure is both stoichiometry and temperature dependent, and dominated by the arrangement of cations and anions in the crystal, resulting in cubic (aka. α -phase), orthorhombic (aka. γ -phase), or tetragonal (aka. β -phase) structures.⁸⁹ For a certain

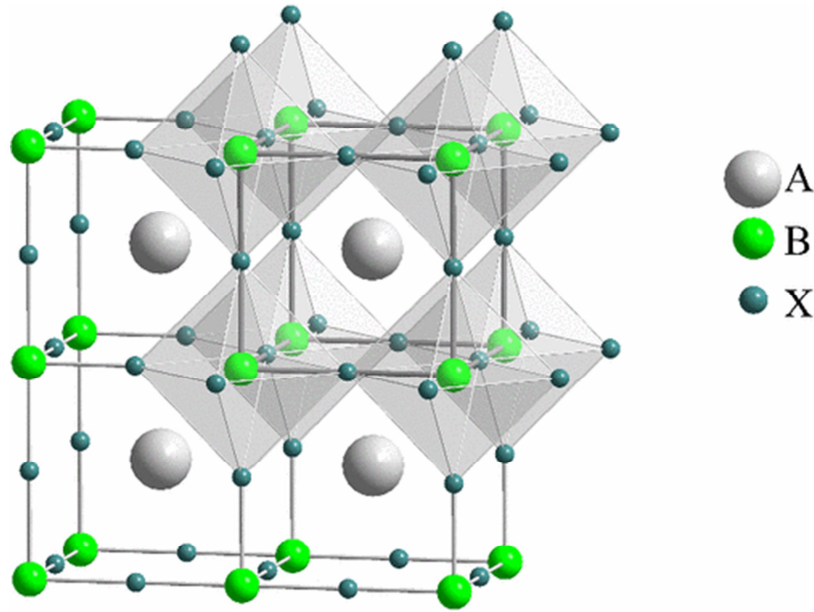


Figure 2.1. Schematic illustration of ABX_3 perovskite structure with BX_6 octahedra sharing the corners. Adapted from ref.³⁵⁷ with permission of the American Physical Society.

organometal halide perovskite, the stability of the crystal structure is governed by the Goldsmith equation as follows:^{86,90}

$$t = \frac{r_A + r_B}{\sqrt{2} (r_B + r_X)} \quad (2.1)$$

Where t is the Goldschmidt's tolerance factor, r_X , r_A , and r_B are the ionic radii of metal halide, organic cation, and metal cation, respectively. Lower values of the tolerance factor ($\sim t < 0.8$) result in decreased symmetry of the structure with a corresponding tilt in BX_6 octahedra.⁹¹ Furthermore, higher values of the tolerance factor ($\sim t \gg 1$) mean that the A-site cations would not fit into the crystal lattice due to their corresponding large size. On the other hand, a typical tolerance factor value in the range of ($1 > t > 0.8$) results in a three-dimensional stable cubic phase.^{85,91}

2.1.2 Optoelectronic properties

Unlike crystalline silicon (Si), which has an indirect optical band gap, where the optical excitation of an electron from the valence band to conduction band is mediated by a phonon (aka. lattice vibration), perovskites are classified as direct band gap semiconductors.⁹² In this regard, a thin layer of perovskite absorber (typically, ~ 350 nm) is sufficient for light harvesting due to the high absorption coefficient (α) that a perovskite absorber layer exhibits ($\alpha > 10^4$ cm^{-1}).⁹¹ In addition, the low binding energy of photogenerated excitons in a perovskite absorber (in the meV range), requires low amounts of energy to separate excitons into electron-hole pairs and therefore, high density of free charge carriers can be generated.⁹³ Although free charge carriers generated in a perovskite absorber demonstrate high mobility ($\mu \approx 10$ $\text{cm}^2 \text{V}^{-1} \text{s}^{-1}$), typical charge carrier diffusion length is considerably low (up to the low μm range) due to the high trap density.⁹⁴

When it comes to band gap engineering and tunability, perovskites exhibit a considerable versatility and flexibility. Such band gap engineering is performed *via* tuning the perovskite stoichiometry.²⁰ Density functional theory studies have indicated that coupling between an antibonding state of the B-site cation s orbital and the p orbital of the X-anion is responsible for generating the valence band maxima.^{19,20,95} In addition, coupling nonbonding B cation and X anion p orbitals is responsible for generating the conduction band minima. Thus, fine-tuning the band gap of perovskite absorbers can be done *via* elemental substitution or a change in the stoichiometry of the B and/or X-sites of the perovskite structure.^{19,20,95} For example, the triple-cation perovskite composition $\text{Cs}_{0.05}\text{MA}_{0.22}\text{FA}_{0.73}\text{Pb}(\text{I}_{0.77}\text{Br}_{0.23})_3$ has a band gap of ~ 1.68 eV, on the other hand, decreasing the Br percentage from 23% to 10% results in a ~ 1.58 eV band gap. Therefore, perovskites with their wide range of possible band gaps are being implemented in multijunction solar cells such as perovskite/Si,^{24,25,100–107,28,29,31,74,96–99} perovskite/CIGS,^{21,108–111} and all perovskite tandems.^{112,113}

2.2 Working principle of perovskite solar cells

A single-junction PSC adopts either *p-i-n* (which we report on in this thesis) or *n-i-p* architecture, where *i* refers to an intrinsic metal-halide semiconducting absorber layer, sandwiched between two charge transport layers (CTLs), which are typically *n* and *p*-type semiconductors.¹¹⁴ The basic operation principle of a PSC can be summarized in five steps as illustrated in Figure 2.2a. (1) under illumination, incident photons are absorbed within the perovskite absorber layer, (2) the absorbed photons generate excitons (bounded electron-hole pairs), (3) the excitons are dissociated into free charge carriers (i.e. free electron-hole pairs), (4) the free charge carriers are separated and collected by the selective contacts (the CTLs), (5) and finally, the electrons are extracted by the conductive electrodes to external circuit and thereby derive a current.^{114–117}

Although excitons generated in a perovskite absorber under illumination exhibit very low binding energy, heterojunction interfaces are necessary to dissociate the photogenerated electron-hole pairs and facilitate their extraction, which indicates the importance of CTLs in a PSC layer stack.^{78,118} The CTLs, which are typically electron transport layer (ETL) and hole transport layer (HTL), modify the work function of electrodes and thereby reduce the built-in potential barriers, thus, they enable efficient charge carrier extraction.⁷⁸ In this regard, band-alignment engineering at the HTL/perovskite and perovskite/ETL also plays a key role in charge carrier extraction.⁷⁸ An ideal ETL for example, would facilitate electrons extraction at the perovskite/ETL interface and simultaneously block holes (consequently, non-radiative recombination losses are mitigated, see Section 2.5), which is fulfilled if the ETL has a deeper (compared to the vacuum energy level) conduction and valence band than that of the perovskite semiconductor.^{78,118} Due to the key role that CTLs play in pushing the PCE of PSCs further, continuous development of CTLs is a major research focus.^{119–121}

The band diagram of a typical PSC is described by a flat band representation,^{122–125} where the Fermi level (E_F) equilibrates over the device (in the absence of bias voltage and light). Under continuous illumination and short-circuit condition (*p* and *n*-type are connected), the photogenerated charge carriers are efficiently extracted at the CTLs due to the sufficiently large band offset at the interfaces. Therefore, there are no buildup of photogenerated charge carriers at the conduction and valence band and consequently, E_F doesn't shift. In this case, photogenerated current (I_{ph}) represents the maximum attainable value by the cell and is

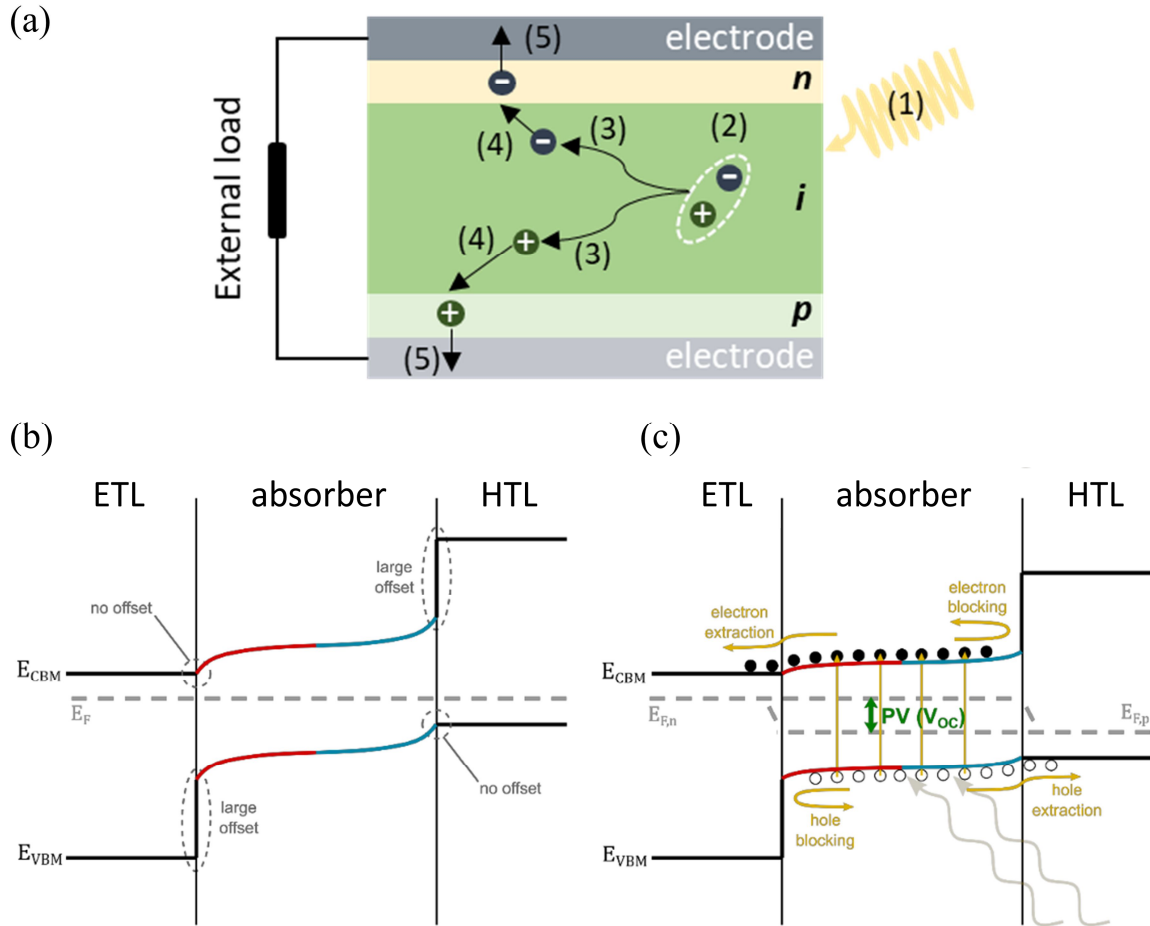


Figure 2.2. (a) Schematic illustration of charge carriers generation and extraction in a perovskite solar cell under illumination. (b) and (c) Schematic illustration of p - i - n energy band diagram in the dark and under illumination, respectively. Part of this figure is adapted from ref.¹²⁵

called short-circuit current (I_{sc}). Under continuous illumination and open-circuit condition (p and n -type are not connected), where the net flow current is zero, the photogenerated charge carriers results in increased charge carrier density in the conduction and valence bands, resulting in the so called quasi-Fermi level splitting (QFLS) (see Figure 2.2).^{122–126} In this regard, the generated photovoltage across the cell is at its maximum and called open-circuit voltage (V_{oc}), which is equivalent to the difference between the two quasi-Fermi levels. Under operation conditions (continuous illumination together with a connected external load), both photocurrent and photovoltage are generated, resulting in output power.

2.3 Electrical representation and characteristics of a solar cell

An ideal solar cell, which does not exhibit any power dissipation due to parasitic resistance or current leakages, can be represented by a current source and a single diode as shown in Figure 2.3a.¹²⁷ In this case, the output current (I) is given by the following equation:

$$I = I_{ph} - I_d \quad (2.2)$$

Where I_{ph} is the photogenerated current and I_d is the diode current, which is defined by the Shockley diode equation as follows:

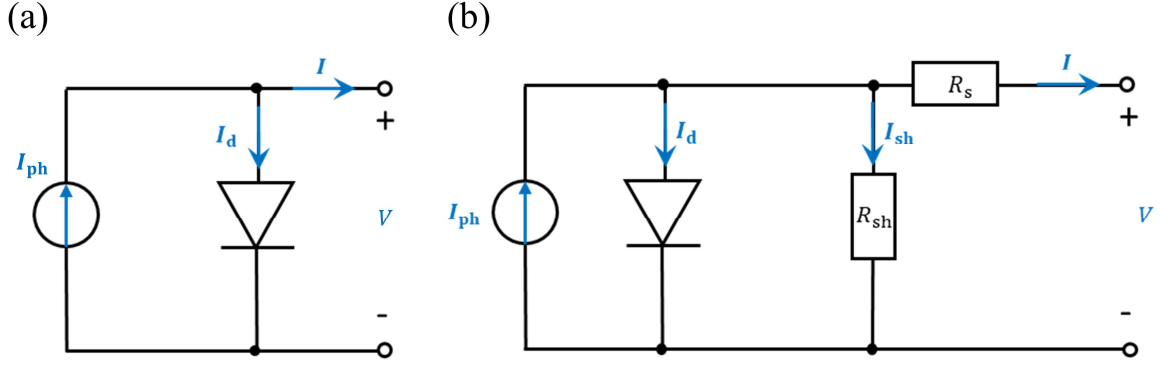


Figure 2.3. Electrical representation of a solar cell in ideal case (a) and considering the one-diode model (b).

$$I_d = I_0 \left(e^{\frac{qV}{n k_B T}} - 1 \right) \quad (2.3)$$

Where I_0 is the reverse saturation current (aka. dark current), q is the electron charge, V is the voltage across the diode, n is the diode ideality factor, k_B is Boltzmann's constant, and T is the temperature.

In fact, the model described above and displayed in Figure 2.3a is far from reality as a solar cell typically encounters electrical resistance as well as leakage current, which should be considered in the electrical representation. Figure 2.3b displays a more plausible model that includes a series resistance (R_s) and shunt resistance (R_{sh}). Accordingly, equation (2.2) will be updated as follows:¹²⁸

$$I = I_{ph} - I_d - I_{sh} \quad (2.4)$$

Thus, the output current density ($J = I/A$), where A is the active area of solar cell, is given by:

$$J(V) = J_{ph} - J_0 \left[\exp \left(\frac{q(V + J(V) A R_s)}{n k_B T} \right) - 1 \right] - \frac{V + J(V) A R_s}{R_{sh}} \quad (2.5)$$

Equation (2.5) provides the current density-voltage (J - V) characteristics of a solar cell represented by one-diode model and considering the effect of shunt and series resistance. The J - V characteristics of an ideal solar cell can be obtained from equation (2.5) by neglecting the effect of parasitic resistance ($R_{sh} = \infty$ and $R_s = 0$), and thus described as:

$$J(V) \approx J_{ph} - J_0 \left[\exp \left(\frac{qV}{n k_B T} \right) - 1 \right] \quad (2.6)$$

A typical J - V curve of a solar cell (see Figure 2.4a) is obtained by sweeping the voltage with a constant scan rate and measuring the output current (and thereby defining the current density from $J = I/A$) under illumination. The resultant J - V curve indicates the metric parameters of solar cell which correlates to its PV performance as follows:

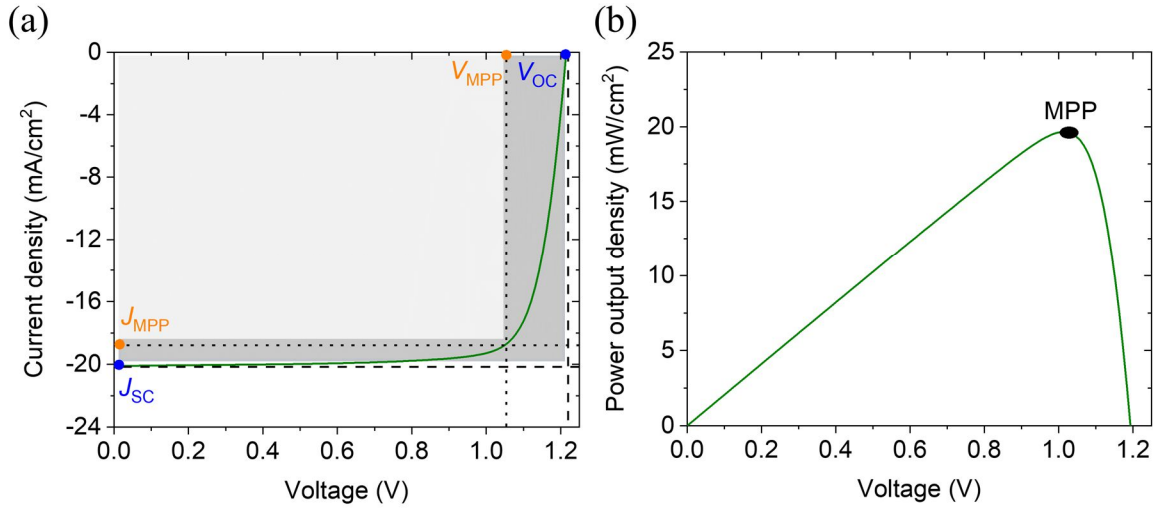


Figure 2.4. (a) Current density-voltage (J - V) characteristic of a solar cell. (b) The corresponding maximum power point.

Open-circuit voltage

As discussed in Section 2.2, when a solar cell is operated under open-circuit condition, current flow is zero and the voltage across output terminals is the maximum attainable value, which is V_{OC} of the cell. Given that the current density is zero under V_{OC} condition, substitution in the characteristics equation (2.6) implies:

$$V_{OC} \approx \frac{n k_B T}{q} \ln \left(\frac{J_{ph}}{J_0} + 1 \right) \quad (2.7)$$

Where equation (2.7) indicates the temperature dependence of V_{OC} .

Short-circuit current density

When a solar cell is operated under short-circuit condition, voltage drop in this particular case is zero and the output current is represented by the maximum attainable value, which is I_{SC} of the cell with a corresponding short-circuit current density $J_{SC} = I_{SC}/A$. Given that the voltage is zero under short-circuit condition, substituting in the characteristics equation (2.6) implies:

$$J_{SC} \approx J_{ph} \quad (2.8)$$

Maximum power point

Having introduced J_{SC} and V_{OC} , it is important to introduce the conditions in which the solar cell is being operated in realistic field applications. Here, the solar cell should be operated at its maximum power point (MPP), which can be identified by plotting the power output density ($P = JV$) versus the sweeping voltage (V) as shown in Figure 2.4b. The MPP is given by ($P_{MPP} = J_{MPP} V_{MPP}$), where J_{MPP} and V_{MPP} are the current density and voltage at MPP, respectively. Tracking the MPP as a function of time provides an indication about the stability of solar cell.

Fill factor

Fill factor (FF) is a measure of the difference between the theoretical maximum attainable output power defined by ($P = J_{SC} V_{OC}$), to the actual output power at the maximum power point as indicated by equation (2.9) and displayed in Figure 2.4a. The fill factor strongly depends on V_{OC} and thus on the prevailing recombination mechanism in a solar cell as will be discussed in Section 2.5.^{129,130} Furthermore, the fill factor in the one-diode model shown in Figure 2.3b is negatively influenced by parasitic resistive losses as a result of either increased R_s and/or reduced R_{sh} as shown in Figure 2.5a,b.^{129,130}

$$FF = \frac{J_{MPP} V_{MPP}}{J_{SC} V_{OC}} < 1 \quad (2.9)$$

Power conversion efficiency

The power conversion efficiency (PCE) of a solar cell is given by the ratio of output (P_{out}) and input power (P_{in}), where P_{out} and P_{in} are typically the maximum power point and the power of incident light, respectively. Under standard testing conditions, where AM1.5G spectrum is used, the integrated power density of 1000 W/m^2 is employed (i.e. $P_{in} = 1000 \text{ W/m}^2$). As P_{MPP} of a solar cell relates to its J_{SC} , V_{OC} , and FF as indicated by equation (2.9), PCE of the solar cell can be calculated from these values as follows:

$$PCE = \frac{J_{SC} V_{OC} FF}{1000 \text{ W/m}^2} \quad (2.10)$$

Hysteresis factor

A typical J - V measurement of a solar cell is performed in reverse scan (from open-circuit to short-circuit condition) and forward scan (from short-circuit to open-circuit condition).¹³¹ An ideal solar cell should exhibit the same J - V characteristic and thereby the exact PCE in both forward and reverse scans. However, hysteresis is a typical phenomenon, especially in perovskite solar cells, which correlates to changes in scan direction, resulting in a change in the J - V characteristics (which is mainly attributes to different FF and V_{OC} as shown in Figure 2.5c).¹³² In this regard, another metric parameter indicates the PV performance of a solar cell is the hysteresis factor (HF) and described by the following equation:

$$HF = \frac{PCE_{Reverse} - PCE_{Forward}}{PCE_{Reverse}} \quad (2.11)$$

Hysteresis is correlated to the quality of the perovskite absorber as well as the interfaces (HTL/perovskite and perovskite/ETL). One of the common hysteresis causes in perovskite solar cells (PSCs) is ion migration,^{133,134} which results in accumulation of the ions at the interfaces of the perovskite absorber with the charge transport layers (CTLs) and thereby impacts extraction efficiency and FF.¹³²⁻¹³⁴ Furthermore, the accumulation of ions at interfaces induce trap states, which results in detrimental non-radiative recombination and thus a reduction in V_{OC} (see Figure 2.5c).¹³³⁻¹³⁵ In the same context, as discussed in Section 2.2, optimum energetic alignment between the perovskite absorber and adjacent CTLs is crucial.¹³⁶ A perfect CTL is energetically aligned such that it allows a smooth extraction of a specific charge type (electron or hole), meanwhile blocks the extraction of the other type, and thus preventing the common S-shape (see Figure 2.5d) that results in high HF.^{132,136}

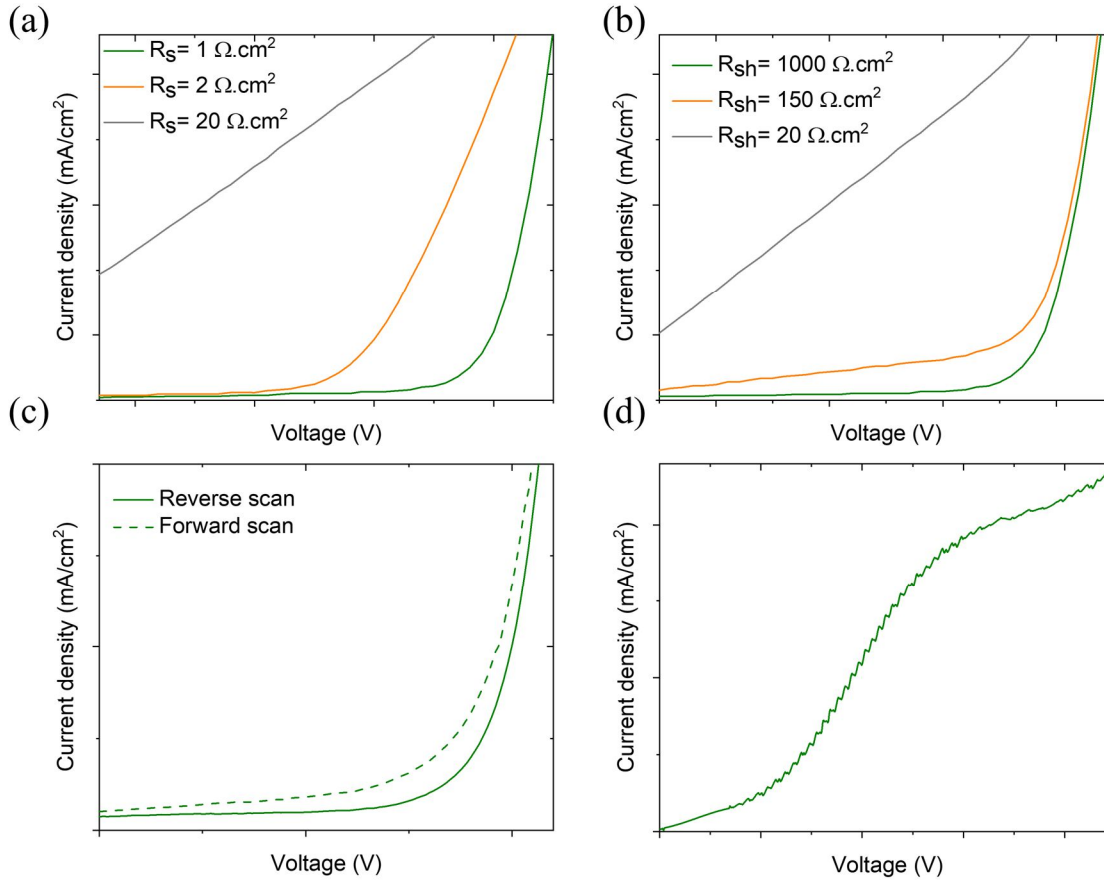


Figure 2.5. (a) and (b) Impact of series and shunt resistance on $J-V$ characteristic, respectively. (c) $J-V$ characteristic in forward and reverse scan, indicating hysteresis. (d) $J-V$ characteristic indicating S-shape due to inefficient charge carrier extraction.

2.4 Theoretical limit of a single-junction solar cell

In 1961, Shockley and Queisser introduced the detailed balance limit model,¹³⁷ which correlates the maximum attainable PCE of a solar cell to its absorber's band gap (known as S-Q limit) considering the following approximations:

- (i) All the incident light is absorbed for photons with energy $h\nu \geq E_g$, where ν is the frequency of the photon and E_g is the absorber's band gap.
- (ii) Each absorbed photon generates an electron-hole pair.
- (iii) All generated charge carriers are extracted and thereby contribute in the output current.
- (iv) The charge carrier can only recombine *via* radiative recombination.

In their model, S-Q considered thermalization losses for photons with energies higher than the band gap. Optical losses represented by the transmission of photons with energies lower than the band gap are also considered. The model represented the maximum theoretical limit of the PV parameters (J_{sc} , V_{oc} , FF, and PCE) as a function of the band gap as indicated in Figure 2.6. Remarkably however, the model is neglecting some important considerations. For example, not all the incident photons with energy higher than the band gap are going to be absorbed as some of the incident light will be reflected (i.e. reflection losses are taking place, will be discussed in Section 2.7).¹³⁸ In addition, the absorption probability near the

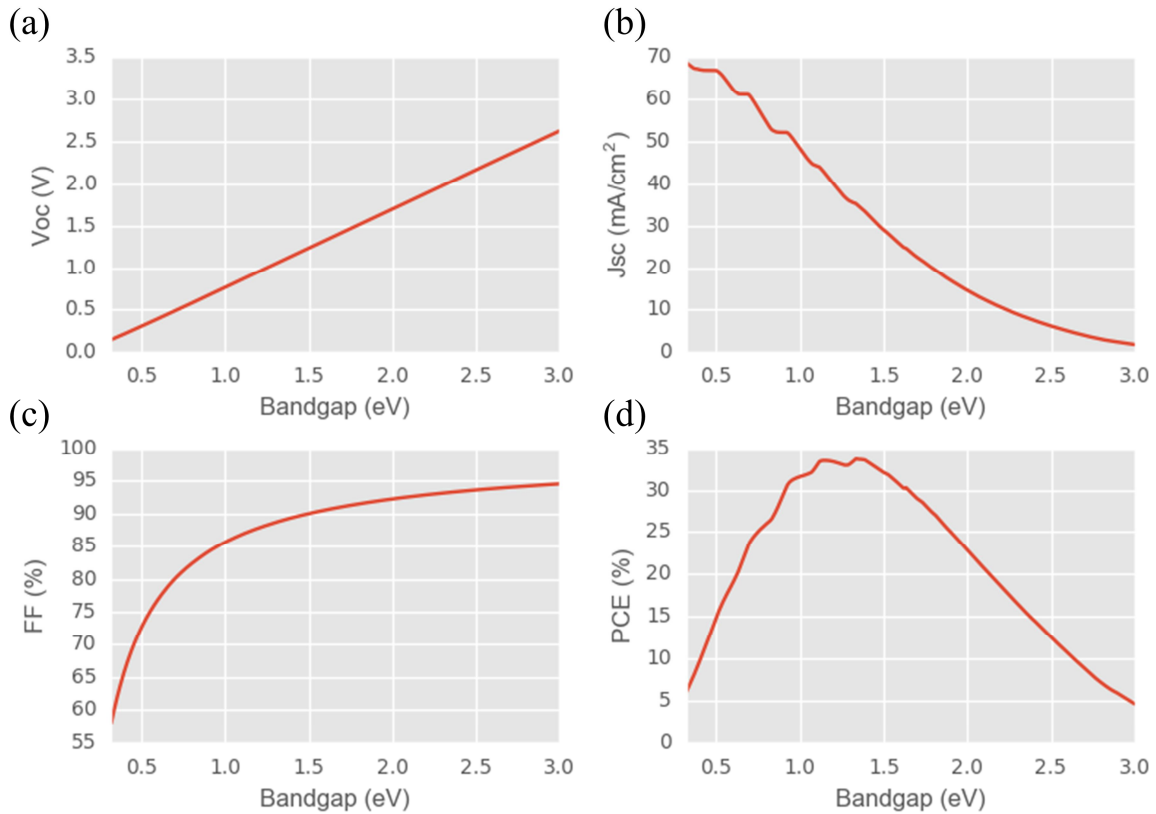


Figure 2.6. Theoretical limit of the photovoltaic parameters as a function of the absorber's band gap based on detailed balance limit of Shockley and Queisser. Adapted from ref.³⁵⁸

band gap decreases at the exponential tail of the absorption edge.¹³⁹ Such optical losses results in J_{sc} deficit in the solar cell and therefore, the maximum attainable current density, which is given by the ratio of the measured J_{sc} to the theoretical current-density limit (J_{SQ}), is less than 100% (the highest reported value in literature is 93.6% by Tockhorn *et al.*³⁷).

Furthermore, the model is considering a diode ideality factor of one, thus, all recombination is radiative, which is not achievable practically as a typical solar cell encounter non-radiative recombination losses (discussed in the following section) and therefore, the solar cell is V_{oc} deficit compared to the theoretical limit (the highest reported value in literature is 90% by Garibzadeh *et al.*¹⁴⁰). Considering these losses, the record single-junction silicon and perovskite solar cell is 27.6% and 25.7%, respectively,⁸ which is still far below the theoretical limit of a single junction solar cell ($\sim 33.7\%$). As this thesis approaches different voltage losses mitigation strategies as well as light management concepts to reduce the gap to the corresponding theoretical limit, we will discuss in the following some of the main voltage and optical losses in PSCs.

2.5 Recombination mechanisms and voltage losses

As discussed in Section 2.4, the detailed balance limit model considers the diode ideality factor to be one, or in other words, all the recombination in solar cell is governed by radiative recombination. In fact, a typical solar cell would exhibit different types of non-radiative recombination mechanisms such as interfacial recombination (due to defects at the HTL/perovskite and perovskite/ETL interface), Shockley-Read-Hall Recombination (SRH),

and Auger recombination as indicated in Figure 2.7.^{141–143} Non-radiative recombination in PSCs is dominated by interfacial as well as SRH recombination under standard testing condition (i.e. at one Sun).¹⁴⁴ At high injection levels with irradiation intensities above 100 Suns, Auger recombination is more prominent.¹⁴⁴ In the following, we briefly discuss the various recombination mechanisms and their impact on V_{OC} of PSCs.^{141,142,144,145}

2.5.1 Radiative recombination

Radiative recombination (aka. direct band to band recombination) is the process of electron relaxation from the conduction band to valence band accompanied with light emission where the emitted photon's energy is almost equivalent to the band gap as illustrated by the schematic diagram in Figure 2.7. The recombination rate is typically dependent on free electrons and free holes concentration, thus, radiative recombination rate (R_r) is written as:

$$R_r = B_r np \quad (2.12)$$

Where n and p are the electron and hole densities, respectively, and B_r is the proportionality constant. Given that hybrid perovskites are direct band gap semiconductors, typical radiative recombination rates are in the range of 10^{-10} - 10^{-11} cm^3/s , which is orders of magnitude higher than that of the indirect band gap Si counterpart ($\sim 10^{-15}$ cm^3/s).^{146,147}

In principle, if all the recombination in a solar cell is governed only by radiative recombination, the photoluminescence quantum yield is 100%, its internal ideality factor is exactly one, and its V_{OC} would be equivalent to the theoretical limit. However, a solar cell exhibits various non-radiative recombination mechanisms, which we discuss briefly in the following.

2.5.2 Interfacial recombination

Interfacial recombination (aka. surface recombination) is dominating non-radiative recombination in PSCs and thereby limiting their V_{OC} .^{76–78} Non-radiative interfacial recombination takes place at the surface of perovskite absorber layer near the HTL/perovskite and perovskite/ETL interface. The surface recombination rate (R_s) of a semiconductor (for example n-type, where the majority charge carriers are electrons and expected to be trapped at the surface by a hole/defect) is given by the following expression:

$$R_s \approx S_r(p_s - p_0) \quad (2.13)$$

Where p_s is the hole concentration at the surface, p_0 is the thermal equilibrium hole concentration, and S_r is the thermal recombination velocity given by:⁷⁶

$$S_r = v_{th} \sigma_p N_{sT} \quad (2.14)$$

Where v_{th} is the thermal velocity, σ_p is the holes capture cross-section, and N_{sT} is the surface trap density.

The interfacial recombination mechanism is attributed to various potential reasons such as (i) trap-assisted recombination at the interface of perovskite thin film with the CTLs. (ii)

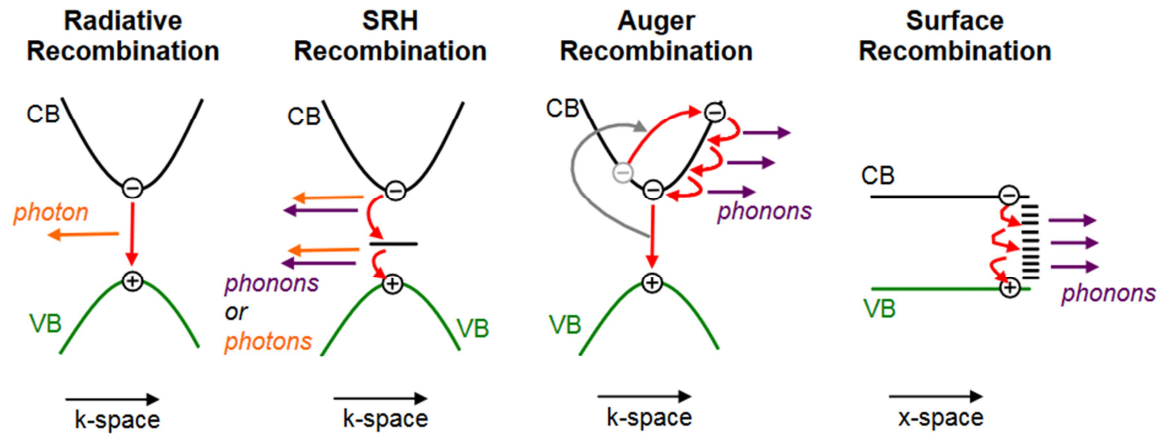


Figure 2.7. Schematic illustration of different recombination mechanisms in solar cells. Adapted from ref.¹⁴³

induced deep trap states because of direct contact between the perovskite film and the CTLs (surface roughness plays a key role here as will be discussed in Chapter 6). (iii) significant mismatch of the energetic alignment between the perovskite and the adjacent CTLs (optimum alignment enables efficient extraction of the charge carriers and thereby decreases their interfacial recombination probability as discussed in Section 2.2).⁷⁸ Such mismatch can also induce back-transfer recombination.¹⁴⁸ (iv) crystal lattice mismatch at the interfaces, which prone to result in high number of dangling bonds and thereby induces high defect density at the surface.¹⁴⁹ Under illumination and considering the previously mentioned various non-radiative interfacial recombination factors, a reduction in the density of steady state charge carriers takes place.^{78,149} Consequently, in non-equilibrium state, quasi-Fermi level splitting of the illuminated absorber is reduced (which correlates to V_{OC} losses, as we will discuss in Section 2.6). As a side note, we are investigating voltage losses mechanisms of thick PSCs processed over micrometer-sized pyramidal textures, hence, the interfacial recombination in such case is more pronounced due to the larger surface area that a textured surface exhibits compared to a planar counterpart. To mitigate the dominant interfacial non-radiative recombination losses, we developed HTLs compatible with textured surfaces to enhance the HTL/perovskite interface optoelectronic quality (will be discussed in Chapter 5). We also applied surface passivation schemes as well as solvent engineering strategies to suppress non-radiative recombination at the perovskite/ETL interface (will be discussed in Chapter 6).

2.5.3 SRH recombination

The theory of non-radiative SRH recombination (aka. trap-assisted recombination) was presented by W. Shockley, W. Read, and R. Hall in 1952.¹⁵⁰ The non-radiative recombination is facilitated by lattice defects or impurities that act as recombination centers. These recombination centers introduce energy levels within the semiconductor's band gap and thereby facilitate charge carrier recombination.^{151–153} The recombination levels are typically classified into two types, namely donor-type traps (residing between the intrinsic Fermi level and the valence band) and acceptor-type traps (residing between the conduction band and the intrinsic Fermi level).¹⁵⁴ The non-radiative recombination mechanisms are (i) capture of an electron from the conduction band (ii), emission of an electron from the trap

state to the conduction band (iii) capture of a hole from the valence band, and (iv) emission of a hole from the valence band. The emission/capture of a charge carrier from/by a trap state is typically accompanied with absorption/emission of phonons (aka. lattice vibration).¹⁵⁴

Foreign atom impurities in addition to crystallographic deformations induce different types of charged defects as well as higher-dimensional defects such as interstitials, vacancies, dislocations, grain boundaries, and anti-site substitutions.^{142,151,152} In this regard, enhancing the quality of perovskite thin film and thereby its optoelectronic properties is necessary to suppress SRH non-radiative recombination losses. Various strategies are followed in literature to enhance the perovskite film quality *via* bulk passivation by employing certain additives to the perovskite precursor solution.^{94,100,163,155–162} In this thesis, we developed a strategy to control the crystallization dynamics of thick perovskite films that enables growing larger grains with a corresponding lower trap density as will be discussed in Chapter 4.

2.5.4 Auger recombination

Another type of non-radiative recombination loss is the trimolecular (three-particle process) Auger recombination.^{151,164–166} In this process, the energy and momentum resulting from an electron-hole pair recombination is transferred to another electron or hole (instead of emitting a photon with energy equivalent to that of the band gap as in radiative recombination described earlier).¹⁶⁴ This third electron/hole is therefore injected deeper into the conduction/valence band, followed by its further relaxation *via* thermalization. The Auger recombination probability is strongly dependent on charge carrier density since three carriers are conditional to interact this way. The Auger recombination rate R_{Aug} is given by the following equation:¹⁶⁵

$$R_{Aug} = C_n n^2 p + C_p n p^2 \quad (2.15)$$

Where n and p are the electron and hole concentration, respectively, C_n , and C_p are the proportionality constants. Although Auger non-radiative recombination is quite dominant in Si solar cells with their indirect band gap, heavily doped absorbers, and consequently the high charge carrier concentration they exhibit, it is less dominant in PSCs compared to the other recombination mechanisms discussed earlier.^{151,166}

2.6 The relation between recombination and V_{OC}

Recalling the detailed balance limit discussed in Section 2.4, where Shockley and Queisser considered (i) radiative recombination between electrons and holes is the only valid mechanism and (ii) all incident light is absorbed, with each absorbed photon generating electron-hole pair, and the generated charge carriers are extracted efficiently. In this regard, the saturation current density ($J_{0,SQ}$) can be expressed by the following equation:¹⁶⁷

$$J_{0,SQ} = q \int_0^{\infty} A(E) \phi_{bb}(E) dE = q \int_{E_g}^{\infty} \phi_{bb}(E) dE \quad (2.16)$$

Where $A(E)$ is the absorptance as a function of incident photon energy, which is zero for photons with energies lower than the absorber's band gap and otherwise one (as assumed in the detailed balance limit). ϕ_{bb} is the black body radiation, which is temperature (T) dependent and expressed as follows:

$$\phi_{bb} = \frac{2\pi E^2}{h^3 c_0^3} \frac{1}{\exp(E/k_B T) - 1} \approx \frac{2\pi E^2}{h^3 c_0^3} \exp\left(\frac{-E}{k_B T}\right) \quad (2.17)$$

Where E is the photon energy, k_B is Boltzmann's constant, c_0 is the speed of light in vacuum, h is Planck's constant, and the right hand side of the equation is obtained by employing the Boltzmann's approximation for $E \geq 3 k_B T$.¹⁶⁷⁻¹⁶⁹

The radiative dark current density ($J_{0,\text{rad}}$ aka. recombination current density) at low mobilities can be calculated by replacing the absorptance in equation (2.16) by the external quantum efficiency (EQE) as follows:¹⁶⁷

$$J_{0,\text{rad}} = q \int_0^{\infty} EQE(E) \phi_{bb}(E) dE \quad (2.18)$$

As per the detailed balance limit approximation, all photo induced charge carriers can only recombine *via* radiative recombination and therefore, radiative current density is equivalent to J_{SC} . As discussed in Section 2.3, the V_{OC} can be expressed by the following equation:

$$V_{OC} \approx \frac{n k_B T}{q} \ln\left(\frac{J_{ph}}{J_0} + 1\right) \quad (2.19)$$

In this regard, radiative open-circuit voltage ($V_{OC-\text{rad}}$) is obtained by substituting in equations (2.19) from equation (2.16) after considering the S-Q approximations: $V_{OC} \rightarrow V_{OC-\text{rad}}$, $J_0 \rightarrow J_{0-\text{rad}}$, $n \rightarrow 1$ and $J_{ph} \rightarrow J_{SC}$ as follows:^{157,170}

$$V_{OC-\text{rad}} \approx \frac{k_B T}{q} \ln\left(\frac{\int_0^{\infty} EQE(E) \phi_{\text{sun}} dE}{\int_0^{\infty} EQE(E) \phi_{bb} dE}\right) \approx \frac{k_B T}{q} \ln\left(\frac{J_{SC}}{J_{0-\text{rad}}}\right) \quad (2.20)$$

Remarkably however, as we came across different recombination mechanisms (discussed in Section 2.5), a typical solar cell suffers non-radiative recombination losses and therefore, external V_{OC} (which takes into account interfacial as well as bulk non-radiative recombination) is always lower than $V_{OC-\text{rad}}$ (which considers only radiative recombination). The open-circuit voltage losses ($\Delta V_{OC,\text{non-rad}}$) can be calculated by implementing photoluminescence quantum yield (PLQY) into the following equation:^{157,170,171}

$$\Delta V_{OC,\text{non-rad}} = V_{OC-\text{rad}} - V_{OC} = -\frac{k_B T}{q} \ln \text{PLQY} \quad (2.21)$$

Where PLQY is given by the ratio of emitted photon flux (φ_{em}) to absorbed photon flux (φ_{abs}) as follows:¹⁷²

$$\text{PLQY} = \frac{\varphi_{\text{em}}}{\varphi_{\text{abs}}} = \frac{J_{\text{rad}}}{J_G} = \frac{J_{\text{rad}}}{J_{\text{non-rad}} + J_{\text{rad}}} \quad (2.22)$$

Where J_G , is the generation current density, which is equivalent to recombination current under open-circuit condition (i.e. the net current flow is zero).

Equations (2.21) and (2.22) imply that for an ideal solar cell, where PLQY is 100%, $\Delta V_{OC,non-rad} = 0$, or in other words, an ideal solar cell would not exhibit any V_{OC} losses. Practically, performing PLQY measurements at one Sun, enables quantifying non-radiative recombination losses in PSCs, determines the QFLS (aka. implied V_{OC}), and sheds light on the nature of the dominant recombination losses.^{157,170–172} The QFLS correlates to V_{OC} via $QFLS = qV_{OC}$, thus, equation (2.21) can be written as follows:

$$QFLS = qV_{OC-rad} + k_B T \ln PLQY \quad (2.23)$$

Furthermore, performing intensity dependent PLQY measurements (instead of measuring at one Sun) enables quantifying the ideality factor of solar cell.^{79,126,157,170,172–174} Recalling the electrical description of a solar cell described by the one-diode as discussed in Section 2.3, and based on the assumption of detailed balance limit (every recombination is radiative) the diode ideality factor equals one. On the other hand, based on our discussion in Section 2.5, where a typical solar cell exhibits various non-radiative recombination losses, a more plausible electrical description would be the two-diode model.^{175,176} The internal ideality factor (n_{id}) can be obtained from the intensity dependent PLQY measurements (and consequently, intensity dependent QFLS as follows):^{157,170–172}

$$n_{id} = \frac{q}{k_B T} \frac{dV_{OC}}{d \ln(I/1 \text{ mW/cm}^2)} \quad (2.24)$$

Where $(I/1 \text{ mW/cm}^2)$ is the irradiance intensity in Sun. In principle, n_{id} is governed by interfacial as well as bulk recombination.^{79,126,173,174} A smaller n_{id} , towards a value of one, is typically associated with a reduced trap-assisted SRH recombination and a predominant bimolecular radiative (in line with S-Q assumption), resulting in higher V_{OC} .^{79,126,173,174} Higher n_{id} values however, indicate that non-radiative recombination is dominating and thus, the quality of certain interfaces can be indicated from the QFLS and n_{id} as will be investigated in Chapter 5 and Chapter 6.

2.7 Light management

As we discussed in Section 2.5, a typical solar cell encounters different types of non-radiative recombination mechanisms, which result in voltage losses, and therefore, external V_{OC} is always lower than the theoretical limit.¹⁴⁰ Similarly, the detailed balance limit is considering the active layer to absorb 100% of incident light for photons energy higher than the band gap, which is far from reality. In fact, a typical device stack consists of multiple layers such as electrodes, HTL, ETL, in addition to the absorber. Such layers induce parasitic absorption of the incident light and thereby optical losses. Furthermore, some of the incident light will be reflected due to the refractive indices difference of the multi-layer stack, resulting in reflection losses.^{37,177,178} Both, reflection and parasitic absorption losses affect the photogenerated current of solar cell, reducing its J_{SC} , and consequently resulting in lower PCE.^{41,179} In this regard, light management concepts that minimize parasitic absorption,

reduce reflection losses, and increase the optical path length within the absorber are pivotal for efficient light harvesting in solar cells.^{25,37,41,43,177–180}

Minimizing parasitic absorption is achieved by optimizing the design of layer stack and the components thereof. Choosing transparent conductive oxides (TCOs) that exhibit low visible as well as near infrared absorption is crucial for minimizing parasitic absorption losses. Optimizing the sputtering parameters of the widely used indium tin oxide (ITO) and indium zinc oxide (IZO), has a strong impact on the optical properties of the resultant films.^{113,181,182} Furthermore, the development of new TCOs with higher transmission such as hydrogenated indium oxide (IO:H) has been shown to push the technology further.^{113,181–184} In addition to TCOs, identifying proper CTLs that encounter low parasitic absorption losses is crucial. For example, replacing the conventional HTLs such as NiO_x and PTAA (which exhibit high parasitic absorption) with the recently developed self-assembled monolayers have shown a positive impact on J_{SC} .^{74,110,185}

Reflection losses on the other hand can be mitigated by applying multiple strategies. The reflectance (R) at the interface of two adjacent layers with refractive indices n_1 and n_2 is given by:¹⁸³

$$R = \left(\frac{n_1 - n_2}{n_1 + n_2} \right)^2 \quad (2.25)$$

Therefore, reducing the refractive index contrast between the two adjacent layers minimizes the reflection losses. For example, introducing magnesium fluoride (MgF₂) antireflection coatings (ARCs) onto the glass side (illumination side) of an opaque PSC reduces the reflection losses and boost the J_{SC} as $n_{MgF_2} \approx 1.37$, while the refractive indices of air and glass are 1 and 1.5, respectively.^{182,183,186} The previous example is more beneficial in semi-transparent single-junction PSCs as well as perovskite-based tandem solar cells due to the high refractive index of the front TCO (roughly in the range of ~ 1.8 to 2.4).^{74,97,111} In addition to reducing the refractive indices contrast between adjacent layers, fine tuning the ARC thickness provides the ability to control the interference pattern (constructive or destructive) at a certain wavelength as indicated by the following equation:¹⁸³

$$d = m \left(\frac{\lambda}{4n} \right) \quad (2.26)$$

Where n is the refractive index of the ARC, d is the typical ARC thickness, which is necessary to fulfill the destructive interference condition (and thereby reduce the reflection losses) for a certain wavelength λ of the incident light.¹⁸³

In addition to ARCs, nanotextures with dimensions smaller than the wavelength of incident light form effective refractive index medium and provide a refractive index grading property.^{37,41,179} Thus, applying nanotextured surfaces mitigates reflection losses and results in efficient light incoupling. For example, Schmager *et al.* replicated the nanotextures of a viola flower over a crystalline Si solar cell, which resulted in efficient broadband light incoupling accompanied with 6% improvement in PCE.⁴¹ In the same context, Tockhorn *et al.* reported the record J_{SC}/J_{SQ} of all PSCs so far, with 93.6% J_{SQ} by processing PSCs over nanotextured surfaces, which exhibited efficient light harvesting compared to planar references.³⁷

Applying microtextures is a common approach to suppress reflection losses as well. For example, micrometer-sized pyramidal textures have shown a strong capability in boosting J_{SC} of single-junction Si solar cells as well as perovskite/Si tandems.^{54,96,99,187,188} The texture enforces the incident light to impinge multiple times on the wall sides, increasing the incoupling probability, and thereby minimizes the reflection losses.^{25,33,186,189} In addition to increased incoupling for all angles of incidence (AOI), the textured surface increases the probability of the first reflected light to fall onto the wall sides with high angles of incidence (higher than critical angle) and therefore, large fraction of reflected light will encounter total internal reflection (aka. retroreflection and light trapping).¹⁸⁹ This light trapping effect reduces the light outcoupling and consequently contributes to mitigating reflection losses. Furthermore, it increases the optical path length through the absorber layer and thereby increases the absorption probability, particularly near the band gap where the probability is at its lowest.^{37,180} In this regard, Yablonovitch *et al.* demonstrated that for a Lambertian surface (i.e. textured surface with isotropic scattering) in an ergodic system, the maximum attainable optical path length (l_{eff}) is given by:⁴⁸

$$l_{eff} = 4n^2d \tag{2.27}$$

Where d is the thickness of the absorber layer and n is the refractive index of the medium.

3. Fabrication and characterization

In this chapter, we demonstrate the fabrication process of perovskite solar cells (PSCs) reported in this thesis. All perovskite thin films reported here are solution-processed *via* spin-coating. For the rest of the device stack, different layers have been employed using various deposition methods such as sputtering, thermal evaporation, and atomic layer deposition (ALD). After shedding the light on the fabrication steps, we introduce the characterization techniques that have been utilized to provide compositional, microstructural, and morphological analysis of the fabricated perovskite thin films. In addition, we introduce the tools used in characterizing the fabricated PSCs in terms of their photovoltaic (PV) performance, spectral response, and stability.

3.1 Fabrication methods

All the PSCs reported in this work have been fabricated in the inverted *p-i-n* architecture over various types of substrates such as planar glass, micrometer-sized textured silicon (Si), and replicated textures over glass substrates. A typical *p-i-n* architecture comprises the following stack: substrate/transparent conductive oxide (TCO) as a front electrode/hole transport layer (HTL)/perovskite absorber/electron transport layer (ETL)/rear electrode. The devices were fabricated in either opaque or semi-transparent layer stack, employing a metal or a TCO rear electrode, respectively. In the following, we introduce the fabrication methods for the whole layer stack starting from preparing the substrates, followed by the deposition of TCO *via* sputtering. Then, HTLs deposition *via* different deposition techniques such as spin-coating, thermal evaporation, and sputtering. Afterwards, we discuss the various perovskite compositions, perovskite precursor solution preparation, and deposition parameters, followed by applying different passivation schemes employing thermally evaporated or solution-processed passivation layers in between the perovskite and ETL. Finally, we introduce the evaporation of ETL and metal electrode that completes the fabrication process of PSCs.

3.1.1 Superstrates preparation

(i) For *planar* PSCs, we used commercially available glass-coated indium tin oxide (ITO) sheets (Luminescence Technology) with a thickness of 1.1 mm and an area of $64 \times 64 \text{ mm}^2$. The corresponding thickness of the commercial ITO films was $\sim 135 \text{ nm}$ with a sheet resistance of $\sim 15 \text{ } \Omega/\text{sq}$. The ITO glass substrates were cut to $16 \times 16 \text{ mm}^2$ area and cleaned with acetone and propanol in an ultrasonic bath for 10 minutes each, respectively. The samples were dried and oxygen plasma treated at 100% power for 3 min, shortly before depositing the subsequent layers.

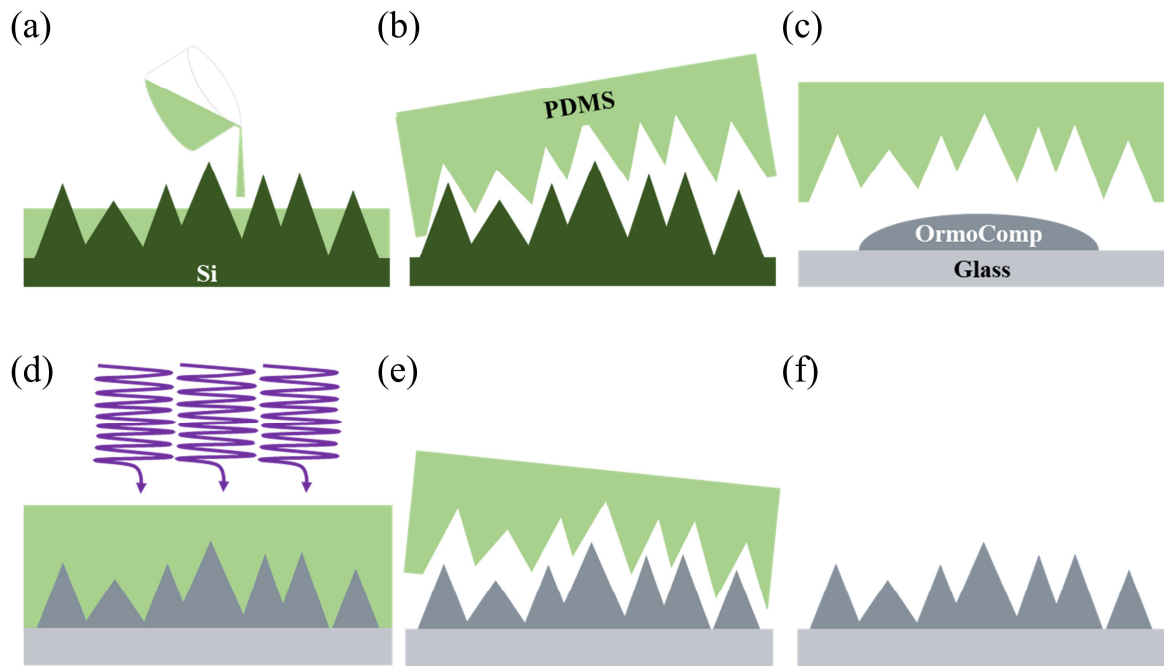


Figure 3.1. The replication process: starting from the micrometer-sized textured silicon substrate, the sample is casted in a mold and the PDMS is poured over it as shown in (a). The PDMS is hardened by backing for 4 h at 60 °C. Once hardened, the PDMS master stamp is removed softly as in (b). The master stamp is pressed against the spin-coated photoresist over a glass substrate as displayed in (c). The photoresist is then exposed to UV-Light as in (d). After 5 min exposure time, the master stamp is removed gently as in (e), resulting in the replicated texture over glass as in (f).

(ii) *Textured Si substrates* were prepared as follows: After cutting the Si wafers (p-type and n-type), a pre-cleaning step was performed to remove the organic contamination and saw damage. Afterwards, a wet chemical etching process was applied to obtain anisotropic etching of <100> monocrystalline silicon wafers using alkaline potassium hydroxide (KOH) solution. Controlling the etching time and employing surface-activating additives enabled the production of different texture sizes. Finally, a post cleaning process using a mixture of hydrofluoric acid (HF) and hydrochloric acid (HCl) was applied to remove the metal residues. The wafer was then cleaved, labeled on the back side, and cut to $16 \times 16 \text{ mm}^2$ area substrates. Unlike the planar glass sheets discussed above, textured Si substrates are missing the front TCO (TCO deposition is discussed in the following subsection). Depositing patterned ITO films (similar to that of the commercial glass substrates) requires insulating the textured Si substrates with a buffer layer beforehand. For this purpose, we deposited $\sim 50 \text{ nm}$ of Al_2O_3 via ALD before sputtering the patterned ITO.

(iii) *Replicated textures*: To replicate the micrometer-sized pyramidal textures of a Si wafer onto planar glass substrates, we utilized nanoimprint lithography. Textured Si samples were put into a beaker and cast into polydimethylsiloxane (PDMS, Sigma Aldrich) mold, followed by heating at 60 °C for 4 h to harden the PDMS. The mold was then peeled off softly and cut to master stamps with an area of $16 \times 16 \text{ mm}^2$. OrmoComp photoresist (micro resist technology) was spin-coated over a glass substrate (cut in $16 \times 16 \text{ mm}^2$ and cleaned using the same procedure discussed above). After spin-coating, the photoresist was homogenous over the glass substrate and the master stamp was pressed against it. After 5 min of curing under ultraviolet (UV) light, the stamp was removed gently, leaving a one-to-one replicated

texture over the glass substrates. We noted that it was crucial to press the master stamp against the photoresist hard enough to make sure that no air bubbles are present between the glass substrate and the replicated texture (which causes optical losses). A schematic illustration of the nanoimprint lithography used in this work is shown in Figure 3.1.

3.1.2 Rear transparent conductive oxide electrode

As discussed in the substrate preparation section, planar PSCs are processed onto commercial glass-coated ITO substrates. For Texture Si substrates and replicated textures, we sputtered patterned ITO (through shadow masks) using a Kurt J. Lesker PVD-75 thin film deposition system. Sputtering ~ 135 nm of patterned ITO onto textured Si substrates was performed at a background pressure of $\sim 2 \times 10^{-7}$ mbar. After the sample holder was loaded into the processing chamber, the samples were heated up to 300 °C at a rate of ~ 5 °C/min starting from room temperature. The samples were kept in the processing chamber at 300 °C for ~ 30 min before the sputtering process started (and the temperature was set to 300 °C during deposition as well). Using a wide range of power from 50 to 250 W (as discussed in detail in Chapter 6) and a gas composition of 3.5% O₂ to 96.5% Ar at a pressure of ~ 0.8 mTorr, we sputtered ITO thin films from a 3.5 inch target (In₂O₃:SnO₂ 90:10, Kurt J. Lesker) at a rate of 3.3 Å/s. The sheet resistance of the resultant ITO films was in the range of 12 to 85 Ω/sq, depending on the applied deposition parameters. For the replicated textures, we noted that the photoresist started to change its color for temperatures > 225 °C. Furthermore, the resist could not withstand the consequent sputter damage and started to exhibit micro-cracks when high power was applied. Hence, the ITO patterns were sputtered over the replicated textures at 225 °C using a power of 200 W (maximum).

3.1.3 Hole transport layer

We reported on using various types of HTLs such as nickel oxide (NiO_x) and self-assembled monolayers (SAMs), deposited *via* different deposition techniques such as sputtering, thermal evaporation, and solution-processing. Furthermore, we presented in some cases the deposition of a double-layer HTL to enhance the quality of the HTL/perovskite interface. In the following, we discuss the deposition processes of the various HTLs.

Sputtered NiO_x hole transport layer

For planar, textured, and replicated samples, 15 nm of NiO_x was non-reactively sputtered using a Kurt J. Lesker PVD-75 thin film deposition system from a 3.5 inch NiO_x target (99.9%, Kurt J. Lesker) at a back ground pressure of $\sim 2 \times 10^{-7}$ mbar using 100 W power with pure Ar at ~ 1 mTorr. The deposition rate was 0.3 Å/s. Although sputtering at room temperature resulted in high quality NiO_x thin films when deposited over planar surfaces, textured surfaces required deposition at higher temperatures. We noted that the quality of the NiO_x thin film, and thereby NiO_x/perovskite interface improved when the deposition process is performed at 150 °C.

Solution-processed SAM-HTLs

The three used PACz derivatives were [4-(3,6-Dimethyl-9H-carbazol-9-yl)butyl]phosphonic acid (Me-4PACz, TCI $> 98\%$), [2-(3,6-Dimethoxy-9H-carbazol-9-yl)ethyl]phosphonic acid (MeO-2PACz, TCI $> 98\%$), and [2-(9H-Carbazol-9-

yl)ethyl]phosphonic acid (2PACz, TCI > 98%). The precursor solutions of 2PACz, MeO-2PACz, and Me-4PACz were prepared by dissolving 1 mmol of the powder in 1 ml ethanol absolute (99.8% anhydrous, VWR Chemicals). The vial was kept in an ultrasonic bath for ~20 min before usage. Monolayers of SAM-HTLs were solution-processed *via* spin coating at 3000 rpm for 30 s, followed by subsequent annealing at 100 °C for ~10 min.

Double-layer HTL

While solution-processed SAM-HTLs enabled high efficiency planar PSCs, they were not compatible with PSCs fabricated on our textured substrates. A double-layer of sputtered NiO_x that provides conformal coating, together with solution-processed SAMs that enables a nearly lossless interface was a good combination. For the double-layer HTL, NiO_x and solution-processed SAMs were deposited using the parameters mentioned above, respectively.

Evaporated SAM-HTLs

SAM-HTLs (Me-4PACz, TCI > 98%), (2PACz, TCI > 98%), and (MeO-2PACz, TCI > 98%) were thermally evaporated from a crucible using a Creaphys OPTIvap thermal evaporation system. The crucible was cleaned with isopropyl alcohol (IPA, VWR Chemicals), dried with an N₂ gun, and filled with 2-3 tips of a small spatula from the material of interest. The crucible and substrates were loaded and the system was pumped down. The films were deposited at a pressure of $\sim 3 \times 10^{-6}$ mbar and a rate of ~ 0.1 - 0.6 Å/s with initial deposition temperatures of ~ 140 °C (loading the crucible with more material initiated the deposition at lower temperatures). We noted that evaporated SAM-HTLs did not display a remarkable change in interface quality with perovskite thin films if deposited without removing previous material from the crucible, hence, cleaning the crucible is recommended only once in a while.

Washing SAM-HTLs

In this work, we investigated the impact of applying an extra washing step to evaporated SAM-HTLs on the quality of SAM-HTLs/perovskite interface as well as the PV performance as discussed in Chapter 5. The evaporated thin films were washed using a single-step spin coating program at a speed of 3000 rpm for 40 s. A 600 μL of ethanol absolute (anhydrous 99.8% VWR Chemicals) is dispensed as follows: 150 μL is dripped statically (~ 3 - 5 s before the spin coating program starts), then ~ 150 μL dynamically dripped every ~ 10 s. Using Chlorobenzene as an alternative solvent to wash very thick films resulted in residual haze on the substrates afterwards, therefore, we did not continue processing onto them. In theory, this washing step could be performed in a bath instead, however, dynamically spin coating at 3000 rpm with a dripping solvent from ~ 2 - 3 cm distance resulted in more effective washing of the unbound molecules.

3.1.4 Perovskite precursor solution preparation and deposition

In this work, we fabricated PSCs employing various perovskite compositions, band gaps, and thicknesses. In the following, we discuss their fabrication steps and processing parameters.

- (i) *Double-cation Cs_{0.17}FA_{0.83}PbI_{2.75}Br_{0.25}*

Starting from our baseline recipe of the double-cation $\text{Cs}_{0.17}\text{FA}_{0.83}\text{PbI}_{2.75}\text{Br}_{0.25}$ perovskite composition with a band gap of ~ 1.58 eV, we developed a thick perovskite absorber layer that assures optimal surface coverage over micrometer-sized pyramidal textures as discussed in Chapter 4. The baseline recipe was 1 M perovskite precursor solution which was prepared by dissolving lead bromide (PbBr_2 , TCI) and lead iodide (PbI_2 , TCI) together in a 1:4 dimethyl sulfoxide (DMSO, Sigma Aldrich): N,N-Dimethylformamide (DMF, Sigma Aldrich) solvent ratio. The PbI_2 and PbBr_2 mixture was heated up at 120°C for ~ 30 min to make sure that all precursor materials are dissolved, then it was removed from the hot plate to cool down. Once it reached room temperature, we transferred it to another vial containing a mixture of formamidinium iodide (FAI, Great Cell Solar) and cesium iodide (CsI , Alfa Aesar). The precursor (which employs 10% excess PbI_2) was then vigorously agitated using an automatic shaker until all the precursor materials were dissolved. The perovskite precursor solution was spin-coated using a two-step spin coating program: 2000 rpm with 1000 rpm/s for 10 s followed by 5000 rpm with 2000 rpm/s for 30 s. The anti-solvent quenching of 120 μL Chlorobenzene ($\text{C}_6\text{H}_5\text{Cl}$, 99.8% Sigma Aldrich) was dispensed 17 s before the end of the 2nd step. The samples were annealed at 100°C for 25 min and the corresponding perovskite film thickness was ~ 350 nm.

The thick perovskite absorber was deposited from a 1.6 M of the double-cation $\text{Cs}_{0.17}\text{FA}_{0.83}\text{PbI}_{2.75}\text{Br}_{0.25}$, which was prepared the same way (employing 1.6 M precursor solution instead of 1 M) and processed over planar surfaces using a slow two-step spin coating program: 200 rpm with 300 rpm/s for 2 s followed by 2000 rpm with 1000 rpm/s for 30 s. The anti-solvent quenching of 150 μL ethyl acetate anhydrous ($\text{C}_4\text{H}_8\text{O}_2$, 99.8% Sigma Aldrich) was dispensed 17 s before the end of the 2nd step. The samples were annealed at 100°C for 25 min and the corresponding perovskite film thickness was ~ 1 μm . For thick perovskite absorbers, we investigated the impact of introducing the Lewis base urea into the perovskite precursor solution on the crystallization dynamics as discussed in Chapter 4, thus, thick perovskite absorbers employing urea were deposited the same way as the reference after introducing 8 mg/ml of urea ($\text{CH}_4\text{N}_2\text{O}$, Sigma Aldrich) to the perovskite precursor solution shortly before deposition.

When processing thick perovskite absorbers over micrometer-sized pyramidal textures, we optimized the spin coating parameters to eliminate the voids near the HTL/perovskite interface as discussed in Chapter 6. We noted that late anti-solvent quenching is favorable, hence, the following deposition parameters were used: 200 rpm with 300 rpm/s for 2 s followed by 2000 rpm with 1000 rpm/s for 60 s (instead of 30 s). The anti-solvent quenching of 150 μL ethyl acetate anhydrous ($\text{C}_4\text{H}_8\text{O}_2$, 99.8% Sigma Aldrich) was dispensed 5 s (instead of 17 s) before the end of the 2nd step. Furthermore, different excess PbI_2 volumes, different solvent ratios, and different perovskite precursor molarities was employed in some specific cases (discussed in detail in Chapter 6).

(ii) *Triple-cation $\text{Cs}_{0.05}\text{MA}_{0.22}\text{FA}_{0.73}\text{Pb}(\text{I}_{0.77}\text{Br}_{0.23})_3$*

In Chapter 5, we employed the triple-cation $\text{Cs}_{0.05}\text{MA}_{0.22}\text{FA}_{0.73}\text{Pb}(\text{I}_{0.77}\text{Br}_{0.23})_3$ perovskite composition with a band gap of ~ 1.68 eV as one of the common and widely used perovskite composition in literature. The 1.53 M perovskite precursor solution was prepared by dissolving PbI_2 (TCI) in a 1:4 DMSO (Sigma Aldrich):DMF (Sigma Aldrich) solvent ratio. The solution was heated up to 130°C for ~ 30 min then removed from the hot plate to cool

down. Afterwards, the PbI_2 solution was transferred to the PbBr_2 (TCI), methylammonium bromide (MABr, Great Cell Solar), CsI (Alfa Aesar), and FAI (Great Cell Solar) and vigorously agitated using automatic shaker until all the powders were dissolved. The deposition was done *via* a two-step spin coating program: 2000 rpm with 1000 rpm/s for 10 s followed by 5000 rpm with 2000 rpm/s for 30 s. The anti-solvent quenching of 150 μL ethyl acetate (Sigma Aldrich) was dispensed 15 s before the end of the 2nd step. The samples were annealed at 100 °C for 45 min and the corresponding perovskite film thickness was ~500-600 nm.

(iii) *Triple-cation $\text{Cs}_{0.05}\text{FA}_{0.85}\text{MA}_{0.10}\text{Pb}(\text{I}_{0.9}\text{Br}_{0.1})_3$*

To assure the compatibility of evaporated SAM-HTLs discussed in Chapter 5 with different perovskite absorber layers, we employed the triple-cation $\text{Cs}_{0.05}\text{FA}_{0.85}\text{MA}_{0.10}\text{Pb}(\text{I}_{0.9}\text{Br}_{0.1})_3$ perovskite composition with a band gap of ~1.58 eV. The perovskite precursor solution preparation (after considering the updated stoichiometry) as well as deposition parameters were similar to the triple-cation perovskite discussed above.

3.1.5 Surface passivation

In this work, we used different surface passivation schemes employing solution-processed as well as thermally evaporated interlayers.

- (i) Thermal evaporation: A ~1-2 nm lithium fluoride (LiF, Sigma Aldrich) was thermally evaporated in between the perovskite thin film and ETL using Lesker Spectros PVD system at a pressure of $\sim 8 \times 10^{-6}$ mbar at a rate of ~ 0.2 Å/s.
- (ii) Solution-processing: The long-chain alkylammonium salt phenethylammonium chloride (PEACl, Sigma Aldrich) precursor was prepared by dissolving ~1-2 mg in 1 ml IPA (Sigma Aldrich). The solution was ready to be used after only 1 min of agitation. Using a one-step spin coating program with 3000 rpm and acceleration of 2000 rpm/s for 30 s, 50 μL of PEACl was dripped dynamically (after ~5 s) followed by annealing the sample at 100 °C for 5 min.

3.1.6 Electron transport layer

- (i) *Opaque devices*: a double-layer of thermally evaporated fullerene (C_{60} , Alfa Aesar) and bathocuproine (BCP, Luminescence Technology) was employed, respectively. 25 nm of C_{60} and 7 nm of BCP were deposited in Angstrom thermal evaporation system at a pressure of $\sim 7 \times 10^{-6}$ mbar at a rate of ~ 0.2 Å/s. The initial deposition temperature for C_{60} and BCP was 370 °C and 140 °C, respectively.
- (ii) *Semi-transparent devices*: 25 nm of C_{60} was deposited as described above, followed by 35 nm of SnO_x was deposited *via* ALD as a buffer layer to protect the devices from any potential sputter damage during the subsequent front TCO deposition. The 35 nm SnO_x films were deposited over 300 cycles using the following parameters: 1.6 s TDMASn pulse time with a 12 s purge then 0.1 s water pulse time with a 16 s purge. A boosting system was utilized instead of the conventional bubbler due to the system layout. Under boosting, line flow was increased to 500 sccm immediately prior to pulsing to increase precursor concentration.

3.1.7 Front electrode

- (i) *Opaque devices:* After ETL deposition, the edges of the samples were either scratched or swiped using γ -butyrolactone (GBL; Merck) to enable the deposition of metal contacts on the rear electrodes and thereby reduce the series resistance of fabricated devices. The front electrode (and the contact pads of the rear electrode) were deposited *via* thermal evaporation using a shadow mask to define the active area of the fabricated PSCs. In this work, we used ~ 100 nm silver (Ag), deposited at a pressure of $\sim 9 \times 10^{-6}$ mbar with a rate of ~ 0.5 Å/s for the first 20 nm (to prevent the devices from any potential spiking damage), followed by an increased rate of ~ 2 Å/s for the rest of the film thickness.
- (ii) *Semi-transparent devices:* ~ 165 nm of the TCO indium zinc oxide (IZO) as a front electrode was sputtered using Kurt J. Lesker PVD-75 thin film deposition system from a 3.5 inch IZO target ($\text{In}_2\text{O}_3:\text{ZnO}$ 90:10, Kurt J. Lesker) at a back ground pressure of $\sim 2 \times 10^{-7}$ mbar using 100 W power with a gas composition of 1% O_2 to 99% Ar at a pressure of ~ 1.5 mTorr and a deposition rate of 0.6 Å/s. The sheet resistance of the resultant IZO films was ~ 45 Ω/sq . Afterwards, a 100 nm Ag grid (two fingers at the edges of the active area) was deposited as described above.

3.1.8 Antireflection coating

For semi-transparent devices where IZO was the front electrode, the devices exhibited remarkable reflection losses due to the big difference between the two refractive indices (of air and IZO) as discussed in Chapter 6. Therefore, we employed thermally evaporated magnesium fluoride (MgF_2 , Sigma Aldrich) as an antireflection coating using Angstrom thermal evaporation system. The films were deposited at a pressure of $\sim 5 \times 10^{-6}$ mbar with a rate of ~ 0.2 Å/s. The thickness of MgF_2 films was optimized depending on the band gap of the perovskite and the overall layer stack in a range from 70 to 165 nm.

3.2 Characterization

In this section, we introduce the characterization techniques utilized to investigate thin films, half-layer stacks, and completed PSCs.

3.2.1 Atomic force microscopy

Atomic force microscopy (AFM) is a surface-sensitive technique that provides information about surface morphology of thin films. An AFM setup consists of a scanning unit, a laser source, a photodiode, and a cantilever with a probing tip at its edge. The setup can be operated in either static or dynamic contact (tapping) mode. In the tapping mode, one sets the cantilever to oscillate at a certain frequency. Various types of interactions between the tip and sample take place once the tip gets closer to the sample surface such as electrostatic forces, dipole-dipole interactions, and Van der Waals forces. Such interactions between the tip and sample result in a change in the oscillation amplitude of the cantilever, which can be tracked by the reflection of the laser beam pointed toward the cantilever's head. Scanning a certain area of a sample *via* AFM provides a three-dimensional (3D) image, which gives insights into surface topography and surface roughness of the scanned area. In this work, a JPK NanoWizard II (Bruker Nano GmbH) AFM setup was used to have an overview about the topography of pyramidal textures produced *via* anisotropic wet chemical etching as

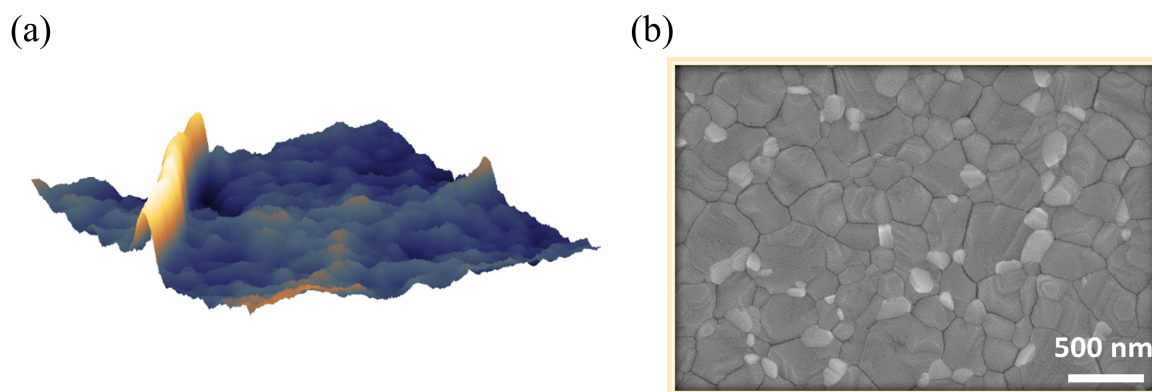


Figure 3.2. (a) An example of a three-dimensional (3D) representation of atomic force microscopy (AFM) image. (b) An example of a top-view scanning electron microscopy (SEM) image.

discussed in Chapter 4. In Chapter 6, we utilized AFM measurements to investigate the surface morphology of perovskite thin films processed over textured surfaces. An example of a 3D representation for an AFM image is displayed in Figure 3.2a.

3.2.2 Scanning electron microscopy

Scanning electron microscopy (SEM) is a surface imaging technique that can be used in investigating microstructure and composition of materials, in addition to their surface morphology. In a scanning electron microscope, an electron beam is thermionically emitted, accelerated, and then focused over the sample *via* condenser lenses. The electron beam can be focused down to a few nm with a wide range of kinetic energy (~ 0.2 to 40 KeV), and deflected to a raster scan of a particular area over the sample surface. When the energetic primary electron beam is focused onto sample surface, the interaction results in multiple by-products such as Auger electrons, back-scattered electrons, X-rays radiation, and finally yet importantly, secondary electrons. Detecting the secondary electrons with their low energies (in the range of a few eV) projects SEM images, which thereby reveal the topographical information with very high resolution. In this work, we employed Zeiss LEO1530 VP SEM with an aperture size of 20 μm and 3-10 kV acceleration voltage to capture cross-sectional as well as top-view SEM images. Prominent examples of utilizing SEM would be investigating the grain size of thick perovskite absorbers with and without additives as discussed in Chapter 4. Top-view SEM images assisted in investigating strain-related surface wrinkles in perovskite thin films processed over textured surfaces and the impact of solvent engineering on mitigating them (discussed in Chapter 6). An example of a top-view SEM image is displayed in Figure 3.2b.

3.2.3 Energy-dispersive X-ray spectroscopy

Energy-dispersive X-ray (EDX) is a spectroscopic technique used in microanalysis and elemental distribution of materials. Recalling the SEM discussion, forming an SEM image is done by detecting the secondary electrons resulting from the interaction of the energetic primary electron beam with the sample. In the same context, another by-product of this interaction is the emitted X-rays. Coupling an energy-dispersive spectrometer with a scanning electron microscope enables EDX analysis. The primary electron beam excites the electrons of the sample's atoms to higher states (if its energy is sufficient to do so) followed by a relaxation of the electrons from the excited states to fill in the vacancy of the lower

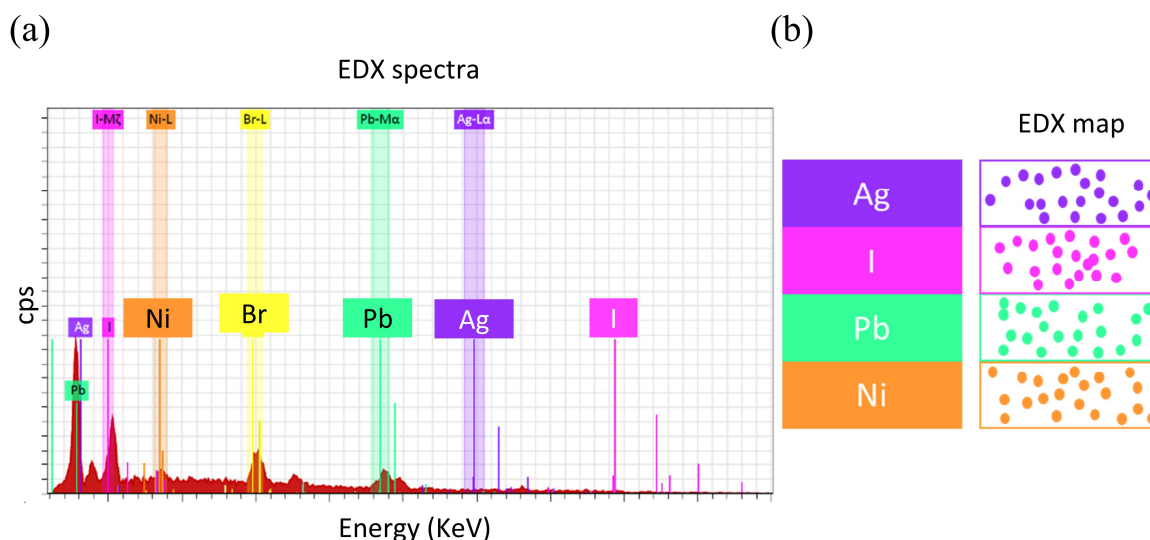


Figure 3.3. (a) An example of energy-dispersive X-ray (EDX) spectra. (b) A schematic diagram of a layer stack and the corresponding EDX map.

energy levels and thereby emitting X-rays with energy equivalent to the energy difference between the two levels. As each element has a unique atomic structure, the emitted X-rays are characteristic. The EDX spectra of a material (see Figure 3.3a) exhibit characteristic peaks with certain intensities that correlates to the components thereof. Furthermore, EDX enables two-dimensional (2D) maps of the elemental distribution as shown in the schematic diagram in Figure 3.3b. We employed EDX measurements to investigate the interaction of the perovskite thin films with the adjacent HTL and TCO as discussed in Chapter 6.

3.2.4 X-ray photoelectron spectroscopy

X-ray photoelectron spectroscopy (XPS) is a surface-sensitive technique that gives insights into the chemical composition and chemical environment of materials. The main idea of the measurement technique is based on the photoelectric effect. The sample is placed in an ultra-high vacuum (as any contamination would mimic the signal) and irradiated with X-rays. Due to the high energy of incident X-rays, electrons are ejected from their atomic orbitals and detected. The electron energy analyzer provides the kinetic energy as well as the number of detected electrons. Having the energy of X-ray known and the kinetic energy of ejected electrons measured, their binding energy can be calculated using the following equation:

$$E_b = h\nu - (E_k + \varphi) \quad (3.1)$$

where φ is the work function (energy difference between Fermi level and vacuum), E_k and E_b are the kinetic energy and binding energy of the electron, respectively, $h\nu$ is the energy of X-ray photons.

As the binding energy of core electrons of an individual element is characteristic, XPS spectra provides information about the chemical environment of the sample. Figure 3.4 displays an example of an XPS survey. In this work, we employed the XPS setup ‘‘Kratos Axis Ultra system’’ equipped with a monochromatic Al k_α X-ray source (1486.6 eV) to investigate the impact of changing the deposition method of SAMs on their chemical environment and whether the molecules exhibit any signs of degradation during the thermal

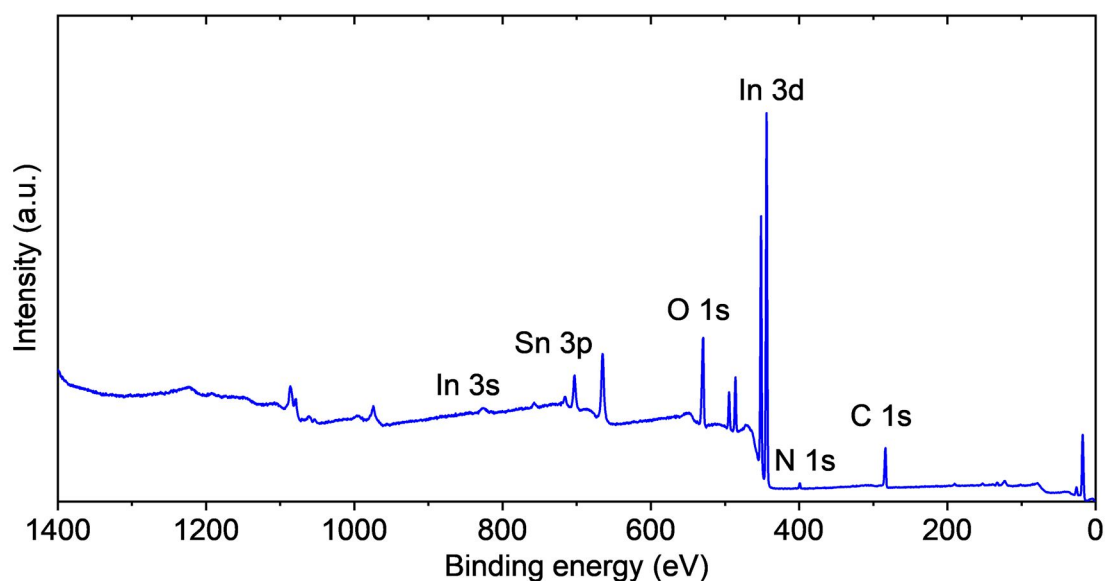


Figure 3.4. An example of a typical X-ray photoelectron spectroscopy (XPS) survey.

evaporation process as discussed in Chapter 5. The survey spectra were acquired with a pass energy of 80 eV, while high-resolution data were acquired with a pass energy of 20 eV.

3.2.5 X-ray diffraction

X-ray diffraction (XRD) is a material characterization technique that provides information about the crystal structure of thin films as well as powders. Incident X-rays are scattered by the crystal planes of material, resulting in constructive and destructive interference, governed by Bragg's law:

$$2d \sin \theta = n\lambda \quad (3.2)$$

Where λ and θ are the wavelength and incident angle of X-rays, respectively, d is the distance between diffraction planes, and n is the diffraction order (integer). The resultant XRD diffractogram exhibits characteristic X-ray diffraction peaks as shown in Figure 3.5. Peak position, intensity, and full width at half maximum (FWHM) provide information about the crystal structure of material. Furthermore, identifying a shift in the characteristic peaks to lower or higher angles provides information about macrostrains. In this work, Bruker D2Phaser system with LynxEye detector and a Cu-K α radiation source ($\lambda = 1.5405 \text{ \AA}$) is used to investigate the impact of employing Lewis base additive to the perovskite precursor solution on the crystal structure of the grown film as discussed in Chapter 4. In addition, we utilized XRD measurements to compare the crystal structure of perovskite thin films processed over planar and textured surfaces as discussed in Chapter 6.

3.2.6 Ultraviolet-visible spectroscopy

Ultraviolet-visible (UV-Vis) spectroscopy is an optical characterization technique that provides information about the total reflectance (R) and transmittance (T) of materials. A typical setup comprises a spectrometer equipped with an integrating sphere, a light source (e.g. halogen lamp), an optical grating, and a beam splitter. The measurement is performed employing two light beams; one probes the sample of interest, while the other one is used as

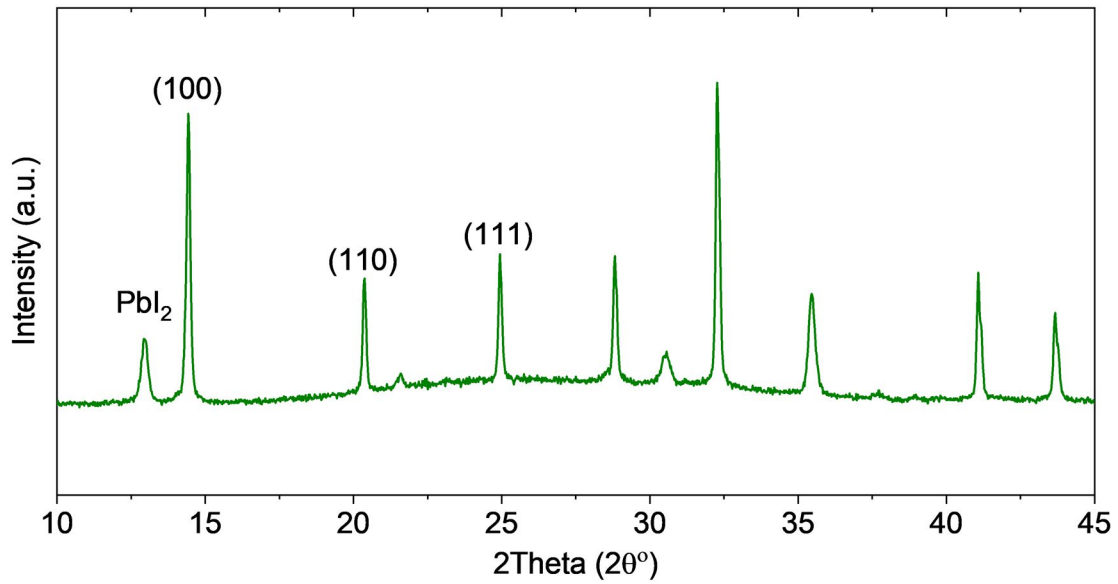


Figure 3.5. An example of a typical X-ray diffraction (XRD) pattern of a perovskite thin film.

a reference. Measuring the intensities of both the probing and the reference beam for a certain wavelength range provides the total T and R spectra of the sample. Thereby, the absorptance (A) of the sample is obtained by applying the following equation:

$$A = 1 - T - R \quad (3.3)$$

In standard testing conditions (STC), where normal incidence is considered, the sample is mounted in the middle of integration sphere perpendicular to the light path. Angle-resolved measurements can be performed by mounting the sample on a rotating holder around its vertical axis. In this work, we utilized a UV-Vis spectrometer (Lambda 1050, PerkinElmer Inc.) equipped with a 150 mm integrating sphere to investigate the R , T , and A of various samples. For example, investigating the impact of fabricating PSCs over replicated micrometer-sized textured surfaces on reducing reflection losses in STC as well as a wide range of angles of incidence (discussed in Chapter 6).

3.2.7 External quantum efficiency

External quantum efficiency (EQE) is a technique used to define the spectral response of solar cells. A typical setup consists of a broad-band light source, a monochromator, a lock-in amplifier, and a chopper. As EQE relates the spectral response (and thereby the current) of the measured solar cell to that of the reference, calibrating the system using a silicon and/or germanium reference is taking place shortly before performing the measurements. A wavelength-dependent EQE measurement provides a spectrum, which is employed into the following equation to calculate the short-circuit current density (J_{SC}) of a solar cell:

$$J_{SC} = \frac{q}{hc} \int EQE(\lambda) \cdot AM1.5G(\lambda) \cdot d\lambda \quad (3.4)$$

where h is Planck's constant, c the speed of light, and q the elementary charge. In this work, we utilized a Bentham system with xenon and halogen lamp at a chopping frequency of ~ 575

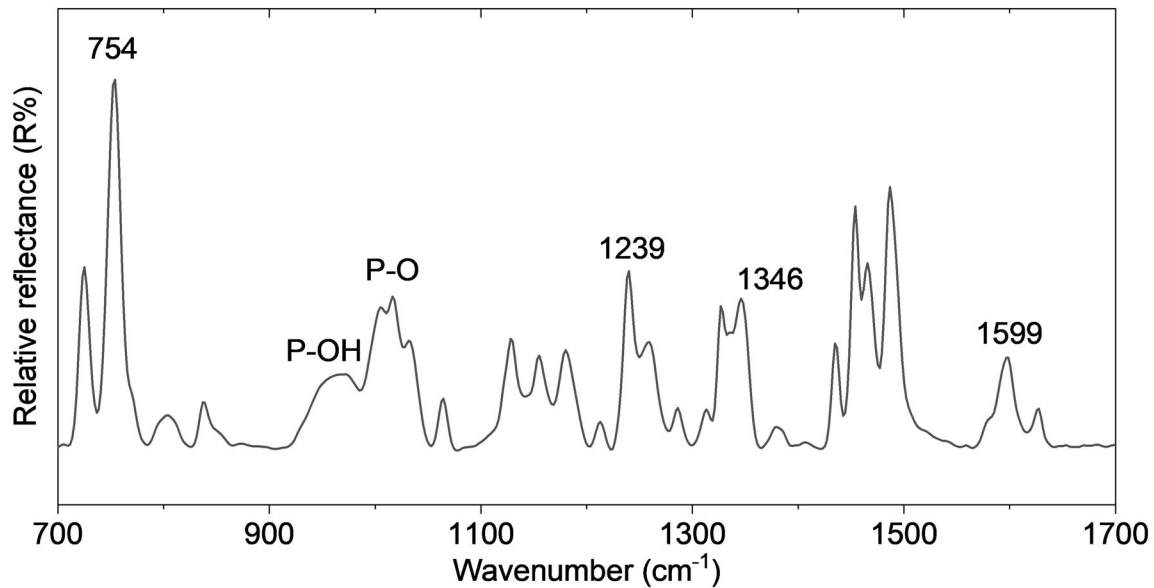


Figure 3.6. An example of a typical Fourier-transformed infrared (FTIR) spectrum of an evaporated 2PACz thin film.

Hz and integration time of 750 ms to calculate the integral J_{sc} in our PSCs. Employing a rotating holder enabled us to determine the angle-dependent spectral response as discussed in Chapter 6.

3.2.8 Current density-voltage characteristics

The photovoltaic (PV) performance of solar cells comprises information about its metric parameters such as J_{sc} , open-circuit voltage (V_{oc}), fill factor (FF), and power conversion efficiency (PCE), in addition to its stability under maximum power point (MPP) tracking. A typical solar simulator setup consists of a light source, multiplexer, and source measure unit (SMU). The measurement is performed in STC, which implies normal incidence with continuous illumination of AM 1.5G light at a temperature of 25 °C. The sample holder is designed in a way to fulfill the normal incidence condition and it is coupled with a temperature controller, thermocouples, and Peltier element to maintain the desired temperature. The intensity of the light source is set to 1000 W/m² and calibrated using a certified silicon solar cell with a KG5 filter shortly before the measurement. Sweeping the voltage roughly from V_{oc} to J_{sc} with a constant scan rate (600 mV/s in our case) provides the J - V characteristics of solar cell. Performing the measurement in forward and reverse scans provides information about hysteresis in the solar cell and enables calculating the hysteresis factor. Furthermore, tracking the MPP as a function of time provides information about the device's stability. In this work, we utilized a solar simulator (Newport, Oriel Sol3A) with a xenon lamp (Osram Licht AG) to obtain the J - V characteristics of the fabricated PSCs. An example of a typical J - V characteristics is shown in Figure 2.4.

3.2.9 Four-point probe measurement

A four-point probe is a common technique to measure the sheet resistance (R_{sh}) of thin films and bulk materials. It comprises four probes separated by an equal distance. An electric

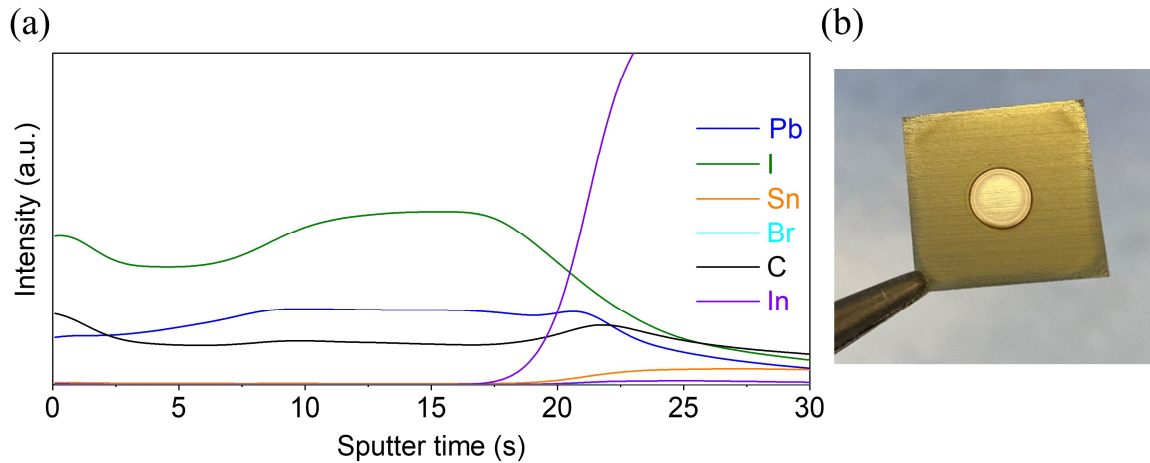


Figure 3.7. (a) An example of a typical glow-discharge optical emission spectrum displays the depth profiling of a perovskite thin film processed onto a textured Si substrate. (b) A photo of the sample after performing the measurement.

current (I) is driven through the outer probes, while the inner probes are measuring the voltage (V). The sheet resistance is obtained by applying the following equation:

$$R_{sh} = \frac{\pi}{\ln(2)} \frac{\Delta V}{I} \quad (3.5)$$

where R_{sh} is the sheet resistance in ohm per square (Ω/sq). In this work, we utilized a four-point probe setup with a Picotest M3500A multi-meter and S-302 four-point probe mounting stand to measure the sheet resistance of thin films. For example, four-point probe measurements were performed on in-house sputtered ITO thin films during the process optimization as discussed in Chapter 6.

3.2.10 Fourier-transformed infrared spectroscopy

Fourier-transformed infrared (FTIR) spectroscopy is one of the absorption spectroscopy techniques which provides information about the molecular vibration bands of materials. A typical setup consists of a broadband light source (different sources can be used based on the wavelength range of interest), a Michelson interferometer with a beam splitter along with fixed and movable mirrors. The incident light is divided into two perpendicular beams by the beam splitter before they are reflected from the mirrors and interfere. The interaction of the probing beam with the sample results in optical path difference (also called retardation), thus, varying the retardation using the movable mirror and recording the light intensity (using various types of detectors depending on the wavelength range) for various values of the retardation results in interferogram. The interferogram is transformed into an FTIR spectrum by applying an inverse Fourier transform to it. A typical FTIR setup enables measuring various types of specimens such as thin films, liquids, and powders (after pressing them into a KBr tablet) in either transmission or reflection mode. In this work, we utilized an FTIR spectrometer (Bruker Vertex 80(v)) to investigate the impact of evaporating SAMs on their characteristic molecular vibration bands and assuring the existence of the monolayer fingerprint in our evaporated thin films on ITO as discussed in Chapter 5. An example of FTIR spectra is displayed in Figure 3.6.

3.2.11 Glow-discharge optical emission spectroscopy

Glow-discharge optical emission spectroscopy (GDOES) is a spectroscopic technique that enables quantitative analysis of materials by providing both surface and depth profiling. A typical GDOES system comprises a small vacuum chamber where the plasma is being ignited, an Ar supply, a power supply, and an optical emission spectrometer. The sample is mounted and fixed such that the surface to be examined is facing the processing chamber and connected as a cathode. After the power is switched on, plasma is ignited and the Ar ions start to sputter through the sample. The sputtered atoms are excited to higher energy states by the free electrons of the plasma before they relax again. The relaxation of the atoms is accompanied by the emission of characteristic optical radiation, which can be detected by a spectrometer. The intensity of each signal correlates to the concentration of sputtered material, thus, measuring the intensity as a function of sputtering time provides a GDOES depth-profiling of the sample as shown in Figure 3.7a. In this regard, GDOES is a destructive test as shown in Figure 3.7b. In this work, we utilized a Horiba Scientific GD-Profilier 2 setup to investigate the compositional elements *via* depth profiling of perovskite thin films processed over micrometer-sized textures to emphasize our hypothesis about interactions between perovskite and the adjacent HTL as discussed in Chapter 6.

3.2.12 Time of flight secondary ion mass spectroscopy

Time of flight secondary ion mass spectroscopy (ToF-SIMS) is a surface-sensitive spectroscopic technique that provides information about elemental and isotopic distribution in solids. A typical setup comprises an ion beam (mostly bismuth) and a mass spectrometer. The energetic primary ion beam (~30 KeV) is focused on sample and raster scans the area of interest (typically in μm range). As the sample surface is bombarded with energetic primary ions, both atomic and molecular ions (secondary ions) are ejected from the outer surface. The mass of the ejected ions is determined by their time of flight using a mass spectrometer, which enables high mass resolution as well as simultaneous detection of all species. Coupling an independent sputtering beam (Ar/Cs/C₆₀/O) to the analysis beam enables depth-profiling spectra (the analysis beam produces secondary ions from the outer layer, meanwhile, the sputtering beam penetrates to the next layer) as shown in Figure 3.8. The main advantage of mass spectroscopic techniques such as ToF-SIMS is the ability to detect species and complex compounds (in addition to single elements), which optical emission spectroscopic techniques such as EDX and GDOES are lacking. In this work, we utilized an IONTOF time-of-flight secondary ion mass spectrometer using a 30 KeV bismuth ion beam for analysis and a 2 KeV cesium ion beam for sputtering to perform depth-profiling measurements. Investigating depth-profiling measurements of perovskite thin films processed over textured surfaces indicated that the HTL/perovskite interface is iodine-rich as discussed in Chapter 6.

3.2.13 Photoluminescence spectroscopy

Photoluminescence (PL) spectroscopy is a widely used characterization technique to investigate the electronic and optical properties of semiconductors. Illuminating a semiconductor with high energy laser beam (where the photons' energy is higher than the semiconductor's band gap) excites the valence band electrons to the conduction band. Afterwards, thermal relaxation takes place accompanied by radiative recombination between

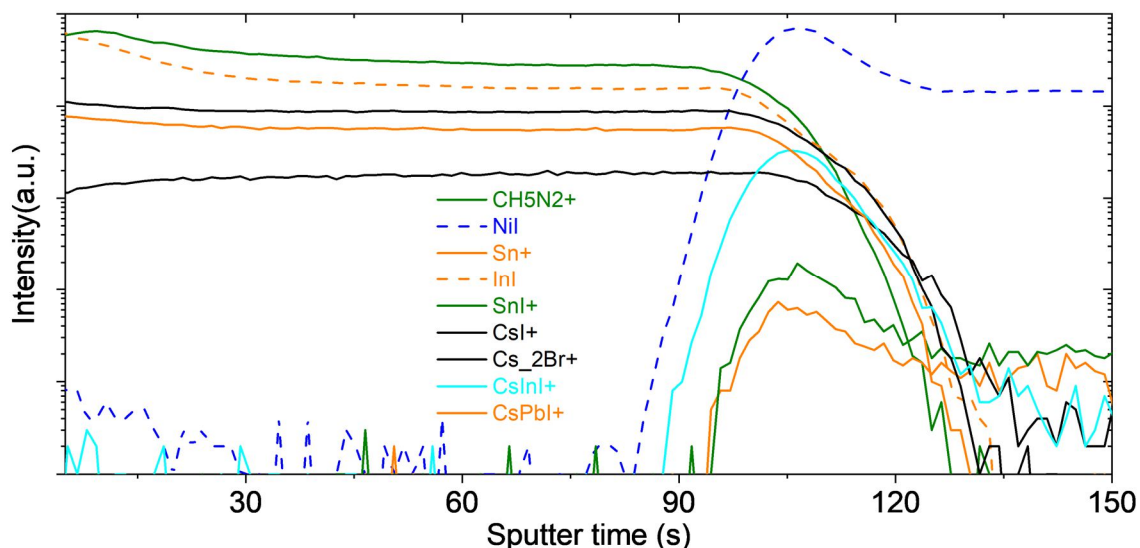


Figure 3.8. An example of a typical time of flight secondary ion mass spectroscopy (ToF-SIMS) depth profiling measurement of a perovskite thin film processed onto a textured Si substrate. The spectrum indicates elemental as well as compounds distribution.

the relaxing electron and the vacant hole with energy comparable to the band gap. The emitted light is then dispersed using a monochromator and detected by a camera. Time-resolved photoluminescence spectroscopy (TRPL) and photoluminescence quantum yield (PLQY) are used in this work (an example of a typical measurement is shown in Figure 3.9).

Time-resolved photoluminescence spectroscopy

TRPL spectroscopy measures the PL decay spectra as a function of time using a narrow detection time window (typically pico-seconds), thus, it provides information about the dominant recombination process. Furthermore, TRPL provides information about the charge carrier dynamics, minority charge carrier lifetime, and charge carrier diffusion length. In this work, we utilized a TRPL setup employing a Hamamatsu Universal Streak Camera C10910 coupled to an Acton SpectraPro SP2300 spectrometer, a 532 nm pulsed laser with a repetition rate of 1 KHz, a pulse width of 0.8 ns, and a pump fluence of $\sim 20\text{-}30$ nJ/cm². The TPRL data provided insights into the impact of growing perovskite thin films with larger grains compared to the smaller grains counterparts due to the extended minority charge carrier life time as discussed in Chapter 4. Another example would be comparing the charge carrier dynamics in perovskite thin films processed over solution-processed and evaporated SAM-HTLs as discussed in Chapter 5.

Photoluminescence quantum yield

As discussed in detail in Section 2.6, PLQY measurements provide information about quasi-Fermi level splitting and thereby a quantitative analysis of non-radiative recombination losses is obtained. A typical PLQY setup employs an integrating sphere, a laser source, an optical fiber, and a spectrometer. The measurements were performed by mounting the samples at an angle of 15° with respect to the laser beam (LD-515-10MG from Roithner Lasertechnik) to avoid specular reflectance inside the integration sphere (LabSphere, 15 cm diameter). The emission was collected from the exit port of the sphere, coupled to the optical fiber, and guided to the spectrometers (QEPro from Ocean Optics). The spectral response

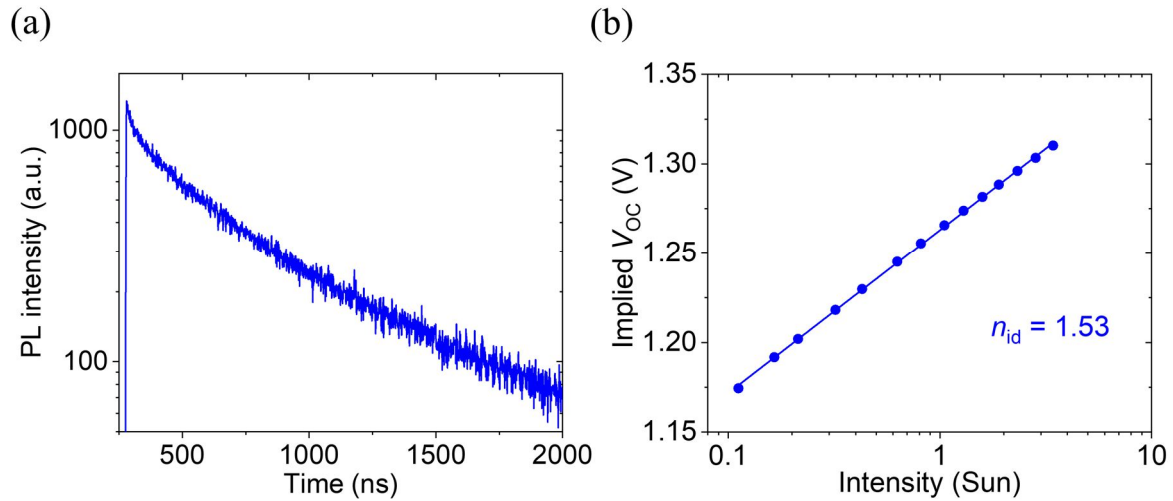


Figure 3.9. (a) An example of a typical time-resolved photoluminescence spectroscopy measurement to determine the minority charge carrier lifetime. (b) An example of a typical intensity-dependent photoluminescence quantum yield measurement to determine the ideality factor.

was calibrated using calibration lamp (HL-3plus-INT-Cal from Ocean Optics) and raw measured spectra were recalculated to give power spectra using the integration time. The ideality factor was obtained by performing intensity-dependent PLQY measurements.

4. Thick absorber perovskite solar cells

Developing a compatible thick perovskite absorber layer with micrometer-sized textured pyramidal surfaces that assures optimal surface coverage is a corner stone. In this chapter, we discuss the optimization process for increasing the perovskite absorber layer thickness from ~350 nm in our baseline recipe to ~1 μm . Although the developed recipe resulted in full surface coverage over the textured surface, perovskite solar cells (PSCs) employing such thick absorbers suffered inefficient charge carrier extraction and consequently low power conversion efficiency (PCE). To overcome this challenge, we investigate the impact of employing a Lewis base additive to the highly concentrated perovskite precursor solution in enhancing the photophysical and morphological properties of the thick perovskite films. Afterwards, we present a comparison of the photovoltaic (PV) performance for planar PSCs employing the developed and the baseline absorbers.

Acknowledgements and contributions

Parts of this chapter, related to the development of thick perovskite absorbers, have been published in ACS APPLIED ENERGY MATERIALS by Ahmed Farag et al. with the title ‘Efficient Light Harvesting in Thick Perovskite Solar Cells Processed on Industry-Applicable Random Pyramidal Textures’.¹⁸⁰ Many graphs in this chapter are reproduced or adapted with permission from American Chemical Society. Ahmed Farag conceived the initial idea. Ahmed Farag planned the lab work, designed the experiments under the supervision of Dr. Ulrich W. Paetzold. Ahmed Farag fabricated the perovskite films and solar cells, performed the current density-voltage, external quantum efficiency, scanning electron microscopy, X-ray diffraction, and ultraviolet-visible measurements. SINGULUS TECHNOLOGIES AG provided the textured silicon wafers. Dr. Ihtez M. Hossain performed the TRPL measurements, and Ahmed Farag analyzed the data. Dr. Paul Fassl performed the atomic force microscopy measurements.

4.1 Introduction

In recent years, monolithic two-terminal (2T) perovskite/silicon (Si) tandem solar cells employing a textured Si sub-cell have achieved a remarkable progress in their power conversion efficiency (PCE), which makes this approach one of the strong candidates to surpass the theoretical limit of a single junction solar cell (~33%).¹⁹⁰ The 2T architecture offers a straightforward integration with less interlayers that induce parasitic absorption losses.^{109,186,191} In addition, employing a textured bottom sub-cell minimizes the reflection losses due to the light trapping effect that the textured surface exhibits, which consequently results in efficient light harvesting.⁴⁶⁻⁴⁹ Furthermore, pyramidal textures are produced *via* anisotropic wet chemical etching process, which is more cost efficient compared to polishing a front planar surface, makes the textured bottom cells commercially favorable and compatible with the industrial standards.¹⁹² For efficient light harvesting in single-junction Si solar cells, the random pyramidal textures exhibit a size of ~5 μm .^{13,50-52} Although processing PSCs over such large size textures could be done *via* hybrid two-step process^{12,13} or vacuum-deposition^{15,16} as they result in conformal coatings, such large size textures are not compatible with perovskite thin films processed *via* spin-coating.^{79,120} Optimizing the pyramidal textures size down to ~1-2 μm has been shown to maintain efficient light harvesting compared to that of the large size textures.⁵³ Meanwhile, assuring full surface coverage over such optimized textures is achievable only if thick perovskite films are employed.⁵³⁻⁵⁷ Spin-coating conventional perovskite thin films, with a thickness of ~350-500 nm over such micrometer-sized textures, still implies that some of the pyramidal tips will reach out to the surface and consequently induce detrimental shunting paths.⁵³ While reducing the texture size further to be compatible with the conventional perovskite absorber layer thickness would facilitate processing PSCs on top, it unfortunately comes at the expense of increased reflection losses due to imperfect texturing.⁵³⁻⁵⁶ Hence, developing a thick enough perovskite absorber layer that assures full surface coverage over such intermediate sized pyramidal textures (~1-2 μm) is pivotal.^{53,54,58,59}

On the other hand, PSCs employing thick perovskite absorbers exhibit inefficient charge carrier extraction.^{193,194} In principle, at solar irradiation conditions, the charge carrier diffusion length in most high-quality perovskite thin films reported in literature is roughly ~500 nm, which implies that thicker absorbers will be comparable or even higher than the charge carrier diffusion length.^{53,195-198} To tackle this problem, various strategies such as vacuum annealing,¹⁹⁹ solvent retarding,²⁰⁰ and hot casting¹⁵⁶ have been suggested to fabricate high quality perovskite thick films. Furthermore, optimization of charge transport layers (CTLs) and enhancing their interface quality with the thick perovskite absorbers by employing surface passivation schemes, has been demonstrated to be effective in terms of charge carrier extraction as well as suppressing non-radiative recombination.^{53,74,79,201,202} Yet, the most efficient and practical routes for enhancing charge carrier diffusion length within the bulk of perovskite absorbers employ certain additives into the perovskite precursor solution. Prominent examples are Lewis acids and bases,^{94,155,203-205} which form complex compounds with the perovskite precursor solutions, reduce the density of nucleation centers, and consequently result in perovskite thin films with significantly large grain size.^{94,203-207} Perovskite thin films with larger grains inherently possess lower trap density compared to their small grains counterparts, thereby enhancing the diffusion length and charge carrier lifetime.^{38,39} Having a stable, efficient, and thick perovskite absorber over a planar surface is a crucial and essential step toward efficient PSCs over micrometer-sized pyramidal textures. In this chapter, we investigate the perovskite precursor solution molarity of the double-cation ($\text{Cs}_{0.17}\text{FA}_{0.83}\text{PbI}_{2.75}\text{Br}_{0.25}$) that enables full surface coverage of the

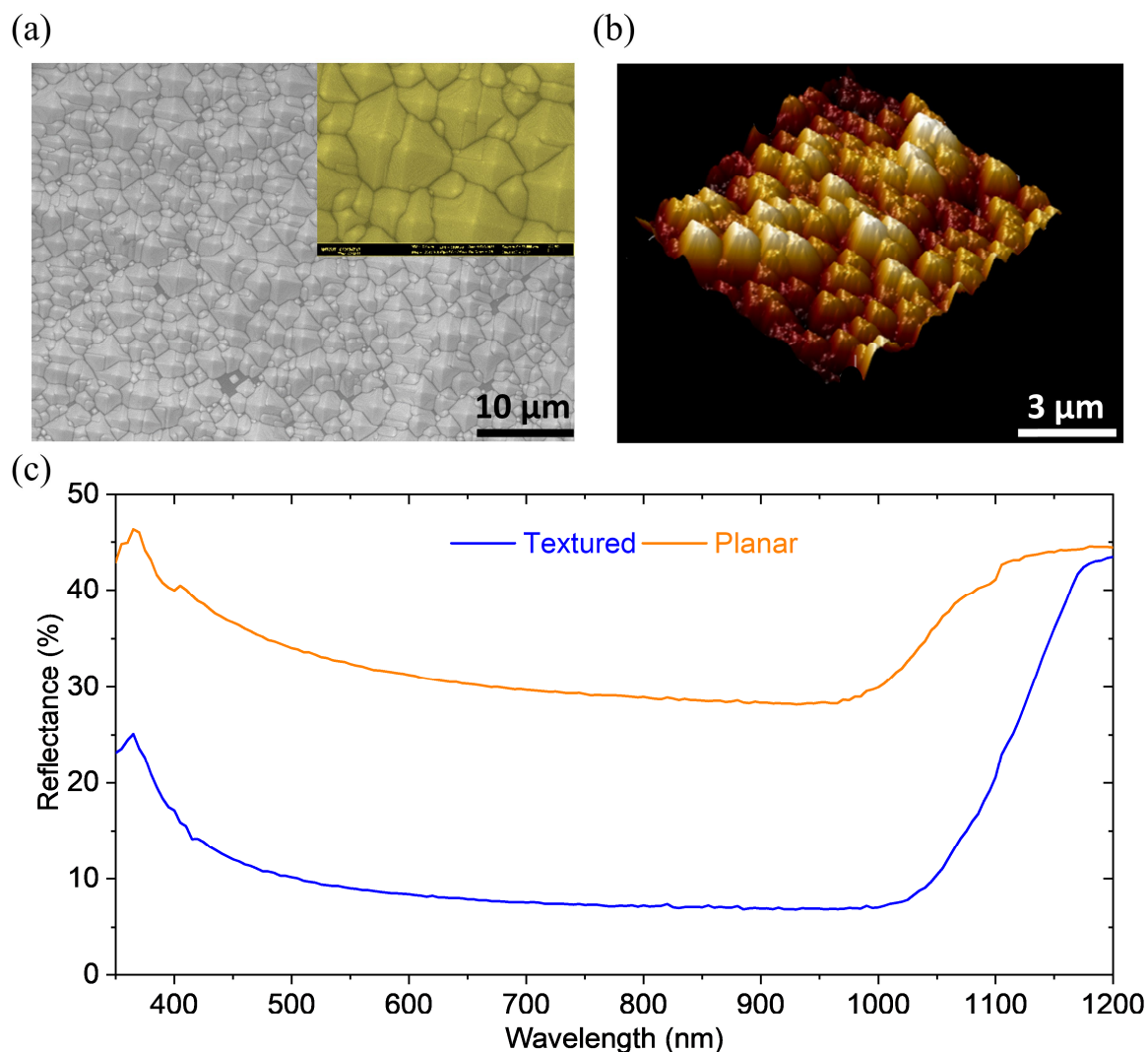


Figure 4.1. (a) and (b) Top-view scanning electron microscope (SEM) image and atomic force microscope (AFM) image of the micrometer-sized pyramidal textured silicon (Si) substrate, respectively. The texture size is in the range of $\sim 1\text{-}2\ \mu\text{m}$. (c) Comparison of the broadband reflectance spectra for the textured Si wafer and a planar polished counterpart. The textured wafer exhibits a remarkably low broadband reflectance over the whole range of interest (from 350 to 1200 nm). Part of this figure is reproduced from ref.¹⁸⁰ with permission from the American Chemical Society.

perovskite film over the micrometer-sized textured surface. Afterwards, we tackle the common drawbacks of such thick perovskite absorbers by employing a Lewis base additive [namely, urea ($\text{CH}_4\text{N}_2\text{O}$)] into the precursor solution. We investigate the crystal structure and crystal growth of micrometer-thick perovskite absorbers employing urea and compare them to the reference films. Furthermore, we investigate the impact of using urea additive on the photovoltaic (PV) performance of thick planar PSCs.

4.2 Thickness optimization, surface coverage, and PV performance

Optimizing the parameters of the anisotropic wet etching process provides the ability to fine-tune the resultant random pyramidal texture size and density. For Si single-junction solar cells, the size of these textures is in the range of $\sim 5\ \mu\text{m}$.^{13,50-52} Although such large textures enable efficient light harvesting, they are not suitable for solution-processing perovskites on top. The key point is getting lower with the texture size to enable optimal coverage of the

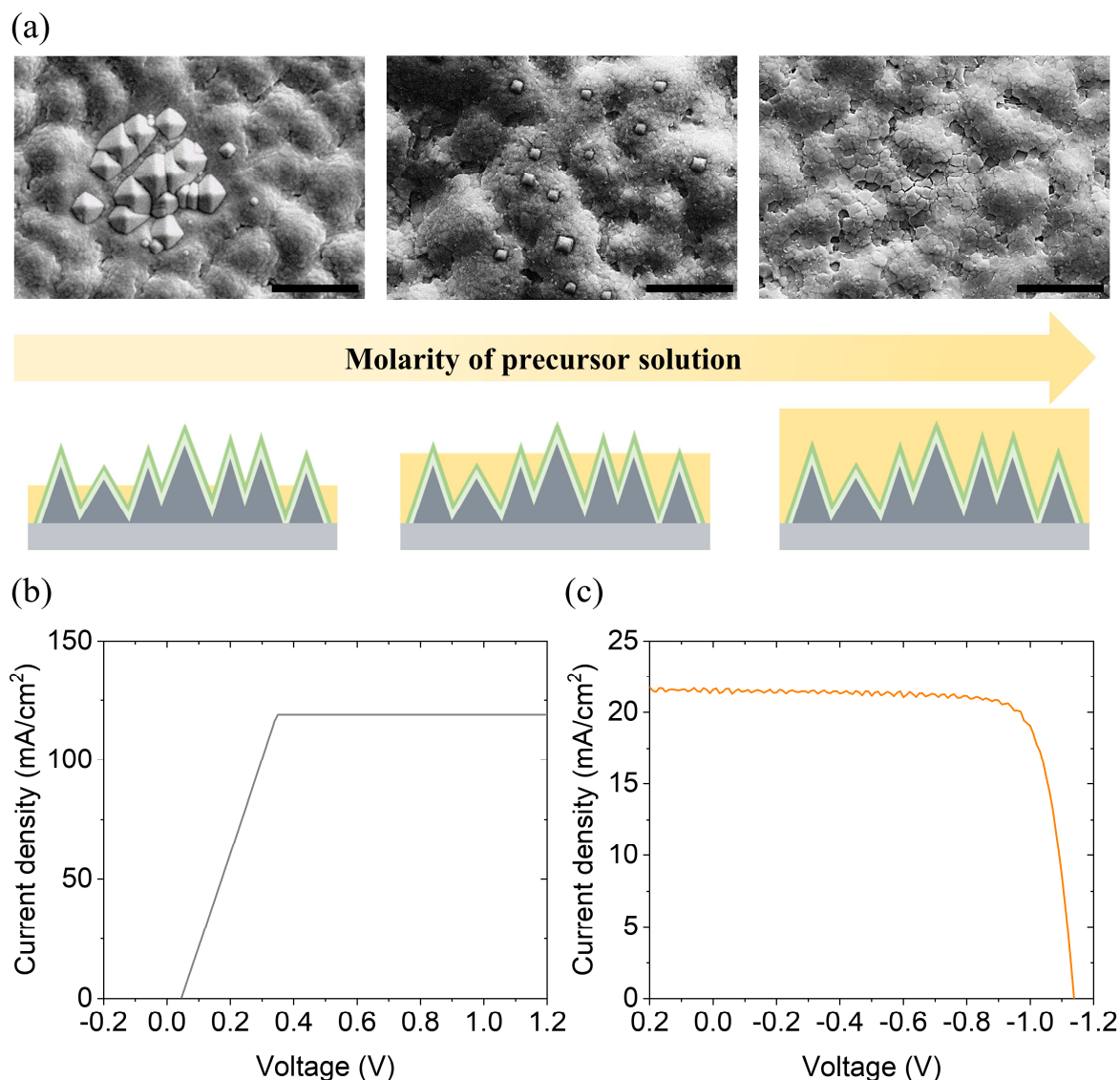


Figure 4.2. (a) Top-view SEM images and schematic illustration of perovskite thin films deposited onto micrometer-sized pyramidal textured substrates, employing different concentration of the double-cation ($\text{Cs}_{0.17}\text{FA}_{0.83}\text{PbI}_{2.75}\text{Br}_{0.25}$) perovskite. The corresponding molarity from left to right is 1.2 M, 1.4 M, and 1.6 M, indicating that optimal surface coverage is fulfilled in the 1.6 M case. The scale bar is 5 μm . (b) Current density versus voltage (J - V) characteristics of perovskite solar cell (PSC) processed onto micrometer-sized textured substrate employing the baseline perovskite recipe (~ 350 nm thick), indicating its incompatibility with the textured surface. (c) J - V characteristics of planar PSC employing the thin perovskite absorber with superior photovoltaic (PV) performance.

solution-processed perovskite films while maintaining high density of the pyramids to minimize reflection losses. We found that texture sizes in the range of ~ 1 - 2 μm still exhibit remarkably low reflectance compared to that of planar polished Si wafers (see Figure 4.1). Furthermore, the broadband reduced reflection that the textured substrate exhibits is comparable to that of the conventional large texture sizes reported in literature.^{13,50–52,208} We note that further reduction in the pyramidal texture size results in higher reflection losses, in line with the previous report of Hou *et al.*⁴⁵ Hence, we will stick to a texture size of ~ 1 - 2 μm range for the rest of the following investigations and discussions.

Our solution-processing baseline recipe of the double-cation ($\text{Cs}_{0.17}\text{FA}_{0.83}\text{PbI}_{2.75}\text{Br}_{0.25}$) perovskite from a 1 M perovskite precursor solution results in perovskite thin films with an

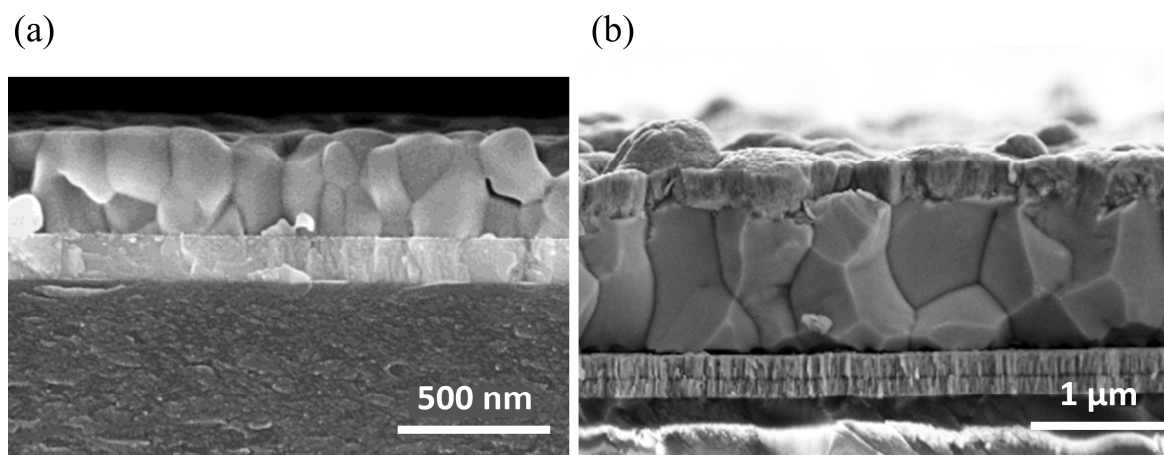


Figure 4.3. (a) and (b) Cross-sectional SEM images of thin and thick perovskite films processed from the baseline (1 M) and the optimized (1.6 M) double-cation ($\text{Cs}_{0.17}\text{FA}_{0.83}\text{PbI}_{2.75}\text{Br}_{0.25}$) perovskite precursor solutions onto planar glass substrates, respectively. The images indicate a corresponding increase in the perovskite absorber thickness from ~ 350 nm in the baseline recipe to $\sim 1\ \mu\text{m}$ in the optimized recipe. Adapted from ref.¹⁸⁰ with permission from the American Chemical Society.

average thickness of ~ 350 nm over planar surfaces. The baseline recipe produces efficient thin planar PSCs with $\sim 20\%$ PCE as indicated by the J - V characteristics in Figure 4.2c. Processing such thin perovskite absorber layer over the optimized micrometer-sized textured surface resulted in poor surface coverage as indicated by the schematic diagram and top-view SEM image in Figure 4.2a. Fabricating efficient or even functional PSCs under these conditions is not possible as the heavily exposed pyramidal tips indicated by the SEM image act as detrimental shunting path (see Figure 4.2b). Hence, it is pivotal to develop a thick perovskite absorber layer that enables full surface coverage over the optimized textured surface.

In order to develop thick perovskite films, we optimized a slow spin coating recipe (2000 rpm instead of 5000 rpm in the baseline recipe) in addition to increasing the concentration of the double-cation perovskite precursor solution ($\text{Cs}_{0.17}\text{FA}_{0.83}\text{PbI}_{2.75}\text{Br}_{0.25}$). To identify the optimum perovskite precursor molarity that provides thick enough perovskite films and thereby completely cover the textured surface, we increased the perovskite precursor molarity of the baseline recipe from 1 M to 1.6 M in 0.2 M steps. We noted that 1.6 M perovskite precursor solution was optimum and compatible with the developed texture size. This high concentration enabled optimal coverage as indicated by the top-view SEM image in Figure 4.2. In addition to optimal coverage, the perovskite film exhibits no sign of pinholes or other surface defects. As a reference, cross-sectional SEM images in Figure 4.3 indicate that the thickness of perovskite thin film employing the baseline recipe (developed for thin PSCs using 1 M of the double-cation perovskite precursor solution and fast spin coating program) is ~ 350 nm. Meanwhile, the developed recipe using 1.6 M solution and slow spin coating program which assures optimal surface coverage over micrometer-sized textures results in a $\sim 1\ \mu\text{m}$ thick perovskite film over planar reference. Although such thick perovskite absorber is crucial to have optimal coverage, increasing the thickness from 350 nm to $\sim 1\ \mu\text{m}$ is expected to negatively affect the PV performance. Thicker perovskite films are prone to remarkably high trap state mediated non-radiative recombination losses, causing a reduction in V_{oc} .^{200,209} Additionally, given the short charge carrier diffusion length in perovskite thin films, a micrometer-thick absorber is comparable or even larger than the charge carrier diffusion length.^{53,195–197,209} Having the perovskite layer thickness comparable or larger than the charge carrier diffusion length would result in inefficient charge carrier

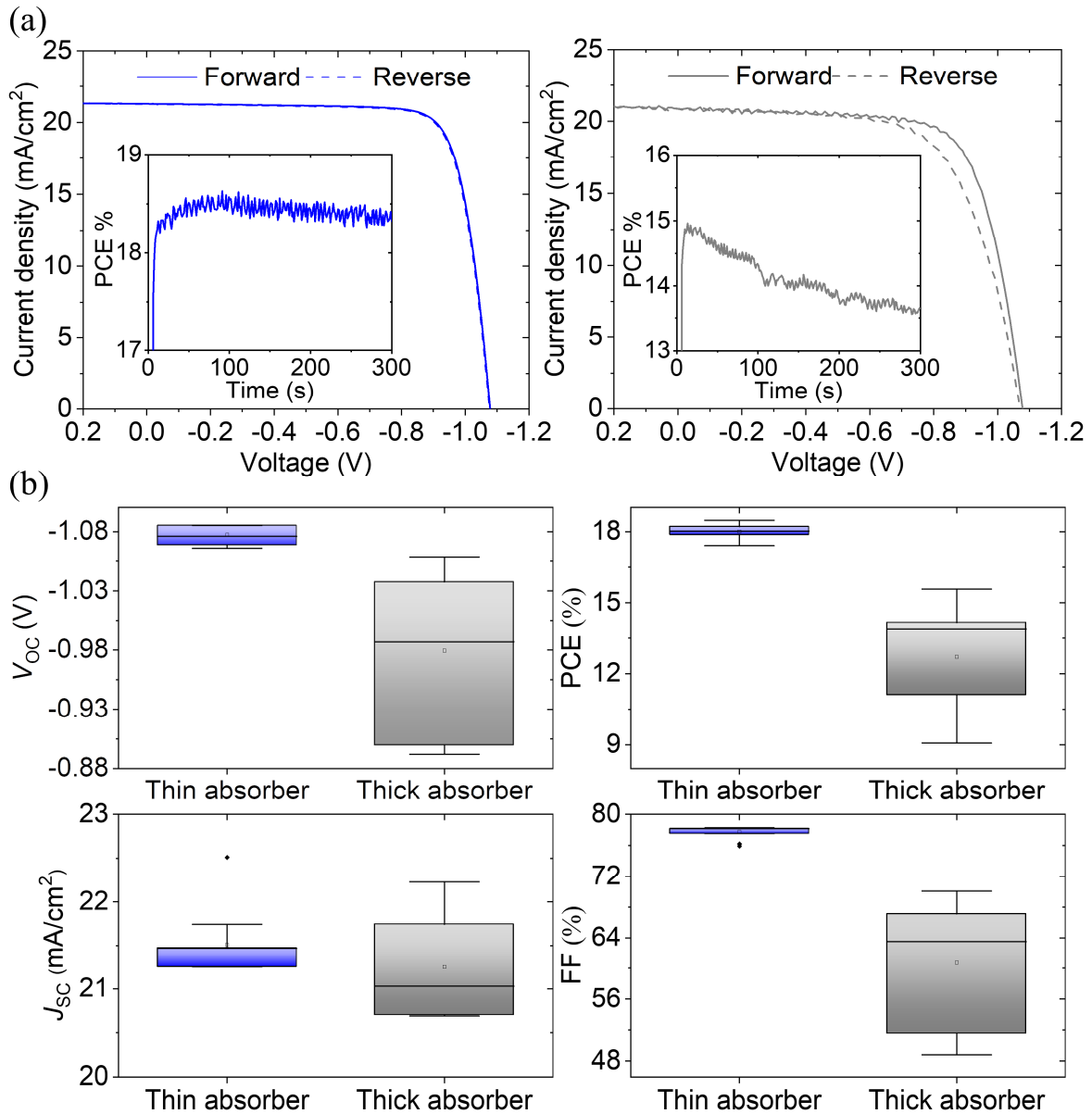


Figure 4.4. (a) $J-V$ characteristics of the best performing PSCs employing the baseline recipe (left) and the optimized recipe (right). The inset represents the corresponding PSCs maximum power point (MPP) tracking for the two PSCs. The thick PSC exhibits high hysteresis and poor short term stability. (b) The corresponding statistical distribution of the open-circuit voltage (V_{oc}), fill factor (FF), short-circuit current density (J_{sc}), and power conversion efficiency (PCE). The overall PV parameters indicate the inferior performance of the thick planar PSCs.

extraction, thereby negatively affecting both J_{sc} and FF.^{94,210} Indeed, employing thin and thick perovskite absorbers in planar PSCs indicates the superiority of the reference (baseline recipe PSCs with ~ 350 nm thick perovskite absorber) in PV performance compared to that of the developed recipe (1.6 M, slow spin coating, and ~ 1 μ m thick absorber) as shown in Figure 4.4.

Starting with the thin PSCs reference, Figure 4.4a displays $J-V$ characteristics of the champion device, with a J_{sc} of 21.5 mA/cm², a FF of 79.4%, a V_{oc} of 1.078 V, and a PCE of 18.4%. The reference performs at a stable PCE of 18.3% under maximum power point (MPP) tracking. Corresponding mean values for J_{sc} , FF, V_{oc} , and PCE are 21.5 mA/cm²,

77.9%, 1.077 V, and 18%, respectively (see Figure 4.4b). Furthermore, the reference champion device exhibits a very low hysteresis factor (HF) with 0.3% and a corresponding mean value of ~0.4%. On the other hand, the champion device employing the micrometer thick perovskite absorber exhibits inferior PV performance with a PCE of 15% (with poor short-term stability as indicated by the remarkable degradation under MPP tracking), a J_{sc} of 20.9 mA/cm², a V_{oc} of 1.076 V, and a FF of 66.6%. The corresponding mean values for PCE, J_{sc} , V_{oc} , and FF are 12.7%, 21.2 mA/cm², 0.979 V, and 60.6%, respectively. In addition to the inferior PV performance and poor short-term stability, PSCs employing the thick absorber suffer huge hysteresis with a corresponding HF of ~23%.

In summary, micrometer-sized pyramidal textures require thick perovskite absorbers to assure full surface coverage, which we achieved by optimizing the perovskite precursor solution molarity and processing parameters. On the other hand, thick planar PSCs exhibited poor PV performance compared to their thin absorber counterparts. The poor performance is attributed to the remarkable increase in the perovskite absorber thickness (~3 times higher). Therefore, enhancing the charge carrier diffusion length, or in other words, increasing the charge carrier lifetime is essential to fabricate efficient thick planar PSCs.

4.3 Urea additive and its impact on morphology and photophysical properties

In PSCs, the grain boundaries of the perovskite thin films have been reported to act as primary trap-assisted recombination channels.^{14,211–213} In this regard, passivating these grain boundaries would enhance the photophysical properties and consequently the PV performance. Many studies have been performed to investigate the impact of certain additives and their consequent bulk passivation effect on the quality of the grown perovskite thin films. For example, Gharibzadeh *et al.* employed the long-chain alkylammonium salt phenethylammonium chloride (PEACl) as an additive to the perovskite precursor solution.¹⁴ Their investigations indicated that the additive results in passivating the grain boundaries, thus, substantial enhancement in charge carrier lifetime and quasi-Fermi level splitting was achieved.¹⁴ In the same context, Rahman *et al.* employed phenyl hydrazinium iodide (PHI) secondary post-treatment to passivate the grain boundaries with a remarkable success.²¹³ A unique approach for passivating grain boundaries of perovskite thin films has been introduced by Yao *et al.* by employing poly(3-aminothiophenol)-coated gold nanoparticles into the perovskite absorber.²¹² They indicated that plasmon excitation can fill trap sites of the grain boundaries and thereby a PCE of ~22% was achievable.²¹² The previous examples among many others in literature aim for passivating the grain boundaries irrespective of the followed passivation scheme.^{94,157–163}

Another successful strategy aims for minimizing the density of grain boundaries by growing perovskite thin films with large grains throughout the whole film, which has been reported to result in enhanced charge carrier lifetime, diffusion length, and mobility.^{100,155,156} Many investigations have been brought forward to increase grain size and benefit from the consequent optoelectronic enhancement. For example, Amalathas *et al.* have reported on the effective growth control of large grains in CH₃NH₃PbI₃ based perovskite thin films.²¹⁴ Introducing methylammonium chloride (MACl) additive to the perovskite precursor solution in addition to modifying the deposition process of the perovskite thin film by applying CH₃NH₂ gas treatment without anti-solvent, enabled large grains (up to ~3 μm).²¹⁴ In the same context, Kim *et al.* reported on increased grain size by introducing MACl additive, which consequently enhanced the charge carrier life time and enabled high efficiency PSCs with PCE >24%.²¹⁵ Furthermore, Wen *et al.* have reported on employing hydriodic acid as

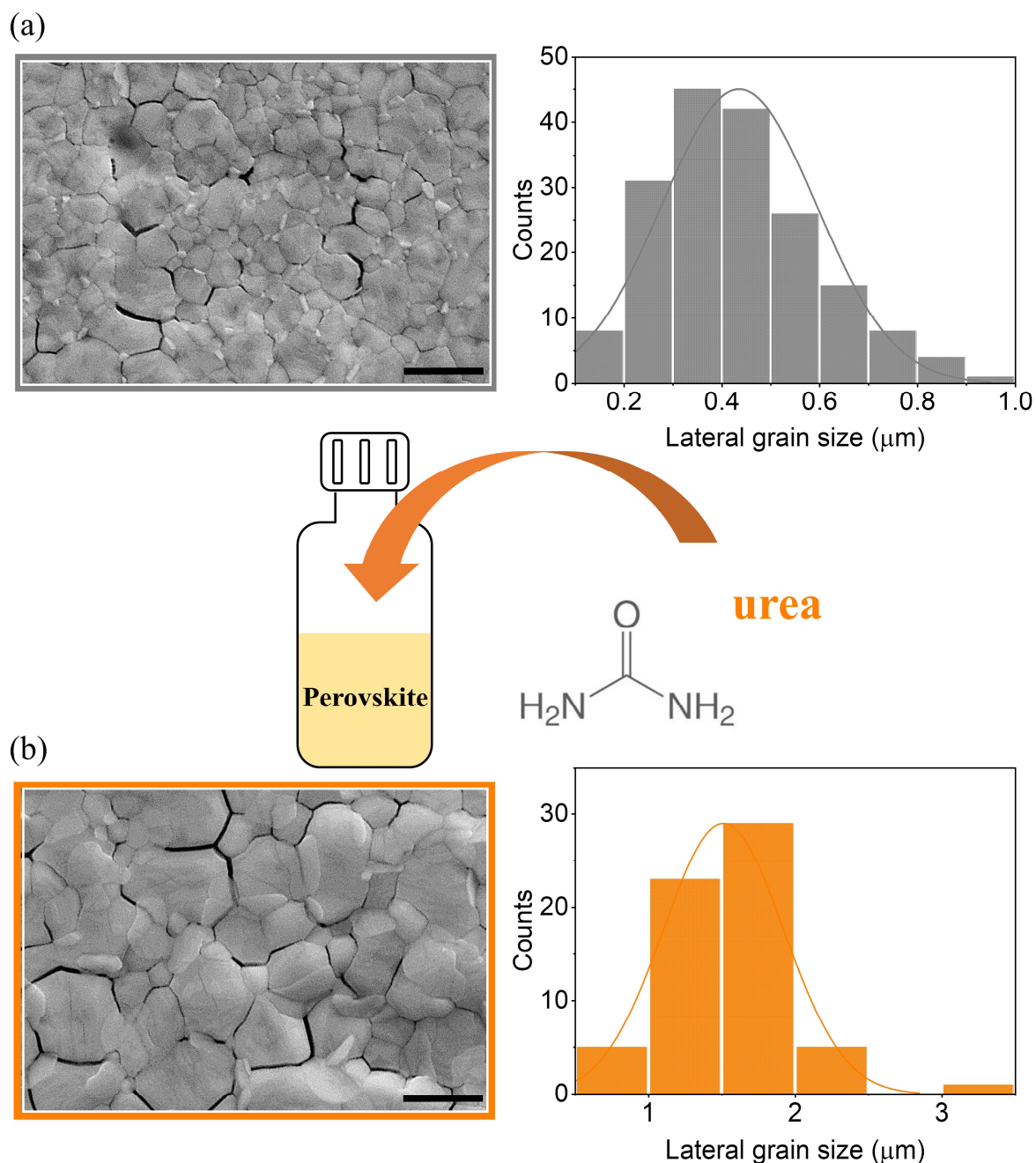


Figure 4.5. (a) and (b) Top-view SEM images and the corresponding lateral grain size histograms of thick perovskite films without and with urea, respectively. The scale bar is 1 μm . The mean value of the lateral grain size for the perovskite film employing urea is remarkably higher than the reference (1010 and 435 nm, respectively). Part of this figure is reproduced from ref.¹⁸⁰ with permission from the American Chemical Society.

an additive to increase the grain size of MAPbI_3 thin films processed *via* hybrid two-step process.²¹⁶

In addition to the chlorine-based additives mentioned above, Lewis acids and bases have been used to grow perovskite thin films with large grains.^{94,155,203–206,217} Hsieh *et al.* have reported on large grain size of MAPbI_3 thin films by introducing 0.5% thiourea to the perovskite precursor solution.²⁰³ Furthermore, employing thiourea into FAPbI_3 resulted in a substantial increase of domain size up to $\sim 7 \mu\text{m}$ as reported by Lee *et al.*²⁰⁶ In the same

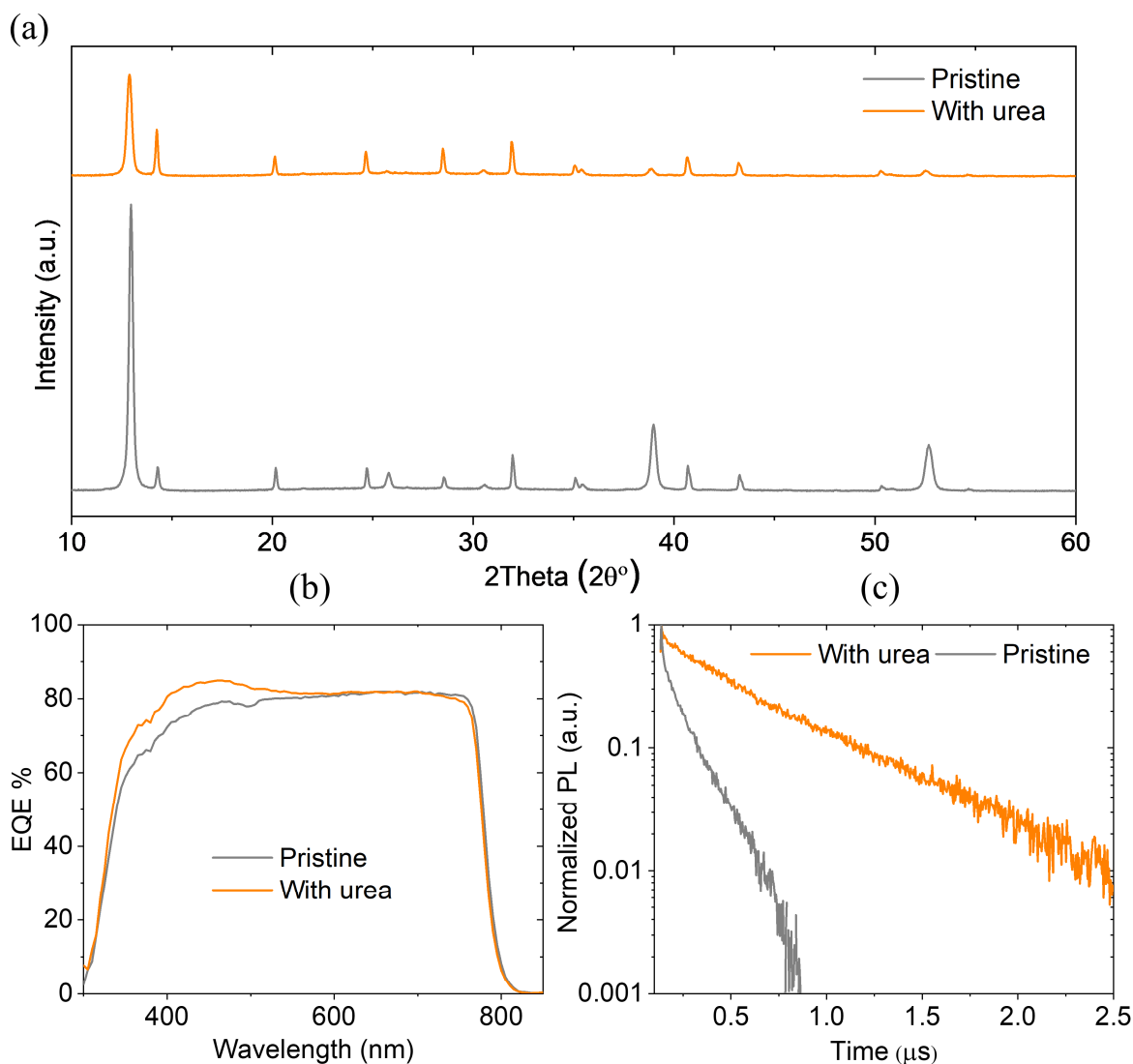


Figure 4.6. (a) X-ray diffraction (XRD) spectra for thick perovskite films with and without urea. The perovskite film employing urea exhibits improved crystallinity as indicated by the (100) peak. PbI_2 peak intensity is damped due to the complex compounds that urea forms in the perovskite precursor solution which consequently consumes PbI_2 . (b) Comparison of external quantum efficiency (EQE) of thick planar PSCs with and without urea. (c) Time-resolved photoluminescence spectra (TRPL) of thick perovskite absorbers processed onto planar glass substrates, indicate longer life time of the minority charge carriers for the film employing urea. Part of this figure is reproduced from ref.¹⁸⁰ with permission from the American Chemical Society.

context, the Lewis base urea has been reported as a promising additive to enhance the grain size and crystallinity of double-cation,¹⁵⁵ triple-cation,⁹⁴ and MAPbI_3 based perovskite thin films.^{203–205,217}

Seeking enhancement in the optoelectronic properties of our developed micrometer thick perovskite absorber, we applied some of the strategies discussed above such as adding PEACl seeking grain boundaries passivation, thiourea, triuret, and biuret to increase the grain size with no remarkable success. On the other hand, the Lewis base additive urea seemed to be a promising candidate and compatible with our thick double-cation perovskite absorber, therefore, we investigate the impact of adding urea to the 1.6 M perovskite precursor solution and compare perovskite films and PSCs employing urea to their pristine counterparts.

Starting with the crystal structure and morphology of perovskite thin films with and without additives, Figure 4.6a displays the XRD spectra of the two thin films. In addition to improved crystallinity of the perovskite thin film employing urea as indicated by the increased intensity of the (100) peak, remarkable dampness in the PbI_2 peak intensity is also noted. Such huge decrease in PbI_2 peak intensity is attributed to the complex compounds that urea has been reported to form in the perovskite precursor solution.^{155,204} The interaction between the Lewis base urea and the Lewis acids of the perovskite precursor solution consumes some of the PbI_2 , and thereby affects the crystallization dynamics of the perovskite thin film. Consequently, during the intermediate phase the wet film employing urea contains fewer crystallization centers compared to the pristine film.^{155,204} According to the heterogeneous nucleation theory,^{11,218} the crystal growth at each nucleation center would stop by the time a neighbor crystal seizes to exist. Given that employing urea into the perovskite precursor solution results in fewer crystallization centers, grains are expected to grow larger in this particular case.²¹⁹

Top-view SEM images of perovskite thin films employing the half-stack ITO/solution-processed 2PACz/perovskite with and without urea additive are shown in Figure 4.5. The corresponding histograms representing the grains lateral size indicate that the average grain size in the perovskite film processed without employing any additives is 435 nm. Interestingly however, the average grain size of the perovskite film employing 8 mg/ml urea is 1.01 μm , which is roughly ~ 2.3 times larger than its pristine counterpart. The big difference in average grain size that correlates to the change in PbI_2 peak intensity in Figure 4.6a and thereby the number of crystallization centers is in full agreement with the heterogeneous nucleation theory.²²⁰ Furthermore, literature indicates that such big difference in grain size as shown in our investigations has a strong impact on photophysical properties, charge carrier dynamics, and PV performance.^{203,204,217,221}

In line with literature reports that correlate improved surface morphology to enhancement in the optoelectronic properties, time-resolved photoluminescence (TRPL) measurements (see Figure 4.6c) indicate the increased minority charge carrier lifetime of thick perovskite films employing urea. Furthermore, an improved crystallinity is evident from XRD measurements as shown in Figure 4.6a. An improved crystallinity together with increased minority charge carrier lifetime are expected to suppress non-radiative recombination losses and thereby enhance the PV performance of PSCs.

In summary, increasing the perovskite film thickness from ~ 350 nm in the baseline recipe to ~ 1 μm is accompanied by a drawback in the optoelectronic properties of the thick film and thereby the PV performance of thick planar PSCs. Seeking a plausible solution to tackle this challenge, we employed the Lewis base urea in our highly concentrated perovskite precursor solution, which played a key role in crystallization dynamics, resulting in thick films with large grains and thereby less density of the grain boundaries. Together with improved crystallinity, thick perovskite absorbers employing urea exhibited a remarkable increase in the minority charge carrier life time compared to the reference counterparts.

4.4 Comparison of the PV performance

Having investigated the impact of employing urea in the high molarity perovskite precursor solution on crystallinity, grain size, and charge carrier diffusion length in the micrometer-thick perovskite absorber, now we compare the PV performance of thick planar PSCs

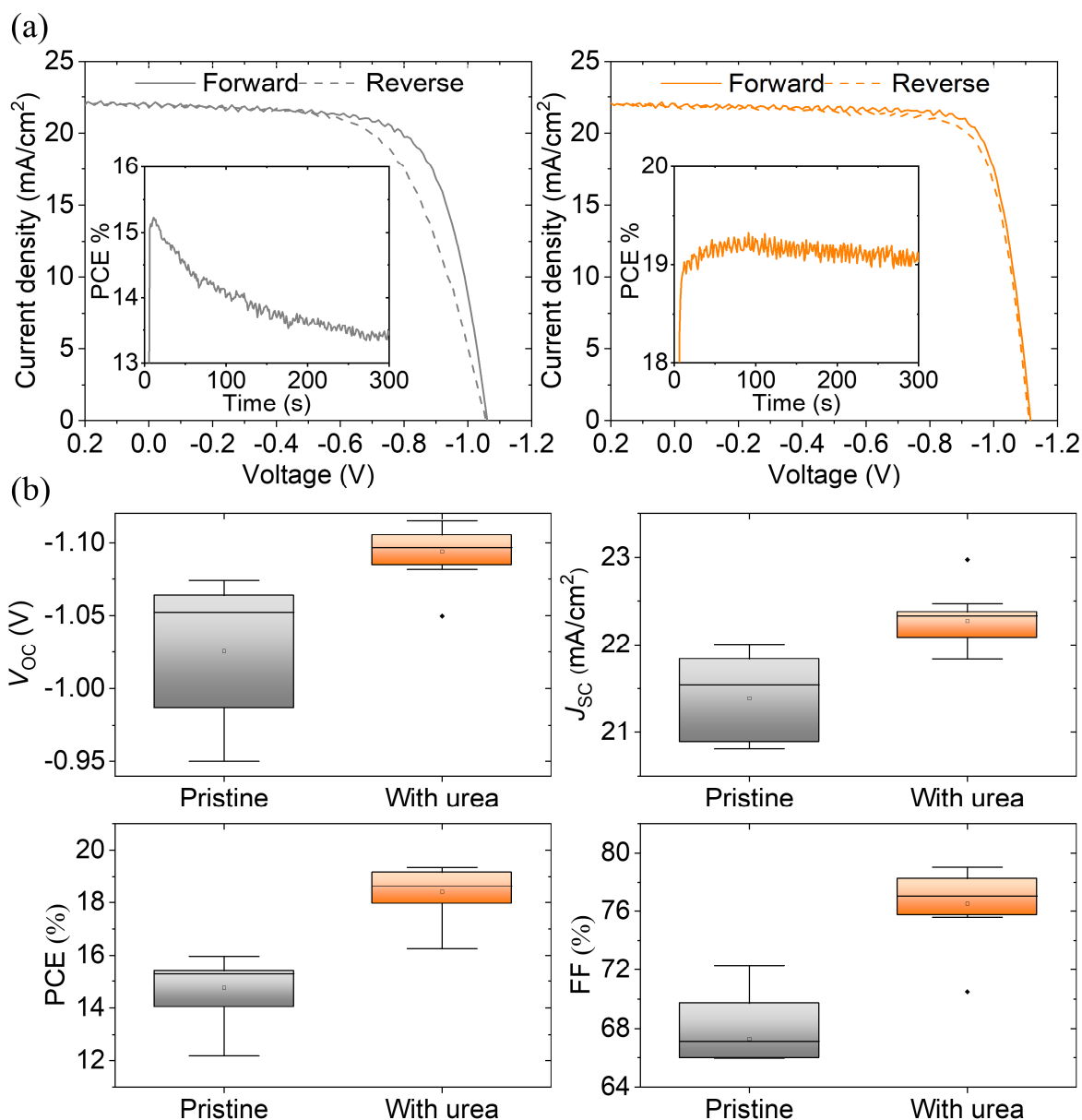


Figure 4.7. (a) $J-V$ characteristics of the best performing PSCs employing micrometer thick perovskite absorber without (left) and with urea additive (right). The inset represents the corresponding MPP tracking for the two PSCs. The thick PSC employing urea exhibit low hysteresis and good short term stability. (b) The corresponding statistical destitution of the V_{OC} , FF, J_{SC} , and PCE. The overall PV parameters indicate the superiority of thick planar PSCs employing urea.

employing urea to their pristine counterparts. Prototype thick PSCs with urea additive comprised of the layer stack ITO/solution-processed 2PACz/perovskite/C₆₀/BCP/Ag exhibit an overall enhanced PV performance as indicated in Figure 4.7.

Starting with the reference PSCs, Figure 4.7a shows the $J-V$ characteristics of the reference champion PSC (employing 1 μm thick perovskite absorber without additives) with a J_{SC} of 22 mA/cm², a FF of 65.9%, a V_{OC} of 1.059 V, and a PCE of 15.4%. Under MPP tracking, the device exhibits very poor short-term stability with a PCE < 13.5% after only 5 minutes. Corresponding mean values for J_{SC} , FF, V_{OC} , and PCE are 21.3 mA/cm², 67.3%, 1.024 V, and 14.7%, respectively (see Figure 4.7b). Interestingly and as expected from the enhanced crystallinity and optoelectronic properties, the champion device employing urea exhibits an

outstanding performance compared to the reference with a PCE of 19.3% (19.1% stabilized under MPP tracking), a J_{sc} of 22 mA/cm², a V_{oc} of 1.112 V, and a FF of 79%. The corresponding mean values for PCE, J_{sc} , V_{oc} , and FF are 18.7%, 22.3 mA/cm², 1.095 V, and 76.4%, respectively.

The average increase in V_{oc} of thick planar PSCs employing urea compared to the reference is ~70 mV, which indicates suppressed non-radiative recombination within the bulk. A plausible explanation for the reduced non-radiative recombination losses and thereby increased V_{oc} would be the key role that urea plays in passivating the grain boundaries of perovskite thin films as reported by Lee *et al.*²²¹ In addition, the FF mean value of the reference PSCs is too low, which indicates inefficient charge carrier extraction due to the considerably thick perovskite absorber. The FF mean value increases from 67.3% for the reference thick PSCs to 76.4% for the thick PSCs employing urea. The average increase in FF is ~10%, which indicates the impact of employing urea in minimizing the density of grain boundaries and the consequent enhancement in minority charge carrier diffusion length. Furthermore, the thick PSCs employing urea exhibit an increase in J_{sc} by ~1 mA/cm². The enhancement in J_{sc} can be attributed to two main factors: (1) Increasing the charge carrier diffusion length and thus enabling efficient charge carrier extraction results in J_{sc} gains as reported by Chen *et al.*⁹⁴ (2) As discussed earlier, introducing urea forms complex compounds in the perovskite precursor solution, which results in damped PbI₂ XRD peak as shown in Figure 4.6a. Hence, thick perovskite absorbers employing urea suffer less parasitic absorption.²²² In line with this explanation, EQE comparison (see Figure 4.6b) of thick PSCs with and without urea indicates higher signals for PSCs employing urea between ~350 and ~550 nm (PbI₂ exhibits high absorption in this wavelength region).^{223,224} Such big improvements in the individual PV parameters result in an average increase in PCE from 14.7% for the reference thick PSCs to 18.7% for thick PSCs employing urea additive as indicated by the statistical comparison in Figure 4.7b.

4.5 Summary

In this chapter, we developed a micrometer-thick perovskite absorber that assures full surface coverage over industrial-like micrometer-sized pyramidal textures. Decreasing the texture size from the standard ~5 μm down to ~1-2 μm while maintaining low broadband reflectance was the starting point for our solution-processed perovskite absorbers. However, employing our baseline recipe, which provides ~350 nm perovskite layer over such textures resulted in poor coverage and consequently, PSCs employing the baseline recipe were fully shunted. Increasing the perovskite precursor solution molarity together with optimizing the deposition parameters resulted in a ~1 μm thick absorber over planar surface, which was sufficient to provide optimal surface coverage over the textured surface with no remarkable signs of pinholes or other defects. Due to the drastic increase of the perovskite absorber thickness, which is comparable or even larger than the charge carrier diffusion length, planar PSCs employing such thick absorbers suffered very low FF and V_{oc} as a consequence of inefficient charge carrier extraction. In addition to their inferior PV performance, thick planar PSCs exhibited huge hysteresis with HF > 20%. To overcome this challenge and enhance the photophysical properties of such thick absorbers and thereby the PV performance of thick planar PSCs, we employed the Lewis base additive urea into the highly concentrated perovskite precursor solution.

As urea tends to form complex compounds in the precursor solution and plays a key role in crystallization dynamics, thick perovskite films employing urea exhibited much larger grain

size compared to their reference counterparts (~ 2.3 times larger). Such increase in grain size inherently resulted in fewer grain boundaries and thereby lower trap density. Consequently, thick perovskite absorbers employing urea exhibited longer charge carrier lifetime compared to the reference. Therefore, PSCs employing urea are superior in charge carrier extraction and FF ($\sim 10\%$ higher than the reference). Furthermore, reducing trap density together with the role that urea plays in passivating grain boundaries as hypothesized by Lee *et al.*²²¹ suppressed non-radiative recombination and thereby enabled high V_{OC} (~ 70 mV higher than the reference). In addition, efficient charge carrier extraction together with improved crystallinity resulted in enhancement in J_{SC} (~ 1 mA/cm² higher than the reference). The remarkable improvement in these individual parameters added up to pronounced superiority in PCE, stability under MPP tracking, and low hysteresis.

5. Hole transport layers with nearly lossless interface

Due to the large surface area that a textured substrate exhibit compared to a planar, non-radiative recombination at the hole transport layer (HTL)/perovskite interface is more pronounced. Hence, identifying a proper HTL is more crucial when processing perovskite films over textured surfaces. In this chapter, we discuss the development of compatible HTLs with micrometer-sized textured surfaces. So far, deposition of self-assembled monolayers (SAM)-HTLs has been limited to solution-processing methods such as spin-coating, dip-coating, and spray-coating. In this regard, the development of alternative vacuum-deposition method is a necessary step towards conformal coating of SAM-HTLs over textured surfaces. Therefore, we report for the first time on a novel method for depositing SAMs *via* thermal evaporation and investigate in-depth the chemical environment of evaporated SAM-HTLs compared to their conventional solution-processed counterparts. We study the impact of evaporating SAMs onto their surface wettability, which tackle the SAM Me-4PACz common wettability issue that has been reported merely in literature. Furthermore, we compare planar layer-stacks and completed perovskite solar cells (PSCs) employing both solution-processed and evaporated SAM-HTLs to study the photophysical properties, morphology, crystal structure, and photovoltaic (PV) performance. Finally, we investigate voltage losses at the HTL/perovskite interface of pyramidal textured surface to check the compatibility of the developed deposition method with micrometer-sized textures compared to other HTLs.

Acknowledgements and contributions

Parts of this chapter on evaporated SAM-HTLs have been published in Advanced Energy Materials by Ahmed Farag and Thomas Feeney as shared first authors with the title ‘‘Evaporated Self-Assembled Monolayer Hole Transport Layers: Lossless Interfaces in p-i-n Perovskite Solar Cells’’.⁶⁰ Many graphs in this chapter are reproduced or adapted with permission of Wiley. Ahmed Farag has planned and designed the experiments under the supervision of Dr. Ulrich W. Paetzold. The idea of evaporating SAMs was first initiated and tested by Dr. Ihteaz M. Hossain. Thomas Feeney performed further optimizations on the evaporation of SAMs. Ahmed Farag fabricated and characterized the perovskite solar cells. The XPS measurements were performed by Dr. Kathrin Küster from the Max Planck Institute for solid-state research, the data were analyzed by Ahmed Farag and Dr. Kathrin Küster. The FTIR measurements were performed by Ahmed Farag and Rainer Bäuerle from the InnovationLab, the samples were prepared and the data were analyzed by Ahmed Farag. The PLQY measurements were performed by Dr. Paul Faßl. Dr. Yang Li has performed the TRPL measurements and Fabian Schackmar has conducted the contact angle measurements. SINGULUS TECHNOLOGIES AG, has provided us with textured silicon wafers. Thomas Feeney performed the X-ray diffraction measurements.

5.1 Introduction

Since inverted (*p-i-n*) PSCs have presented themselves as a competitive candidate for eventual commercialization,^{225–227} many researchers have been trying to develop efficient charge transport layers (CTLs) that can boost the power conversion efficiency (PCE) of *p-i-n* PSCs further.^{74,110,118,185,228,229} The last few years have witnessed a remarkable improvement in the quality and process flexibility of the commonly used HTLs. For example, NiO_x is widely used HTL in the *p-i-n* architecture and can be deposited *via* various physical vapor deposition (PVD) methods such as e-beam evaporation, sputtering, and atomic layer deposition (ALD).^{53,230} PSCs employing NiO_x as HTL have shown good long-term stability,^{62,63,65} however, depositing efficient NiO_x HTLs requires extra processing steps such as introducing gasses during the deposition, thermal treatment during/after deposition, and/or doping.^{65,69,231–234} Furthermore, the metal oxide has been reported to interact with the perovskite thin films leading to interfacial degradation and consequently, relatively high hysteresis and voltage losses are main drawbacks in PSCs employing this conventional HTL.^{67–71} Meanwhile, solution-processed HTLs such as poly[bis(4-phenyl)(2,4,6-trimethylphenyl)amine (PTAA) and poly(N,N'-bis(4-butylphenyl)-N,N'-bis(phenyl)benzidine) (PTPD) have been reported to enable high V_{OC} , only if defect modulation and/or doping is considered.^{69,162,163,235–240} The major drawback of such solution-processed HTLs is the poor surface wettability they exhibit and the consequent poor coverage of the perovskite film even on planar surfaces.^{69,162,163,235–240}

SAMs,^{110,241–246} which generally tend to form covalent bonds with the subjacent transparent conductive oxide (TCO) and develop self-limiting functional layers, have presented themselves as a strong candidate.^{74,110,185,247–249} The most common three SAMs in perovskite community (due to their commercial availability and exceptional properties) are [2-(9H-Carbazol-9-yl)ethyl]phosphonic acid (2PACz), [2-(3,6-Dimethoxy-9H-carbazol-9-yl)ethyl]phosphonic acid (MeO-2PACz), and [4-(3,6-Dimethyl-9H-carbazol-9-yl)butyl]phosphonic acid (Me-4PACz).^{74,110} These three SAM materials have phosphonic acid functional group that exhibit self-assembling growth, leading to formation of a very thin layer (e.g. monolayer) when deposited on TCOs. Together with the presence of carbazole bodies in the three materials, which are known to form hole selective layers, make SAM-HTLs very efficient in charge carrier extraction (precisely, holes extraction) and minimize non-radiative recombination losses at SAM-HTL/perovskite interface.^{74,110,118}

As discussed in Chapter 4, utilizing textured bottom silicon (Si) sub-cells is not only beneficial from the industrial perspective; it is rather favorable due to the exceptional optical gains when employed in monolithic tandems (so far, a PCE of 31.25% has been reported utilizing a textured Si sub-cell).^{8,13,24,25,75,96,99,102,250,251} However, the complex geometry of a micrometer-sized pyramidal textured surface (which consists of wall sides, tips, and valleys) makes it challenging to have a conformal HTL using the conventional solution-processed deposition methods. The absence of uniform coverage might lead to inefficient charge carrier extraction at the HTL/perovskite interface. In addition, the accumulation of HTL material in the valleys can lead to a degradation in performance.¹³ Furthermore, conformal coverage of the HTL is necessary to prevent the detrimental shunting paths that exposed regions can lead to.⁶¹ Finally yet importantly, the large surface area that a textured surface exhibits compared to a planar surface is expected to result in high non-radiative recombination at the

HTL/perovskite interface. Hence, selecting a proper HTL and ensuring uniform surface coverage when processing perovskite thin films over textured surfaces is necessary to guarantee high fabrication yield and to minimize voltage losses at the HTL/perovskite interface.^{31,252}

The development of evaporated SAM-HTLs, which we are reporting in this chapter, are expected to possess the virtues of NiO_x without the associated issues. They ensure conformal surface coverage akin to a vacuum-deposited NiO_x layer, preventing detrimental shunting paths. Simultaneously, SAM-HTLs suppress non-radiative recombination, leading to the desired reduced V_{oc} losses at the HTL/perovskite interface.^{74,110,118}

In this chapter, we report for the first time on thermal-evaporated vacuum-based SAM-HTLs. We investigate the impact of evaporating SAM materials onto their chemical environment and molecular vibration bands utilizing X-ray photoelectron spectroscopy (XPS) and Fourier-transform infrared spectroscopy (FTIR) measurements. To corroborate that the previously reported efficient charge carrier extraction and lossless interface properties of solution-processed SAMs are preserved when deposited *via* thermal evaporation, we employ time resolved photoluminescence spectroscopy (TRPL) and photoluminescence quantum yield (PLQY). Afterwards, we investigate the impact of evaporating SAMs on their surface wettability and the corresponding surface morphology and crystal structure of the grown perovskite thin film. We compare the PV performance of PSCs employing evaporated and solution-processed SAMs. To confirm our expectations of processing evaporated SAM-HTLs onto textured surfaces, specifically with regards to non-radiative recombination at the HTL/perovskite interface, we evaporate 2PACz over micrometer-sized textures and compare the PLQY to that of NiO_x and the double-layer NiO_x/solution-processed 2PACz HTL.

5.2 Thermally evaporated SAMs and their chemical environment

In this section, we demonstrate the thermal evaporation process of SAM-HTLs. As SAMs have been so far deposited only *via* solution-processed methods, it is necessary to investigate if the resultant films would show any signs of degradation when deposited *via* thermal evaporation instead. We utilize XPS and FTIR measurements on evaporated 2PACz thin films for these investigations.

5.2.1 Evaporation of SAM-HTLs

We performed the PVD of SAMs from a crucible using thermal evaporation system (OPTIvap). The crucible was cleaned with IPA and dried with N₂ gun before each deposition process, then filled with 3-4 tips of a small spatula from the SAM of interest. After loading the samples and the crucible, the system is pumped down to $\sim 5 \times 10^{-6}$ mbar before the deposition process takes place. At ~ 150 °C the deposition process starts with evaporation rate of ~ 2 Ås⁻¹ as measured by a quartz crystal microbalance. At first sight, it would be reasonable to assume that the quality of the SAMs itself and, thus, of the SAM-HTLs/perovskite interface, degrades if they are rather deposited *via* thermal evaporation. However, as the PACz derivatives evaporate at rather low temperatures ~ 150 °C, the chances that the chemical environment of evaporated SAM-HTLs remains almost unchanged are quite high.

5.2.2 Atomic species and chemical environment of evaporated SAMs

To investigate the impact of evaporating 2PACz on the atomic species and chemical environment, we utilized XPS as a surface sensitive technique on a glass/ITO substrate coated with evaporated 2PACz thin film (~6 nm). The X-ray photoelectron spectrum of the evaporated 2PACz film exhibits a signal at the C 1s binding energy region (see Figure 5.1a). The signal can be fitted with different characteristic peaks using a mixed Lorentzian/Gaussian function with a Shirley background. Previous XPS investigations of solution-processed 2PACz layers have shown comparable distinct peaks in the C 1s region (see Figure A5.1, adapted with a permission from the Royal Society of Chemistry).¹¹⁰ Considering our evaporated 2PACz sample, there is a strong peak at a binding energy of ~283.9 eV that can be assigned to C-C and C-H bonds, with a relative area of 53.37%.¹¹⁰ The second remarkable peak emerges at ~284.7 eV and arises from the C-N bonds with a relative area of 33.1%.¹¹⁰ In addition, a third peak with a relative area of 13.5% is present at ~285.8 eV. This peak has been hypothesized by Albrecht and coworkers to be correlated to C atoms bonded to three other atoms as in the carbazole fragment.¹¹⁰ On the other hand, another study on solution-processed 2PACz by Levine *et al.* has correlated this peak to C-P bonds.¹¹⁸ Furthermore, additional hypothesis correlates this peak to C-OH and/or C-O-C contamination.²⁵³

Table 5.1. A comparison between the peak position and corresponding relative weight/area of the C 1s energy region for 2PACz powder, evaporated 2PACz thin film onto glass coated ITO, and previously reported solution-processed 2PACz layer onto glass/ITO substrate.¹¹⁰

2PACz powder		Evaporated 2PACz		Solution-processed 2PACz	
<i>Peak position (eV)</i>	<i>Relative area (%)</i>	<i>Peak position (eV)</i>	<i>Relative area (%)</i>	<i>Peak position (eV)</i>	<i>Relative area (%)</i>
284	54.7	283.9	53.4	283.5	57
284.9	35.5	284.7	33.1	284.8	30
286.2	9.8	285.8	13.5	285.9	13

In any case, and irrespective of the previous hypothesis about the kind of bonds or chemical compounds that the third peak represents, it is critical to check if the original material undergoes a chemical change or degrades by the presence or absence of certain peaks, hence, we investigate the X-ray photoelectron spectrum of the original 2PACz powder and compare it to our evaporated 2PACz thin film discussed above. The 2PACz powder sample was prepared by pressing ~1.7 mg of the 2PACz into indium foil and mounted to the holder using double-sided tape. Strikingly, the prominent peak of the C 1s energy region for the 2PACz powder is comparable to that of the evaporated 2PACz thin film (see Figure 5.1b). Similarly, it is fitted to three peaks at 284 eV, 284.9 eV, and 286.2 eV, which are comparable to the peak positions of the evaporated 2PACz thin film. Interestingly and yet more importantly; the relative weight/area is 54.7%, 35.5%, and 9.8% for the peak position 284 eV, 284.9 eV, and 286.2 eV, respectively. The comparison of the peak position and relative weight/area of

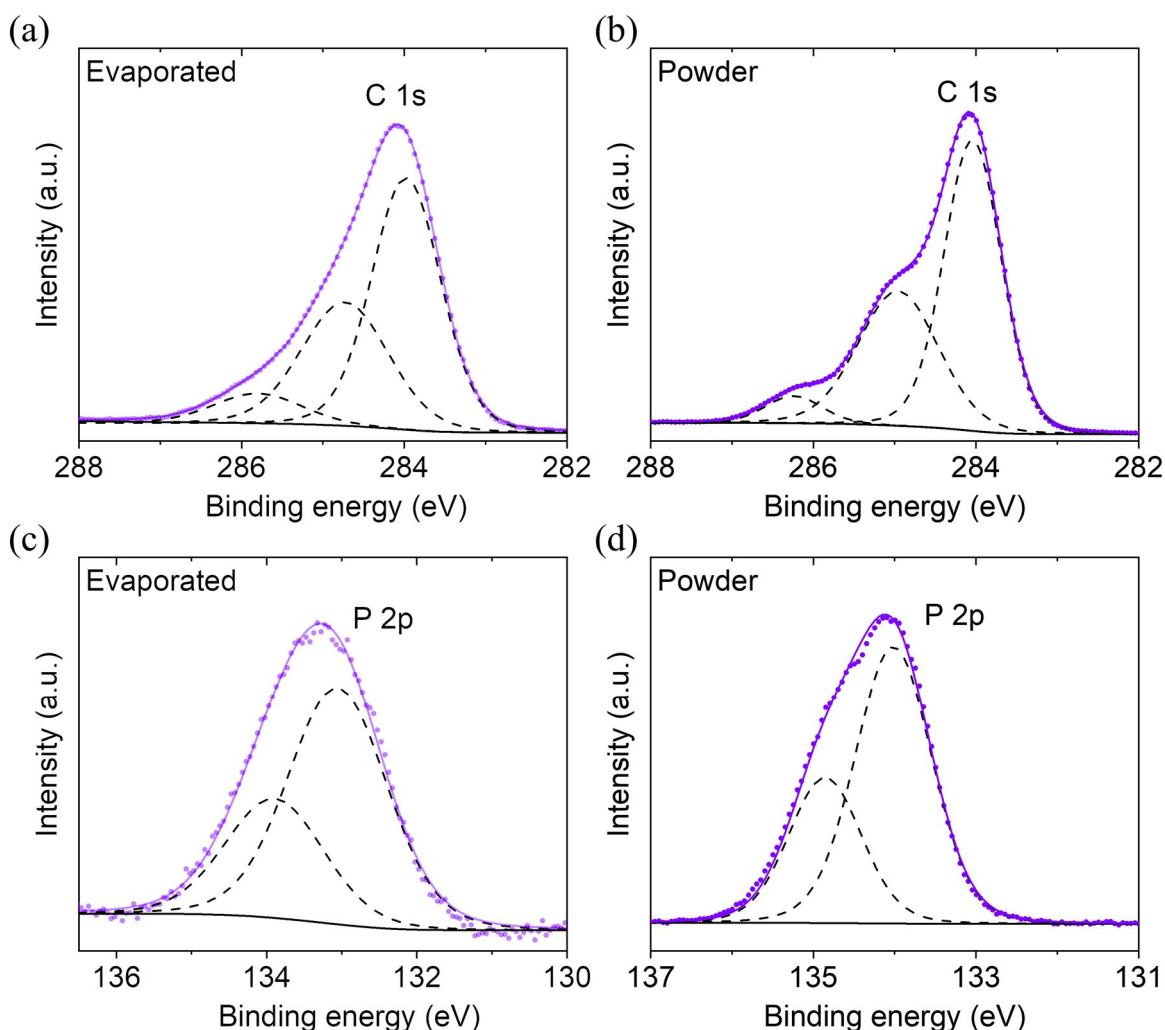


Figure 5.1. (a) and (b) X-ray photoelectron spectra for the C 1s region of evaporated 2PACz thin film and 2PACz powder, respectively. The evaporated film (~ 6 nm) was deposited onto glass/ITO substrate, while the powder sample was prepared by pressing ~ 1.7 mg of the 2PACz powder into indium foil. The violet solid line represents a fit to the real data points (violet dots) and the dashed black lines show the components thereof. (c) and (d) X-ray photoelectron spectra for the P 2p region of the corresponding two samples, respectively.

C 1s region for 2PACz powder, our ~ 6 nm evaporated 2PACz thin film, and previously reported solution-processed 2PACz in Table 5.1, indicate that evaporating the 2PACz does not seem to exhibit a remarkable sign of degradation or chemical changes.

Having investigated the C 1s region for the evaporated 2PACz thin film, where the carbon bonds show strong dominance; the phosphorus presence has to be investigated in depth, due to the importance of the phosphonic acid as the corresponding functional group of the 2PACz. Furthermore, the key advantage of SAM-HTLs in PSCs is their monolayer signature indicated by the covalent bonds between the phosphorus of the SAM itself and the oxygen of the adjacent TCO (ITO in our case) resulting in P-O fingerprint. By investigating the P 2p binding energy region (see Figure 5.1c), we note a strong phosphorus presence, with a signal that can be extracted into two peaks representing P 2p_{3/2} and P 2p_{1/2} at ~ 133 eV and ~ 134 eV, respectively. It has been reported in literature that these peaks might correlate to P-O species.^{254–257} However, there is no evidence to confirm they indicate covalent bonds between the evaporated 2PACz thin film and the adjacent ITO, or in other words, the

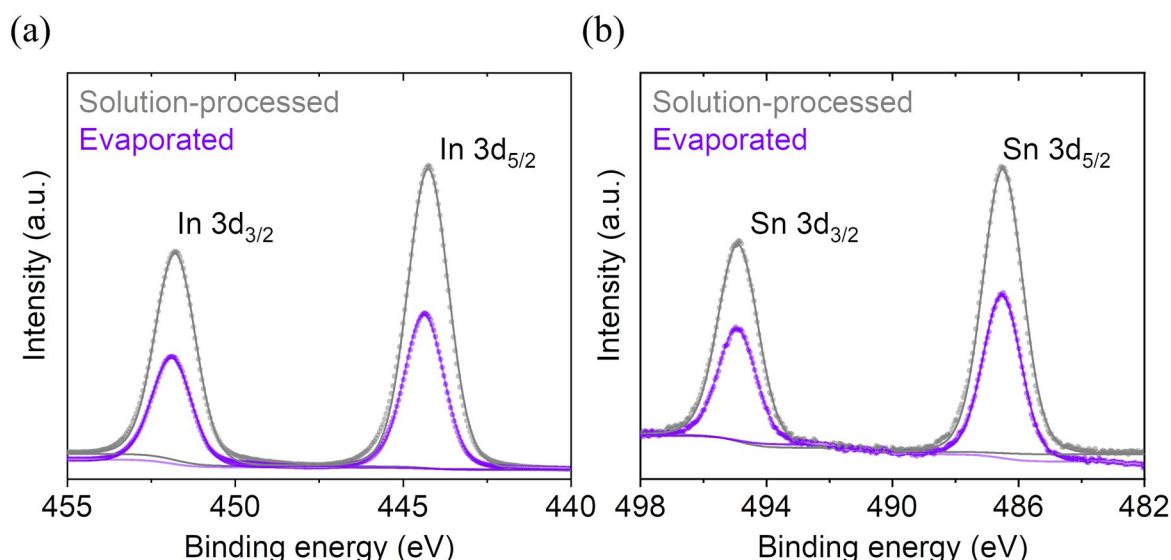


Figure 5.2. (a) and (b) Comparison of the X-ray photoelectron spectra of solution-processed and evaporated 2PACz, deposited onto glass/ITO substrates for the In 3d and Sn 3d energy regions, respectively. In and Sn intensities are quenched in the evaporated film due to its corresponding thickness increase. Part of this figure is reproduced from ref.⁶⁰ with permission from Wiley.

presence of these P-O species in this particular case is not necessarily indicating the formation of a monolayer signature. To further our understanding about the presence of such P-O species in the P 2p energy region, we investigate the P 2p region for 2PACz powder. Interestingly, the XPS spectrum of the P 2p region of the powder sample exhibit similar peaks with comparable relative area to that of the evaporated 2PACz thin film over ITO (see Figure 5.1d). The presence of the P-O species in the powder 2PACz sample indicates that the phosphorus is bounded to oxygen irrespective of the monolayer signature existence. Thus, it creates doubts about the detected species in the evaporated thin film, or in other words, the presence of P-O peaks in the evaporated thin film is not necessarily an indication to covalent bonds between the evaporated SAM and the ITO, simply because similar signals are obtained from the powder itself. Hence, further investigations is needed to claim the presence of monolayer signature in the evaporated 2PACz film (see next section).

An interesting comparison between the indium and tin (the main components of ITO which the 2PACz thin film is deposited onto) XPS signals for evaporated ~ 6 nm 2PACz film and solution-processed counterparts is shown in Figure 5.2. The intensity of In and Sn signals are quenched in the evaporated thin film case. This drop in signals intensity is expected due to the thickness increase of evaporated 2PACz film (~ 6 nm) compared to the solution-processed 2PACz layer (~ 2 -3 nm).²⁵⁸

In general, we see no significant differences in XPS characteristic peak position and relative area for the evaporated film compared to previously reported solution-processed layers.^{110,118} In addition, we see no evidence towards the emergence of new C 1s signals that would indicate a degradation or other chemical change in the 2PACz molecule upon evaporation. Furthermore, phosphorus, which is essential component of 2PACz has shown a strong presence in the P 2p regions and the presence of P-O species needs further investigation before assigning it to monolayer signature in the evaporated film case.

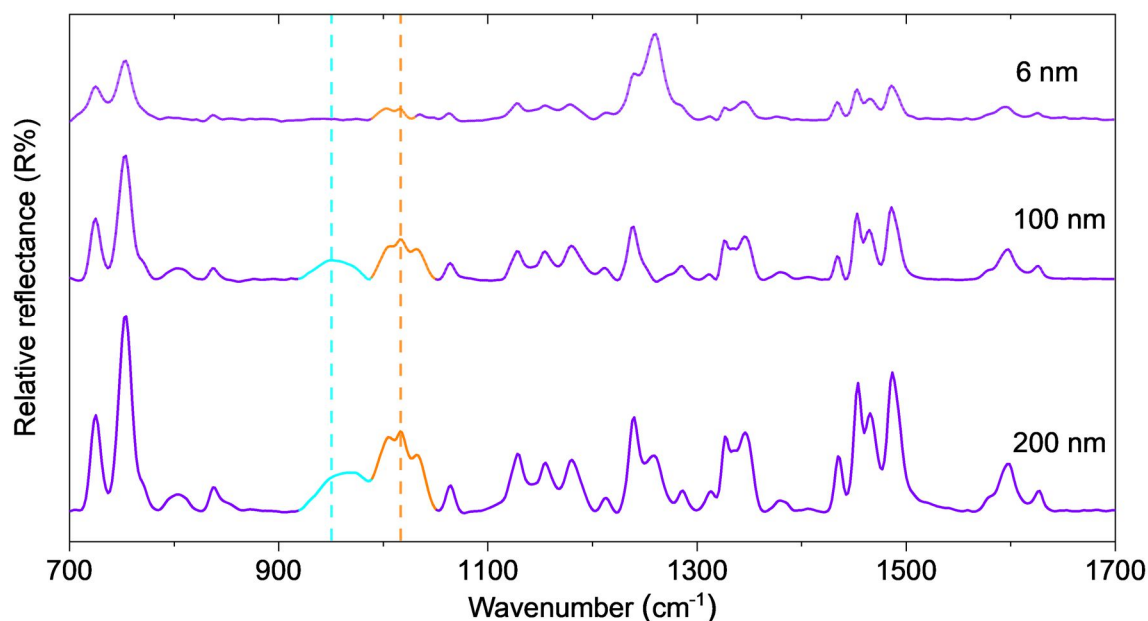


Figure 5.3. Reflection-absorption infrared (RAIR) spectra of evaporated 2PACz thin films with different thickness (6, 100, and 200 nm) onto glass/ITO substrates. The light blue dashed line represents the peak position of P-OH vibration band of the bulk 2PACz reported in ref.¹¹⁰ while the orange dashed line represents the P-O monolayer signature in a solution-processed 2PACz layer.¹¹⁰ Part of this figure is reproduced from ref.⁶⁰ with permission from Wiley.

5.2.3 Evaporated 2PACz and the monolayer signature

To strengthen our understanding of the impact that evaporating 2PACz has on absorption bands of the molecular vibrational modes when compared to a solution-processed layer, we employed reflection-absorption infrared spectroscopy (RAIRS). Compared to the RAIR spectrum of solution-processed 2PACz on an ITO coated substrate (reported in ref.¹¹⁰, and reproduced/adapted in Figure A5.1 with a permission from the Royal Society of Chemistry) the evaporated film exhibits similar characteristic molecular vibrational bands (see Figure 5.3). Notably, at 1346 and 1239 cm^{-1} the two characteristic stretching modes of carbazole are present. Together with the carbazole ring stretching vibration bands, which are present in the 1454-1486 cm^{-1} region, is a strong indication that the carbazole ring is intact. Strikingly, the peak at 1017 cm^{-1} which has been reported to represent the P-O species in solution-processed 2PACz on ITO substrate (see orange dashed line in Figure 5.3) is also present in the RAIR spectrum of our evaporated 2PACz layers.¹¹⁰ The emergence of the P-O vibrations in the RAIR spectrum of the evaporated 2PACz film is a strong evidence on the formation of covalent bonds between the organic phosphonic acid functional group and the subjacent ITO surface. As the P-O species, which has been reported to enable efficient charge carrier extraction in PSCs,^{110,118} exist in evaporated 2PACz films as well, we can assure the presence of monolayer signature in the evaporated films.

The presence of the P-O species in the evaporated 2PACz films is quite interesting as it opens up the possibility of utilizing evaporated SAM-HTLs in potentially efficient PSCs, however it is a bit surprising as the monolayer signature has been exclusively related to solution-processed SAM-HTLs. That raised up an interesting question, whether the monolayer signature would be still present even if we increase the evaporated film thickness.

To answer this question, and strengthen our understanding regarding the monolayer signature in evaporated SAMs, we evaporate thicker 2PACz thin films on glass coated ITO substrates and perform further RAIRS measurements. The RAIR spectra of the thicker films exhibit a broad peak at $\sim 951\text{ cm}^{-1}$ (see Figure 5.3), notably, this peak is absent in the thin evaporated film as well as the previously reported solution-processed layer. Interestingly, the emerged peak in the thicker film is comparable to the bulk 2PACz itself and correlates to P-OH species, which is reported to be prominent in the bulk as indicated by the FTIR spectrum of a KBr 2PACz tablet (reported in ref. ¹¹⁰, and reproduced/adapted in Figure A5.1 with a permission from the Royal Society of Chemistry). The presence of this broad P-OH peak in the evaporated thick films (~ 100 and ~ 200 nm) together with its absence in the thin evaporated film (~ 6 nm) and the previously reported solution-processed layers might indicate that thicker films possess similar chemical properties to that of the bulk material. Interestingly, the presence of the P-OH species does not seem to have an impact on the monolayer signature presence and the self-assembling behavior seize to exist, independent of the evaporated film thickness (e.g., even a ~ 200 nm thick evaporated film exhibits the P-O species vibration bands). In other words, the P-O species signature to the formation of a monolayer on ITO is present even if not all the phosphonic anchoring groups are deprotonated. In this regard, one can still fabricate efficient PSCs utilizing thick evaporated SAM-HTLs (will be discussed in Section 5.6)

Based on the RAIRS and XPS data, we conclude that there is no clear evidence on remarkable changes in the chemical environment of the evaporated 2PACz films compared to their solution-processed counterparts. Furthermore, the evaporated films maintain the self-assembling behavior by the evidence of monolayer signature expected in solution-processed counterparts, independent of the evaporated film thickness, which is essential for fabricating efficient PSCs.

5.3 Wettability and surface coverage

Having the evaporated SAMs showing comparable chemical environment to that of solution-processed counterparts and after the evidence of monolayer signature presence in our evaporated thin films, which is essential for efficient PSCs fabrication, it is necessary to investigate the impact of evaporating SAMs on their surface wettability. Many solution-processed HTLs, which have been reported to enable high V_{OC} exhibit poor surface wettability.^{69,162,163,235–240} Consequently, spin-coating perovskites over such HTLs tend to form inhomogeneous perovskite thin films, which negatively affects the PV performance and fabrication yield. Although there are no reports that indicate such wettability issue for either solution-processed 2PACz or MeO-2PACz, it is a main drawback of the SAM Me-4PACz.^{21,43,230,249,259}

Me-4PACz, introduced to the perovskite community by Albrecht and co-workers in 2020,⁷⁴ is relatively underutilized SAM. It has shown outstanding performance as an HTL in terms of long-term stability of PSCs, further voltage loss mitigation at the HTL/perovskite interface, and more efficient charge carrier extraction compared to other related SAMs (2PACz and MeO-2PACz). However, to the best of our knowledge, it has been employed in relatively little reports since its introduction,^{21,43,118,249,259,260} which doesn't match the reported superior capabilities. We hypothesize the primary reason for this is the poor surface coverage exhibited by perovskite thin films deposited onto a Me-4PACz coated ITO surface

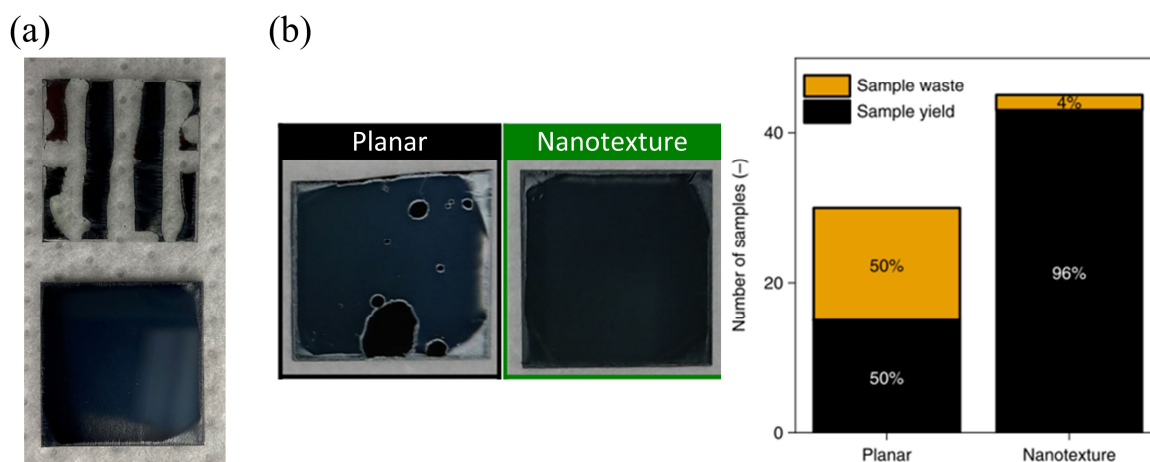


Figure 5.4. (a) Comparison between perovskite thin film coverage over solution-processed (top) and evaporated (bottom) Me-4PACz indicates poor surface coverage of the perovskite film in the solution-processed Me-4PACz case. Both solution-processed and evaporated Me-4PACz HTLs were deposited onto planar patterned glass/ITO. (b) Reproduced and adapted figure with permission from Springer Nature,⁴³ indicates poor surface coverage of perovskite thin film deposited onto solution-processed Me-4PACz HTL and a consequence drop in the fabrication yield to 50% when processed onto planar surface.

(see Figure 5.4a), which results in very low fabrication yield.^{21,261} This hypothesis is supported by literature utilizing Me-4PACz, indicating it is not an issue exclusively present in our work.^{21,43,249,259,260}

Recently, Becker and co-workers reported a 29.80% PCE for a 2T monolithic perovskite/silicon tandem solar cell employing Me-4PACz as an HTL (the world record as of the 24th of May, 2022).²⁶¹ In their work, they have commented on problems with low fabrication yield ($\sim 50\%$), caused by poor surface coverage of the perovskite layer when Me-4PACz is employed as an HTL on top of planar Si bottom cells. Fabrication yield improved drastically (from $\sim 50\%$ to $\sim 95\%$) by utilizing nano-textured Si bottom cell, accredited to a significant improvement in surface coverage (see reproduced/adapted image with permission of Springer Nature in Figure 5.4b).⁴³ The authors highlighted the principal cause for this improvement in coverage for nano-textured Si cell/ITO/Me-4PACz to be the physical attributes texturing imposes on substrates. Nano-textured surfaces were shown to exhibit higher roll-off angle for perovskite solutions compared to planar surfaces (25° and 18° , respectively), enabling the textured surface to retain the perovskite solution. We posit three additional potential contributions toward efficient surface coverage when a nano-textured surface is employed. First, if the coverage issue is due to a reduction in adsorption rate for Me-4PACz compared to 2PACz and MeO-2PACz, a rate reduction that has been previously correlated to anchoring chain length in alkanethiol SAMs,²⁴⁴ then the increased roll-off angle would increase surface exposure time and hence SAM layer density. Second, the ITO recombination junction has a larger surface area when deposited over a textured surface compared to a planar one, enabling more phosphonic anchoring groups to covalently bond with the ITO surface and consequently improve Me-4PACz surface coverage. Finally, based on the Wenzel and Cassie-Baxter models, a textured surface will make the hydrophilic surface more hydrophilic and in this case, the effective contact angle would be lower on a textured surface than on a planar one.^{262–264} The correlation between contact angle and perovskite wettability consequently implies improved surface coverage for the perovskite thin film.^{219,220,265}

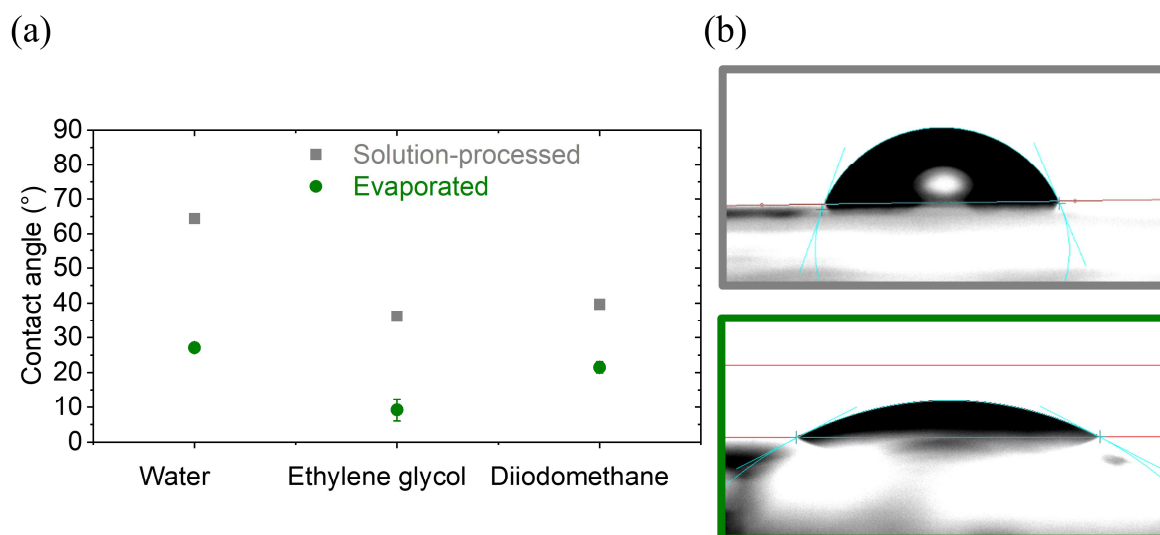


Figure 5.5. (a) Comparison of the contact angle measurements of different solvent droplets with the half-stack glass/ITO/SAM-HTL. The HTL applies for solution-processed and evaporated Me-4PACz. The data indicate a remarkable decrease of the contact angle for water, ethylene glycol, and diiodomethane droplets with the evaporated Me-4PACz surface compared to the solution-processed counterpart. (b) Images of the water droplet onto solution-processed (top) and evaporated (bottom) Me-4PACz layers. Part of this figure is reproduced from ref.⁶⁰ with permission from Wiley.

In the same context, Topic and co-workers have reported a certified PCE of 24.2% on perovskite/CIGS monolithic tandem solar cell (the current world record), employing Me-4PACz as an HTL.²¹ In their work, they have addressed the low fabrication yield issue and assigned it to inferior wetting when using Me-4PACz, in full agreement with Becker and co-workers as discussed earlier. Their discussion on methods to further improve PCE theorizes that the FF of their current world record device will increase from 71% to ~80% if the Me-4PACz wettability issue is solved.²¹ Taddei *et al.* have also reported on poor surface coverage of the perovskite thin film when deposited onto solution-processed Me-4PACz HTL. To enhance the surface wettability of solution-processed Me-4PACz, they employed Al₂O₃ nanoparticles layer on top of it.²⁵⁹

To investigate surface coverage of planar surfaces when solution-processed SAM-HTLs are replaced with evaporated counterparts, we utilize contact angle measurements for different solutions (namely deionized water (H₂O), ethylene glycol [(CH₂OH)₂], and diiodomethane [(CH₂I₂)] over the half-stack glass/ITO/SAM-HTLs. Low contact angles are desirable due to their correlation with perovskite wettability,^{219,220,265} with a relative decrease in water contact angle for a given surface also correlated to improved perovskite morphology.²⁶⁵

Our contact angle investigations will focus primarily on Me-4PACz due to its merely reported poor wetting issue, however, similar investigations on the contact angle for 2PACz and MeO-2PACz were executed and will be discussed. It is important to first disclaim that contact angle measurements of SAMs have a degree of inherent inaccuracy due to spontaneous liquid-surface interactions. These interactions may impact the contact angle measurement,²⁶⁶ precluding precise calculations of surface energetics. To minimize such effects, we utilize a high-speed camera (2450 fps) in our measurements. We hence consider comparisons of contact angle between layers of comparable materials (evaporated and solution-processed SAMs) sufficient to indicate wettability trends.

Indeed, as expected from the resultant poor surface coverage in Figure 5.4 and confirmed by previous reports,^{21,261} we measure rather high contact angles over solution-processed Me-4PACz surface (64.4°, 39.6°, and 36.2° for H₂O, CH₂I₂, and (CH₂OH)₂, respectively) as shown in Figure 5.5 and Table 5.2, which indicate remarkable poor surface wettability.^{219,220,265} Having high contact angle, and consequently poor surface wettability will lead to inefficient surface coverage of the perovskite thin film (as shown in Figure 5.4) which makes processing efficient PSCs technically challenging and will lead to a reduction in fabrication yield. Strikingly, on the other hand, we measure rather low contact angles over evaporated

Table 5.2. Contact angle measurements for evaporated and solution-processed self-assembled monolayers (SAMs) with different solvents. The polar, dispersive, and total free energies are calculated using the OWRK method.²⁶⁷

Film onto glass/ITO	Contact angle (θ°)			Surface Free energy (mN/m)		
	H ₂ O	(CH ₂ OH) ₂	CH ₂ I ₂	Dispersive	Polar	Total
Solution-processed Me-4PACz	64.4±0.4	36.2±0.2	39.6±0.4	39.8±1.1	10.1±1.1	49.9±2.2
Evaporated Me-4PACz	27.1±1.3	9.2±3.7	21.5±2.1	47.3±0.8	26.4±0.8	73.7±1.6
Solution-processed 2PACz	52±0.2	31.7±0.8	29.7±1.4	44.4±1.6	15.1±1.6	59.4±3.2
Evaporated 2PACz	17.7±1.9	CW	25.7±0.6	45.9±0.4	30.5±0.4	76.4±0.8
Solution-processed MeO-2PACz	62.5±0.5	39.1±0.6	29.6±0.9	44.4±1.3	9.6±1.3	54±2.6
Evaporated MeO-2PACz	63.6±0.6	39.7±0.9	22.9±1.5	46.9±0.5	8.3±0.5	55.2±1.0

Me-4PACz surface (27.1°, 21.5°, and 9.2° for H₂O, CH₂I₂, and (CH₂OH)₂, respectively) which corresponds to a dramatic reduction of the contact angle compared to the solution-processed counterpart (58%, 46%, and 75% for H₂O, CH₂I₂, and (CH₂OH)₂, respectively). A reduction in contact angle and hence enhanced surface wettability results in considerably improved surface coverage for solution-processed perovskites over evaporated Me-4PACz as indicated in Figure 5.4a.

By investigating the 2PACz surface, and even though the commonly used solution-processed layers have not been reported to cause any wettability issues, further contact angle measurements indicate that the surface of evaporated 2PACz also benefits from the uniform surface coverage that evaporation process leads to. The corresponding contact angles over

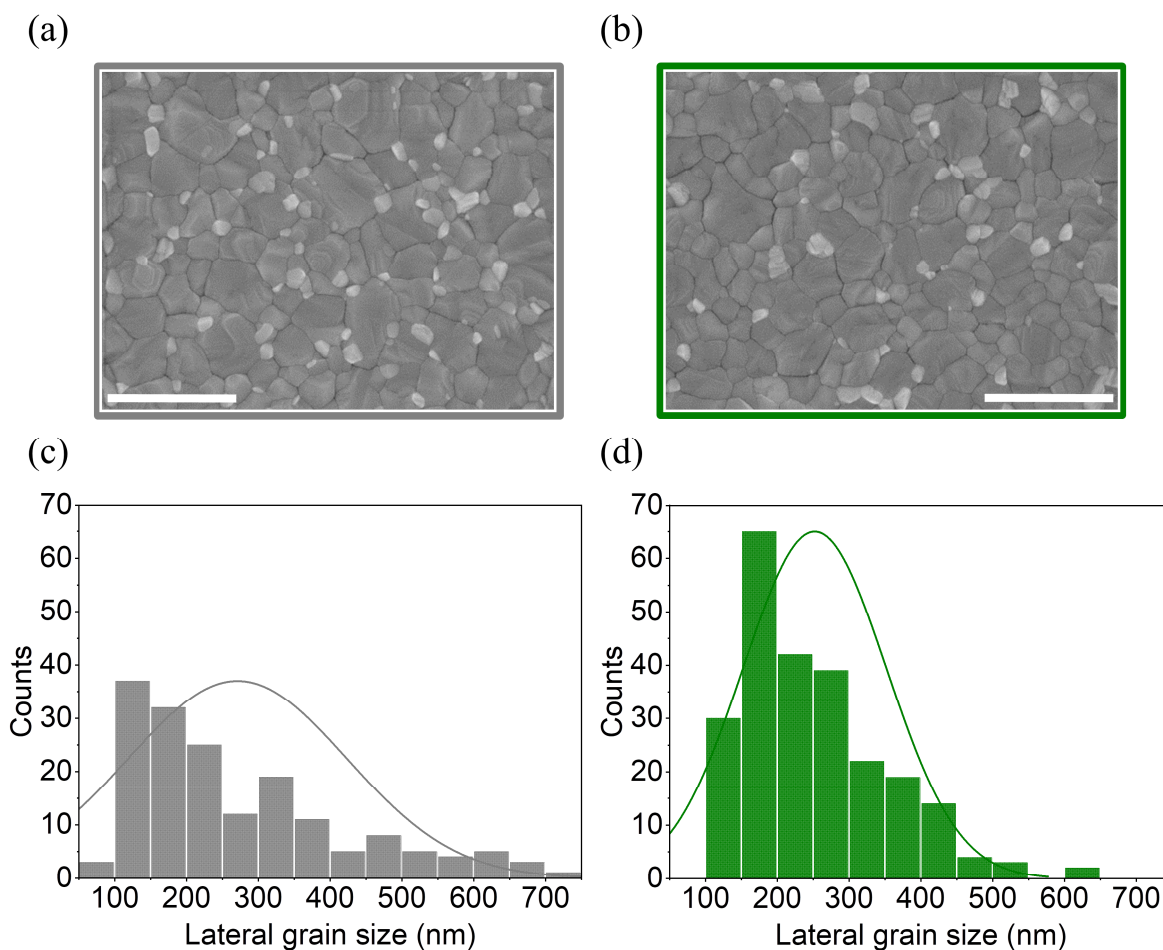


Figure 5.6. (a) and (b) Top-view scanning electron microscope (SEM) images of perovskite thin films deposited over solution-processed and evaporated Me-4PACz, respectively. The scale bar is 1 μm . (c) and (d) The corresponding lateral grain size histograms, respectively. The mean value of the lateral grain size for the perovskite film deposited over solution-processed Me-4PACz is slightly higher than the evaporated counterpart (272 and 251 nm, respectively).

solution-processed 2PACz are 52° , 29.7° , and 31.7° for H_2O , $(\text{CH}_2\text{OH})_2$, and CH_2I_2 , respectively, which remarkably decrease to 17.7° , 25.7° , and complete wetting, respectively for the evaporated counterparts (see Table 5.2). As a consequent of improved surface wettability of evaporated 2PACz, we note a remarkable decrease in the volume of perovskite precursor solution required to assure optimum surface coverage of the perovskite thin film over the substrate (from 70 μl in solution-processed 2PACz case to 40 μl in the evaporated one). Contact angle measurements on MeO-2PACz exhibit no remarkable difference when evaporated as compared to solution-processed. For H_2O , $(\text{CH}_2\text{OH})_2$, and CH_2I_2 the contact angles on solution-processed and evaporated MeO-2PACz are $62.5^\circ/63.6^\circ$, $39.1^\circ/39.7^\circ$, and $29.6^\circ/22.9^\circ$, respectively (see Table 5.2).

Overall, evaporated SAMs with their conformal surface coverage over the adjacent ITO exhibit clear trends of improved wettability as indicated by their low contact angles for a variety of liquids compared to the solution-processed counterparts. Improved wettability, which correlates to enhanced surface coverage of the perovskite thin film, will have a positive impact on the fabrication yield of PSCs employing evaporated SAM-HTLs. Although we focus mainly on 2PACz as the widely used SAM-HTL in high efficiency PSCs

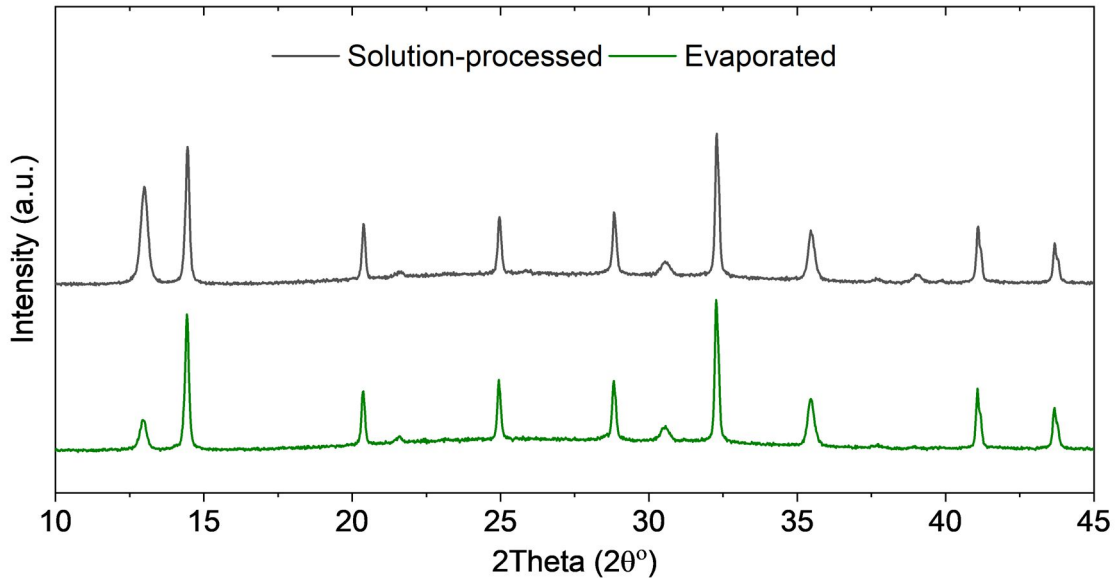


Figure 5.7. X-ray diffraction (XRD) spectra for perovskite thin films processed onto the half-stack ITO/HTL/perovskite. The HTL applies for solution-processed and evaporated Me-4PACz.

reported in literature, it was necessary to indicate how evaporating Me-4PACz can mitigate/eliminate its well-known wettability issue and enable further employment of this exceptional HTL.

5.4 Surface morphology and crystal structure

The crystallization dynamics of perovskite thin films are known to be substrate dependent.^{160,268–271} Different materials when employed as HTLs in the inverted *p-i-n* architecture (or ETLs in the regular *n-i-p* architecture) tend to have a strong impact on the grain size and crystal structure of the perovskite thin film.¹⁸ Due to the strong correlation between surface wettability and crystal growth of perovskite thin films,^{218,268,271} and considering the huge impact of the utilized deposition methods of SAMs (solution-processed and evaporated) onto their surface wettability as discussed in the previous section, we investigate the morphology of perovskite thin films, deposited over evaporated SAM-HTLs and compare them to their solution-processed counterpart. Furthermore, it is critical to investigate the impact of deposition method of SAM-HTLs on the grain size due to the important role that the grain boundaries play in non-radiative recombination losses, which affects the V_{oc} and consequently PCE of PSCs.

According to the heterogeneous nucleation theory, hydrophilic surfaces with their lower contact angles tend to have higher density of nuclei on the surface.^{11,218} As these high-density nuclei act as crystallization centers, the crystal growth at each nucleation center would stop by the time a neighbor crystal seize to exist, resulting in overall smaller grain size.²¹⁹ Considering the enhancement in surface wettability when replacing solution-processed Me-4PACz with evaporated counterpart was quite remarkable, we will focus our investigation on it.

Top-view scanning electron microscope (SEM) images of perovskite films deposited on Me-4PACz HTL in both its solution-processed and evaporated form (see Figure 5.6) show no

presence of holes or signs of defects. The SEM images indicate that the number of larger grains (> 500 nm) in perovskite thin film deposited onto solution-processed Me-4PACz HTL (which exhibit high contact angles and poor surface wettability) is slightly higher than its evaporated counterpart. The corresponding histograms representing the grains lateral size in Figure 5.6 indicate the average grain size in perovskite film processed on solution-processed Me-4PACz is 272 nm. Interestingly however, the average grain size of perovskite film on evaporated Me-4PACz is 251 nm, which is comparable to the solution-processed case.

The small difference in average grain size that correlate to change in surface wettability between perovskite thin films processed over solution-processed and evaporated Me-4PACz is in full agreement with the heterogeneous nucleation theory. In the same context, Pylnev *et al.* have shown that contact angle reduction from 72° to 3° resulted in only 14% larger grain size which is in full agreement with the small change occurs in our case study.²²⁰ Furthermore, literature indicate that such small difference in the grain size as shown in our investigations ($\sim 8\%$) does not seem to have a strong impact on photophysical properties, charge carrier dynamics, or photovoltaic performance.^{120,272}

To investigate whether changing Me-4PACz deposition method has an impact on the crystal structure of perovskite films, we investigate XRD measurements. Interestingly, the common expected peaks of the (111), (110), and (100) crystal planes are having almost the exact same intensity for the two stacks as shown in Figure 5.7. At $\sim 13^\circ$ the PbI_2 peak emerges in the two spectra, however, the intensity is remarkably high in the solution-processed Me-4PACz case. Literature have reported on PACz derivatives with their phosphonic acid (PA) functional group to behave like Lewis bases.²⁵⁸ In such case, the function group of SAM-HTL is potentially washed/mixed at the interface with the perovskite precursor solution during perovskite deposition. Consequently, the PA groups of SAM is expected to form coordination bonding with metal ions (e.g. Pb), similar to the Lewis bases behavior when added to a perovskite precursor solution prior deposition.^{94,180,204,206,221,273} Given the fact that evaporated Me-4PACz thin film ($\sim 6-8$ nm), would have more PA available for the claimed interaction compared to a solution-processed layer ($\sim 2-3$ nm),²⁵⁸ this is reasonable for the damped PbI_2 intensity for the perovskite film deposited onto the evaporated Me-4PACz depicted from the XRD data.

We conclude that the tackled surface coverage issue by utilizing evaporated SAM-HTLs as a result of enhanced surface wettability doesn't come on the expense of surface morphology or crystal structure of the grown perovskite film.

5.5 Photophysical properties

As 2PACz and MeO-2PACz were first introduced to the community as conformal monolayers with lossless interfaces in the *p-i-n* architecture, with resultant high V_{oc} compared to other HTLs,¹¹⁰ it is not unreasonable to assume the quality of the HTL/perovskite interface to degrade if SAMs are rather deposited *via* thermal evaporation. That has brought our interest to quantitatively analyze and compare non-radiative recombination at the HTL/perovskite interface for both evaporated and solution-processed SAMs.

We first seek to quantitatively analyze non-radiative recombination losses at the 2PACz/perovskite interface. For this purpose, we perform PLQY measurements on samples

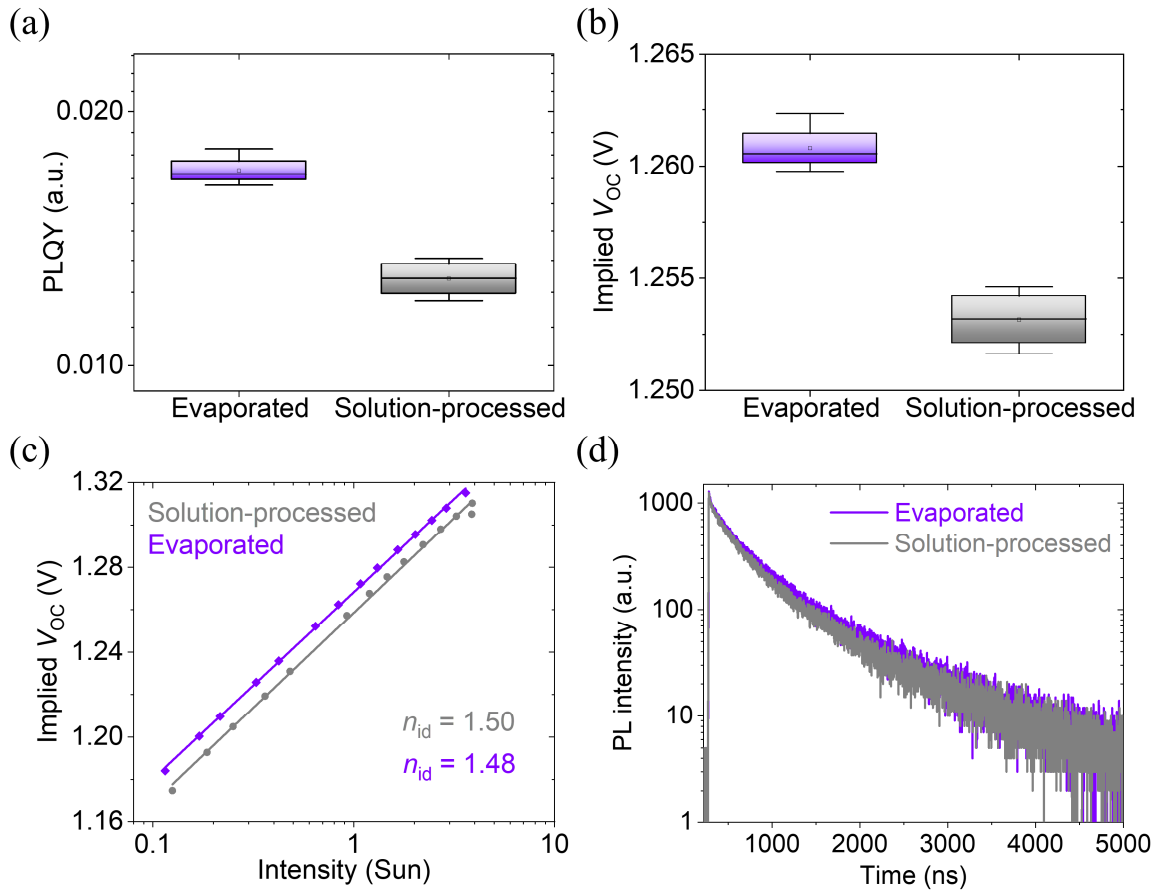


Figure 5.8. (a) Photoluminescence quantum yield (PLQY) comparison of the half-stacks ITO/HTL/perovskite, employing solution-processed and evaporated 2PACz. (b) The corresponding implied open-circuit voltage (V_{oc}). (c) Ideality factor (n_{id}) extracted from a fit to the intensity-dependent implied V_{oc} . (d) Time resolved photoluminescence (TRPL) comparison of the corresponding half-stacks. The TRPL data indicate a comparable decay trend for solution-processed and evaporated 2PACz. Reproduced from ref.⁶⁰ with permission from Wiley.

prepared with either evaporated or solution-processed 2PACz as HTLs in the half-stack ITO/2PACz/perovskite. We employ the widely used triple-cation perovskite with a composition of $\text{Cs}_{0.05}\text{MA}_{0.22}\text{FA}_{0.73}\text{Pb}(\text{I}_{0.77}\text{Br}_{0.23})_3$ and a band gap of ~ 1.68 eV, due to its current ubiquitous nature in recent literature, being particularly prevalent in perovskite/Si monolithic tandem solar cells as it has been shown to fulfill the current matching condition.^{43,74} As non-radiative recombination is mostly dominated by the perovskite/ETL interface in the $p-i-n$ architecture, we refrained from introducing an ETL to exclude these losses and reliably account only on V_{oc} losses at the SAM-HTL/perovskite interface. PLQY of the reference stack (employing solution-processed 2PACz HTL) has an average value of $\sim 1.26\%$ (Figure 5.8a), in line with the expected PLQY for previously reported perovskite with lossless interface and similar composition.^{74,274} PLQY is slightly increased to an average value of $\sim 1.7\%$ for the evaporated 2PACz stack. Figure 5.8b indicates a comparable implied V_{oc} for solution-processed and evaporated 2PACz half-stacks with 1.253 V and 1.261 V, respectively. The internal ideality factor (n_{id}) is obtained, by performing intensity-dependent PLQY measurement for the corresponding half-stacks and apply a fit to the calculated implied V_{oc} .^{14,171} Half-stack employing evaporated 2PACz HTL exhibits an ideality factor of $n_{id} = 1.48$, which is comparable to $n_{id} = 1.50$ for the reference half-stack

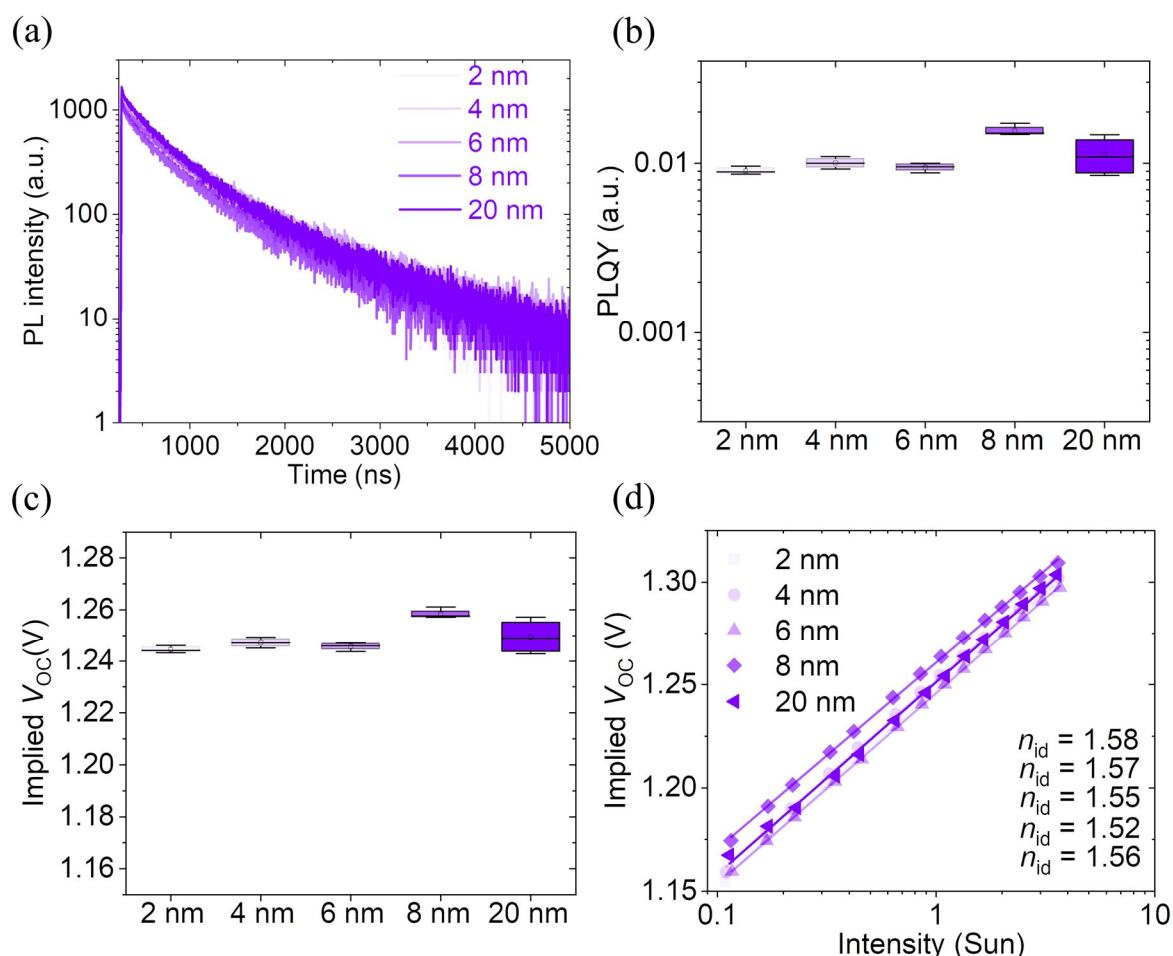


Figure 5.9. (a) Thickness dependent TRPL measurements for the half-stack ITO/Evaporated 2PACz/perovskite. The various evaporated 2PACz thin film thickness (2, 4, 6, 8, and 20 nm) exhibit a comparable decay trend indicating the charge carrier dynamics are independent of the evaporated 2PACz film thickness. (b)-(d) Comparison of the PLQY, implied V_{oc} , and internal ideality factor for similar half-stacks, respectively. The comparable PLQY, implied V_{oc} , and internal ideality factor, indicate that non-radiative recombination is suppressed and the evaporated SAM-HTL/perovskite interface is of a high quality, irrespective of the evaporated 2PACz film thickness. Part of this figure is reproduced from ref.⁶⁰ with permission from Wiley.

(Figure 5.8c). Furthermore, TRPL transient measurements of the ITO/2PACz/perovskite layer stack exhibit a similar decay trend for both evaporated and solution-processed 2PACz with an average lifetime of 474 ns and 435 ns, respectively (see Figure 5.8d).

Similarly, we investigate the photophysical properties of evaporated MeO-2PACz employed in the ITO/MeO-2PACz/perovskite layer stack. As shown in Figure A5.2, half-stacks employing MeO-2PACz exhibit comparable results to those of their solution-processed counterpart, in full agreement with the 2PACz comparison. PLQY of the evaporated stack has an average of 0.35% with a corresponding implied V_{oc} of 1.220 V, which is quite comparable to 0.33% and 1.219 V for the reference stack. The ideality factor of the evaporated stack and the solution-processed stack is 1.73 and 1.79, respectively. In addition, TRPL measurements indicate a similar decay trend with an average lifetime of 83 ns for the evaporated MeO-2PACz, which is equivalent to 84 ns for the solution-processed counterpart.

While evaporating Me-4PACz films tend to significantly enhance their surface wettability compared to the solution-processed counterparts and consequently the perovskite film surface coverage as discussed in the previous section, it is important to ensure this has not occurred at the expense of its voltage loss mitigation and efficient charge carrier extraction properties. Similar to 2PACz and MeO-2PACz, we investigated the impact of evaporating Me-4PACz on the photophysical properties of the half-stack ITO/Me-4PACz/perovskite and compare it to the solution-processed counterpart. In line with the previous comparable charge carrier dynamics and suppressed non-radiative recombination between layer stacks employing solution-processed and evaporated 2PACz and MeO-2PACz, a comparison between the TRPL spectra of the half-stack employing evaporated and solution-processed Me-4PACz HTL exhibits no significant difference in charge carrier life time (568 ns and 585 ns for solution-processed and evaporated Me-4PACz, respectively) as shown in Figure A5.3. Furthermore, measurements assessing the quality of the perovskite/HTL interface with an optimal evaporated Me-4PACz (PLQY, implied V_{oc} , and ideality factor) indicate evaporated Me-4PACz layer is comparable or even slightly outperforming its solution-processed counterpart.

Overall, the comparable behavior in charge carrier lifetime and suppressed non-radiative recombination between evaporated and solution-processed SAM-HTLs (see Table A5.1) indicate that the evaporation process of SAMs doesn't have negative impact on photophysical properties and the high quality of evaporated SAM-HTL/perovskite interface is maintained, irrespective of deposition method.

To further our understanding of evaporated SAM-HTLs and the quality of evaporated SAM-HTL/perovskite interface, it is necessary to check the impact of layer thickness on photophysical properties. The importance of this investigation is stemming from the fact that the exceptional hole transporting property of solution-processed SAMs arises from the monolayer signature formation (i.e. very thin layer), thus, it is critical to check if these properties would be negatively affected once the evaporated film thickness is varied. To provide a systematic study on the effect of evaporated SAM layer thickness on photophysical properties, we employed different thickness of evaporated 2PACz thin films (2, 4, 6, 8, and 20 nm) into the layer stack ITO/evaporated 2PACz/perovskite. Strikingly, thickness dependent PLQY and TRPL measurements (see Figure 5.9) indicate that the high quality of evaporated 2PACz/perovskite interface is maintained, irrespective of evaporated 2PACz film thickness. As shown in Table A5.1, the average PLQY values for the 2, 4, 6, 8, 20 nm thick films are 0.89%, 1.0%, 0.94%, 1.54%, and 1.13%, respectively, with a corresponding implied V_{oc} of 1.245, 1.247, 1.246, 1.259, and 1.249 V, respectively. The corresponding internal ideality factor is 1.58, 1.57, 1.55, 1.52, and 1.56, respectively. The comparable implied V_{oc} and ideality factor values indicate that non-radiative recombination is effectively suppressed and independent of the evaporated 2PACz film thickness. Furthermore, The TRPL data (see Figure 5.9a) did not show any different decay trend by employing different thicknesses of evaporated 2PACz and the average lifetime is 500, 546, 493, 475, and 503 ns for 2, 4, 6, 8, 20 nm, respectively. Similar thickness dependent investigations for MeO-2PACz and Me-4PACz ended up with the same conclusion as shown in Table A5.1.

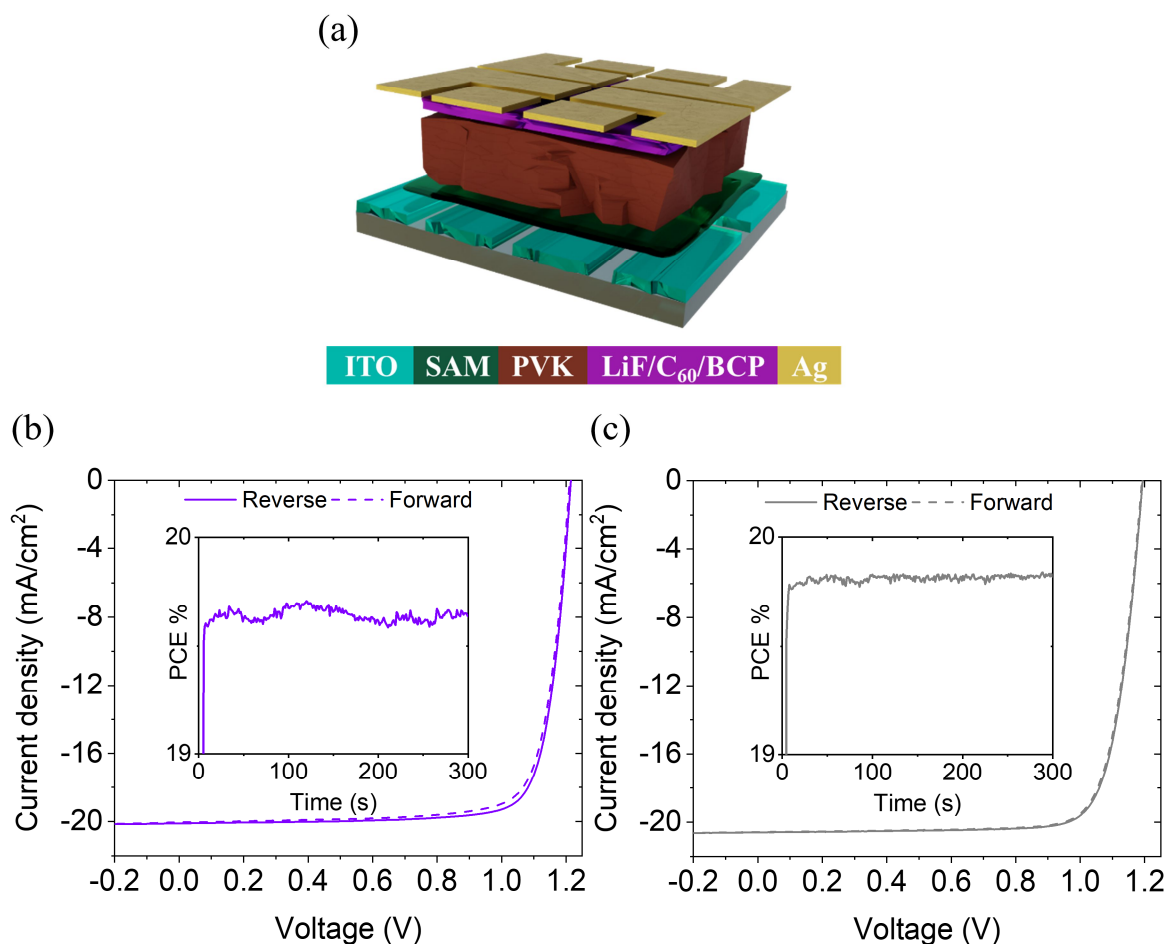


Figure 5.10. (a) Schematic diagram of the device stack employing triple-cation perovskite (PVK) composition ($\text{Cs}_{0.17}\text{FA}_{0.83}\text{PbI}_{2.75}\text{Br}_{0.25}$) with a band gap of 1.68 eV. The SAM-HTL refers to solution-processed/evaporated 2PACz. (b) and (c) Current density versus voltage (J - I) characteristics of the best performing perovskite solar cells (PSCs) employing evaporated (~ 6 nm) and solution-processed 2PACz, respectively. The inset represents the corresponding maximum power point (MPP) tracking for the two PSCs. Part of this figure is reproduced from ref.⁶⁰ with permission from Wiley.

In summary, the comparable implied V_{OC} and ideality factor, together with the charge carrier lifetime in half-stacks employing evaporated and solution-processed SAM-HTLs, indicate that evaporated SAM-HTLs/perovskite interface is of a high quality and non-radiative recombination is effectively suppressed, irrespective of SAM-HTLs deposition method. Furthermore, the high quality of the interface is maintained independent of the evaporated SAM-HTL thickness.

5.6 Photovoltaic performance

Having optimized the deposition process of evaporated SAMs and assuring the high quality SAMs/perovskite interface is maintained, now we investigate the PV performance of PSCs employing evaporated SAM-HTLs and compare them to the solution-processed counterpart. To evaluate comparative performance, we fabricate devices in the layer stack ITO/SAM/perovskite/LiF/C₆₀/BCP/Ag, as shown in Figure 5.10a, with either evaporated or solution-processed SAMs.

5.6.1 Comparison between solution-processed and evaporated SAM-HTLs

Starting with 2PACz as the common and widely used HTL in literature, Figure 5.10 shows J - V characteristics corresponding to PSCs employing solution-processed and evaporated 2PACz HTL. The champion reference PSC (employing solution-processed 2PACz HTL) exhibits a J_{sc} of 20.6 mA/cm², a FF of 79.9%, a V_{oc} of 1.195 V, and a PCE of 19.6%. Under MPP tracking, it performs at a stable 19.3%. Corresponding mean values as measured in the reverse scan are 19.7 mA/cm², 78.9%, 1.19 V, and 18.47%, respectively (see Figure 5.11a). Our reported mean values of the PV parameters for PSCs employing solution-processed 2PACz-HTL are comparable to p - i - n PSCs, fabricated using similar perovskite composition and band gap.^{43,74} Interestingly, the champion device employing evaporated 2PACz HTL exhibits a comparable PV performance to its solution-processed counterpart with a PCE of 19.5% (19.1% stabilized under MPP tracking), a J_{sc} of 20.1 mA/cm², a V_{oc} of 1.214 V, and a FF of 80.1%. The corresponding mean values for PCE, J_{sc} , V_{oc} , and FF are 18.9%, 20 mA/cm², 1.205 V, and 78.5%, respectively. Although there is no pronounced improvement in overall PV parameters in favor of PSCs employing evaporated 2PACz, the fact that the devices PV parameters are not negatively affected when employing evaporated 2PACz is astonishing, particularly when overall PV performance indicated by mean values of the statistical distribution in Figure 5.11 is comparable. We note that the FF mean value drops slightly (~1-2 %) for PSCs employing evaporated 2PACz-HTL, which we consider a rather small but noticeable difference. Given that our study of the photophysical properties indicated similar trends for both evaporated and solution-processed SAM-HTLs, we cannot attribute the FF losses to inefficient charge carrier extraction. On the other hand, the optimized thickness of evaporated 2PACz layer is roughly ~6 nm (thinner layers result in a reduction in fabrication yield, meanwhile, thicker layers would require an extra washing step as discussed in Section 5.7) which is 2-3 times thicker than the solution-processed 2PACz layer (~2-3 nm as estimated by Tan *et al.*²⁵⁸). In this regard, we attribute the FF drop to increased series resistance in PSCs employing evaporated SAM-HTLs.

In the same context, we employ MeO-2PACz in both solution-processed and the evaporated forms into the same device stack. Interestingly, and in full agreement with 2PACz, the statistical comparison of PV parameters shown in Figure 5.11b indicates comparable results for PSCs employing evaporated and solution-processed MeO-2PACz. For the reference PSCs, the corresponding mean values for PCE, J_{sc} , V_{oc} , and FF are 18.1%, 20.3 mA/cm², 1.166 V, and 76.4%, respectively. PSCs employing evaporated MeO-2PACz exhibit a comparable PV performance with 18.4%, 20.5 mA/cm², 1.167 V, and 76.7% for PCE, J_{sc} , V_{oc} , and FF, respectively. We note a slight drop in V_{oc} for PSCs employing MeO-2PACz (both, solution-processed and evaporated) compared to PSCs employing 2PACz (both, solution-processed and evaporated). The difference is about 30-40 mV and in full agreement with previous reports, which highlighted 2PACz superiority in terms of voltage losses mitigation.¹¹⁰

Similarly, and after overcoming the Me-4PACz wettability issue, which has been standing against fabricating efficient PSCs with high fabrication yield since it has been reported in 2020 for the first time,^{21,43,74,118,249,259,260} we investigate the PV performance as well as the previously reported fabrication yield issue. Strikingly, the fabrication yield of PSCs employing evaporated Me-4PACz HTL is remarkably high (~100%). Unfortunately, we did not succeed in fabricating comparable devices employing the solution-processed counterpart for the above-discussed reasons, consequently, a direct comparison between PSCs

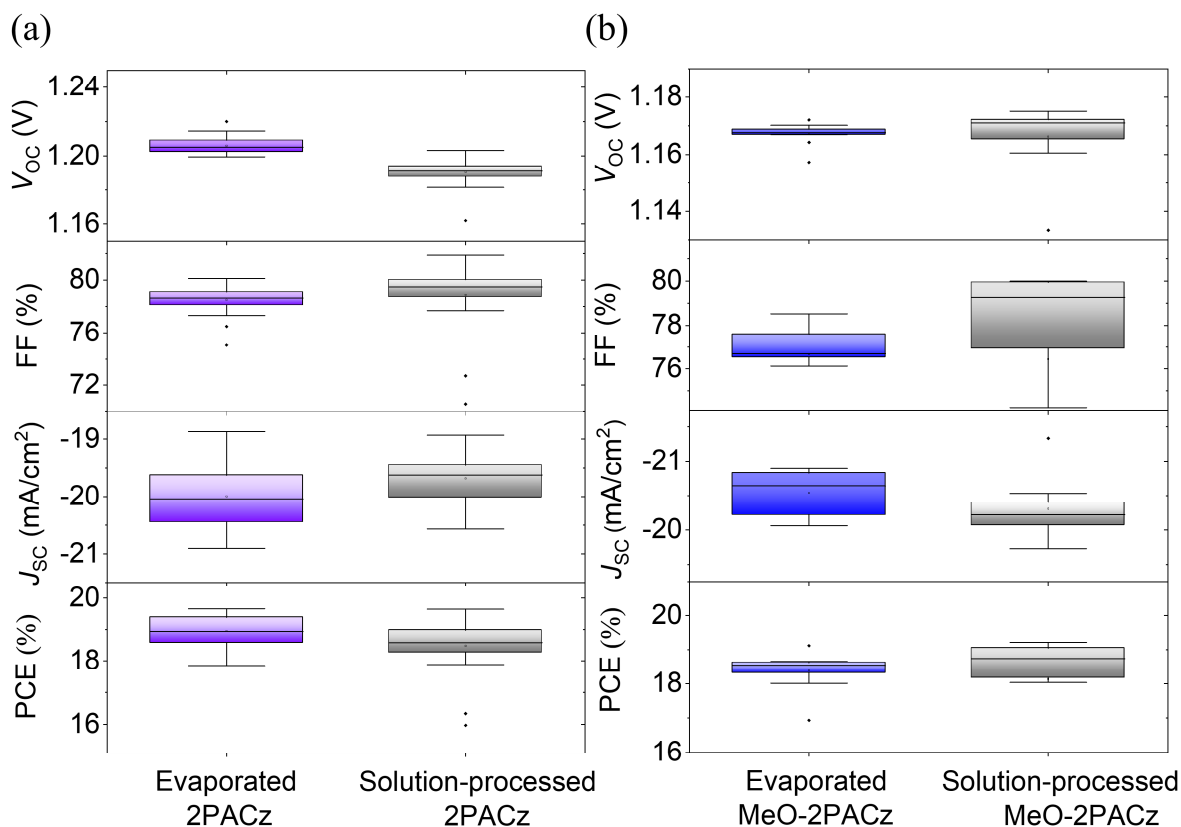


Figure 5.11. Statistical distribution of the V_{OC} , FF, J_{SC} , and PCE of PSCs employing a triple-cation perovskite composition $CS_{0.17}FA_{0.83}PbI_{2.75}Br_{0.25}$ with a band gap of 1.68 eV. (a) The employed HTLs are evaporated and solution-processed 2PACz. (b) The employed HTLs are evaporated and solution-processed MeO-2PACz. (c) The employed HTLs are evaporated Me-4PACz and solution-processed 2PACz.

employing solution-processed and evaporated Me-4PACz is not trustworthy. Instead, we compare the PV performance of PSCs employing evaporated Me-4PACz HTL to PSCs employing solution-processed 2PACz, processed in the same run.

Figure A5.4 displays statistical comparison of the PV performance of PSCs employing solution-processed 2PACz (reference) and evaporated Me-4PACz HTL. For the reference PSCs, the corresponding mean values for PCE, J_{SC} , V_{OC} , and FF are 19%, 20 mA/cm², 1.200 V, and 79.5%, respectively. PSCs employing evaporated Me-4PACz exhibit a comparable PV performance with 18.9%, 20.3 mA/cm², 1.221 V, and 77.6% for PCE, J_{SC} , V_{OC} , and FF, respectively.

As indicated by the statistics, the average V_{OC} of PSCs employing evaporated Me-4PACz-HTL is ~ 1.22 V, which is roughly ~ 20 mV higher than the equivalent device stack employing solution-processed 2PACz. This enhancement in V_{OC} in the favor of Me-4PACz based PSCs is in full agreement with the previous reports on solution-processed SAMs employed in the same device stack.⁷⁴ We attributed the slight drop in FF for PSCs employing evaporating Me-4PACz to a slight increase in series resistance as a consequence of the thicker evaporated HTL compared to the solution-processed counterpart. However, the overall performance, represented by the PCE statistics, indicate that devices employing evaporated Me-4PACz exhibit a higher average PCE than comparable devices with a solution-processed 2PACz HTL.

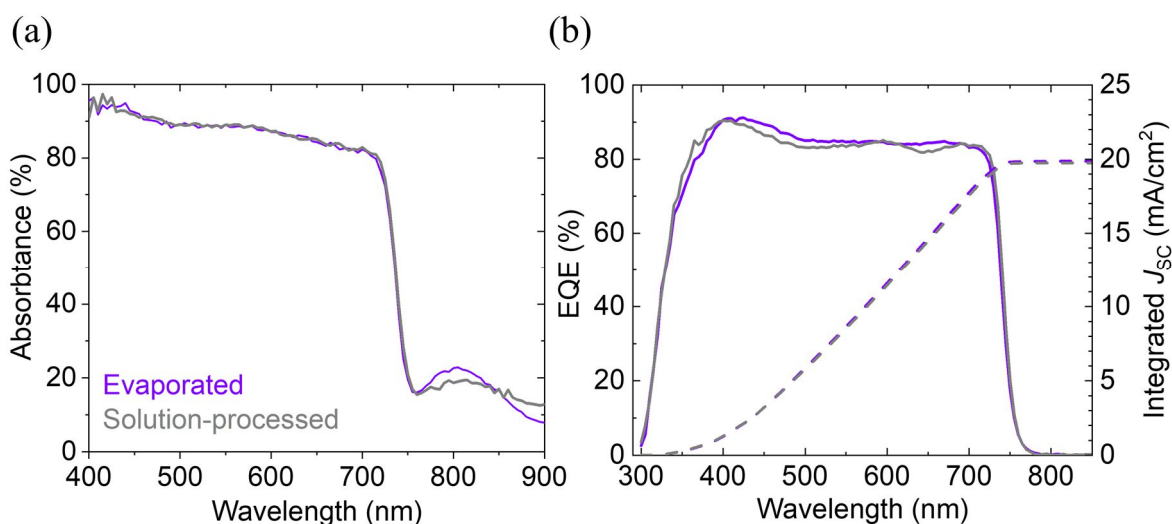


Figure 5.12. (a) Absorption spectra of the half-stack glass/ITO/HTL/perovskite. The HTL applies for solution-processed and evaporated 2PACz. (b) and (c) EQE and corresponding integral current density of PSCs employing evaporated and solution-processed 2PACz HTL, respectively. Part of this figure is reproduced from ref.⁶⁰ with permission from Wiley.

5.6.2 EQE and absorption spectra

To check the impact of changing the deposition method of SAM-HTLs on the optical properties, we perform UV-vis measurements on glass/ITO/2PACz/perovskite half-stacks employing both solution-processed and evaporated 2PACz-HTL. Figure 5.12 indicate that half-stack employing evaporated 2PACz exhibit a comparable broadband absorption spectrum to that of the solution-processed counterpart. Furthermore, EQE measurements indicate a comparable spectral response for the full device stack as well. The mean value of the current density (calculated from EQE) is 19.7 mA/cm² and 19.8 mA/cm² for solution-processed and evaporated 2PACz, respectively. The integral current density of the champion devices is comparable with a value of 19.8 mA/cm² and 19.9 mA/cm² for solution-processed and evaporated 2PACz, respectively. The J_{SC} values in our devices are comparable to similar perovskite composition and band gap reported in literature.^{43,74,275} Furthermore, the values obtained from EQE is comparable to the mean values obtained from the solar simulator and reported in the above comparisons.

5.6.3 Hysteresis factor

As we have noticed a slight drop in FF for PSCs employing evaporated SAM-HTLs compared to the solution-processed counterparts, which we attributed to the thickness difference between the optimized evaporated layers thickness (~6 nm) compared to ~2-3 nm in the solution-processed case, we now investigate the impact of this thickness difference on hysteresis factor (HF). HF of the champion devices shown in Figure 5.10 is 1.2% and 0.3% for evaporated and solution-processed 2PACz, respectively. The corresponding HF mean values in the whole batch is 1.1% and 0.5% for evaporated and solution-processed 2PACz, respectively. Further investigations and statistical comparison between the reverse and forward scan of PSCs as shown in Figure A5.5, Figure A5.6, and Figure A5.7, indicate very low HF difference between evaporated and solution-processed counterparts.

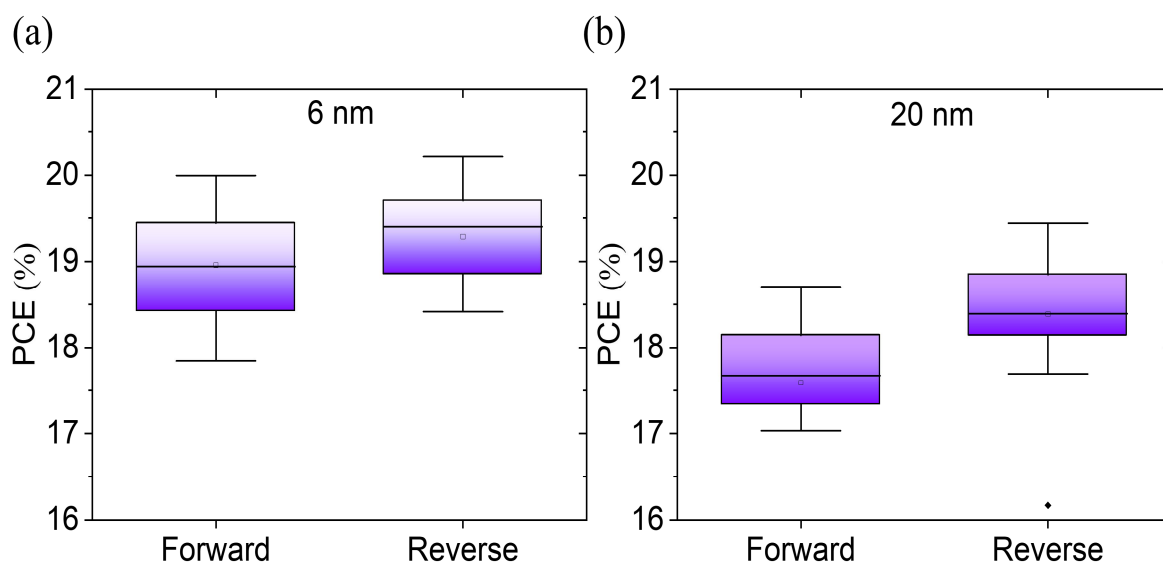


Figure 5.13. (a) and (b) Statistical distribution and comparison of PCE for PSCs in forward and reverse scan. Hysteresis factor increases from 1.7% to 4.7% when the evaporated 2PACz thickness increased from the optimum thickness (~ 6 nm) in (a) to ~ 20 nm in (b). Part of this figure is reproduced from ref.⁶⁰ with permission from Wiley.

To emphasize that the difference in thickness between the optimized evaporated film and solution-processed counterpart is the main reason for the slight increase in HF, we compare the HF of PSCs employing the optimized evaporated thickness (~ 6 nm) and a higher thickness (namely ~ 20 nm) of evaporated 2PACz-HTLs. Indeed, HF in this batch increased from 1.7% to 4.7% by increasing the evaporated 2PACz-HTL thickness from ~ 6 nm to 20 nm, as indicated by the PCE statistical distribution in reverse and forward scan (see Figure 5.13).

In conclusion, we recommend using the optimized evaporated SAM-HTLs thickness (~ 6 nm) as PSCs employing them exhibit very low HF compared to the solution-processed counterparts. Thicker layers are not recommended as they will have not only negative impact on the device's series resistance, rather they will exhibit increased HF.

5.7 Washing the evaporated SAM-HTLs

In their previous work, Albrecht and co-workers have shown there is no remarkable difference in PCE of PSCs employing solution-processed 2PACz if the 2PACz layer is washed or employed as deposited (without extra washing step). They attributed the comparable performance to the presence of monolayer signature in both cases.¹¹⁰ Furthermore, a similar study utilizing solution-processed Me-4PACz HTL with and without extra washing step ended up with the same conclusion.⁷⁴ In this regard, investigating the interface quality after performing an extra washing step on evaporated 2PACz films is of interest. Photophysical properties of glass/ITO/evaporated 2PACz/perovskite half-stacks indicate no remarkable difference between the washed and unwashed evaporated 2PACz-HTLs (see Figure 5.14). TRPL measurements exhibit a similar decay trend with a charge carrier lifetime of 540 ns and 546 ns for washed and unwashed evaporated 2PACz, respectively, indicating no considerable change in the charge carrier dynamics. Furthermore, the comparable PLQY, implied V_{oc} , and internal ideality factor as shown in Figure 5.14,

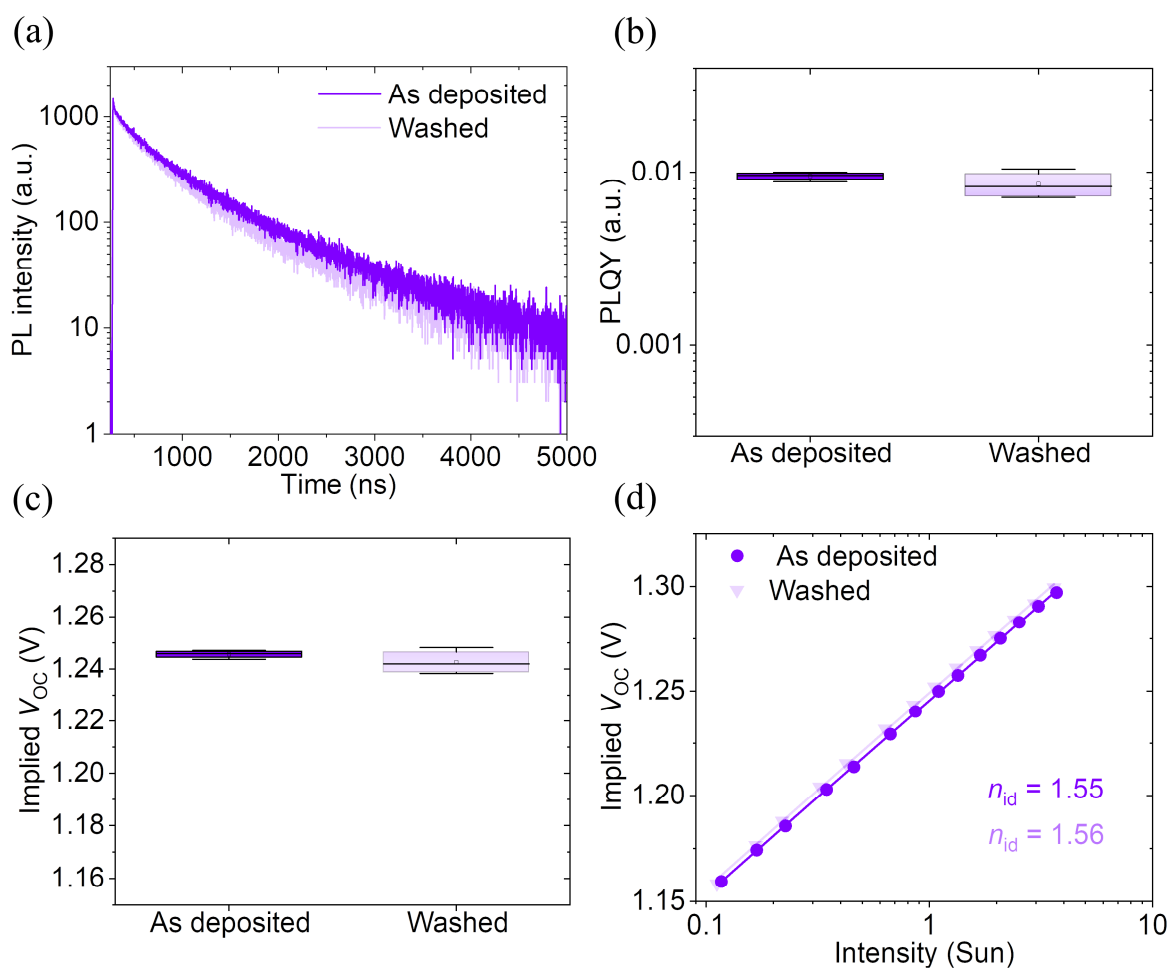


Figure 5.14. (a) Comparison of TRPL for the half-stack ITO/HTL/perovskite, the HTL applies for evaporated 2PACz with and without extra washing step. (b)-(d) The corresponding PLQY, implied V_{oc} , and ideality factor (n_{id}) extracted from a fit to the intensity-dependent implied V_{oc} . Part of this figure is reproduced from ref.⁶⁰ with permission from Wiley.

indicate that non-radiative recombination is unaffected by the extra washing step of the evaporated 2PACz films.

Having checked the quality of the interface, which turned out to be comparable, one would expect a comparable PV performance as well. In principle, the presence of a monolayer signature in a 200 nm evaporated 2PACz film (discussed in Section 5.2.3) means one could fabricate functional PSCs independent of the evaporated film thickness. In theory, washing a thick evaporated 2PACz film thoroughly, would remove all unbound SAM molecules, leaving only a monolayer of the SAM material, which is strongly bound to the adjacent ITO and essential for efficient PSCs fabrication.^{105,110,118} Indeed, 200 nm films, washed with 500 μ l ethanol using a spin coating program with a speed of 3000 rpm for 30 s, enabled fabrication of PSCs with $\sim 80\%$ FF and an average PCE of $\sim 19\%$ as shown in Figure 5.15. The results are comparable to PSCs fabricated using solution-processed 2PACz and the ~ 6 nm evaporated films reported above.

Although washing very thick evaporated SAM-HTL led to efficient PSCs, we do not recommend washing in general as it is an extra processing step, which negatively influences the throughput/productivity. We used the extra washing step to our evaporated SAM-HTLs

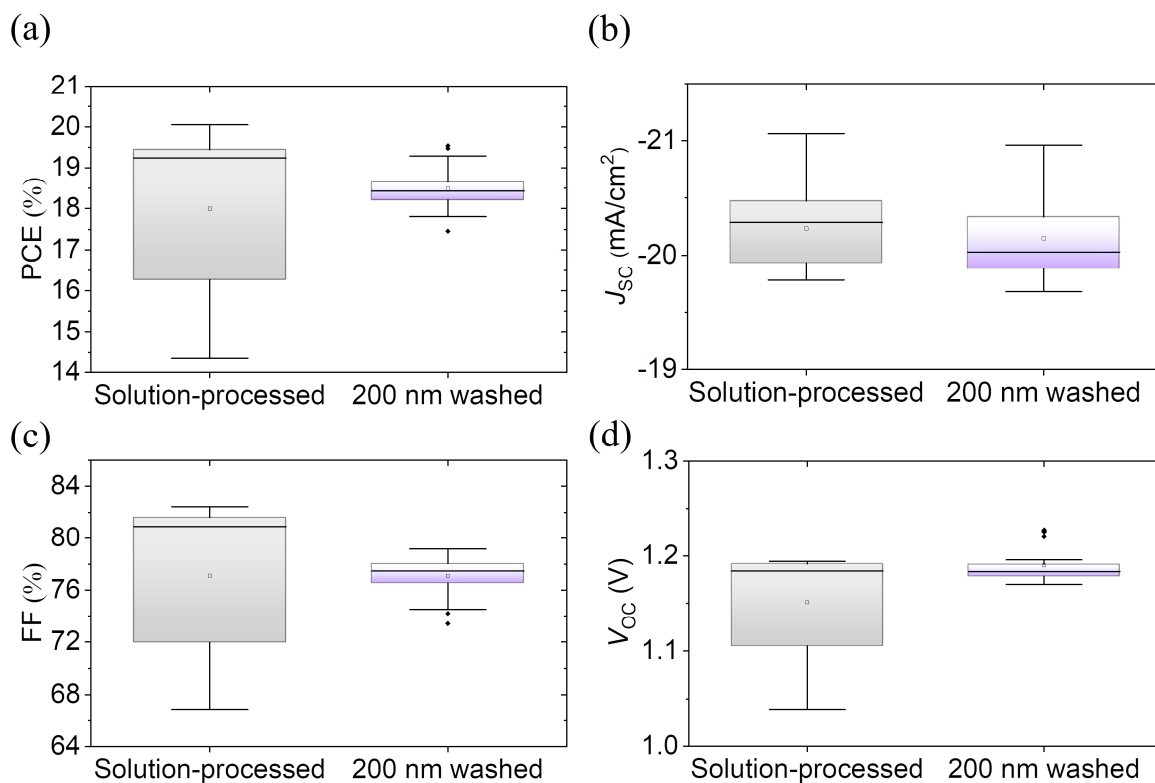


Figure 5.15. (a)-(d) Statistical distribution and comparison of the PV parameters for PSCs employing ~ 200 nm evaporated 2PACz (after applying a washing step) or solution-processed 2PACz as HTLs. Samples employing the ~ 200 nm thick evaporated 2PACz were washed with 500 μ l ethanol before depositing the perovskite onto them. Part of this figure is reproduced from ref.⁶⁰ with permission from Wiley.

to investigate/prove the above-discussed aspects, however we recommend using the optimized thickness for fabricating efficient PSCs with high throughput.

5.8 Compatibility with other perovskite absorbers

So far, we have performed our investigations on SAM-HTLs deposited with the new developed evaporation method and compared them to the conventional solution-processed counterparts, employing the widely used triple-cation perovskite with a composition of $\text{Cs}_{0.05}\text{MA}_{0.22}\text{FA}_{0.73}\text{Pb}(\text{I}_{0.77}\text{Br}_{0.23})_3$. As the band gap of this particular perovskite absorber layer is ~ 1.68 eV, it is prevalent in monolithic 2T perovskite/Si tandem solar cells as it has been shown to fulfill the current matching condition.^{43,74} On the other hand, such perovskite absorber layer with its corresponding band gap, will result in current mismatch if applied in 2T monolithic perovskite/CIGS tandems. In this regard, perovskite absorbers with lower band gap are necessary to boost the efficiency of perovskite/CIGS tandems further. Recently, Ruiz-Preciado *et al.* have reported on high efficiency perovskite/CIS employing a triple-cation perovskite composition of $\text{Cs}_{0.05}\text{MA}_{0.22}\text{FA}_{0.73}\text{Pb}(\text{I}_{0.9}\text{Br}_{0.1})_3$, with a band gap of 1.59 eV.¹¹¹ Employing this perovskite absorber with its corresponding band gap enabled a J_{sc} of 20.4 mA/cm² in the perovskite sub-cell. Furthermore, the band gap engineering has enabled a J_{sc} of 20.7 mA/cm² in the bottom CIS sub-cell, indicating the current matching condition is almost fulfilled.¹¹¹

To assure that the outstanding performance that evaporated SAM-HTLs exhibited, is a general principle and independent of perovskite composition/band gap, we investigate the

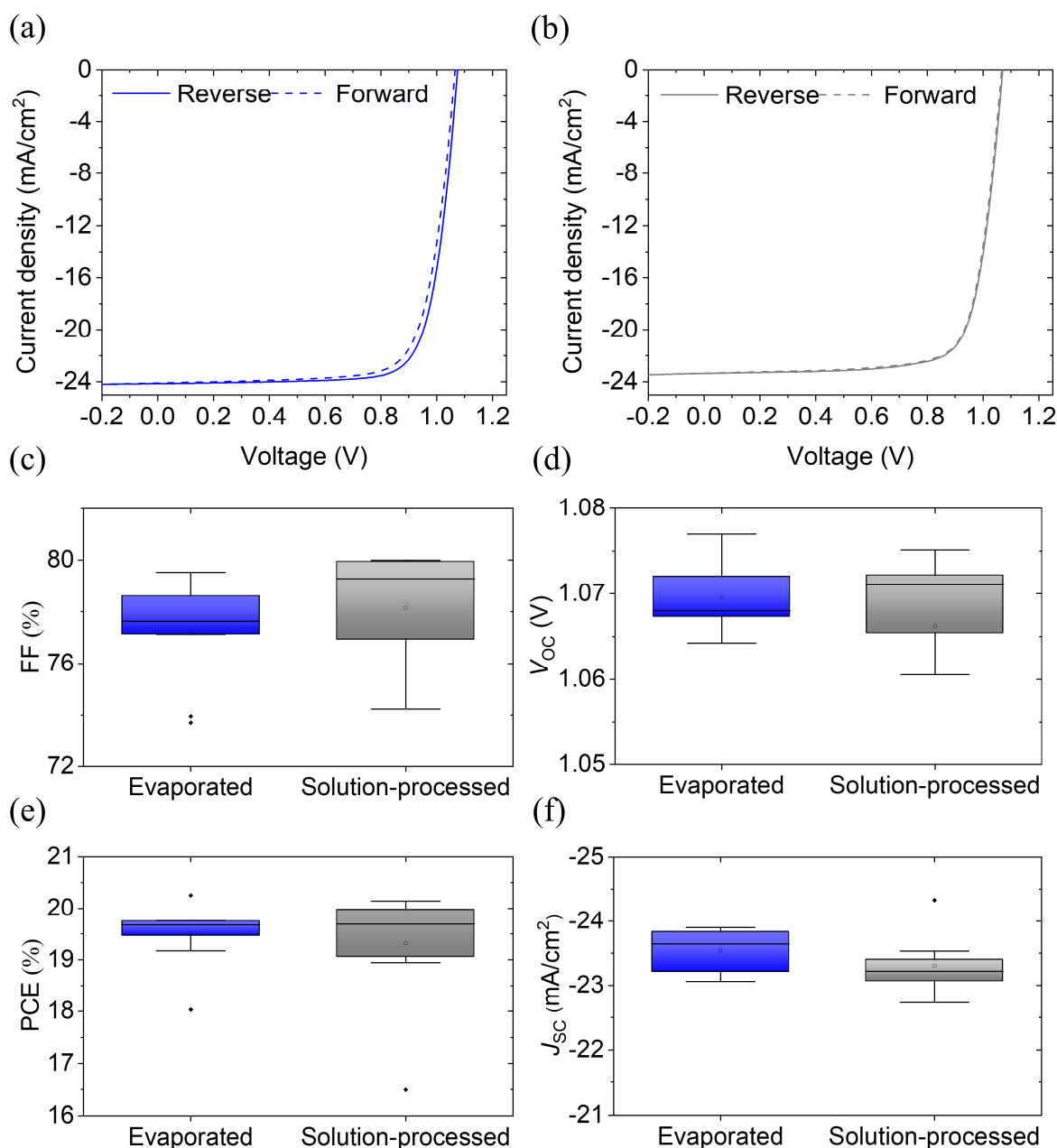


Figure 5.16. (a) and (b) $J-V$ characteristics of the best performing PSCs employing evaporated and solution-processed MeO-2PACz, respectively. (c)-(f) Statistical distribution and comparison of the PV parameters for the corresponding PSCs.

PV performance of PSCs employing the perovskite composition reported by Ruiz *et al.* with solution-processed and evaporated SAM-HTLs. To evaluate comparative performance, we fabricate devices in the layer stack ITO/SAM/perovskite/ C_{60} /BCP/Ag.

Figure 5.16 shows $J-V$ characteristics corresponding to PSCs employing evaporated and solution-processed MeO-2PACz as an HTL. The champion reference PSC (employing solution-processed MeO-2PACz HTL) exhibits a J_{sc} of 23.6 mA/cm^2 , a FF of 77.8%, a V_{oc} of 1.068 V, a PCE of 19.6%, and a HF of 0.3%. Corresponding mean values as measured in the reverse scan are 23.3 mA/cm^2 , 78.1%, 1.066 V, 19.3%, and 0.4%, respectively. Interestingly, the champion device employing evaporated 2PACz as an HTL exhibits a comparable PV performance to its solution-processed counterpart with a PCE of 19.7%, a

J_{sc} of 24.1 mA/cm², a V_{oc} of 1.069 V, a FF of 76.5%, and a HF of 3.8%. The corresponding mean values for PCE, J_{sc} , V_{oc} , and FF are 19.5%, 23.5 mA/cm², 1.069 V, 76.2%, and 3.6%, respectively.

5.9 Compatibility with textured surfaces

Having assured the high quality/nearly lossless SAM-HTLs/perovskite interface is preserved for evaporated SAMs as compared to their solution-processed counterparts, and after planar PSCs employing evaporated SAM-HTLs have shown to exhibit a comparable PV performance, which is valid for different perovskites. Now we investigate the compatibility of evaporated SAM-HTLs with micrometer-sized textured surfaces by studying the quality of evaporated SAM-HTL/perovskite interface and compare it to other HTLs.

The first challenge comes to mind when depositing solution-processed perovskites onto micrometer-sized pyramidal textured surfaces in the size of ~1-2 μm , is assuring full surface coverage of the perovskite thin film to prevent the pyramidal tips from causing detrimental shunting path, which consequently will have a negative impact on device performance as well as fabrication yield. This is indeed a valid point and requires optimization, however, optimizing an efficient HTL that can be processed over such a complex geometry is not less challenging. Efficient and practical HTLs such as solution-processed SAMs has been reported to have very low fabrication yield when processed over such pyramidal textures. For example, Isikgor *et al.* attributes the reduction in fabrication yield to the lack of conformal surface coverage of solution-processed SAM-HTLs, particularly, with regard to covering the very sharp pointy pyramidal tips.⁷⁵ PTAA has been used *via* blade coating in perovskite/Si monolithic tandems with mild PCE by Chen *et al.*, however, the authors haven't provided any information about the fabrication yield, which one would expect to be very low.⁵⁴ Seeking conformal CTLs over such micrometer sized textures, Aydin *et al.* has developed a sputtered NbO_x layer, which is compatible with the *n-i-p* architecture. For the *p-i-n* architecture, Sahli *et al.* have tried thermally evaporated spiro-TTB, however, the absence of uniform coverage has led to inefficient charge carrier extraction due to the low quality HTL/perovskite interface.¹³ In addition, accumulation of spiro-TTB in the valleys can lead to a degradation in overall PV performance.¹³

NiO_x has been employed *via* PVD methods over micrometer-sized textures, which reported to enable conformal surface coverage, however, the devices were lagging in terms of V_{oc} .^{53,97,102,227,276} In full agreement with literature, PLQY of the half-stack textured Si/ITO/NiO_x/perovskite shown in Figure 5.17 is rather low (0.3%). In this experiment, we employed in house sputtered 15nm NiO_x as HTL and the developed double-cation thick perovskite absorber layer discussed in Chapter 4.

To overcome the low fabrication yield issue and simultaneously benefit from the addressed advantages of solution-processed SAMs, combining a sputtered NiO_x layer to provide uniform and conformal coverage with solution-processed SAMs on top as a double-layer HTL has been brought forward as a practical solution. PSCs employing the double-layer HTL over planar as well as micrometer-sized textured substrates have demonstrated comparable or even superior PCEs compared to PSCs using stand-alone solution-processed SAM-HTLs.^{107,111,180,185,277-279} Recently, Mao *et al.* have reported on ~29% PCE for production line compatible monolithic perovskite/Si tandem solar cells, utilizing a textured

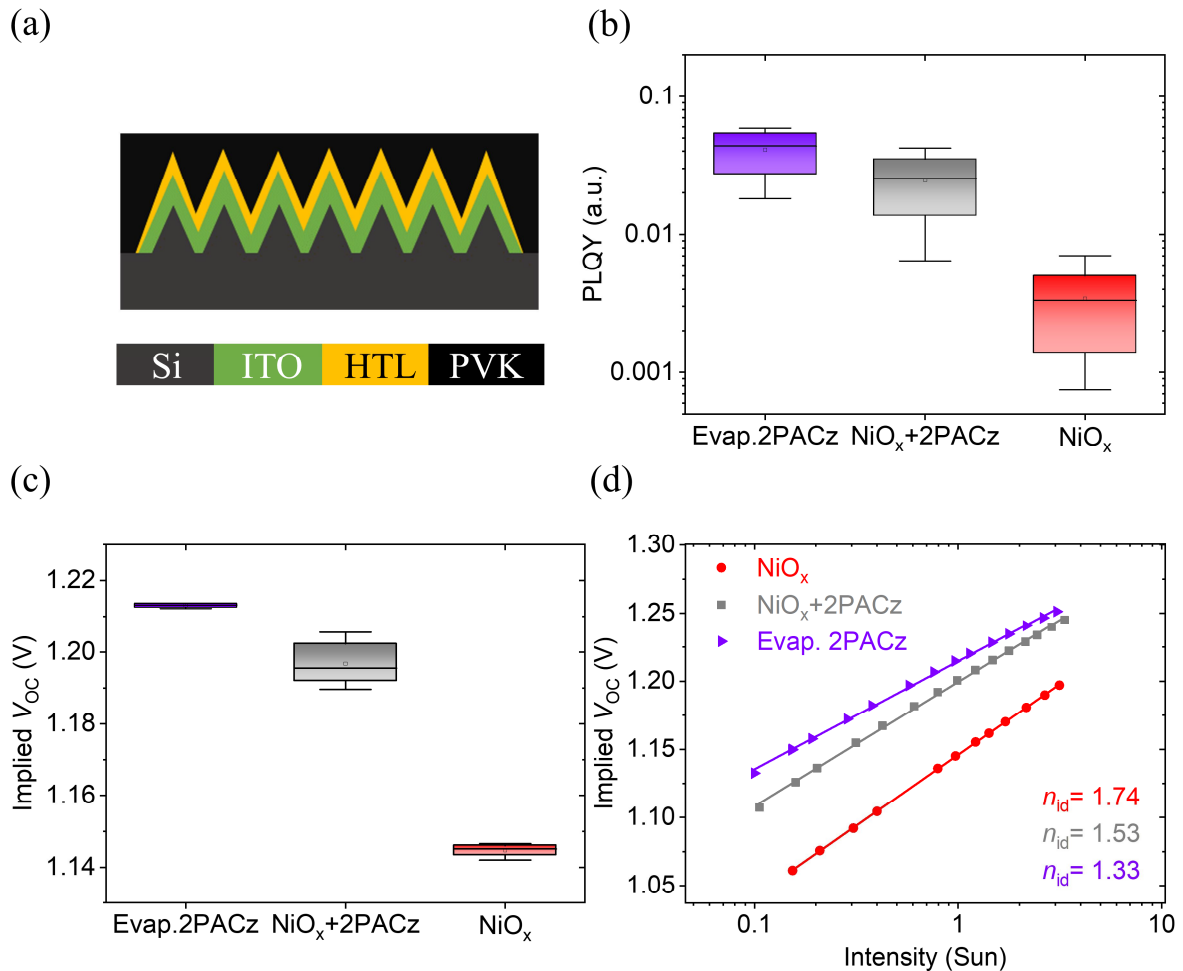


Figure 5.17. (a) Schematic diagram of the textured Si/ITO/HTL/perovskite half-stack. The HTL applies for standalone evaporated (Evap.) 2PACz, standalone NiO_x, and a double-layer of NiO_x and solution-processed 2PACz. (b) PLQY comparison between the half-stack employing the three different HTLs. (c) the corresponding implied V_{oc}. (d) Corresponding ideality factor (n_{id}). Part of this figure is reproduced from ref.⁶⁰ with permission from Wiley.

Si sub-cell.²⁷⁹ In their work, they have shown that introducing a double-layer HTL of NiO_x and solution-processed 2PACz is very beneficial and outperforming both standalone NiO_x and standalone solution-processed SAM-HTLs. In agreement with literature, introducing a solution-processed 2PACz layer onto NiO_x in the half-stack textured Si/ITO/NiO_x/solution-processed 2PACz/perovskite, led to increase of the PLQY signal by roughly one order of magnitude compared to the similar stack employing standalone NiO_x (see Figure 5.17).

Although having a double-layer HTL comprising of NiO_x, deposited *via* PVD to assure conformal surface coverage over pyramidal textures and solution-processed SAMs to mitigate non-radiative losses, has enhanced the quality of HTL/perovskite interface of the textured surface, employing a double-layer HTL is neither practical nor cost efficient. The development of evaporated SAM-HTLs are expected to possess the virtues of the conformal NiO_x layer without the associated issues, meanwhile, suppresses non-radiative recombination as they have shown when compared to their solution-processed counterparts. Indeed, as expected, PLQY of the half-stack textured Si/ITO/evaporated 2PACz/perovskite

is out performing half-stacks employing both standalone NiO_x and the double-layer NiO_x /solution-processed 2PACz.

Figure 5.17 indicates the high quality evaporated 2PACz/perovskite interface compared to other HTLs. For the reference stack (employing single-layer NiO_x as an HTL), PLQY is remarkably low, with an average value of 0.3%, at least one order of magnitude lower than the other two HTL configurations, indicating worse interfacial recombination and consequent voltage losses. PLQY signal is enhanced to an average value of 2.5% by employing a double-layer NiO_x /solution-processed 2PACz. With an average value of 4.3%, evaporated 2PACz exhibits roughly double this PLQY. The corresponding implied V_{oc} is 1.213 V, 1.195 V, and 1.145 V for half-stacks employing standalone evaporated 2PACz, a double-layer NiO_x /solution-processed 2PACz, and standalone NiO_x , respectively. The ideality factor for the corresponding three half-stacks is 1.33, 1.53, and 1.74, respectively, indicates the superiority of evaporated 2PACz over the micrometer-sized texture.

5.10 Summary

After developing efficient thick perovskite absorber layer that assures full surface coverage over micrometer-sized pyramidal textures in Chapter 4, we presented in this chapter the development of compatible HTLs that enable conformal coverage over the textured surface, meanwhile maintain high quality HTL/perovskite interface. We introduced for the first time thermal evaporation of SAM-HTLs (MeO-2PACz, Me-4PACz, and 2PACz) to enhance their process flexibility and compatibility with textured surfaces.

Utilizing XPS measurements have indicated no remarkable difference in XPS characteristic peak position and relative weight/area of evaporated SAM-HTLs compared to their solution-processed counterpart. In addition, we saw no evidence toward the emergence or absence of new C 1s signals in the evaporated thin film compared to that of the SAM powder, which emphasizes that SAM molecules didn't degrade or exhibit chemical change upon evaporation. Furthermore, phosphorus as one of the essential elements of the SAM's functional group, has shown a strong presence in the P 2p region of the evaporated thin film. In the same context, FTIR data emphasized further that chemical properties of SAMs are unchanged by the thermal evaporation process, indicated by the presence of the characteristic molecular vibration bands. The data indicated the presence of monolayer signature in evaporated SAM-HTLs at the ITO interface independent of final film thickness. Although FTIR spectra of thick films (~200 nm) indicated the emergence of P-OH broad peak, which is dominant in the bulk of SAM powder, the presence of P-O vibration bands is a clear evidence that thick films possess monolayer signature at the ITO interface. Washing such thick films get rid of unbound bulk molecules leaving only the strongly bound monolayer with the adjacent ITO and enabled fabrication of efficient PSCs with high FF (~80%).

Evaporated SAM-HTLs with their conformal surface coverage over the adjacent ITO exhibited clear trends of improved wettability as indicated by their low contact angles for various liquids compared to their solution-processed counterparts. Improved wettability, which correlates to enhanced surface coverage of the perovskite thin film, had a positive impact on fabrication yield of PSCs employing evaporated SAM-HTLs. PSCs employing evaporated Me-4PACz HTL particularly, exhibited a fabrication yield of ~100% by overcoming the wettability issue of solution-processed Me-4PACz reported in literature.

Such improvement in evaporated Me-4PACz surface wettability didn't come on the expense of surface morphology or crystal structure of the grown perovskite thin film as indicated by top-view SEM images and XRD measurements.

While solution-processed PACz derivatives have been introduced to the community as conformal monolayers with lossless interfaces, we investigated whether changing the deposition method of SAM-HTLs might have a negative impact on the interface quality. Through analysis of PLQY indicated that high quality of the SAM-HTLs/perovskite interface is maintained irrespective of SAM-HTLs deposition method. Implied V_{oc} as well as internal ideality factor data for half-stacks employing evaporated SAMs exhibited a comparable trend to that of solution-processed counterparts, indicated that non-radiative recombination is suppressed. In addition, thickness dependent PLQY measurements indicated the high quality SAM-HTL/perovskite interface is preserved, irrespective of evaporated SAM-HTL thickness. Furthermore, TRPL measurements indicated no remarkable changes in charge carrier dynamics of half-stacks employing both solution-processed and evaporated SAM-HTLs. The preserved interface quality is reflected in PV parameter data, with planar PSCs employing evaporated SAM-HTLs exhibiting comparable PV performance to their solution-processed counterpart.

Finally yet importantly, we demonstrated that high quality layers are uniformly deposited over micrometer-sized pyramidal textures, which have previously typically required an additional NiO_x layer to ensure conformal coating and prevent detrimental shunting paths. Half-stacks employing evaporated SAM-HTLs exhibited an improved implied V_{oc} compared to NiO_x layers from 1.145 V to 1.213 V. An improvement of ~ 68 mV indicates the superiority of evaporated SAMs, making them a strong candidate in pushing the technology further.

6. Voltage losses mitigation and efficient light harvesting in PSCs processed over textured surfaces

Perovskite solar cells (PSCs) processed over textured surfaces typically exhibit lower open-circuit voltage (V_{oc}) compared to their planar counterparts. In this chapter, we report on potential reasons behind the various voltage losses that accompanies processing perovskite thin films onto micrometer-sized pyramidal textures. We quantify voltage losses at the interfaces as well as in the bulk of perovskite thin films processed over these textures using photoluminescence quantum yield (PLQY) measurements. Furthermore, we investigate the causes of these voltage losses *via* in-depth compositional, microstructural, and morphological analysis. Afterwards, we provide a guideline on how to mitigate voltage losses using one or more of the following strategies: interfacial engineering, surface passivation, processing parameters optimization, solvent engineering, precursor molarity and stoichiometry optimization. Finally yet importantly, we compare the quantified interfacial losses obtained from PLQY to the external V_{oc} of PSCs and investigate the impact of mitigating these losses on photovoltaic (PV) performance.

After boosting the PV performance of PSCs processed over textured surface to be equivalent to planar counterparts, we investigate the consequent optical gains when processing PSCs over replicated textures and the impact of efficient light harvesting on power conversion efficiency (PCE).

Acknowledgements and contributions

*Parts of this chapter, related to voltage losses in PSCs processed over textured surfaces, have been published in Advanced Functional Materials by Ahmed Farag et al. with the title ‘Mitigation of Open-Circuit Voltage Losses in Perovskite Solar Cells Processed over Micrometer-Sized-Textured Si Substrates’.*⁶¹ *Parts of this chapter, related to light management using replicated textures, have been published in ACS APPLIED ENERGY MATERIALS by Ahmed Farag et al. with the title ‘Efficient Light Harvesting in Thick Perovskite Solar Cells Processed on Industry-Applicable Random Pyramidal Textures’.*¹⁸⁰ *Many graphs in this chapter are reproduced or adapted with permission from American Chemical Society and Wiley. Ahmed Farag planned the lab work, designed the experiments and arranged for the external measurements under the supervision of Dr. Ulrich W.*

Paetzold. Ahmed Farag fabricated all the samples for characterization and fabricated all the PSCs. Ahmed Farag performed the current density-voltage, external quantum efficiency, scanning electron microscopy, X-ray diffraction, atomic force microscopy, energy dispersive X-ray, and ultraviolet-visible measurements. SINGULUS TECHNOLOGIES AG provided the textured silicon wafers. The PLQY measurements were performed by Dr. Paul Faßl. Dominik Bagrowski and Dr. Wolfram Hempel from Zentrum für Sonnenenergie- und Wasserstoff-Forschung (ZSW) performed the glow-discharge optical emission spectroscopy (GDOES) and time-of-flight secondary ion mass spectrometry (ToF-SIMS) measurements. Ahmed Farag analyzed the GDOES and ToF-SIMS data. Hang Hu and Thomas Feeney performed the atomic layer deposition of SnO_x. Raphael Schmager assisted by transferring his knowledge in nanoimprint lithography. Ahmed Farag performed the replication process.

6.1 Introduction

Within the last decade, monolithic perovskite/silicon (Si) tandem solar cells^{24,25,100–107,28,29,31,74,96–99} have experienced a massive improvement in their PCE, which makes this configuration one of the most promising candidates to surpass the theoretical limit of a single junction solar cell (33%).¹⁹⁰ For a monolithic perovskite/Si two-terminal (2T) and two-terminal (3T) tandem, choosing a textured Si bottom cell is commercially favorable as it is more cost efficient compared to its planar polished front surface counterpart. Furthermore, while the latter has dominated the record PCE for all monolithic perovskite/Si tandems for a substantial period, tandem devices using a textured bottom cell have shown recent great potential by achieving a certified PCE of 29.3 %²⁸⁰ followed shortly by a PCE of 31.3%.⁸ Seeking highly efficient monolithic perovskite/textured Si tandem solar cells, different deposition techniques have been used to deposit perovskite thin films onto micrometer-sized textured surface, such as hybrid 2-step process, vacuum-deposition, slot die coating, blade coating, and spin coating.^{13,15,275,280–282,31,32,53,59,102,105,250,252}

There is no doubt that a textured surface enables efficient light harvesting due to the light trapping effect,^{25,75,96,99,102,250} however, understanding the crystallization dynamics of perovskite thin films deposited over such textured surface is challenging due to the complexity of the processing surface. Furthermore, processing perovskite thin films over such micrometer-sized pyramidal textures is always accompanied with remarkable voltage losses compared to planar polished surfaces.^{12,98,283} When investigating voltage losses in PSCs, non-radiative recombination at the interfaces (hole transport layer (HTL)/perovskite and perovskite/electron transport layer (ETL)) dominates the V_{OC} losses, however, defects in the bulk and at grain boundaries also need to be considered. Additionally, stoichiometry of the perovskite precursor solution and introduced additives can influence both the bulk and interfaces. More specifically, many high V_{OC} /PCE PSCs reported to date introduce excess PbI_2 (roughly ~10%) into the perovskite precursor solution.^{14,284–286} Extensive studies have been made to understand the impact of excess PbI_2 in the perovskite precursor solution on the perovskite film quality and the consequent enhancement in photocurrent and fill factor (FF).^{222,287–293} Furthermore, PSCs employing excess PbI_2 exhibit considerably higher V_{OC} compared to the stoichiometric counterparts, indicating the key role that excess PbI_2 plays in passivating grain boundaries.^{294–298} As the interaction between HTL and perovskite is common in *p-i-n* PSCs and might lead to PbI_2 deficiency in the bulk,^{69,299–302} these interactions are expected to have a dominant effect due to the large interaction surface area when a textured substrate is used, hence, the optimal amount of excess PbI_2 requires further investigation for this particular case.

Choosing a compatible HTL with the textured surface (as discussed in Chapter 5) and optimizing the excess PbI_2 will suppress non-radiative recombination within the bulk as well as at the HTL/perovskite interface, leaving perovskite/ C_{60} to be the limiting interface. Considering the high non-radiative recombination reported to be present at the perovskite/ETL interface in *p-i-n* planar PSCs,^{14,108,159} losses are expected to be even higher if the perovskite thin film is deposited onto micrometer-sized pyramidal textures as a result of the expected high surface roughness of the resultant perovskite thin film. Furthermore, depositing a perovskite thin film over a micrometer-sized textured substrate requires a

perovskite precursor solution with relatively high concentration to ensure full surface coverage and prevent the pyramidal tips from causing detrimental shunting paths (as discussed in Chapter 4).^{32,53,102,180,280} However, perovskite films processed using such highly concentrated solutions tend to form surface wrinkles that increase film surface roughness and consequently degrade the perovskite/ETL interface quality.^{94,303} Controlling the formation of strain-related surface wrinkles in perovskite thin films can have a strong impact on surface morphology and consequently mitigate voltage losses.^{94,303,312,304–311}

In this chapter, we present a detailed study on crystallization dynamics and various voltage losses mechanisms in double cation $\text{Cs}_{0.17}\text{FA}_{0.83}\text{PbI}_{2.75}\text{Br}_{0.25}$ perovskite thin film stacks deposited over micrometer-sized textured Si substrates. We analyze the microstructure, composition, and crystallinity of the perovskite thin films using scanning electron microscopy (SEM), atomic force microscopy (AFM), X-ray diffraction (XRD), time-of-flight secondary ion mass spectrometry (ToF-SIMS), and glow-discharge optical emission spectroscopy (GDOES). Furthermore, we quantify voltage losses using PLQY and provide a step by step guidance on how to mitigate these losses. We further investigate in-depth the interactions of HTL and transparent conductive oxide (TCO) with perovskite that causes PbI_2 deficiency within the bulk. Using a proper perovskite precursor solution molarity and solvent ratio we provide a guide to control surface morphology, and, using proper surface passivation strategies, we reduce detrimental voltage losses at the perovskite/ C_{60} interface. We apply these voltage losses mitigation strategies to complete PSCs fabricated onto micrometer-sized pyramidal textures and investigate their PV performance.

After applying the voltage losses mitigation strategies, we investigate the optical gains in PSCs processed over replicated textured surfaces and compare them to planar PSCs.

6.2 Anti-solvent quenching and the presence of voids

A large amount of reported PCSs displaying high V_{OC} and PCE, fabricated using the anti-solvent quenching technique, have the anti-solvent dispensed in a time window between 12–20 s during the second spin-coating step (which we will hereafter refer to as early quenching).^{14,140,284,285} We note that early quenching is not ideal when processing perovskite thin films over textured surfaces. Half-stacks employing perovskite thin films processed using early quenching exhibit high voltage losses at the HTL/perovskite interface as indicated by the implied V_{OC} data in Figure 6.1b. In this section we investigate the potential reasons behind these voltage losses.

When a perovskite thin film is processed over a textured surface using early quenching, we note that deep inside the valleys of pyramidal textures, there are perovskite-free regions (aka. voids) as illustrated by the schematic diagram and emphasized by the cross-sectional SEM image in Figure 6.1a. We hypothesize the presence of such voids can be attributed to one of two reasons: (1) Textured surfaces exhibit high inherent complexity as they consist of three different surface types in a micrometer scale (i.e. tips, wall sides, and valleys). Hence, the time it takes for the perovskite precursor solution to reach/soak over each of the different surfaces is not equivalent, and it is expected to be longer in the valleys case. Once the anti-solvent is dispensed during deposition, the intermediate phase of the perovskite film starts to form immediately,³¹³ and in the early quenching case, film formation starts to take place before the perovskite precursor solution reaches the valleys. Consequently, perovskite-free

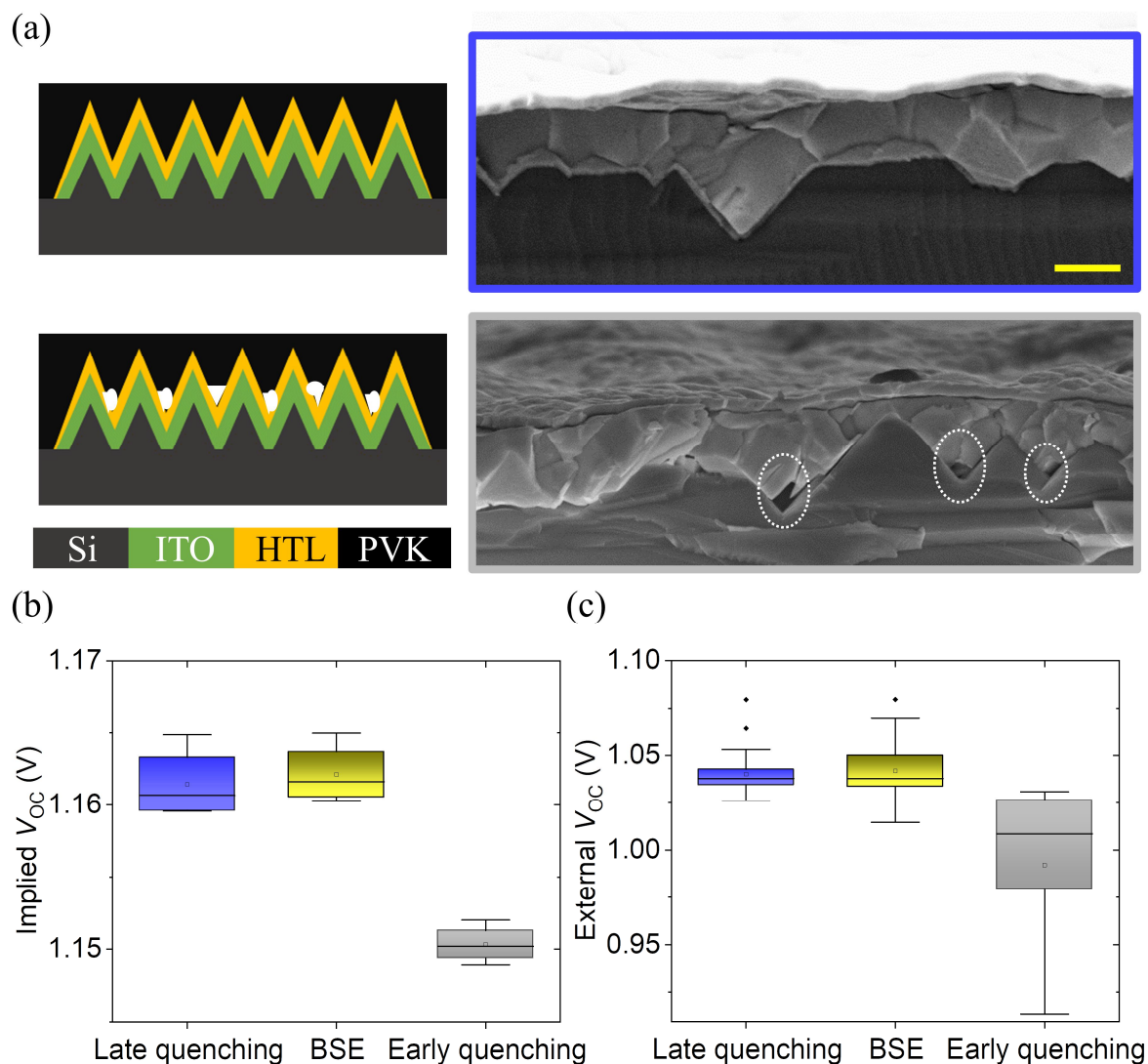


Figure 6.1. (a) Schematic diagram and cross-sectional SEM images of perovskite thin films processed onto textured Si substrates using late (top) and early quenching (bottom). Perovskite film processed using early quenching displays voids in the valleys as highlighted. The scale bar is 1 μm . (b) Implied V_{oc} comparison between half-stacks employing perovskite thin films processed onto micrometer-sized textures using three different anti-solvent quenching methods. Late quenching and boosted solvent extraction (BSE) are superior in suppressing non-radiative recombination at the HTL/perovskite interface. (c) The corresponding external V_{oc} obtained from full device stacks. Implied and external V_{oc} exhibit a similar trend.

regions might exist at the bottom side of the perovskite thin film. (2) Based on a study about the presence of voids near the HTL/perovskite interface in perovskite thin films processed over planar surfaces by Huang and co-workers, the presence of such voids is correlated to volume collapse caused by late escape of the high boiling point dimethyl sulfoxide (DMSO) solvent.^{314,315} They highlighted that crystallization/perovskite film formation starts at the film/air interface immediately during quenching. Film formation at the surface will temporarily trap the adjacent wet film near HTL/perovskite interface. During the annealing step, DMSO will eventually evaporate from the trapped wet film, causing volume change and results in voids near the substrate.³¹⁴⁻³¹⁶ This approach is more realistic and dominant in the textured surface case, assuming that DMSO is being challenged to escape from valleys during anti-solvent quenching or spin coating in general because, unlike planar surfaces where the distance from perovskite/air interface to HTL/perovskite interface is uniform

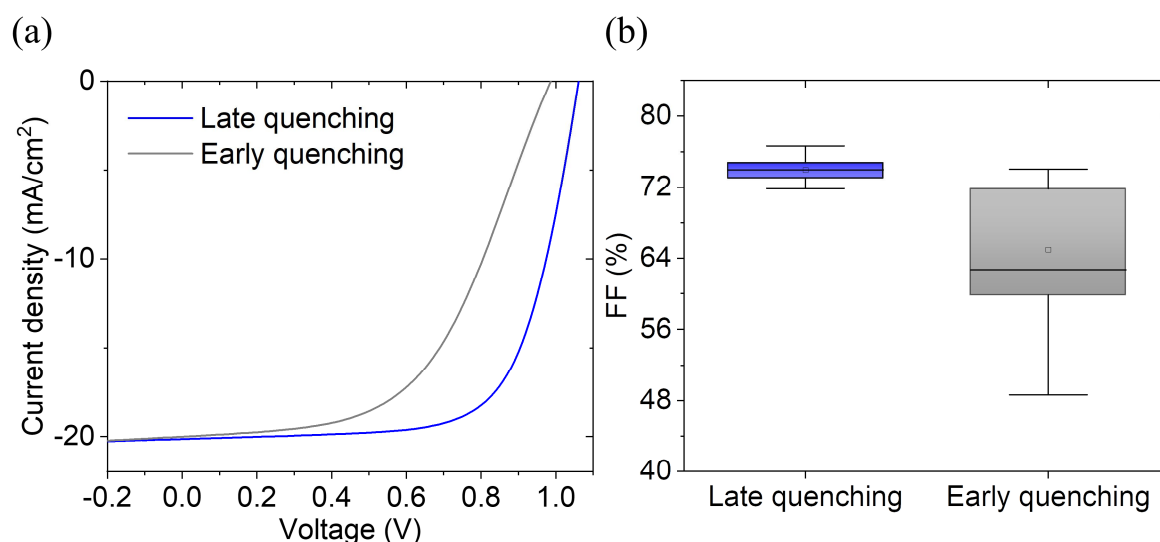


Figure 6.2. (a) J - V characteristics of PSCs fabricated over textured Si substrates using late and early quenching. The early quenched PSC suffers high series resistance. (b) Statistical distribution and comparison of FF for the corresponding PSCs. Part of this figure is reproduced from ref.⁶¹ with permission from Wiley.

(roughly ~ 500 nm), the peak to valley distance when processing over textured surface is roughly ~ 1.5 μm , making it more challenging for DMSO to escape during the deposition process.

To tackle this issue and minimize the volume of trapped DMSO in the valleys of pyramidal textured substrates, we optimized the anti-solvent dropping time to 55 s (which we refer to as late quenching). Late quenching enables a large volume of DMSO near the valleys to evaporate during the spin coating process (before quenching) and consequently there are no signs of voids or other defects, as shown in the cross-sectional SEM image in Figure 6.1a. The presence of voids (as in the early quenching case) causes imperfect mechanical contact of perovskite with the adjacent HTL, resulting in increased series resistance and a consequent drop in FF. Indeed, the J - V curve of an early quenched device exhibits high series resistance and, statistically, PSCs fabricated using early quenching have lower FF compared to devices that have been quenched at a later stage (i.e. late quenching) as shown in Figure 6.2. However, it should not be neglected that these perovskite-free regions also act as recombination centers,^{317,318} which negatively impact V_{OC} as depicted from the implied V_{OC} data in Figure 6.1b. The external V_{OC} gains, observed in PSCs fabricated using late quenching, exhibit a similar trend to the implied V_{OC} data (see Figure 6.1c).

In the same context, Chen *et al.* have introduced a new anti-solvent quenching method, which they called boosted solvent extraction (BSE).⁹⁴ They reported on a deposition process employing three steps (instead of the standard and widely used 2 steps) spin coating program. In their method, the anti-solvent is dripped in the last step after the program reaches very high rpm (~ 10000), which enables efficient and uniform solvent extraction, resulting in optimum crystallization conditions.⁹⁴ Although half-stacks processed over textured Si substrates using the BSE method exhibit high implied and external V_{OC} (see Figure 6.1), fabrication yield of PSCs processed using BSE is drastically low due to the limited time window of dispensing the anti-solvent. Hence, we will stick to our own optimized deposition parameters (late quenching) in the following investigations.

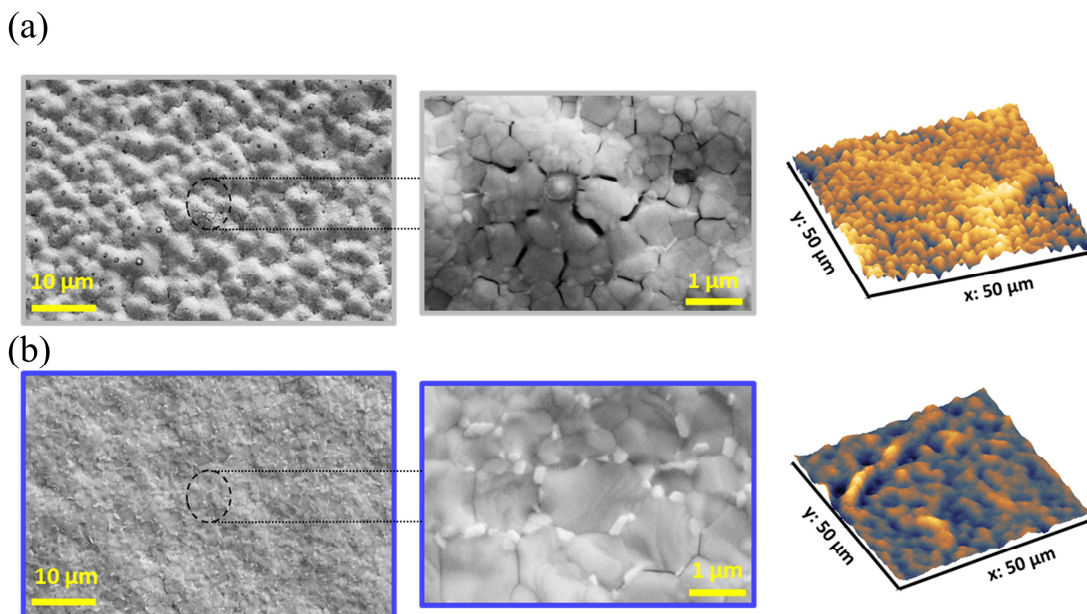


Figure 6.3. (a) and (b) Top-view SEM images and 3D AFM representations of perovskite thin films processed over textured Si substrates from perovskite precursor solutions with 1.4 and 1.6 M, respectively. The perovskite film processed using lower concentration exhibits high surface roughness and surface cracks.

We want to highlight that PLQY measurements were performed using the half-stacks textured Si/ITO/evaporated 2PACz/perovskite. As we wanted to investigate the impact of voids (which will deteriorate the quality of HTL/perovskite interface) on implied V_{OC} , we refrained from introducing C_{60} onto the half-stack to exclude non-radiative recombination at perovskite/ C_{60} interface. On the other hand, the external V_{OC} data of a full device stack shown in Figure 6.1c include non-radiative recombination losses at all interfaces and the bulk. Consequently, the implied V_{OC} values of half-stacks are higher than the external V_{OC} obtained from complete devices.

We conclude that late quenching (after 55 s instead of 12 s), gives room for the perovskite precursor solution to reach the valleys and, simultaneously, there is sufficient time for DMSO to evaporate during spin coating, resulting in less trapped DMSO, promoting better morphology and mechanical contact with the HTL. This consequently enhances FF and minimizes voltage losses caused by the resultant voids in the early quenching case.

6.3 Surface coverage, micro cracks, and voltage losses

As discussed in Chapter 4, assuring full surface coverage of the perovskite thin film deposited onto textured surfaces is necessary to prevent detrimental shunting paths caused by pyramidal tips that extend out of the perovskite film surface. In addition to the evident low shunt resistance that PSCs employing perovskite precursor solution with insufficient concentration exhibit when deposited over textured surfaces (see Figure 6.4a), exposed tips have a strong contribution in surface roughness as indicated by the 3D representation of AFM measurements in Figure 6.3a. Depositing a perovskite thin film from 1.4 M precursor solution of the double-cation ($CS_{0.17}FA_{0.83}PbI_{2.75}Br_{0.25}$) perovskite over micrometer-sized textures results in root mean square (RMS) roughness of ~ 150 nm compared to ~ 115 nm when higher concentration is used (namely 1.6 M). As a reference, corresponding thicknesses

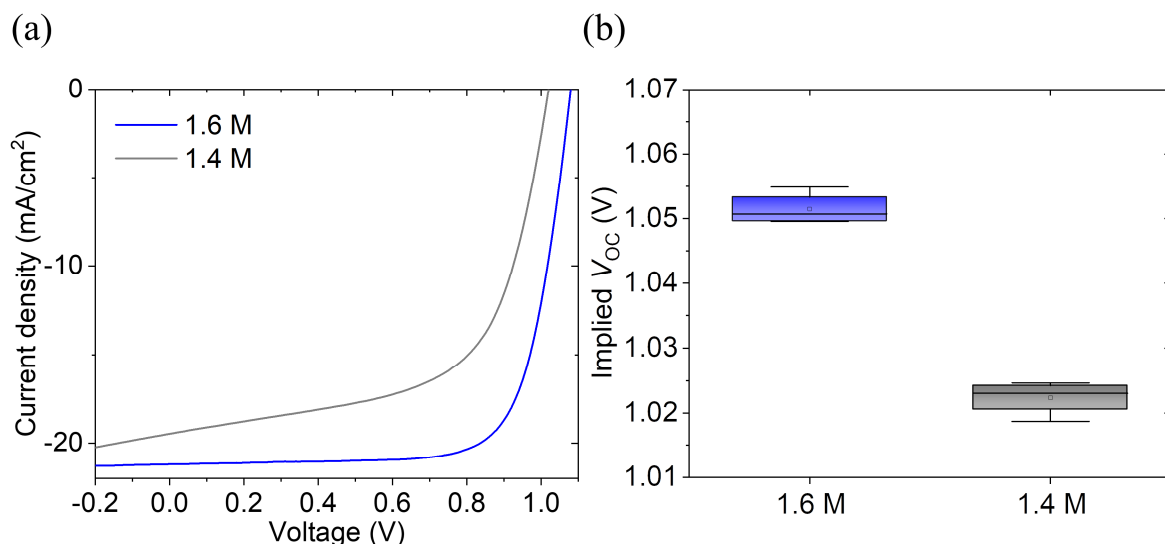


Figure 6.4. (a) J - V characteristics of PSCs fabricated over textured Si substrates using 1.6 and 1.4 M perovskite precursor solution. The PSC fabricated using the lower concentration suffers very low shunt resistance. (b) Statistical distribution and comparison of implied V_{OC} for the corresponding half-stacks. Part of this figure is reproduced from ref.⁶¹ with permission from Wiley.

of perovskite thin films deposited over planar substrates using 1.6 and 1.4 M of the double-cation ($\text{Cs}_{0.17}\text{FA}_{0.83}\text{PbI}_{2.75}\text{Br}_{0.25}$) perovskite are $\sim 1 \mu\text{m}$ and $\sim 720 \text{ nm}$, respectively.

In addition to the remarkably high surface roughness depicted from AFM measurements, top-view SEM images in Figure 6.3a indicate that perovskite thin films deposited using the low concentration solution tend to form surface cracks around the pyramidal tips. High surface roughness along with micro cracks are expected to result in high non-radiative recombination as a consequence of such a defective perovskite/ETL interface.³¹¹ Indeed, PLQY measurements indicate that voltage losses in half-stacks processed using the 1.6 M precursor solution are much lower compared to the 1.4 M counterpart, with an implied V_{OC} of 1.050 V and 1.021 V, respectively (see Figure 6.4b).

To conclude, assuring full surface coverage by employing the optimized perovskite precursor solution concentration prevents detrimental shunting paths, results in a reduction in surface roughness, and eliminate surface cracks. Consequently, the perovskite/ETL interface is enhanced and voltage losses are mitigated.

6.4 Precursor stoichiometry, excess PbI_2 , and voltage losses

A 10% PbI_2 excess is commonly used in planar PSCs that report high V_{OC} , however, a slightly higher or lower percentage might negatively impact PSC's performance.^{287,296} We noted that slightly higher percentage of excess PbI_2 minimizes voltage losses further when processing perovskite thin film over a textured surface. This observation motivated us to investigate in-depth the optimal amount of excess PbI_2 to maximize V_{OC} of PSCs processed over textured surfaces.

6.4.1 Crystal structure of perovskite thin films over textured vs planar surface

Highly concentrated perovskite precursor solutions (which are essential to provide full surface coverage over pyramidal textures) with 10% excess PbI_2 , result in high volume

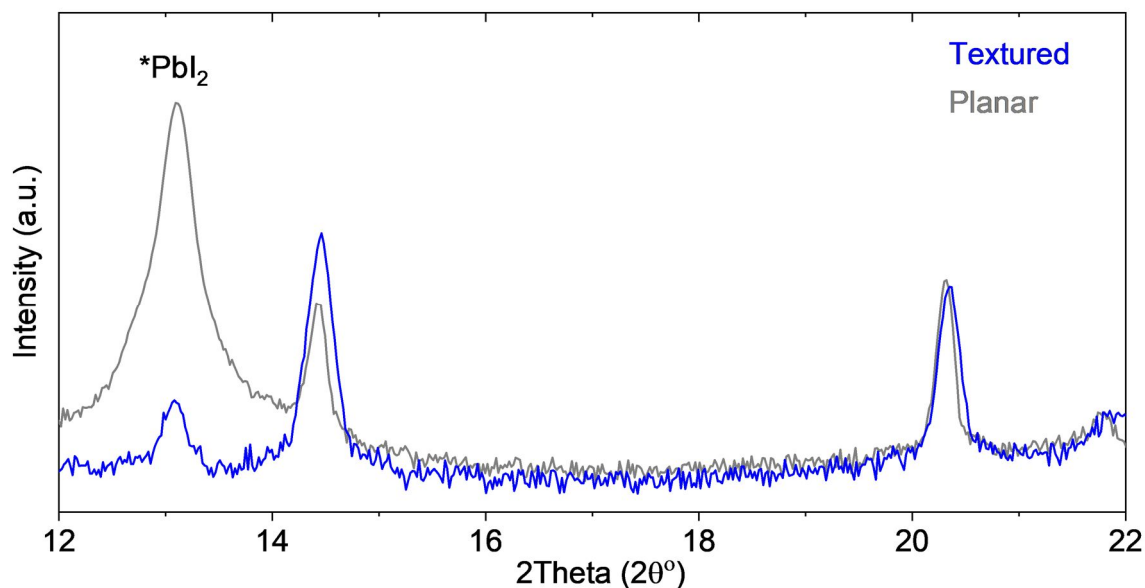


Figure 6.5. Comparison of XRD spectra for perovskite thin films processed from 1.6 M double-cation perovskite ($\text{Cs}_{0.17}\text{FA}_{0.83}\text{PbI}_{2.75}\text{Br}_{0.25}$) with 10% excess PbI_2 over planar and textured Si substrates, employing the half-stack ITO/Evaporated 2PACz/perovskite. Reduced PbI_2 volume fraction is noted in the perovskite thin film processed over textured half-stack.

fraction of PbI_2 when processed over a planar surface, as indicated by the XRD spectra in Figure 6.5.^{94,180} Surprisingly, the intensity of the PbI_2 diffraction peak is damped when the perovskite film is deposited over textured surfaces (see Figure 6.5). We would hereby like to emphasize that we used the same perovskite precursor solution [1.6 M of the double-cation ($\text{Cs}_{0.17}\text{FA}_{0.83}\text{PbI}_{2.75}\text{Br}_{0.25}$) perovskite] and the same processing parameters (as optimized in Chapter 4) for both planar and textured Si substrates. We also noticed a slight shift in the characteristic peaks, which could be attributed to residual strain in the formed film over textured substrates.³¹⁰ As the results are interesting and a bit intriguing, we performed the experiment multiple times to ensure the results weren't an outlier, every experiment supported our initial conclusion. Additionally, we note that the PbI_2 diffraction peak intensity is damped irrespective of the size or the density of the pyramidal textures by depositing the same perovskite onto different textures types. Furthermore, depositing thinner layers of the perovskite thin film (regardless of their poor surface coverage discussed in Section 6.3 and Chapter 4) using lower concentration perovskite precursor solution (namely 1.0 M and 1.3 M), led to the same results.

Literature has reported on a similar decrease in crystalline PbI_2 volume fraction. For example, recipes employing additives such as Lewis acids and bases in the perovskite precursor solution tend to form complex compounds with the PbI_2 , resulting in a decreased PbI_2 diffraction peak intensity.^{155,180,205,206} However, given that we use the same perovskite precursor solution and change only the substrate type (textured vs planar), this explanation is not plausible. Due to the key role that excess PbI_2 plays in passivating grain boundaries, we further investigate potential reasons behind the reduced intensity when processing over textured surface.

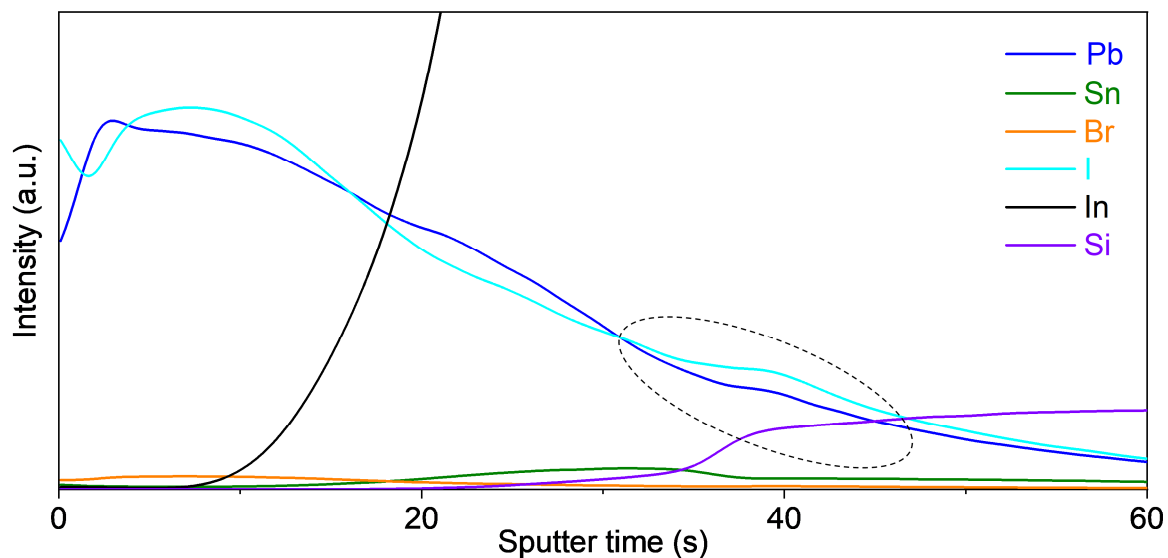


Figure 6.6. Glow discharge optical emission spectroscopy (GDOES) spectra of the half-stack textured Si/ITO/Evaporated 2PACz/perovskite, indicating the depth-profiling of Pb, I, Br (representing the perovskite thin film), In and Sn (representing the ITO), and Si (representing the substrate). The depth-profiling of iodine indicates an increased signal (compared to Pb) at the bottom side of the perovskite thin film. Reproduced from ref.⁶¹ with permission from Wiley.

6.4.2 Interaction of perovskite thin films with the adjacent HTL/TCO

Seeking a plausible explanation for the reduced PbI_2 volume fraction discussed above, one can correlate the reduced intensity as a result of interaction between the perovskite thin film and the adjacent HTL and/or TCO. Literature has shed light on chemical reactions between perovskites with NiO_x in planar *p-i-n* PSCs.^{69,71,299,301,302,319} For example, Boyd *et al.* have shown that Ni^{3+} species on NiO_x films are consuming A-site cations (FAI in our case) by chemical redox reactions (i.e. they deprotonate cationic amines and oxidize iodide species), resulting in a potentially Pb-rich/I-poor and defective interface.⁶⁹ Replacing NiO_x with a different HTL (evaporated 2PACz for example) doesn't necessarily mean these interactions are not taking place. Although there are no investigations/studies to indicate similar interactions between perovskites and the adjacent TCO, one should take into account that the main components of widely used ITO [indium (In) and tin (Sn)] have similar oxidization states to that of Ni,^{228,320,321} thus, the previously reported interactions between perovskite and NiO_x could extend further to the adjacent ITO. Should these chemical interactions take place, their strength and consequently the amount of consumed iodine is notably higher in textured surfaces compared to their planar counterparts due to the larger surface area that a textured surface exhibits (i.e. TCO and HTL also exhibit larger area when deposited over textured surfaces compared to planar counterparts).

To investigate if the iodine of the perovskite thin film is interacting with adjacent layers, which could be one of the potential reasons for the reduced PbI_2 peak intensity discussed above, we utilize GDOES depth-profiling measurements to study the elemental distribution throughout the perovskite film and at the HTL/perovskite interface. Although GDOES is being widely used in CIGS solar cells characterization,^{322–324} it has been shown to be powerful tool in characterizing PSCs, particularly in investigating elemental distribution of bulk passivation additives.^{325,326}

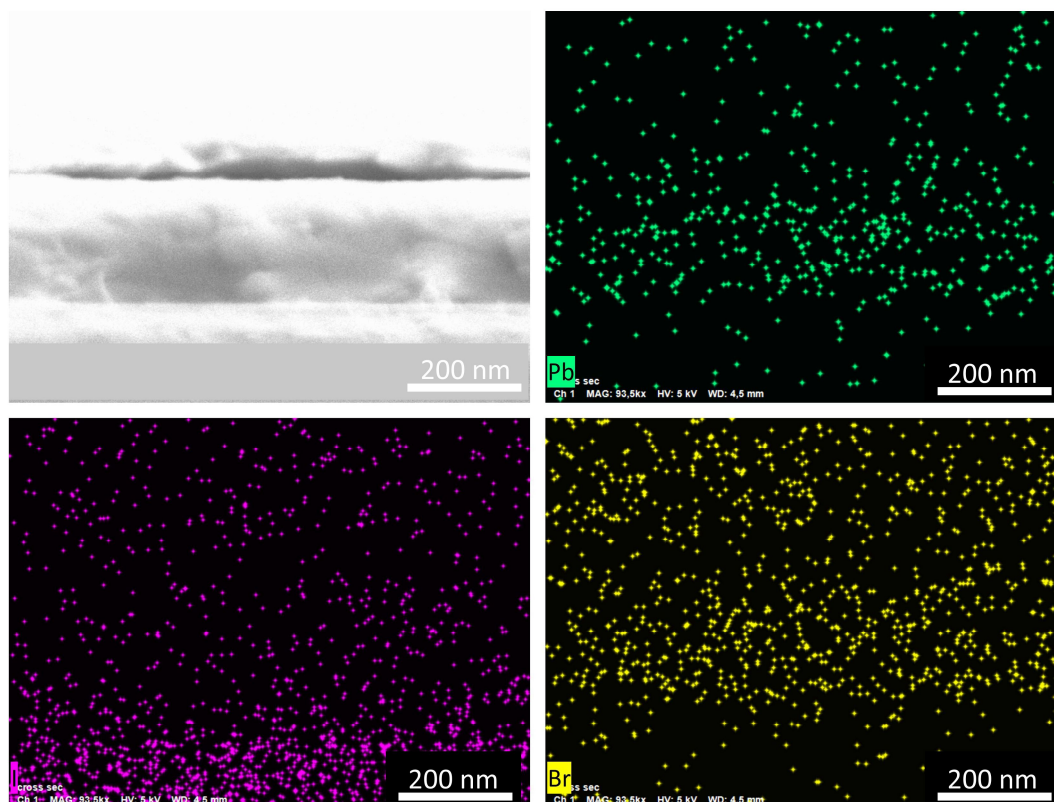


Figure 6.7. Cross-sectional SEM image of perovskite thin film processed over planar glass substrate, along with the corresponding energy dispersive X-ray mapping of the perovskite elements, indicating high I intensity at the bottom side of the perovskite thin film. Adapted from ref.⁶¹ with permission from Wiley.

Regarding perovskite thin films processed onto textured surfaces, Figure 6.6 displays the GDOES depth-profiling data of the half-stack textured Si/ITO/evaporated 2PACz/perovskite. The signal intensities of Br, I, and Pb indicate a strong presence at the beginning of sputtering (i.e. at the surface of the perovskite layer) and stay high through the perovskite thin film. After ~10 s, In and Sn (representing the ITO) signals start to arise, followed by the presence of Si (representing the substrate) signal after ~20 s of sputtering. The Si signal is remarkably increased after ~40 s sputtering, along with the remarkable decrease of Br, I, and Pb signals intensities, indicating that most of the perovskite layer has been removed from the valleys. By taking a closer look at the distribution of both Pb and I, we note a slight increase of the I signal compared to Pb, coinciding with the increased Si signal as highlighted in Figure 6.6. Although the HTL employed in the investigated half-stack is evaporated 2PACz (not NiO_x that interacts with the iodine and might cause a higher iodine signal near the HTL/perovskite interface), the increased I signal near the HTL/perovskite interface emphasizes that the bottom side of the perovskite thin film is iodine-rich, irrespective of the employed HTL.

GDOES measurements have indicated the bottom side of the perovskite thin film to be iodine-rich, which could be the answer to PbI₂ deficiency in the bulk as discussed earlier, however, we cannot speculate the existence of chemical reaction between the iodine and the adjacent HTL and/or ITO. In the same context, energy dispersive X-ray (EDX) maps of

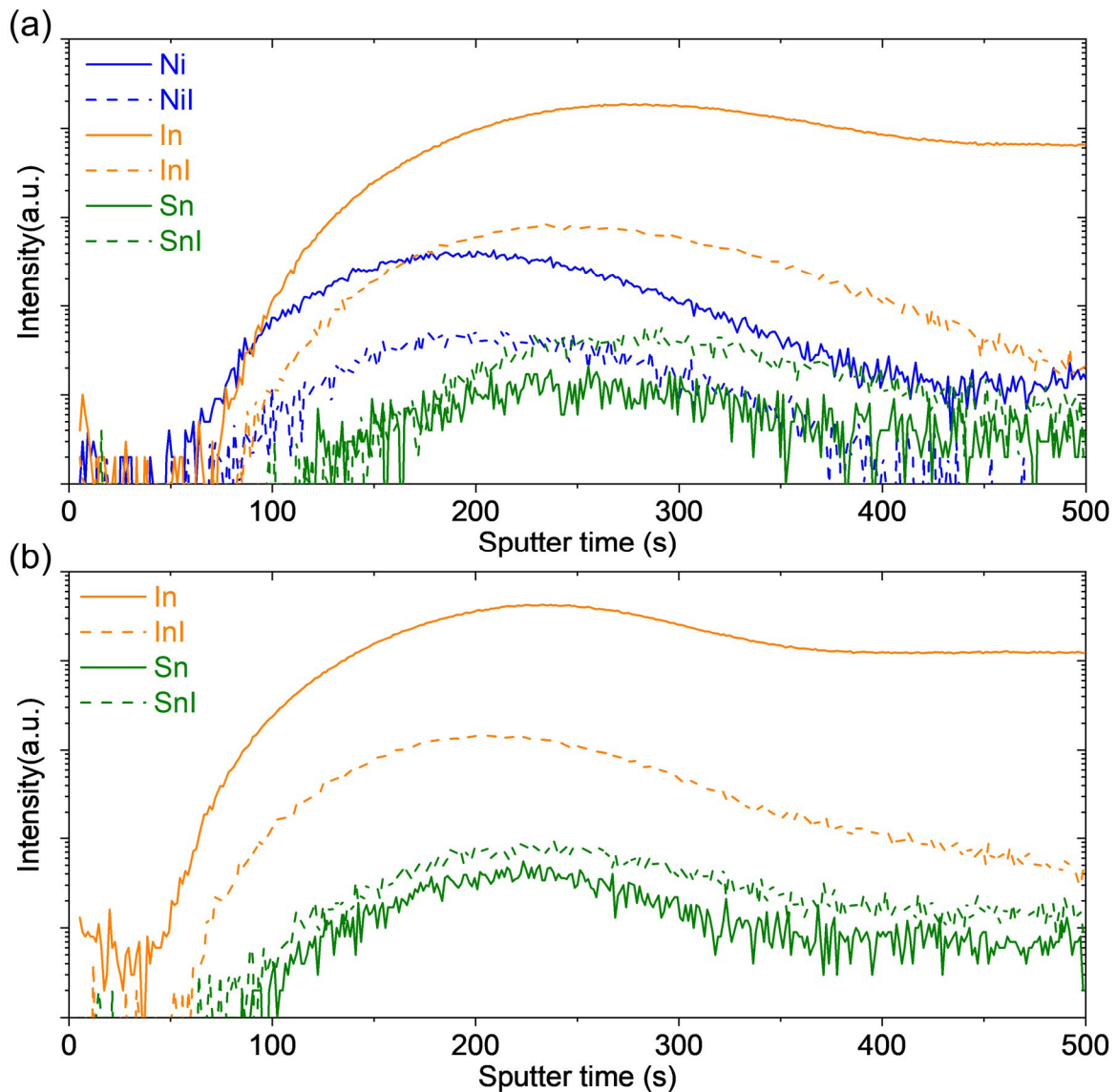


Figure 6.8. (a) Time-of-flight secondary ion mass spectrometry (ToF-SIMS) data of the half-stack textured Si/ITO/NiO_x/perovskite. The depth-profiling data indicate the interaction of perovskite with HTL (NiO_x in this case) as indicated by the NiI signal. The interaction is extended further to the adjacent ITO as indicated by the presence of InI and SnI signals. (b) ToF-SIMS data of a similar stack employing 2PACz-HTL instead of NiO_x, emphasizing the interaction of perovskite with ITO.

perovskite thin film processed onto planar half-stack: glass/ITO/NiO_x/perovskite, indicate higher intensity of I near the HTL/perovskite interface as shown in Figure 6.7.

As GDOES and EDX can only provide information about the distribution of single elements, further characterization techniques that enable detection of chemical compounds should be utilized to further our understanding on the nature of chemical reactions taking place at HTL/perovskite interface, hence, we utilize ToF-SIMS. ToF-SIMS is a powerful technique that has been used extensively in the field of PSCs to investigate various aspects.^{80,87,327–330} For example, Yang *et al.* have utilized ToF-SIMS depth-profiling measurements to differentiate between 2D and the bulk of a 3D perovskite layers.³³¹ Domanski *et al.* utilized ToF-SIMS 3D mapping to investigate ion migration in PSCs and its impact on long term stability.³³² Mahmud *et al.* have utilized ToF-SIMS depth-profiling

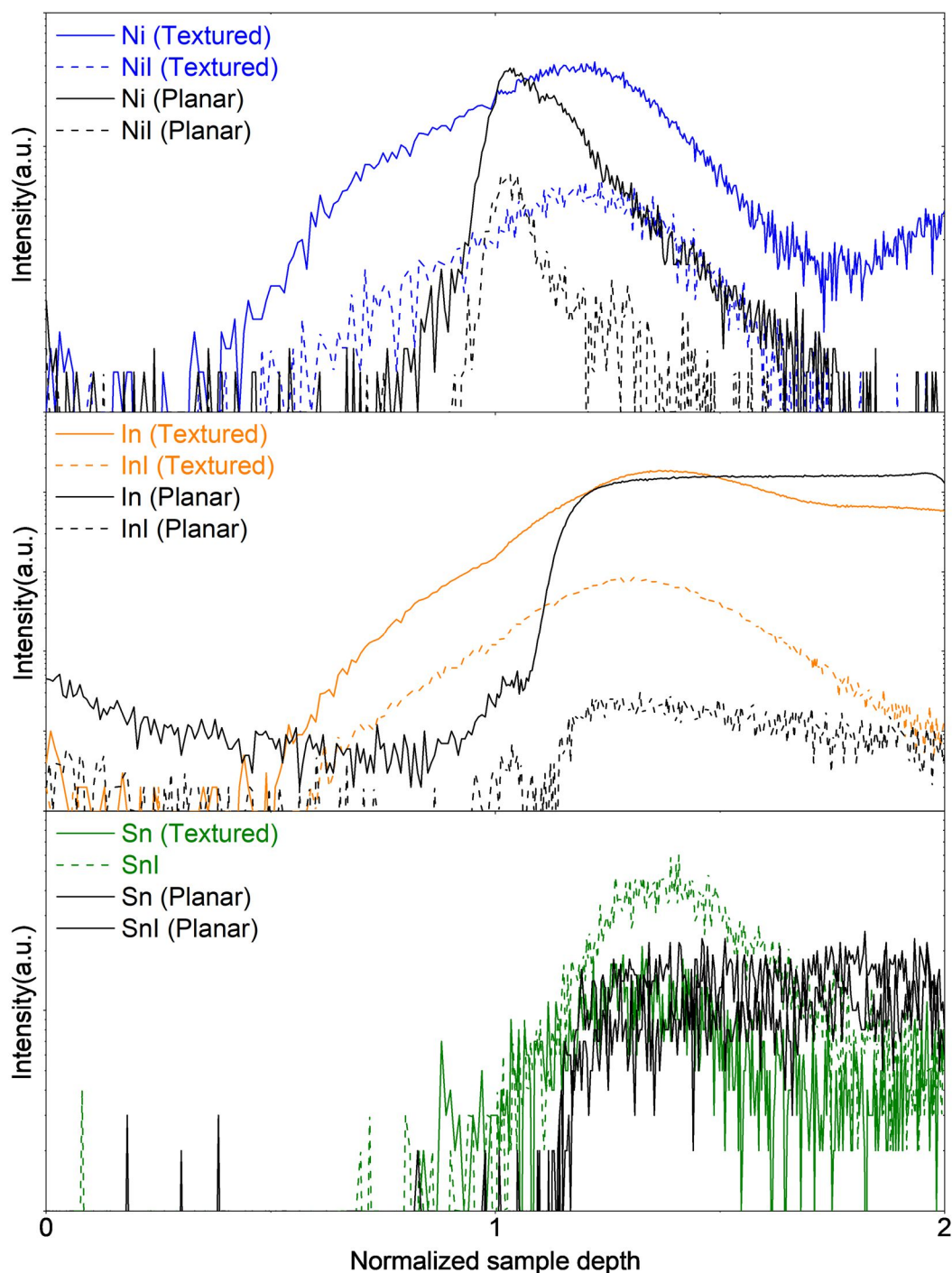


Figure 6.9. Comparison between ToF-SIMS depth-profiling of the half-stack ITO/NiO_x/perovskite processed over textured and planar Si substrates. The interaction of perovskite with HTL and ITO is evident, irrespective of substrate type, however, signals intensities are higher and arises earlier in the textured substrate due to its larger surface area. Adapted from ref.⁶¹ with permission from Wiley.

measurements to emphasize the presence of their developed double-layer passivation scheme at perovskite/ETL and HTL/perovskite interfaces in *p-i-n* PSCs.⁸⁰

Similarly, we investigate the potential reasons behind the increased I signal near the HTL/perovskite interface utilizing ToF-SIMS. Depth-profiling measurements of the half-stack textured Si/ITO/NiO_x/perovskite in Figure 6.8a (full data set can be found in Figure

A6.1a), indicate the interaction of iodine with the positive ions of HTL. When employing sputtered NiO_x as an HTL, the iodine interacts with nickel (Ni), forming nickel iodide, and the nickel iodide signal starts to arise simultaneously with the Ni signal. Our results are in full agreement with literature, regarding the interaction of iodine with metal oxides in the *p-i-n* stack.^{69,299–301}

Surprisingly, the interaction does not stop at the HTL, we note a similar interaction is taking place with the adjacent ITO. Tin iodide and indium iodide signals are present simultaneously with the Sn and In signals, respectively. Indium iodide and tin iodide signals are also present when evaporated 2PACz is employed as an HTL (see Figure 6.8b). Performing similar ToF-SIMS depth-profiling measurements on planar references indicated that the same interactions are taking place (in line with EDX maps of the planar perovskite thin film shown in Figure 6.7). The evidence of such chemical interactions on a planar reference employing same HTL and TCO is expected (Figure A6.1b, c), furthermore it indicates the consistency of the reaction mechanism. However, due to the remarkably larger surface area of a textured substrate compared to a planar, and the consequent larger surface area of both ITO and HTL in the textured case, interaction surface area is drastically increased. Indeed, the comparison between signal intensities indicated by ToF-SIMS measurements for textured and planar half-stacks indicate higher signals in the textured surface case, furthermore, the signals start to arise earlier as well (see Figure 6.9). This indicates that the amount of iodine consumed during the interaction with HTL and TCO for films processed over textured surface is higher and thus justifies the reduced PbI₂ intensity discussed above.

6.4.3 Excess PbI₂ and its impact on V_{OC}

To compensate for the iodine (and consequently PbI₂) deficiency in the bulk of perovskite thin films processed over textured surfaces, we found it necessary to revisit the universal 10% excess PbI₂ to determine the suitable value for textured surfaces. For textured Si/ITO/HTL/Perovskite half-stacks, we observe the absence of PbI₂ peak in the stoichiometric film as depicted from XRD data in Figure 6.10a. XRD data of perovskite thin films processed over textured half-stacks employing excess PbI₂ (10%, 15%, and 20%) indicate a gradual increase in PbI₂ peak intensity with increased excess PbI₂ in the perovskite precursor solution. To investigate the excess PbI₂ percentage that enables the highest V_{OC} when processing over textured surfaces, we perform PLQY measurements on textured Si/ITO/evaporated 2PACz/perovskite/C₆₀ half-stacks, employing stoichiometric perovskite thin films and different volumes of excess PbI₂ (0%, 10%, 15%, and 20%). As expected, non-radiative recombination losses are highest for the stoichiometric film as indicated by the rather low implied V_{OC} (see Figure 6.10b). The average implied V_{OC} increases from 0.992 V in the 0% case to 1.040 V, 1.046 V, and 1.030 V for 10%, 15%, and 20% excess PbI₂, respectively.

We conclude that, although 10% excess PbI₂ is widely used and results in highest V_{OC} for planar PSCs, a higher percentage (namely ~15%) of excess PbI₂ is favorable when processing perovskite thin films over textured surfaces as indicated by PLQY measurements. Furthermore, implied V_{OC} data, which is in favor of 15% excess PbI₂, are in line with external V_{OC} data obtained from PSCs using the full device stack: textured Si/ITO/evaporated 2PACz/perovskite (0%, 10%, 15%, and 20% excess PbI₂)/C₆₀/SnO_x/IZO/Ag grid as shown in Figure 6.10c.

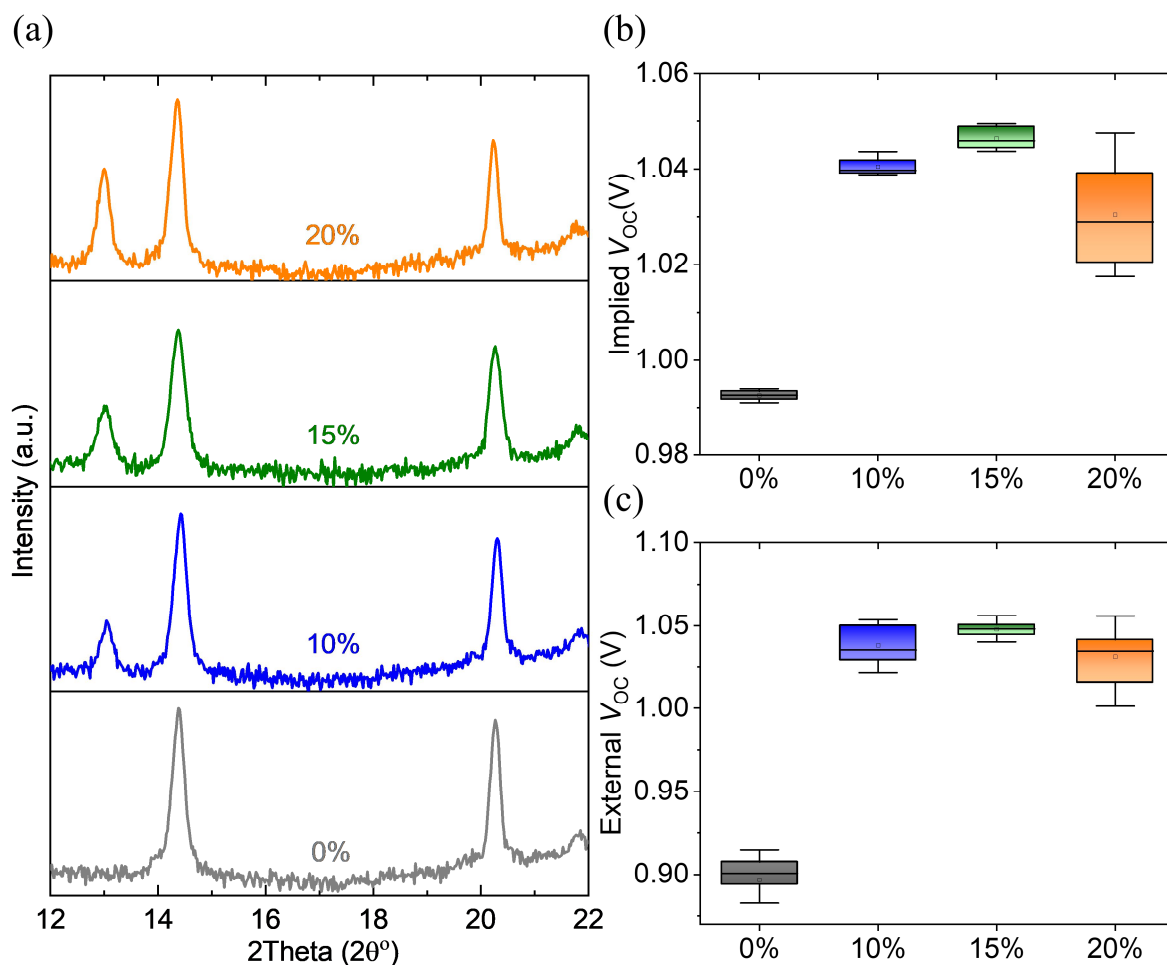


Figure 6.10. (a) Comparison between XRD spectra of perovskite thin films processed from 1.6 M double-cation perovskite ($\text{Cs}_{0.17}\text{FA}_{0.83}\text{PbI}_{2.75}\text{Br}_{0.25}$) employing 0%, 10%, 15%, and 20% excess PbI_2 over textured Si substrates. The PbI_2 peak is absent in the stoichiometric film, with a gradual increase in its intensity proportional to the excess PbI_2 employed in the perovskite precursor solution. (b) Implied V_{OC} comparison of the corresponding half-stacks after introducing 20 nm of C_{60} as ETL on top. 15% excess PbI_2 outperforms the conventional 10% in suppressing non-radiative recombination. (c) The corresponding external V_{OC} obtained from full device stacks. Implied and external V_{OC} data exhibit a similar trend. Part of this figure is reproduced from ref.⁶¹ with permission from Wiley.

6.5 Solvent engineering, surface morphology, and voltage losses

As discussed in Section 6.3, efficient surface coverage by using the optimum perovskite precursor concentration and processing parameters can suppress non-radiative recombination and enhance V_{OC} . Although using lower perovskite precursor concentration resulted in exposed pyramidal tips, which had a strong contribution into surface roughness, we found these uncovered pyramidal tips are not the only reason for such high surface roughness. We noted that perovskite thin films deposited using the high concentration solution (1.6 M) with standard 4:1 dimethylformamide (DMF):DMSO (20% DMSO) volume ratio, exhibit a poor perovskite/ETL interface and consequently suffer from high voltage losses, even when the thorough surface coverage condition is fulfilled (i.e. no pyramidal tips are reaching out to the surface).

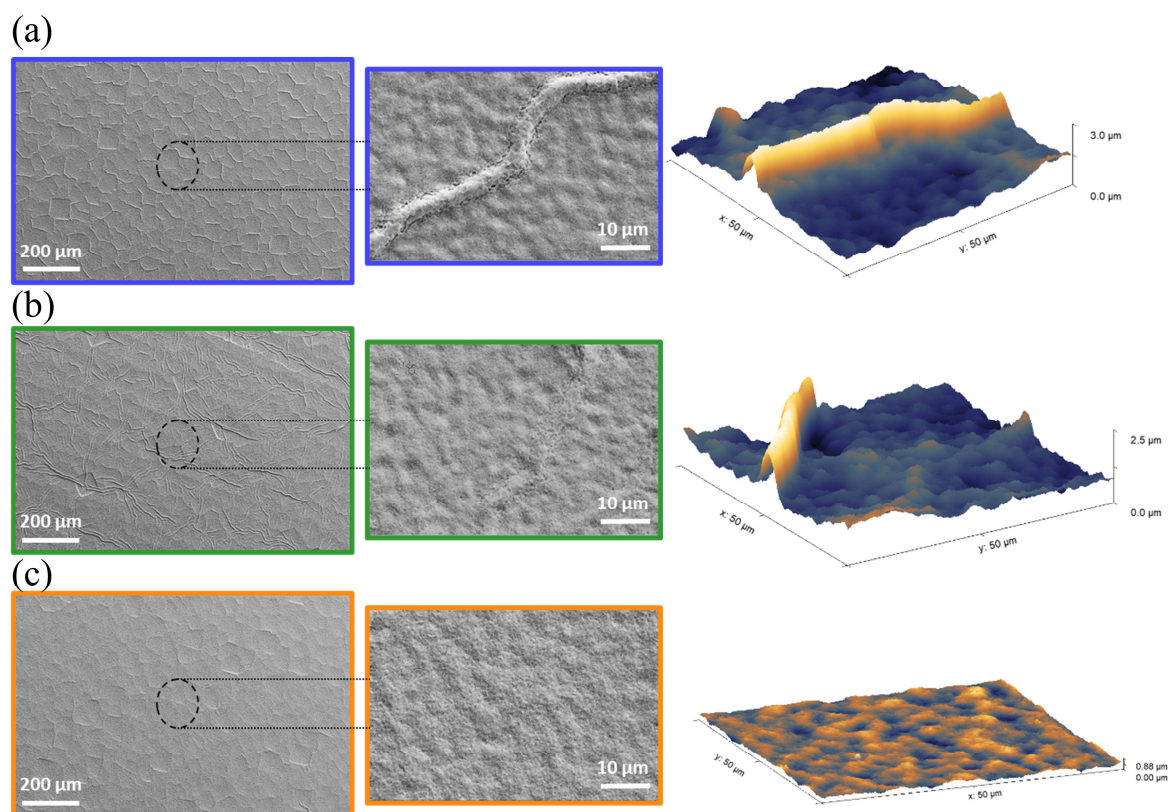


Figure 6.11. (a)-(c) Top-view SEM images and 3D representation of AFM measurements for perovskite thin films processed over the textured half-stack from a 1.6 M double-cation perovskite ($\text{CS}_{0.17}\text{FA}_{0.83}\text{PbI}_{2.75}\text{Br}_{0.25}$) employing 20% (a), 35% (b), and 50% (c) DMSO ratio, respectively. Surface wrinkles width, height, and density decreases with increased DMSO ratio. Part of this figure is reproduced from ref.⁶¹ with permission from Wiley.

Further investigations utilizing SEM indicate that perovskite thin films processed over textured substrates employing the standard 20% DMSO exhibits randomly distributed, high density surface wrinkles with considerable height and width. These surface wrinkles, as depicted from top-view SEM images in Figure 6.11a, can be attributed to residual strain in the perovskite thin film.^{304,308} The 3D representation of a $50 \times 50 \mu\text{m}^2$ AFM scan in Figure 6.11a displays a surface wrinkle of a perovskite film processed using the standard 20% DMSO with an average height of $\sim 1.5 \mu\text{m}$ and average width of $\sim 4.8 \mu\text{m}$. Such high and wide wrinkle would absolutely have a strong influence in RMS roughness ($\sim 500 \text{ nm}$) of the scanned area. Consequently, such increase in perovskite thin film surface roughness is expected to result in a poor perovskite/ETL interface.^{81,82,334,83,94,303–305,311,312,333} Hence, controlling strain-related surface wrinkles is the key toward better surface morphology, a high quality perovskite/ETL interface, and consequently higher V_{OC} . Surface wrinkles in perovskite thin films occur if the substrate constrains the thin film from expansion (during anti-solvent quenching).³⁰⁵ Consequently, during the intermediate phase of thin film formation, in-plane compressive stress takes place, followed by an energy release in the form of wrinkles.³⁰⁴ Many parameters influence the formation of surface wrinkles in perovskite thin films, some are substrate related such as: substrate temperature, morphology and/or type.^{81–83} Controlling other parameters such as solvent type and/or ratio, perovskite composition, and spin coating parameters have been reported to mitigate or eliminate such surface wrinkles.^{82,94,303,305,333,334} In the following, we implement solvent engineering

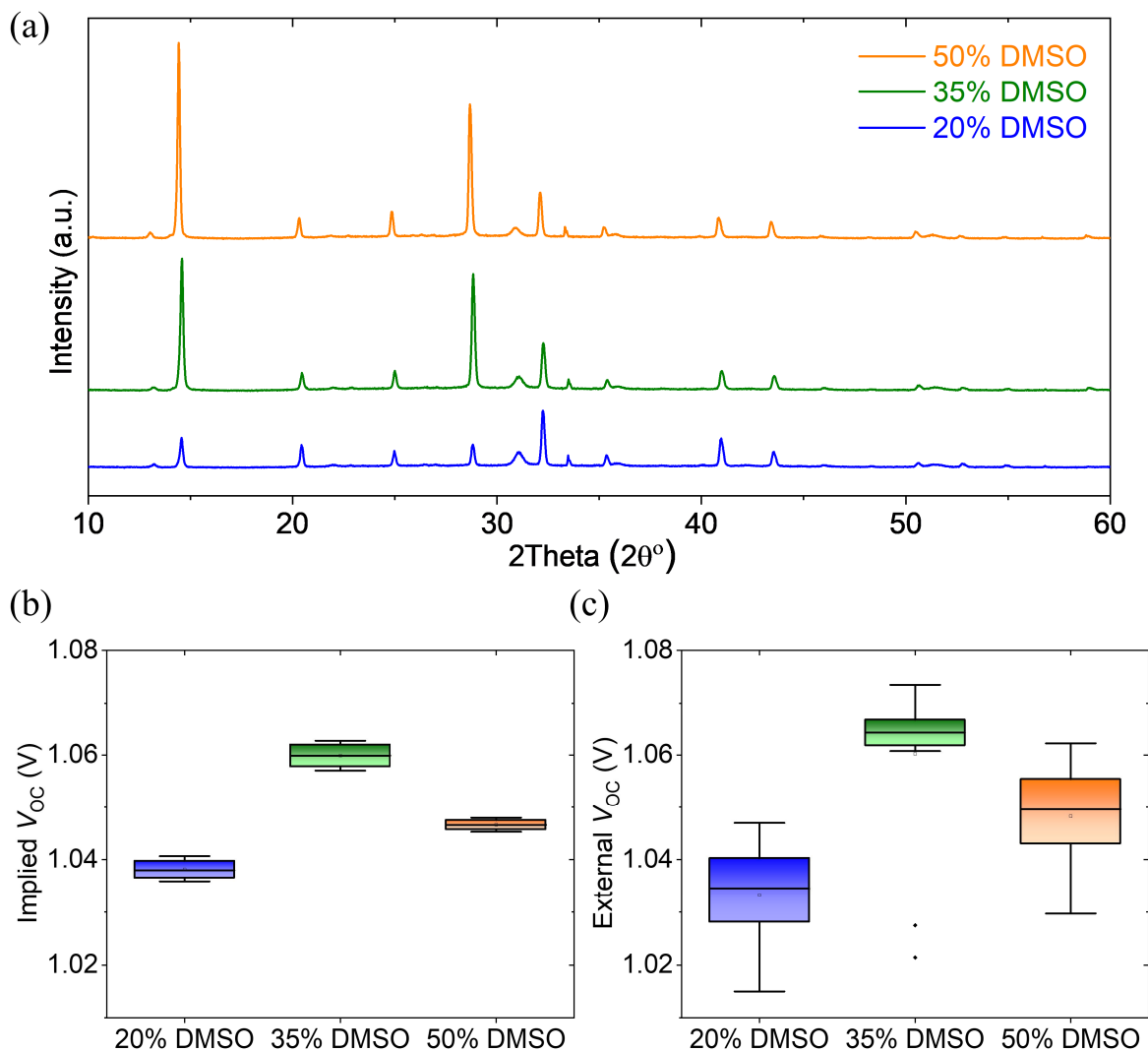


Figure 6.12. (a) Comparison of XRD spectra for perovskite thin films processed from a 1.6 M double-cation perovskite ($\text{Cs}_{0.17}\text{FA}_{0.83}\text{PbI}_{2.75}\text{Br}_{0.25}$) employing 20%, 35%, and 50% DMSO over textured Si substrates. The (100) and (200) peak intensities, indicate improved crystallinity in perovskite thin films employing higher DMSO volume. (b) Implied V_{OC} comparison of the corresponding half-stacks after introducing ETL on top the perovskite thin films. 35% DMSO is outperforming the standard 20% reference as well as the higher volume of DMSO (50%) in suppressing non-radiative recombination at the perovskite/ETL interface. (c) Corresponding external V_{OC} obtained from the full device stacks. Implied and external V_{OC} exhibit a similar trend. Part of this figure is reproduced from ref.⁶¹ with permission from Wiley.

strategy to control these surface wrinkles and minimize the consequent surface roughness. Furthermore, we study the impact of controlling surface wrinkles on ETL/perovskite interface quality by performing PLQY measurements.

Top-view SEM images (see Figure 6.11) indicate that height, density, and width of surface wrinkles tend to decrease when increasing the DMSO volume ratio from the standard 20% to 35% and 50%. Although the 35% DMSO film still exhibit considerably high surface wrinkles as indicated by 3D representation of the AFM measurement (see Figure 6.11b), which is comparable to that of the standard 20% DMSO film, however, wrinkle width is at least 25% smaller (see Figure A6.2). Furthermore, top-view SEM images in Figure 6.11b indicate reduced wrinkle density in the 35% DMSO film. Reduced wrinkle density and width

in the 35% DMSO film results in a reduction of RMS roughness from ~500 nm in the reference (20% DMSO) to ~335 nm when 35% DMSO is employed. Increasing DMSO ratio further to 50% results in substantially improved morphology (see Figure 6.11c) and consequently, RMS roughness sinks to ~93 nm with barely noticeable surface wrinkles. In addition to the enhanced surface morphology, increasing DMSO ratio plays a key role in the crystallization dynamics.^{161,304,335–337} Figure 6.12a shows XRD measurements for the corresponding three perovskite films deposited onto textured half-stacks, employing different DMSO volume ratio. The data displays an increase of the (100) and (200) peak intensities for films employing higher DMSO ratio, indicating their improved crystallinity compared to the reference.

Having studied the impact of DMSO volume ratio on surface morphology, and considering the direct relation between surface roughness and non-radiative recombination losses,^{81,82,334,83,94,303–305,311,312,333} we further investigate PLQY measurements on the half-stack: textured Si/ITO/evaporated 2PACz/perovskite/C₆₀, where the perovskite precursor solutions employ different DMSO volume ratios (20%, 35%, and 50%). As expected, reduced surface roughness in the 35% DMSO film compared to the reference results in a significant enhancement in perovskite/C₆₀ interface quality. Consequently, we measure high PLQY (0.011%) in the 35% DMSO stack with a corresponding implied V_{OC} of 1.059 V compared to 0.005% and 1.038 V for the reference stack, respectively (see Figure 6.12b). Although surface roughness of perovskite thin films employing 50% DMSO is considerably reduced compared to the other two ratios (20% and 35%), PLQY and implied V_{OC} were found to be only higher than the reference but lower than the 35% DMSO case with 0.007% and 1.046, respectively. Literature has shown that controlled wrinkled morphology could potentially lead to increased V_{OC} , because hill sites, which have higher amplitude of wrinkles, exhibit less defects.³⁰⁸ This hypothesis is a reasonable explanation for why eliminating the wrinkles completely (as happens when employing 50% DMSO) does not lead to further increase in V_{OC} .

In summary, controlling surface morphology of perovskite thin films processed over textured surfaces is necessary to enhance the quality of perovskite/ETL interface. By applying solvent engineering strategy, we note that perovskite precursor solution employing a 35% DMSO volume ratio is more favorable as it results in films with better surface morphology and consequently suppresses non-radiative recombination at the perovskite/ETL interface, compared to the standard 20% DMSO films. Implied V_{OC} data are in line with external V_{OC} data of the full device stacks, emphasizing the superiority of the optimized solvent ratio as shown in Figure 6.12.

6.6 Solution-processed and evaporated passivation schemes for higher V_{OC}

Developing a compatible HTL with textured surfaces (thermally evaporated SAMs discussed in Chapter 5) and optimizing deposition parameters to eliminate void formation has enhanced the quality of the HTL/perovskite interface. Furthermore, optimizing excess PbI₂ in the perovskite precursor solution suppressed non-radiative recombination within the bulk, leaving perovskite/ETL to be the limiting interface. Considering a significant portion of voltage losses in planar *p-i-n* PSCs is dominated by perovskite/ETL interface,^{79,108,159,338} and taking into account the expected increase in surface roughness of perovskite thin films

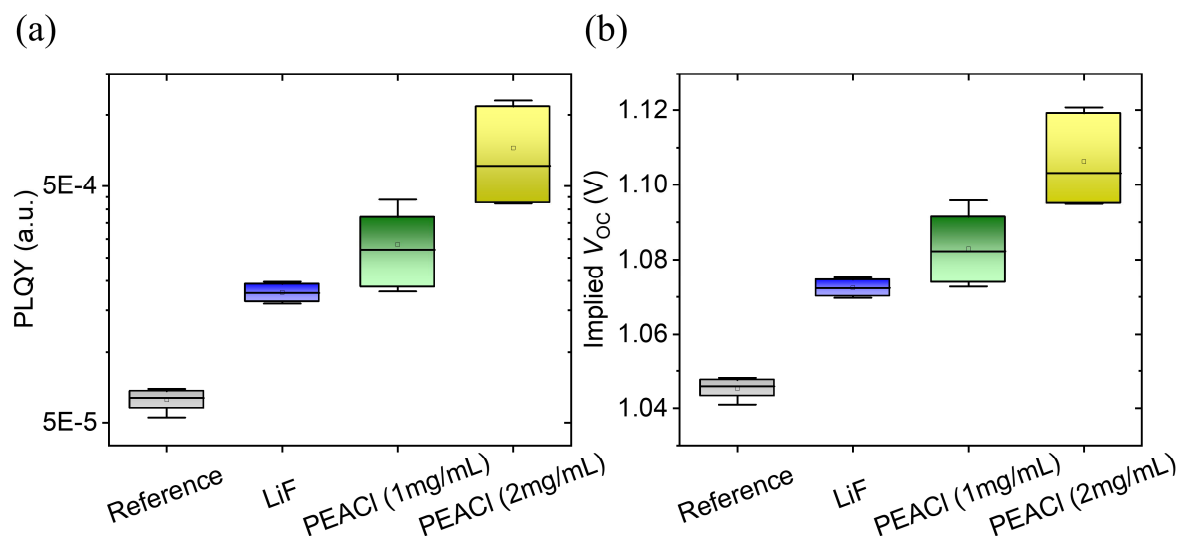


Figure 6.13. (a) and (b) PLQY and implied V_{OC} comparison between half-stacks ITO/ NiO_x /2PACz/perovskite/ C_{60} processed over textured Si substrates and employing different surface passivation layers in between the perovskite and C_{60} . Solution-processed passivation using 1 and 2 mg/ml PEACI is outperforming both the reference and half-stacks employing thermally evaporated LiF in suppressing non-radiative recombination at perovskite/ETL interface. Reproduced from ref.⁶¹ with permission from Wiley.

processed over a textured surface compared to a planar, these losses are expected to be much higher in the textured case.

Assuring surface coverage as well as controlling strain related surface wrinkles by optimizing perovskite precursor solution concentration and applying a proper solvent engineering strategy, have reduced surface roughness drastically, and a remarkable increase in V_{OC} was obtained. Now, we investigate the impact of employing surface passivation in between perovskite and C_{60} layers on suppressing non-radiative recombination further at this interface. Our surface passivation scheme employs both thermally evaporated and solution-processed surface passivation interlayers.

For the reference stack: textured Si/ITO/evaporated 2PACz/perovskite/ C_{60} , we measure a rather low PLQY with an average value of 0.006%. The low PLQY of reference stack is expected and attributed to a high defect density at the perovskite/ C_{60} interface, in full agreement with literature.^{53,73,79,338} Corresponding implied V_{OC} is only 1.045 V (see Figure 6.13). Lithium fluoride (LiF), deposited *via* thermal evaporation, has been reported to passivate the perovskite/ETL interface in planar *p-i-n* PSCs.^{74,76-78} Introducing ~1 nm of thermally evaporated LiF interlayer at perovskite/ C_{60} interface, already increases the average PLQY to 0.018% with a corresponding implied V_{OC} of 1.073 V. The improvement in interface quality obtained by introducing LiF results in roughly ~30 mV higher implied V_{OC} , in good agreement with previous reports introducing LiF in a similar stack.^{74,76-78} While LiF is widely used as a passivation interlayer, it has been shown to have a strong negative impact on long term device stability.⁷³ Recently, different interlayers processed *via* thermal evaporation or solution-processing, have shown a comparable defects passivation effect to that of LiF, without exhibiting its drawbacks.^{73,80} For example, Gharibzadeh *et al.* demonstrated the long chain alkylammonium salt phenethylammonium chloride (PEACI) to play a key role in passivating perovskite/ C_{60} interface, and consequently suppressing non-

radiative recombination losses in planar *p-i-n* PSCs.⁷⁹ To investigate the role that PEACl plays in suppressing non-radiative recombination at perovskite/C₆₀ interface when perovskite thin films are deposited over micrometer-sized pyramidal textures, we employ PLQY measurements on half-stacks: textured Si/ITO/evaporated 2PACz/perovskite/solution-processed PEACl/C₆₀, employing two different concentrations of PEACl (namely 2 and 1 mg/ml) *via* spin-coating. Already, the lower concentration of PEACl (1 mg/ml) contributed significantly in enhancing PLQY to an average of 0.027%, with a corresponding implied V_{OC} of 1.083 V. The increase of implied V_{OC} indicates that the lower concentration of PEACl is outperforming the reference stack (with roughly ~40 mV), and is comparable to that of the stack employing LiF interlayer. The stack employing higher concentration of PEACl (2 mg/ml) exhibits almost one order of magnitude higher PLQY than the reference stack. The corresponding implied V_{OC} is 1.106 V, which is roughly ~61 mV higher than the reference and ~33 mV higher than the stack employing the conventional LiF. Although higher concentrations of PEACl might result in further implied V_{OC} enhancement, it has been reported to cause a negative impact on FF and J_{SC} .⁷⁹

In summary, when processing perovskite thin films onto micrometer-sized textured surfaces, different passivation schemes can suppress non-radiative recombination and mitigate voltage losses at the perovskite/ETL interface further.

6.7 Device performance

Having optimized the perovskite absorber as discussed in Chapter 4, the HTL developed as discussed in Chapter 5, along with voltage losses mitigation strategies investigated in this chapter, we now study the optimum deposition condition for the back TCO, define the compatible wafer type, mitigate the optical losses, and finally yet importantly, investigate the PV performance of PSCs processed over textured surfaces.

6.7.1 Optimizing the back TCO

For our baseline process, planar PSCs are fabricated over commercially available glass/ITO substrates. The ITO film thickness is ~135 nm with a corresponding sheet resistance of ~15 Ω /sq, which is optimum for processing PSCs. Using our in-house sputter system, we can sputter ITO films with comparable quality for the same film thickness using a power of 50 W and a gas composition of 97.5% Ar to 2.5% O₂ at a pressure of 0.8 mTorr. The resultant sheet resistance of sputtered ITO films is ~24 Ω /sq on average when the films are sputtered over planar glass or planar Si substrates, which is still low enough for producing efficient PSCs with >80% FF. Surprisingly, sputtering ITO films using our baseline recipe onto textured Si substrates resulted in very high series resistance (~85 Ω /sq). Processing PSCs employing ITO films with such high sheet resistance will lead to detrimental high series resistance, consequently reduced FF and PCE of the PSC (see Figure 6.14a). We speculate that sputtering using low power while substrates are kept at room temperature (as in our baseline recipe), leads to a short diffusion length for the sputtered atoms/molecules after they reach the substrate surface. Short diffusion length for sputtered molecules means the crystallization/film formation starts immediately after they reach the substrate's surface, which is not an issue if they are being deposited onto a planar surface. On the other hand, longer diffusion length (which is fulfilled if the substrate is kept at elevated temperatures before and during deposition)^{339,340} along with high sputtering power (which results in high

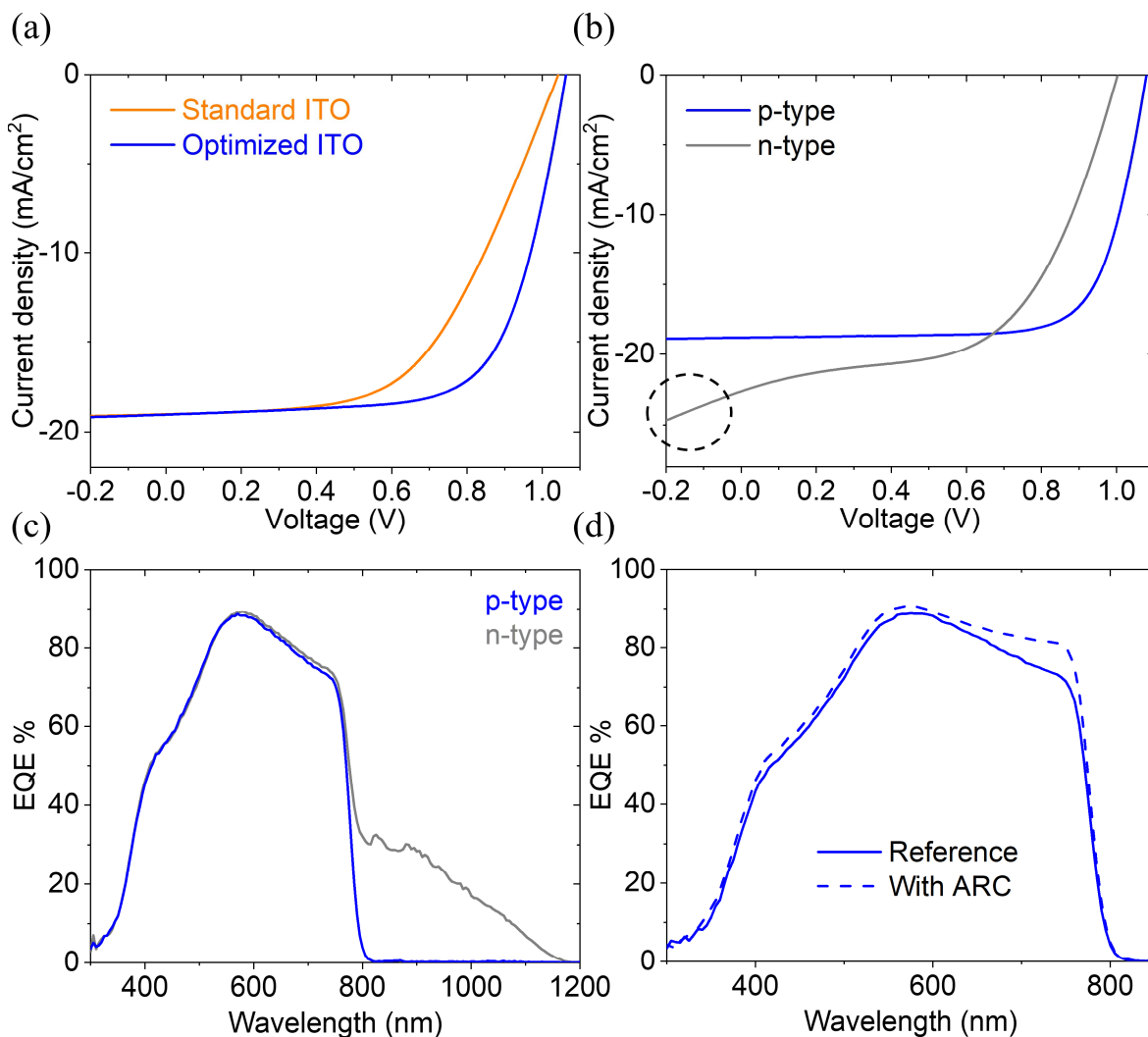


Figure 6.14. (a) J - V characteristics of PSCs fabricated over textured Si substrates employing 135 nm of sputtered ITO as back electrode. The comparison between the baseline sputtering recipe and optimized recipe displays the superiority of the latter. (b) and (c) J - V characteristics and EQE of PSCs fabricated over textured Si substrates employing p-type and n-type Si wafers, respectively. A strong bending in the J - V curve of the PSC employing n-type wafer is observed near the J_{sc} , indicating a contribution from the substrate itself. The contribution is emphasized by the spectral response of the PSC beyond the band gap of the perovskite absorber as shown in c. (d) EQE comparison of a PSC fabricated over textured Si substrates employing the compatible p-type wafer before and after introducing ~ 100 nm MgF_2 anti-reflection coating (ARC). The ARC mitigates the optical losses and enhances J_{sc} .

kinetic energy of the sputtered molecules)^{340,341} is expected to be more suitable for textured surfaces with their surface complexity. Indeed, performing a series of ITO sputtering processes to identify the most suitable deposition parameters for the ITO film over textured substrates, we found that sputtering using a power of 250 W (instead of 50 W) at high substrate temperature (300 °C instead of room temperature) results in the desirable low sheet resistance ($\sim 15 \Omega/sq$), which is comparable to the commercially available planar glass/ITO substrates.

6.7.2 Identifying a suitable textured Si wafer type (p vs n-type)

During the optimization phase of our PSCs processed over textured surfaces, we noted that wafer type of the textured Si substrates plays a huge role in the device's performance. J - V

characteristics of *p-i-n* PSCs processed onto textured Si substrates from n-type wafer, exhibit an unexpected strong bend in the $J-V$ curve near J_{sc} (see Figure 6.14b). Such bending near J_{sc} is far from the common low shunt resistance behavior. Further investigation utilizing EQE measurements (see Figure 6.14c), indicate the existence of spectral response beyond the perovskite's band gap, thus, a contribution to J_{sc} is coming from the textured Si substrate itself. We speculate that under illumination, incident light generates electron-hole pairs in the Si substrate as well as the perovskite absorber. Processing *p-i-n* PSCs over n-type Si substrate is to some extent forming a *p-n* junction at the Si/PSC interface (*n/p-i-n*), which eases the charge carriers extraction generated in the Si substrate. Given the long charge carrier diffusion length in Si compared to perovskite,^{94,342–345} a considerable amount of the generated holes in the Si substrate can easily be extracted at the back electrode (the near side). Electrons generated in the Si substrate however, have to make their way through perovskite to reach the front electrode (the far side). Electron extraction is less likely to happen for electrons generated at the valleys of the Si substrate, while electrons generated near the pyramidal tips can be extracted, considering the very short distance between the pyramidal tips and the front electrode (separated by a very thin layer of perovskite).

Although absorbing light and generating current beyond the perovskite's band gap have a positive impact on J_{sc} ; voltage losses, poor FF, and consequently low PCE are always accompanied with processing *p-i-n* PSC over textured n-type Si substrates. On the other hand, such issue is wafer-type dependent and processing *p-i-n* PSCs is expected to be compatible with p-type textured Si substrate (*p/p-i-n*). Indeed, as indicated by $J-V$ characteristics in Figure 6.14b, a *p-i-n* PSC processed over a p-type textured Si substrate exhibit normal behavior near J_{sc} . Furthermore, EQE data indicate no contribution in the current from the processing substrate (see Figure 6.14c).

Seeking a suitable alternative to increase J_{sc} without a drawback in PV performance of PSCs processed using the following stack: Textured Si (p-type)/ITO/evaporated 2PACz/perovskite/ C_{60} /SnO_x/IZO/Ag grid, we introduce anti-reflection coating onto the device stack. MgF₂ and LiF are common and widely used anti-reflection coatings in PSCs employing similar device stack.^{74,111} Introducing anti-reflection coating causes refractive index grading at air/IZO interface (the illumination side), results in reduced reflectance and enhanced transmittance.^{74,111,182} Indeed, introducing ~100 nm of MgF₂ onto our PSCs enhanced EQE (see Figure 6.14d) and increased the average J_{sc} from 19.2 mA/cm² in the reference stack to 20.6 mA/cm². Employing anti-reflection coating attributed to an average increase of ~1.4 mA/cm², in line with previously reported values in literature.^{74,111,182}

6.7.3 PV parameters and stability of PSCs processed over textured surfaces

After optimizing the back ITO to decrease its sheet resistance, defining the appropriate wafer type to block any negative impact from the substrate, and applying anti-reflection coating to mitigate optical losses, we investigate the PV performance of PSCs processed onto micrometer-sized pyramidal textured substrates using the device stack Textured Si (p-type)/ITO/HTL/perovskite/ C_{60} /SnO_x/IZO/Ag grid as shown in Figure 6.15a. We first introduce both the reference and developed stack before discussing the results to avoid confusion.

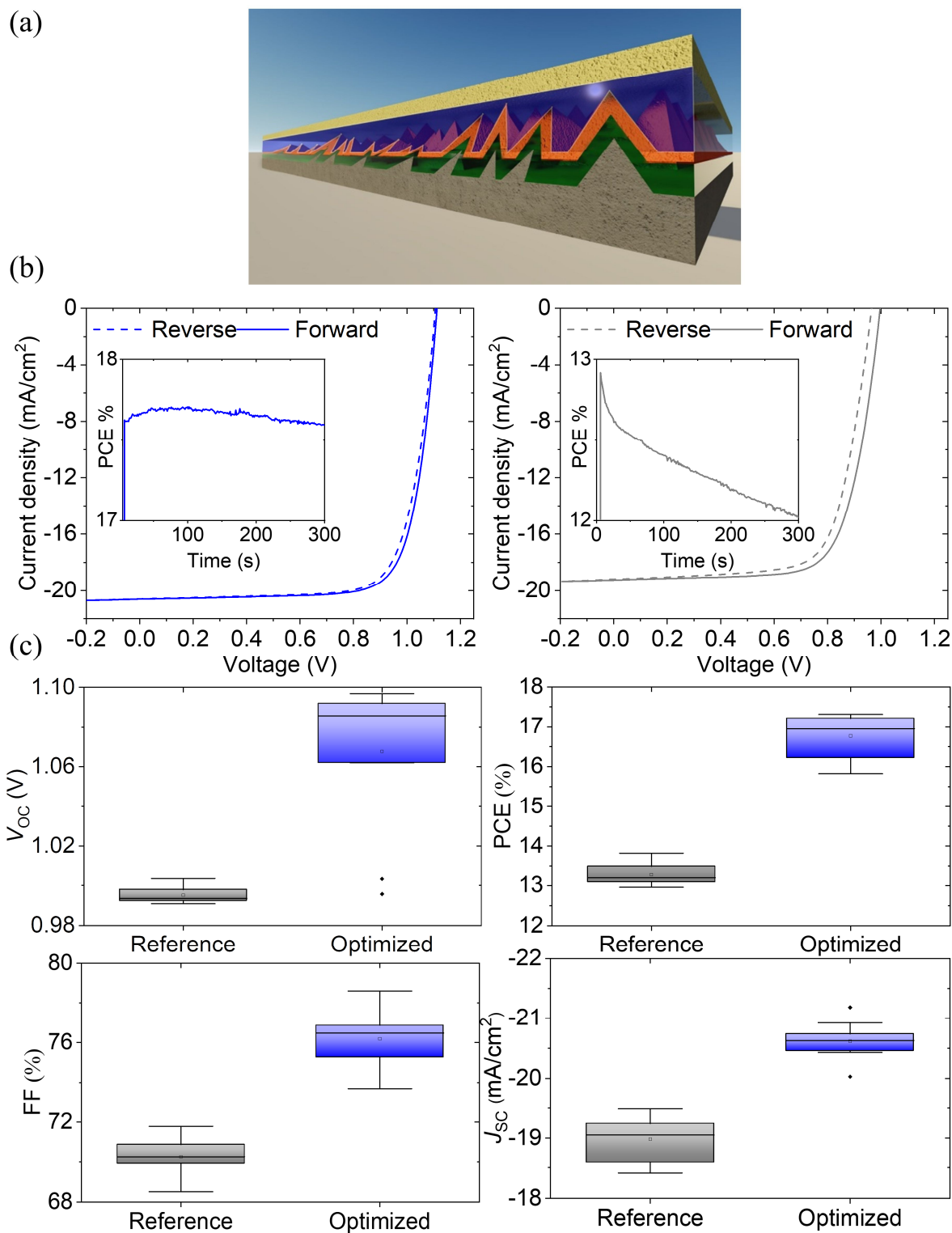


Figure 6.15. (a) Schematic diagram of semi-transparent PSC employing the following stack: Textured Si/patterned ITO/evaporated 2PACz/perovskite/ $\text{C}_{60}/\text{SnO}_x/\text{IZO}/\text{Ag}$ grid. (b) J - V characteristics and MPP tracking of the champion PSCs representing the developed (left) and reference (right) stack. The reference PSC exhibits huge hysteresis and poor short-term stability. (c) Corresponding statistical comparison of the PV parameters. The superiority of developed stack is indicated by the enhancement in the overall PV performance.

Reference stack: The textured Si wafer is p-type. ITO is ~ 135 nm deposited using the baseline recipe with a sheet resistance of $\sim 85 \Omega/\text{sq}$. HTL is a double-layer of NiO_x and

solution-processed 2PACz. The perovskite precursor solution is 1.6 M, with 10% excess PbI₂ and 20% DMSO, processed using early quenching. No surface passivation is employed between the perovskite and C₆₀. No anti-reflection coating is applied.

Developed stack: The textured Si wafer is p-type. ITO is ~135 nm with a sheet resistance of ~15 Ω/sq. HTL is evaporated 2PACz. The perovskite precursor solution is 1.6 M, with 15% excess PbI₂ and 35% DMSO, processed using late quenching. Surface passivation in between perovskite and C₆₀ is done by spin coating PEACl (2 mg/ml). 100 nm MgF₂ anti-reflection coating is thermally evaporated on top of IZO.

The best PSC representing the reference stack is suffering from low overall PV performance with a FF of 71.8%, a J_{SC} of 19.2 mA/cm², a V_{OC} of 0.998 V, and a PCE of 13.8% (see Figure 6.15b). In addition to its low PCE, the device suffers from a high HF (~12.6%) and exhibits poor long term stability. On the other hand, the champion device employing the developed stack is stable, with a negligible HF (3.4%), in addition to superiority in PV parameters with a FF of 76.5%, a J_{SC} of 20.6 mA/cm², a V_{OC} of 1.10 V, and a PCE of 17.3%.

Statistical distribution of PV parameters indicates the mean value of V_{OC} increases from 0.995 V in the reference stack to 1.072 V in the developed stack. Such clear superiority is attributed to the considered voltage losses mitigation strategies employed in the developed stack. As per our previous investigations in Chapter 5, utilizing evaporated 2PACz have shown superiority over the double-layer NiO_x/solution-processed 2PACz HTL in terms of suppressing non-radiative recombination at HTL/perovskite interface. In addition, processing perovskite thin films from a precursor solution that contains 15% excess PbI₂ as discussed in Section 6.4 results in higher V_{OC} as it compensates for the iodine deficiency consumed by the large surface area ITO in the textured surface case. In the same context, preparing the perovskite precursor solution using 35% DMSO as discussed in Section 6.5 results in better surface morphology of the perovskite thin film as a consequent of controlled surface wrinkles formation and enhances the quality of perovskite/ETL interface. Hence, non-radiative recombination is suppressed and higher V_{OC} is obtained. Finally, introducing surface passivation mitigates voltage losses at perovskite/ETL interface. V_{OC} values obtained from our developed stack over micrometer-sized textured surface are comparable to those of planar PSCs employing perovskite absorber layer with similar band gap.^{140,346–348}

Regarding J_{SC} , the mean values are 18.9 and 20.6 mA/cm² for the reference and developed stack, respectively. An increase of ~1.7 mA/cm² indicates that optical losses are mitigated by introducing anti-reflection coating as discussed earlier, consequently, the optical gains translate to an increase in J_{SC} . Concerning FF, we attribute the enhancement from 70.2% in the reference to 76.2% in the developed stack to two primary reasons. (1) The application of an optimized ITO film with its low sheet resistance as discussed in Section 6.7.1, enabled lower series resistance of the developed stack's devices, and consequently resulted in higher FF. (2) Processing perovskite thin film *via* late quenching as investigated in Section 6.2, results in perovskite thin film without voids in the valleys of the textured substrate and consequently, the perovskite thin film is in good contact with the adjacent HTL, which is necessary for efficient charge carrier extraction and high FF.

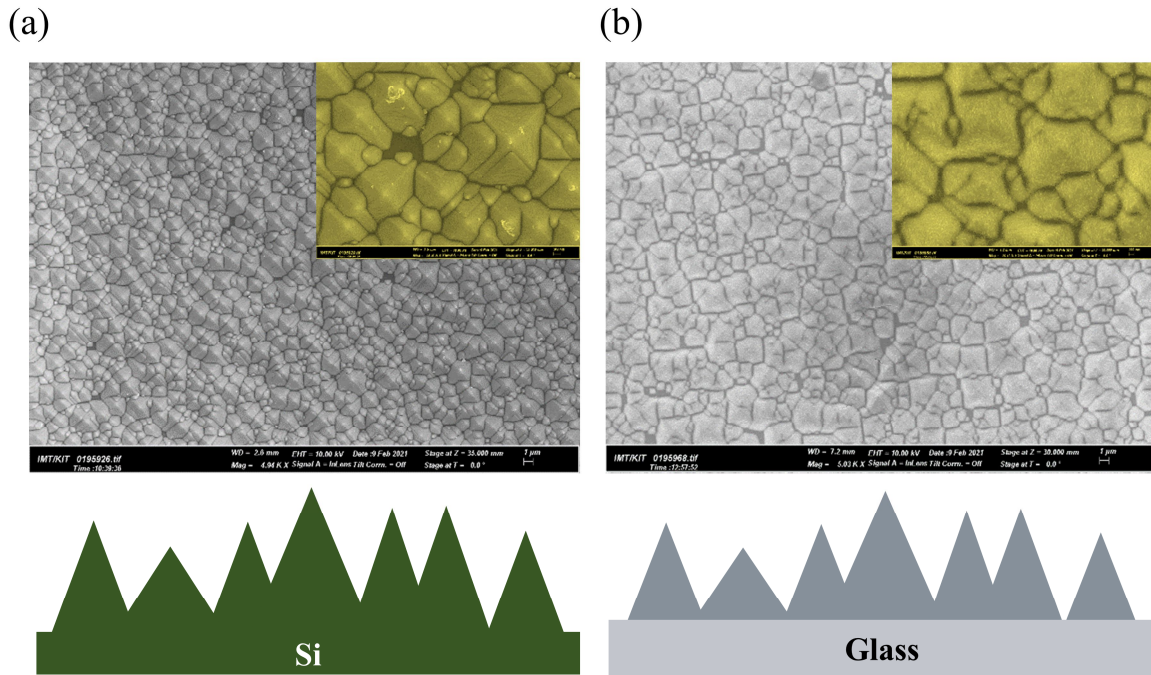


Figure 6.16. (a) and (b) Top-view SEM images of the textured Si substrate (a) and the corresponding replicated texture onto glass substrate (b), respectively. The replication process is done *via* nanoimprint lithography employing a PDMS master stamp and OrmoComp photoresist. Part of this figure is reproduced from ref.¹⁸⁰ with permission from the American Chemical Society.

6.8 Efficient light harvesting (textured vs planar PSCs)

Having voltage losses that comes along with processing perovskite thin films over micrometer-sized textures mitigated using the above discussed strategies has brought V_{OC} of PSCs employing textured surfaces forward to level up with their planar counterpart. In addition, considerably high FF (up to 78%), which is comparable or even slightly higher than thick planar PSCs has been achieved.^{193,201,349} Now we investigate the optical gains of processing perovskites over textured surfaces compared to planar.

6.8.1 Replicating the micrometer-sized textures onto glass substrates

The main advantage of processing PSCs over textured surfaces is efficient light harvesting as a result of reduced reflection losses and the light trapping effect. However, processing single-junction semi-transparent PSC onto a textured surface (the rear side), while illuminating the solar cell from the front side (which is planar IZO surface) will not shed light on the optical gains of processing PSCs over textured surfaces as most of the incident light will be absorbed in the perovskite layer before it reaches the rear side in both case (planar or texture). To enable a reliable comparison of the optical gains between PSCs processed over the micrometer-sized pyramidal textures and their planar counterparts, we utilize nanoimprint lithography to replicate the Si wafer textures onto glass substrates. Nanoimprint lithography is well known to produce high quality replica of nano- and microstructures.^{41,189} Light trapping *via* periodic nanostructures fabricated using nanoimprint lithography could be used for efficient light incoupling due to refractive index grading as has been demonstrated for single junction PSCs³⁴⁻³⁷ and Si solar cells.³⁸⁻⁴⁰ Recently, Tockhorn *et al.* have reported on enhanced quantum efficiency in PSCs processed

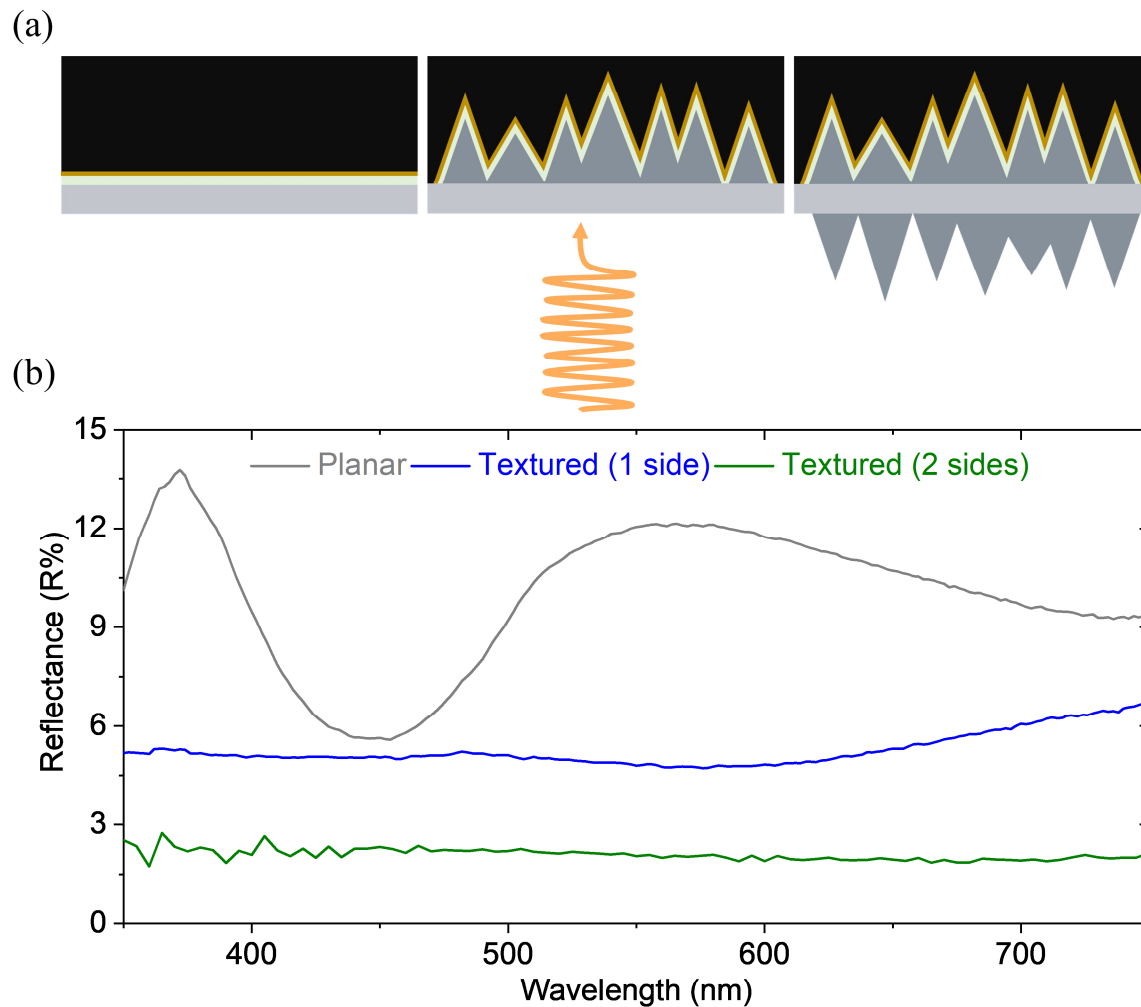


Figure 6.17. (a) Schematic illustration of incident light in standard testing condition. The half-stacks from left to right employ planar glass, one side replicated texture, and double-sided replicated texture substrates, respectively. (b) The corresponding normal incidence reflectance spectra of the three half-stacks. Half-stacks employing replicated textures exhibit lower reflection losses. Reproduced from ref.¹⁸⁰ with permission from the American Chemical Society.

over replicated periodic nanotextures. Using nanoimprint lithography, they replicated different types of textures (in height, width, and periodicity).³⁷ Fabricating PSCs over these textures enabled exceptional light harvesting and consequently increased J_{SC} by ~ 1 mA/cm². Efficient light harvesting and the consequent enhancement in J_{SC} enabled them to achieve the highest J_{SC}/J_{SQ} in all PSCs reported in literature so far, with 93.6% J_{SQ} (where 100% J_{SQ} is the theoretical maximum attainable current density for a certain band gap). Although using periodic nanotextures have shown efficient light harvesting, it is more compatible with laboratory scale rather than industrial standards due to high cost and mass production challenges, which is not the case in random pyramidal textures fabricated *via* wet etching.^{44,45}

Top-view SEM images of textured Si substrate and the replicated texture over glass substrate (see Figure 6.16), indicate that replication process is successful. We want to highlight that replication is performed using OrmoComp photoresist, which has a refractive index of ~ 1.5 (equivalent to glass),³⁵⁰ hence, a comparison between PSC fabricated on replicated textures and planar glass reference is feasible and trust worthy. In this case we are sure that any

optical gains correlate to light trapping caused by the textures, not due to a change in the photoresist's refractive index.

6.8.2 Reduced reflection losses and its impact on J_{sc}

Reflection in high efficiency planar tandem solar cells dominates the current density losses (up to 7 mA/cm²).²² To investigate the role that a textured surface plays in mitigating reflection losses, we deposit our optimized perovskite thin film over the replicated textured substrates (employing single and double-sided textures as indicated by the schematic diagram in Figure 6.17a) and compare the reflectance of the textured half-stacks to a planar counterpart. In standard testing conditions, where normal incidence is being considered, broadband reflectance spectra (see Figure 6.17b) highlights the superiority of the textured half-stacks in mitigating reflection losses. Textured half-stacks exhibit significantly lower reflectance over the entire spectral range of interest (from 350 nm to 750 nm) compared to the planar reference. While the reflectance spectrum of textured half-stacks indicates a remarkable antireflection behavior over the broadband spectrum, thin film interference patterns are dominating the reflectance spectra of the planar half-stack, resulting in higher reflection losses. The amplitude of the interference pattern is minima at roughly ~450 nm for the planar stack, where it approaches the reflectance of the textured counterpart. However, the amplitude increases over the rest of the entire spectrum leading to broadband reflection losses. For example, the reflectance of the planar half-stack is ~2.5 times higher than the textured half-stack at ~569 nm. Overall, AM1.5G weighted reflectance of the textured half-stack is 5.2%, which is way lower than the planar half-stack with 9.9%. Furthermore, applying a double-sided texture by replicating the texture to the air/glass interface as indicated by the schematic diagram in Figure 6.17a, reduces the broadband reflectance further. However, processing PSCs *via* spin coating over a double-sided texture is technically challenging and results in low fabrication yield. Furthermore, applying vacuum to the back side of the substrate during perovskite deposition over the spin coater results in air gap between the replicated texture and the glass substrate, which led to optical losses. In this regard, we continue our investigation by comparing planar stack to single-sided textured stack.

In addition to reduced reflection losses, the textured surface enhances light incoupling to the perovskite thin film due to efficient light trapping. Light trapping results in longer optical path length inside the perovskite absorber as indicated by the schematic diagram in Figure 6.18a.^{46,351} Having longer optical path length inside the perovskite absorber increases the near band gap absorption probability, which is considerably low due to the exponential tail of the absorption edge.^{46,351} Indeed, a comparison between the absorption spectra of planar and textured half-stacks (see Figure 6.18a), indicate enhanced absorption near the perovskite's band gap when processed over replicated textures.

To investigate the impact of optical gains corresponding to mitigated reflection losses on J_{sc} , we compare EQE of full device stacks, employing replicated texture and planar substrates. Reducing reflection losses implies that more light is being coupled to the whole PSC, however, photogenerated current is increased only when this light gets absorbed by the perovskite absorber layer, not by other functional layers (HTL and/or TCO). At a wavelength of 450 nm, where the planar reference exhibited a comparable reflectance value to that of the textured stack (see Figure 6.17b), EQE signals display almost the same value at this wavelength (see Figure 6.18b). In addition, the broadband reduced reflectance of the textured stack, results in broadband increase in the device's spectral response. Furthermore, the

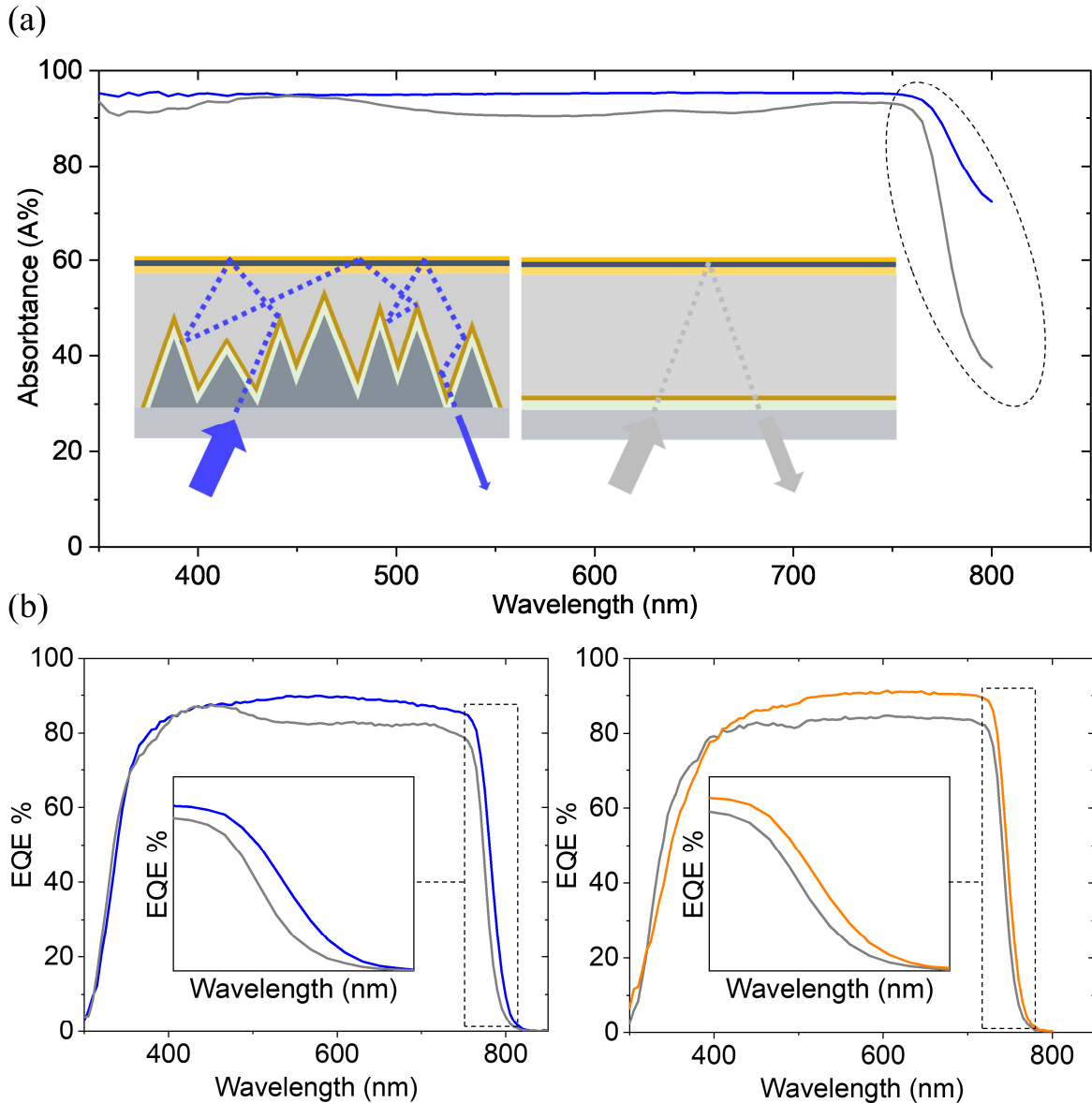


Figure 6.18. (a) Comparison of the absorption spectra for the full device stack employing replicated texture and planar reference. The textured surface enables longer optical path length compared to the planar reference due to efficient light trapping. Consequently, the textured stack exhibit broadband absorption enhancement. Furthermore, absorption near the band gap of the perovskite thin film processed onto the textured stack is enhanced. (b) EQE comparison of PSCs fabricated over planar and replicated texture substrates employing double-cation (left) and triple-cation (right) perovskite absorber layers. The EQE comparison indicate the superiority of PSCs processed onto replicated textures, irrespective of perovskite composition or band gap. The insets indicate enhanced EQE near the band gap for the replicated textures case. Part of this figure is reproduced from ref.¹⁸⁰ with permission from the American Chemical Society.

increased absorption probability near the band gap of the perovskite absorber, which corresponds to light trapping effect of the textured surface, is also present in the device's EQE (see Figure 6.18b). It emphasizes that reducing reflection losses by employing textured stack led to efficient light incoupling to the absorber layer, resulting in optical gains, and consequently higher J_{SC} . Interestingly, integrated J_{SC} of the champion PSC processed over the textured stack is 22.7 mA/cm^2 compared to 21.1 mA/cm^2 for the planar counterpart. This increase corresponds to $\sim 1.6 \text{ mA/cm}^2$ which is higher than the gains reported by Tockhorn *et al.* employing replicated periodic nanotextures.³⁷ As 26.04 mA/cm^2 is the maximum

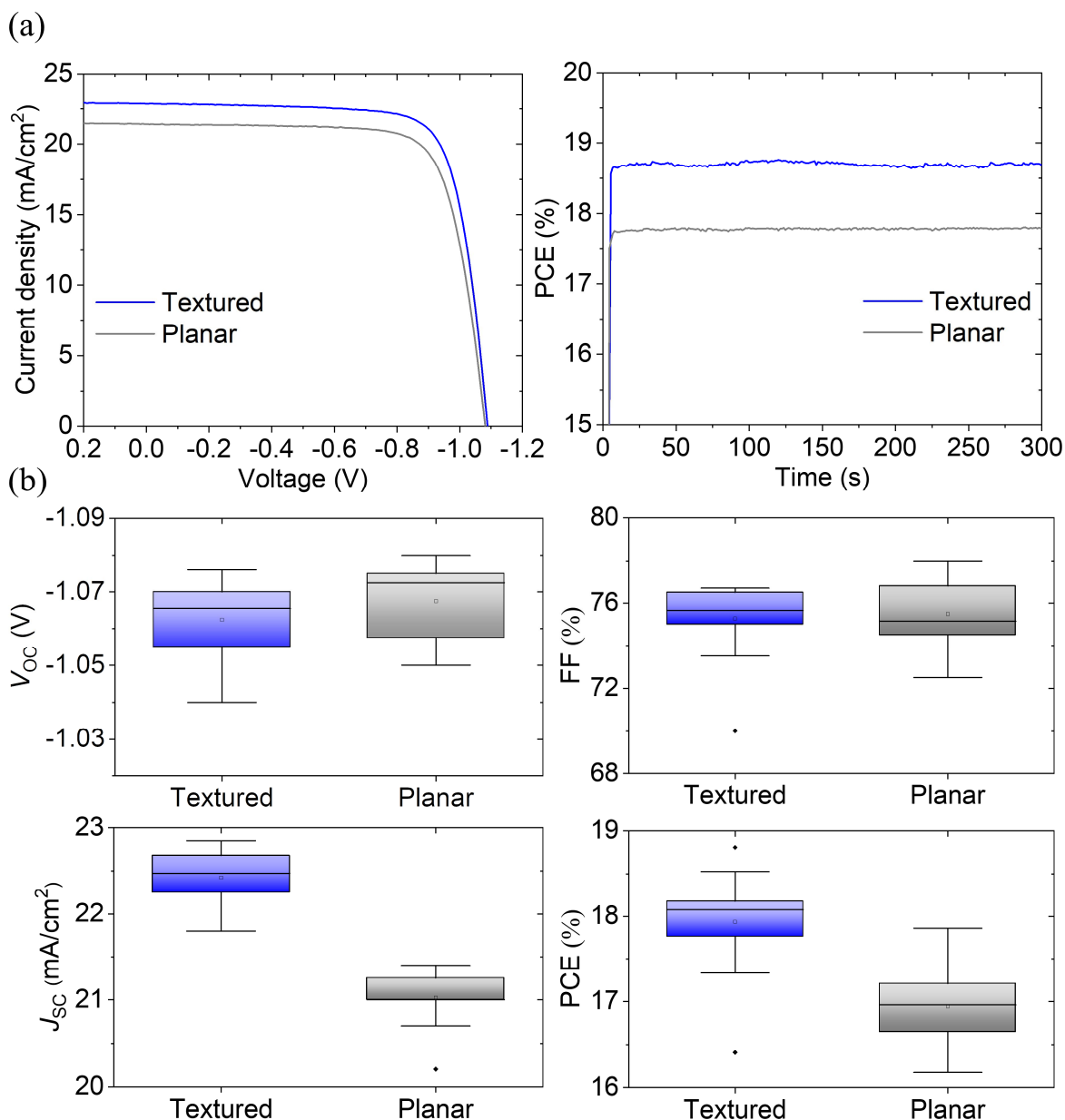


Figure 6.19. (a) J - V characteristics and MPP tracking of the champion PSCs processed over replicated textures and planar reference. (b) Corresponding statistical comparison of the PV parameters. The textured stack indicates superiority in J_{SC} due to efficient light harvesting. Having comparable FF and V_{OC} , make the enhancement in J_{SC} translate to enhancement in PCE for PSCs processed over replicated textures.

attainable current density (J_{SQ}) for our perovskite's band gap, our approach is not only meeting the industrial standard, it is rather achieving a J_{SC}/J_{SQ} ratio of $\sim 87.3\%$, which makes it among one of the highest reported values to date.³⁷

To shed light on the consistency of efficient light harvesting when utilizing micrometer-sized randomly-distributed pyramidal textures, irrespective of perovskite absorber type and/or band gap, we replace the double-cation perovskite that has a band gap of ~ 1.58 eV with a triple-cation perovskite composition and a corresponding band gap of 1.68 eV. As expected, the EQE comparison (see Figure 6.18b) between planar and textured stacks indicate the superiority of the textured stack with a broadband enhancement, and increased response near the band gap, in line with the double-cation perovskite.

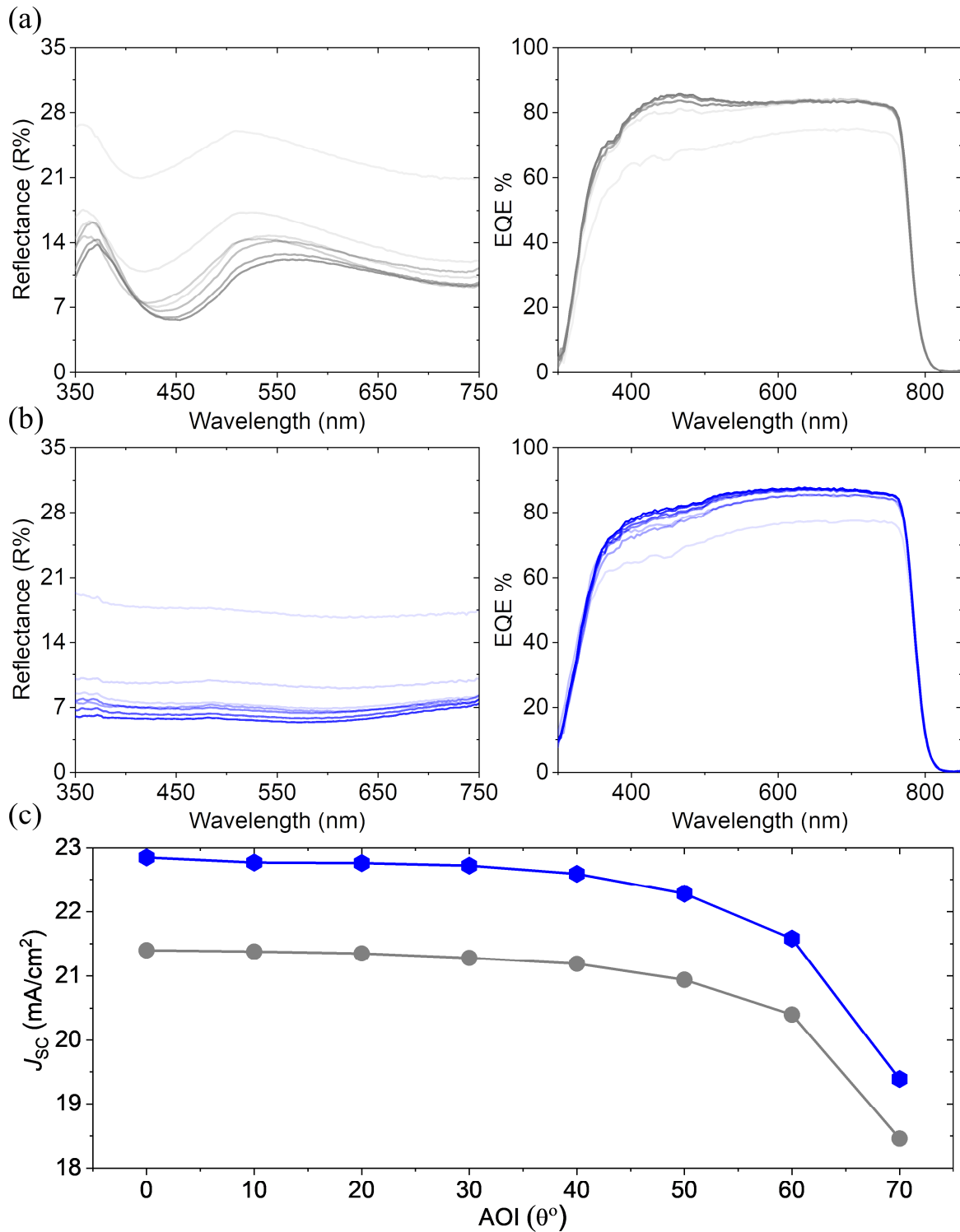


Figure 6.20. (a) Reflection spectra of PSCs processed onto planar glass substrates at wide range of angles of incidence (AOI) (from 10° to 70° in 10° steps) (left) and the corresponding EQE (right). (b) Reflection spectra of PSCs processed onto replicated textures at the same range of AOI in (a) (left) and the corresponding EQE (right). (c) Comparison of the corresponding integrated J_{sc} at each AOI. PSCs processed onto replicated textures are superior at standard testing condition as well as realistic irradiation conditions. Part of this figure is reproduced from ref.¹⁸⁰ with permission from the American Chemical Society.

6.8.3 PV performance (textured vs planar)

Having FF and V_{OC} of PSCs processed over textured surfaces comparable to that of planar PSCs (by employing the previously discussed and in-depth investigated optimization processes), enables optical gains in terms of the amplified J_{SC} to directly reflect on the textured device's PCE. Starting with the reference planar stack, Figure 6.19a displays J - V characteristics of the champion planar PSC, with a J_{SC} of 21.5 mA/cm², a FF of 76.4%, a V_{OC} of 1.083 V, and a PCE of 17.8%. The planar reference performs at a stable 17.8% under MPP tracking. Corresponding mean values are 21 mA/cm², 75.4%, 1.067 V, and 16.9%, respectively (see Figure 6.19b). Interestingly, the champion device employing the textured stack is superior in PV performance with a PCE of 18.8% (18.7% stabilized under MPP tracking), a J_{SC} of 22.9 mA/cm², a V_{OC} of 1.091 V, and a FF of 75.2%. The corresponding mean values for PCE, J_{SC} , V_{OC} , and FF are 17.9%, 22.4 mA/cm², 1.062 V, and 75.2%, respectively. As indicated by the statistical distribution comparison of the PV parameters, the mean value of FF and V_{OC} is comparable in the textured and planar stack, indicating that the superiority in PCE of PSCs employing the textured stack is stemming from the optical gains and the consequent improved J_{SC} .

6.8.4 Reflection losses at variable angles of incidence

Under realistic irradiation conditions, the incident light is rarely normal to the solar cell's plane, which leads to considerable angular reflection losses for some device architectures.^{352,353} Having demonstrated efficient light harvesting in thick PSC processed over micrometer-sized industry-applicable replicated textures at standard testing conditions (i.e. normal incidence), we investigate the angular dependence of reflectance and its impact on J_{SC} . We note that replicated textures facilitate light incoupling not only at standard testing conditions, but also for any given angle of incidence (AOI) $\theta > 0^\circ$. The textured surface forces incident light to impinge multiple times on the surface of the replicated texture/perovskite absorber and thereby minimizes reflection losses.^{33,186,189} In this regard, PSCs fabricated over the replicated textured surface are expected to tolerate a large range of incident angles. Indeed, a comparison of reflectance spectra (see Figure 6.20) between PSCs processed onto replicated textures and their planar counterpart for wide range of AOI (from 10° to 70° in 10° steps), indicates the superiority of the textured stack in suppressing reflection losses for all AOI. For the highest AOI (70°), the interference pattern of the planar PSC is blue shifted with a maxima at ~510 nm and a corresponding reflectance value of ~26%, meanwhile, PSC processed onto the textured stack exhibits reflection losses of only ~17.4% at the same wavelength, indicating the superiority of the textured stack by efficient light incoupling at large AOI.

Finally, yet importantly, as a consequence of the suppressed reflection losses that the textured stack exhibited, angle dependence of current generation in the textured PSC outperforms the planar counterpart for all AOI as indicated by EQE data in Figure 6.20, in full agreement with the angle dependent reflectance data.¹⁸⁶ Integrated J_{SC} values for various AOI is shown in Figure 6.20c, indicating that improved light harvesting characteristics of PSC processed over textured surface is superior in standard testing conditions as well realistic irradiation scenarios and real field application.^{354,355}

6.9 Summary

In this chapter, we presented a comprehensive study on the reasons behind various voltage losses in solution-processed perovskite thin films processed over micrometer-sized textured Si substrates. We quantified these losses using PLQY and compared the corresponding implied V_{OC} to the external V_{OC} of full device stacks, which exhibited a comparable trend in each case. With in-depth microstructural, compositional, and morphological analysis, we identified potential reasons behind these losses and offered one or more strategies to tackle them. Choosing optimum deposition parameters by adjusting the anti-solvent quenching time (late instead of early quenching) eliminates formation of voids near the pyramid valleys, resulting in optimum contact between the bottom side of perovskite thin film and the adjacent HTL, suppressing non-radiative recombination (i.e., $\sim 10\text{-}15$ mV higher V_{OC}) and enabling efficient charge carrier extraction (i.e., $\sim 8.5\%$ higher FF). Optimizing perovskite precursor solution concentration (1.6 instead of 1.4 M), enabled full surface coverage, and prevented surface micro-cracks formation around the pyramidal tips, consequently, non-radiative recombination at perovskite/ETL is suppressed, which attributed to average gains of ~ 30 mV. Applying a solvent engineering strategy by varying DMSO volume ratio has controlled the formation of strain-related surface wrinkles, decreased the perovskite thin film surface roughness, enhanced the quality of perovskite/ETL interface further, and consequently resulted in higher V_{OC} with average gains up to ~ 20 mV. Utilizing GDOES, EDX, and ToF-SIMS measurements shed light on the nature of chemical reactions between perovskite with the adjacent HTL and TCO, which resulted in iodine rich interface and a consequent PbI_2 deficiency in the bulk of perovskite thin film processed over textured surface as indicated by XRD measurements. By optimizing excess PbI_2 , we compensated for the deficiency in the bulk and gained an average of ~ 55 mV compared to perovskite films processed using a stoichiometric solution. In addition, employing a passivation interlayer in between perovskite and ETL using different surface passivation methods, mitigated voltage losses in the defective perovskite/ C_{60} interface, resulted in further V_{OC} gains ($\sim 30\text{-}60$ mV). Applying the developed voltage losses mitigation strategies together, enabled fabricating PSCs over micrometer-sized textures with considerably high V_{OC} (~ 1.12 V) which is comparable or even slightly outperforming planar PSCs reported in literature employing similar perovskite composition and/or band gap.

After enhancing V_{OC} of PSCs on textured surfaces *via* applying the developed voltage losses mitigation strategies, we optimized the back ITO. Starting with the baseline recipe, which resulted in high sheet resistance ITO films ($85 \Omega/\text{sq}$) over textured surfaces and consequently high series resistance in PSCs employing them, we performed a series of sputtering runs to achieve better quality. The optimized recipe (using 250 instead of 50 W at 300°C instead of room temperature), enabled higher quality ITO films with a corresponding sheet resistance of $\sim 15 \Omega/\text{sq}$. PSCs processed over textured surface employing the optimized ITO exhibited lower series resistance and a consequent enhancement in FF was achieved. Furthermore, we studied the impact of Si wafer type on PV performance as well as spectral response by comparing PSCs processed employing p and n-type Si wafers. Absorbing beyond the band gap of perovskite absorber was the limiting factor for n-type wafers (unlike p-type) and caused a drawback in the overall PV performance, which indicated their incompatibility with *p-i-n* PSCs.

Having V_{OC} and FF of PSCs processed over textured surfaces comparable to their planar counterpart enabled us to investigate the optical gains of processing perovskites over textured surface and their impact on PCE. For this reason, we replicated the micrometer-sized textures onto glass substrates using nanoimprint lithography and investigated their efficient light harvesting compared to planar references. PSCs processed over replicated textures exhibited lower reflection losses compared to their planar counterparts with AM1.5G weighted reflectance values of 5.2% and 9.9%, respectively. Furthermore, the textured stack displayed absorption enhancement near the perovskite's band gap, which indicated their light trapping behavior. Mitigated reflection losses and increased absorption probability of PSCs processed over replicated textures resulted in broadband enhancement in the device's spectral response compared to the planar reference. Integrated J_{SC} emphasized the superiority of the textured stack in light harvesting with 22.7 mA/cm² compared to 21.1 mA/cm² for the planar counterpart, which makes it one of the highest reported values in literature for the corresponding band gap, in addition to continued outperformance under realistic irradiation conditions.

7. Conclusion and Outlook

In recent years, single-junction perovskite solar cells (PSCs) encountered massive progress in power conversion efficiency (PCE) with a current record of 25.7%.^{8,356} Seeking a roadmap to overcome the theoretical limit of a single-junction solar cell (~33.7%), the monolithic two-terminal (2T) perovskite/silicon (Si) tandem architecture presented itself as a strong candidate with a current PCE record of 32.5%.⁸ Employing textured Si sub-cells in the 2T architecture is more cost efficient compared to front planar polished counterparts, which makes them more favorable from the industrial perspective.^{190,192} In addition to compatibility with the industrial standards, employing a textured bottom sub-cell mitigates the reflection losses due to light trapping effect, which consequently results in efficient light harvesting.^{46–49} However, while typical perovskite film thickness ranges from ~350-500 nm, which is not sufficient to cover a micrometer-sized textured surface, increasing the perovskite absorber layer thickness is accompanied with poor optoelectronic properties of the absorber.

Therefore, in Chapter 4 we investigated the perovskite precursor solution molarity of the double-cation ($\text{Cs}_{0.17}\text{FA}_{0.83}\text{PbI}_{2.75}\text{Br}_{0.25}$) that enables optimal surface coverage over micrometer-sized textured surface. Afterwards, we tackled the common drawbacks of such thick perovskite absorbers by enhancing their optoelectronic quality. Furthermore, we investigated the consequent impact on the photovoltaic (PV) performance of thick planar PSCs. Our investigations indicated that increasing the perovskite precursor solution molarity from 1.0 M to 1.6 M, together with optimizing the deposition parameters, resulted in ~1 μm thick absorber over a planar surface, which was sufficient to provide optimal surface coverage over the textured surface with no remarkable signs of defects or pinholes. Due to the considerable increase in perovskite absorber thickness (~3 times thicker than the baseline recipe), which is comparable or even larger than the charge carrier diffusion length, planar PSCs employing such thick absorbers suffered very low V_{OC} and FF as a result of inefficient charge carrier extraction. In addition to their inferior PV performance, these thick planar PSCs exhibited huge hysteresis with hysteresis factor (HF) > 20%.

To overcome this challenge and enhance the photophysical properties of such thick absorbers and thereby the PV performance of PSCs employing them, we employed ~8 mg/ml urea into the highly concentrated perovskite precursor solution. As urea plays a key role in crystallization dynamics, thick perovskite films employing urea exhibited much larger grain size compared to their reference counterparts (~2.3 times larger). Such increase in grain size inherently resulted in less grain boundaries and thereby lower trap density. Consequently,

thick perovskite absorbers employing urea exhibited longer charge carrier lifetime compared to the reference. Therefore, PSCs employing them were superior in charge carrier extraction and FF (~10% higher than the reference). Furthermore, reducing trap density together with the role that urea plays in passivating grain boundaries, suppressed non-radiative recombination and thereby enabled high V_{OC} (~70 mV higher than the reference). In addition, efficient charge carrier extraction together with improved crystallinity resulted in J_{SC} gains (~1 mA/cm² higher than the reference). The remarkable improvement in these individual parameters added up to pronounced superiority in PCE (~4% absolute higher), stability under MPP tracking, and low hysteresis.

As a textured surface typically exhibits larger surface area compared to a planar counterpart, identifying a proper hole transport layer (HTL) is of a key role to suppress non-radiative recombination at the HTL/perovskite interface. Furthermore, most of the high quality HTLs reported in literature, which exhibit low parasitic absorption and enable high quality HTL/perovskite interface are solution-processed, which makes it challenging to conformally coat a textured surface and thereby result in low fabrication yield. Therefore, we developed a vacuum-deposition method of self-assembled monolayers (SAMs), which was compatible with textured surfaces and provided a nearly lossless interface as discussed in Chapter 5. Utilizing X-ray photoelectron spectroscopy and Fourier-transformed infrared spectroscopy indicated that evaporated SAMs did not exhibit any signs of chemical change or degradation upon evaporation. Furthermore, the data indicated the presence of monolayer signature in evaporated SAM-HTLs at the indium tin oxide (ITO) interface independent of final film thickness, which is essential for fabricating efficient PSCs. In addition, contact angle measurements indicated that evaporated SAM-HTLs exhibited clear trends of improved wettability as emphasized by their low contact angles for various liquids compared to their solution-processed counterparts, which resulted in fabricating PSCs with ~100% fabrication yield. Such improvement in evaporated SAM-HTLs surface wettability did not come on the expense of surface morphology or crystal structure of the grown perovskite thin film when investigated by morphological and microstructural analysis.

Photoluminescence quantum yield (PLQY) and time resolved photoluminescence spectroscopy measurements indicated that the quality of the evaporated SAM-HTLs/perovskite interface is maintained or even slightly improved compared to their solution-processed counterparts. Furthermore, we demonstrated that high quality evaporated SAM-HTLs are uniformly deposited over micrometer-sized pyramidal textures, which was challenging to obtain by solution-processing SAMs and has previously required an additional vacuum-deposited NiO_x layer to ensure conformal coating and prevent detrimental shunting paths. In this regard, half-stacks employing evaporated SAM-HTLs exhibited an improved implied V_{OC} compared to NiO_x layers from 1.145 V to 1.213 V. An improvement of ~68 mV indicates the superiority of evaporated SAMs.

Having an efficient thick perovskite absorber that assures optimal surface coverage of the micrometer-sized pyramidal texture, together with a conformal and nearly lossless HTL, prevented detrimental shunting path and suppressed non-radiative recombination at the HTL/perovskite interface. However, processing perovskites over textured surfaces is accompanied with various voltage losses mechanisms due to the processing surface complexity, therefore, the PV performance of PSCs processed over textured surfaces was

lagging behind their planar surface counterparts. To tackle this problem, we quantified these losses by employing PLQY measurements and investigated the potential reasons behind these losses *via* in-depth morphological, microstructural, and compositional analysis in Chapter 6. Furthermore, we applied voltage losses mitigation strategies including interfacial engineering, solvent engineering, surface passivation, processing parameters optimization, precursor molarity and stoichiometry optimization. Applying these voltage losses mitigation strategies enabled fabricating PSCs over micrometer-sized textured substrates with a comparable V_{OC} to that of the planar reference. Having pushed the V_{OC} of PSCs processed over textures to match the planar PSCs, we investigated the optical gains accompanied with processing over textured surfaces. PSCs processed over replicated textures (*via* nanoimprint lithography) exhibited lower reflection losses compared to their planar counterparts with AM1.5G weighted reflectance values of 5.2% and 9.9%, respectively. Furthermore, due to light trapping that a textured surface exhibits, the textured stack displayed absorption enhancement near the perovskite's band gap. Mitigated reflection losses and increased absorption probability of PSCs processed over replicated textures resulted in broadband enhancement in the device's spectral response compared to the planar reference. Integrated J_{SC} emphasized the superiority of the textured stack in light harvesting with 22.7 mA/cm² (compared to 21.1 mA/cm² for the planar counterpart) with a 87.3% J_{SQ} , which makes it one of the highest reported values in literature. In addition, PSCs processed over textured surface displayed continued outperformance under realistic irradiation conditions.

Further light management strategies

As discussed in Chapter 6, introducing anti-reflection coatings at the air/indium zinc oxide (IZO) interface mitigates the reflection losses due to refractive index grading. However, parasitic absorption losses induced by the transparent conductive oxides (TCOs) are quite remarkable. In this regard, replacing IZO with less absorptive TCOs such as hydrogenated indium oxide (IO:H) would be beneficial in mitigating optical losses, particularly the latter has shown higher transmission in visible and near infrared spectral range compared to IZO and ITO.^{181,183,184}

Seeking efficient light harvesting in four-terminal perovskite/Si tandems, Hossain *et al.* have introduced nanostructured front ITO electrodes using polystyrene nanospheres.¹⁷⁹ The nanotextured electrodes enabled ~7% higher transmission and a consequent increase in J_{SC} with ~2.9 mA/cm². Unfortunately, the gains in J_{SC} did not have a remarkable impact on PCE because of the accompanied losses in V_{OC} (due to high surface roughness of the resultant perovskite thin film) and FF (due to increased sheet resistance of the nanotextured ITO). However, applying such approach in monolithic tandems employing planar Si sub-cells, by nanotexturing the recombination junction might have a positive impact in terms of light harvesting without encountering the accompanied disadvantages (considering the texture height of the recombination junction is much lower than the front electrode, which can be easily covered by a thin perovskite layer). First trials of nanotexturing a thin ITO layer over planar Si substrates, resulted in a remarkable reduction in reflection losses compared to the planar reference as indicated in Figure 7.1a. Further optimizations considering different nanospheres size, TCO type, TCO thickness, etc. can reduce the reflection further toward that of the micrometer-sized pyramidal textures. In addition, the addressed nanotexturing

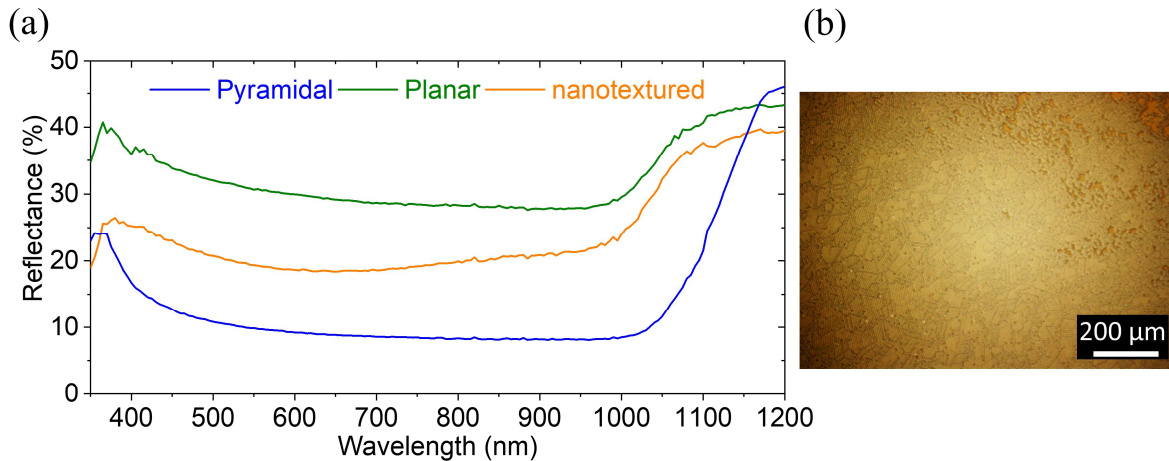


Figure 7.1. (a) Reflectance spectra of micrometer-sized pyramidal textured silicon (Si) substrate coated with 15 nm indium tin oxide (ITO), planar polished Si substrate coated with 15 nm ITO, and planar polished Si substrate with nanotextured ITO. (b) Optical microscope image of inkjet printed polystyrene nanospheres indicate their homogeneity.

method is scalable, which is necessary for industrial applications. First trials of nanospheres inkjet printing (instead of spin coating) have indicated a compact and uniform distribution of the nanospheres over the sample's surface as shown in Figure 7.1b.

Surface passivation

As discussed in Chapter 6, the perovskite/ C_{60} interface is already defective in planar *p-i-n* PSCs, which makes it the dominant interface in terms of non-radiative recombination losses. These voltage losses are even higher when processing PSCs over textured surface due to the increased surface roughness of the resultant perovskite film. Therefore, the impact of introducing surface passivation layers in between the perovskite and C_{60} resulted in a remarkable V_{OC} gains. In the same context and in addition to solution-processed PEACl and evaporated LiF passivation layers introduced in Chapter 6, Liu *et al.* have reported recently on employing ~ 1 nm of MgF_2 passivation layer for the first time.²⁵¹ The developed passivation scheme have shown an outstanding performance in terms of voltage losses mitigation at the perovskite/ C_{60} interface of monolithic tandems employing textured Si sub-cell. Furthermore, it overcomes the ion migration problem accompanied with LiF passivation layers that result in poor long-term stability. In this regard, devices employing a MgF_2 passivation layer retained $\sim 95\%$ of its initial PCE after 1000 h.

Lamination

Recently, Roger *et al.* reported on a novel lamination approach for fabricating monolithic perovskite/Si tandems with PCE $> 20\%$.¹⁰⁷ In their work, they highlighted that laminated perovskite absorbers *via* hot pressing exhibited a drastic improve in their surface morphology. Larger grain size and reduced surface roughness of laminated perovskite films resulted in PSCs with improved PV performance in addition to long-term thermal stability at 80 °C for 100 h. In this regard, laminating perovskite absorbers onto textured surfaces could outperform the standard sequential layer deposition methods. First results of laminated double-cation perovskite absorber over micrometer-sized textured surfaces (similar to what has been reported in this thesis) shed light on the great potential lamination could contribute in pushing the technology further. As displayed by top-view SEM images in Figure 7.2a and

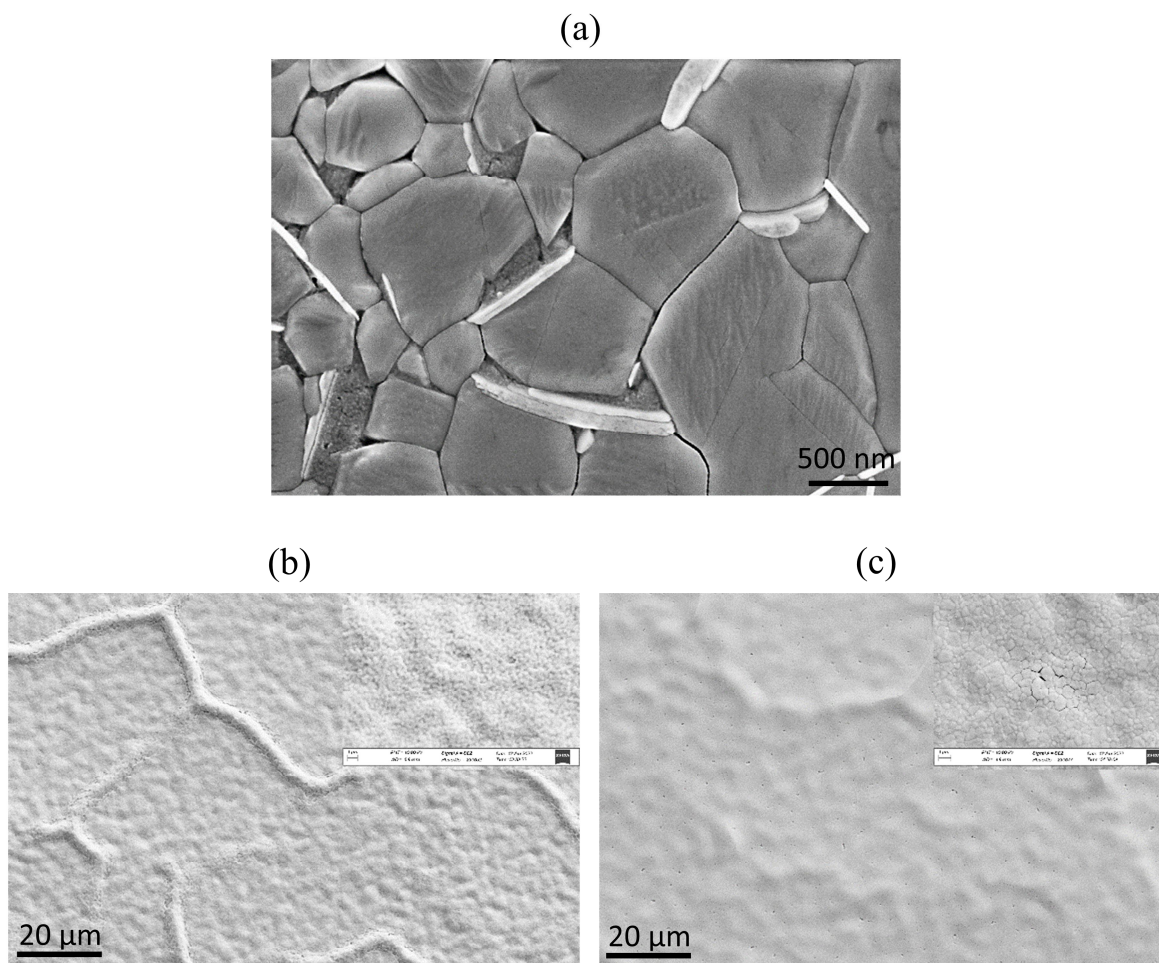


Figure 7.2. (a) Top-view scanning electron microscope (SEM) image of laminated perovskite absorber over micrometer-sized pyramidal texture. (b) and (c) Top-view SEM images of spin-coated perovskite absorbers over micrometer-sized textured substrates before (b) and after hot pressing (c).

b, laminated perovskite absorber exhibits larger grains and remarkably smoother surface compared to the sequential layer deposited counterpart.

As discussed in Chapter 6, solvent engineering together with optimal surface coverage reduce the resultant perovskite film roughness, however, a RMS roughness of ~ 50 nm in best-case scenario is still remarkably high and have a negative impact on the perovskite/ETL interface. In this regard, hot pressing a sequential layer deposited perovskite film over a textured surface resulted in a smoother surface (see Figure 7.2c), indicating that the technique could be helpful to mitigate voltage losses further.

Appendix

Table A5.1. Comparison of the photoluminescence quantum yield (PLQY), implied V_{OC} , ideality factor (n_{id}), and minority charge carrier lifetime (τ) of half-stacks employing solution-processed and evaporated SAM-HTLs.

Material	Deposition	t (nm)	PLQY(%)	V_{OC_imp} (V)	n_{id}	τ (ns)
2PACz	Solution-processed	~3	1.26	1.253	1.50	435
	Evaporated	2	0.89	1.245	1.58	500
		4	1.0	1.247	1.57	546
		6	1.54	1.259	1.48	474
		8	0.94	1.246	1.55	493
		20	1.13	1.249	1.56	503
MeO-2PACz	Solution-processed	~3	0.33	1.219	1.79	83
	Evaporated	2	0.01	1.178	1.7	72
		4	0.01	1.180	1.7	69
		6	0.35	1.220	1.73	84
		8	0.22	1.198	1.66	81
Me-4PACz	Solution-processed	~3	1.60	1.25	1.53	568
	Evaporated	2	0.81	1.234	1.51	540
		4	1.44	1.250	1.51	519
		6	2.04	1.260	1.48	585
		8	1.79	1.256	1.50	573

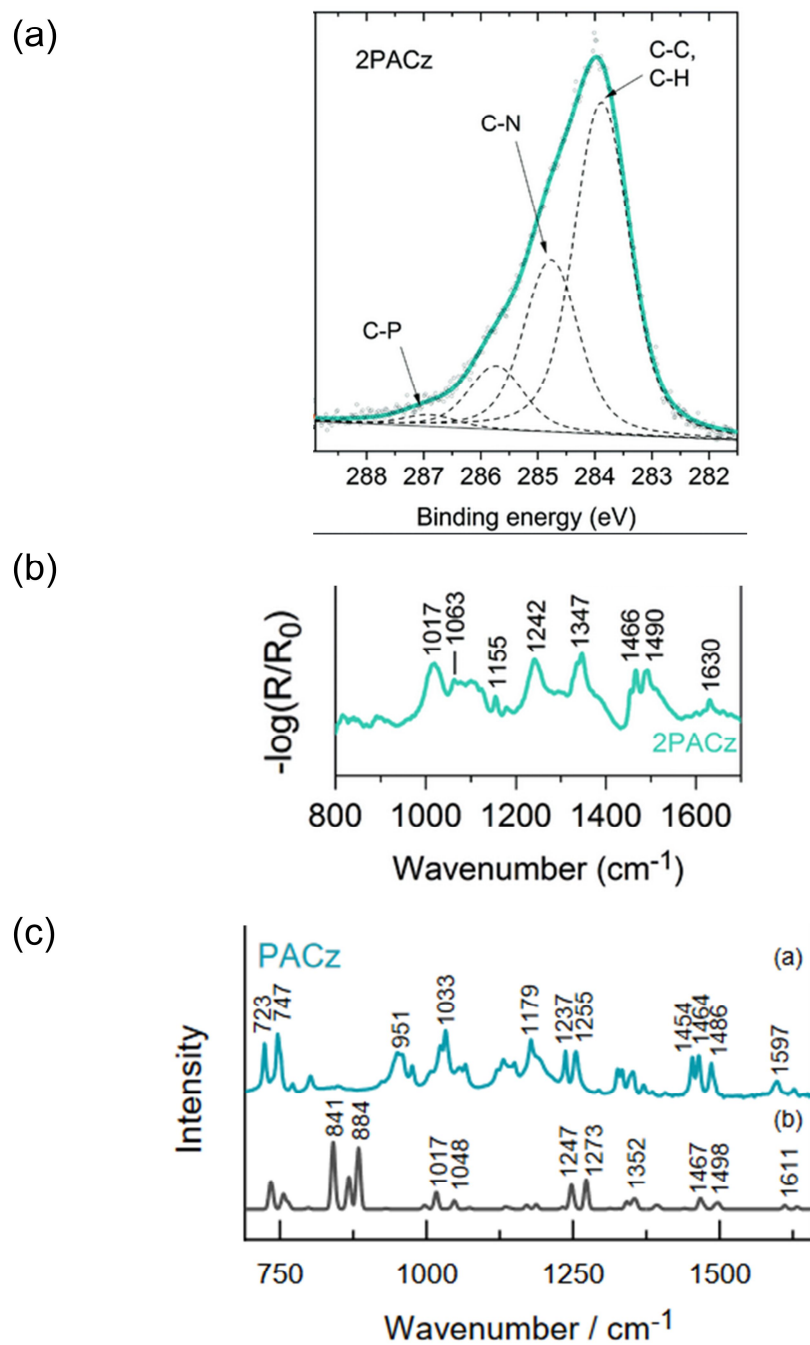


Figure A5.1. (a) X-ray photoelectron spectrum for the C 1s energy region of solution-processed 2PACz. (b) Reflection-absorption infrared spectrum of solution-processed 2PACz. (c) Fourier-transformed infrared spectrum of 2PACz powder. The data are reported and adopted from ref.¹¹⁰ with a permission from the Royal Society of Chemistry.

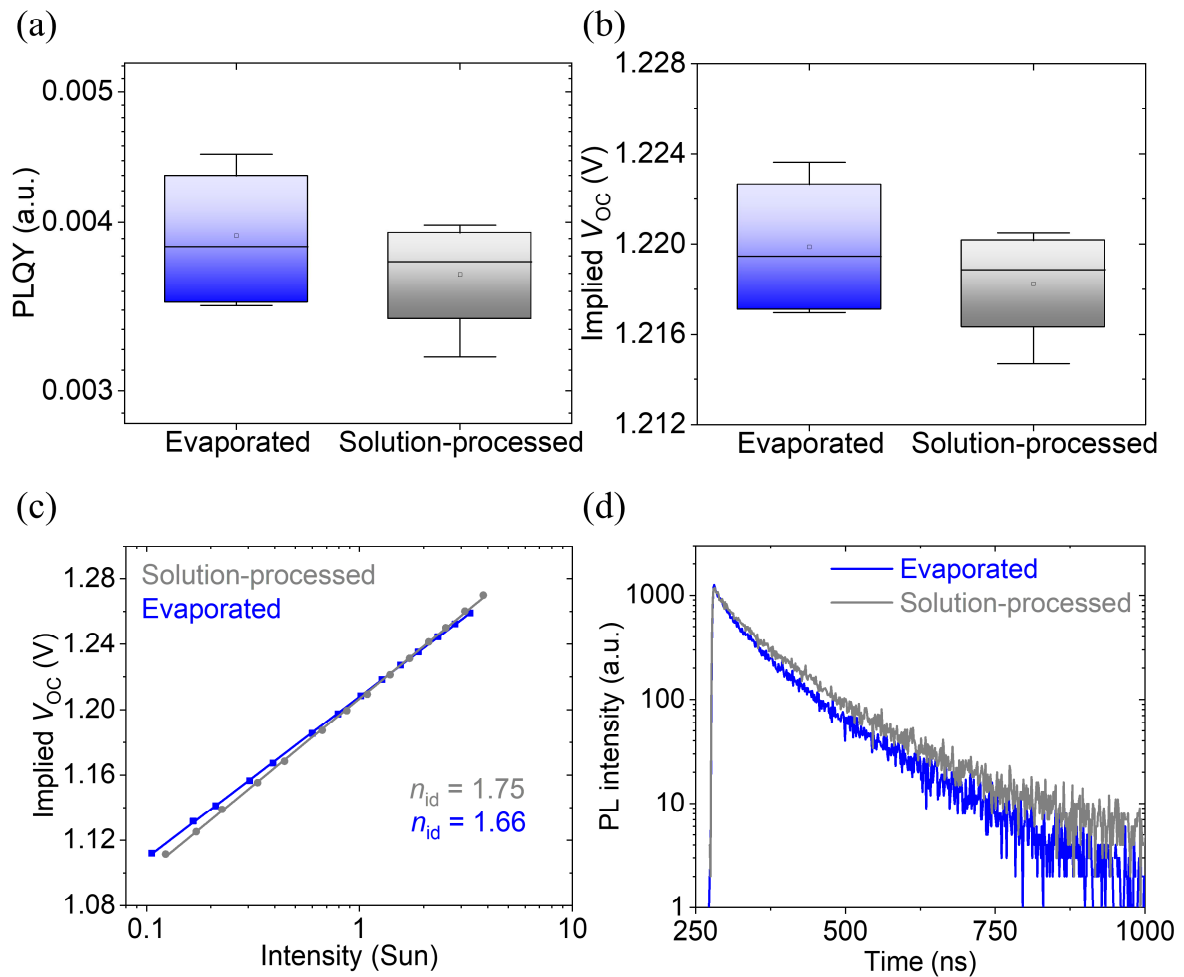


Figure A5.2. (a) Photoluminescence quantum yield (PLQY) comparison of the half-stacks ITO/hole transport layer (HTL)/perovskite, employing solution-processed and evaporated MeO-2PACz. (b) The corresponding implied open-circuit voltage (V_{OC}). (c) Ideality factor (n_{id}) extracted from a fit to the intensity-dependent implied V_{OC} . (d) Time resolved photoluminescence (TRPL) comparison of the corresponding half-stacks. The TRPL data indicate a comparable decay trend for solution-processed and evaporated MeO-2PACz. Reproduced from ref.⁶⁰ with permission from Wiley.

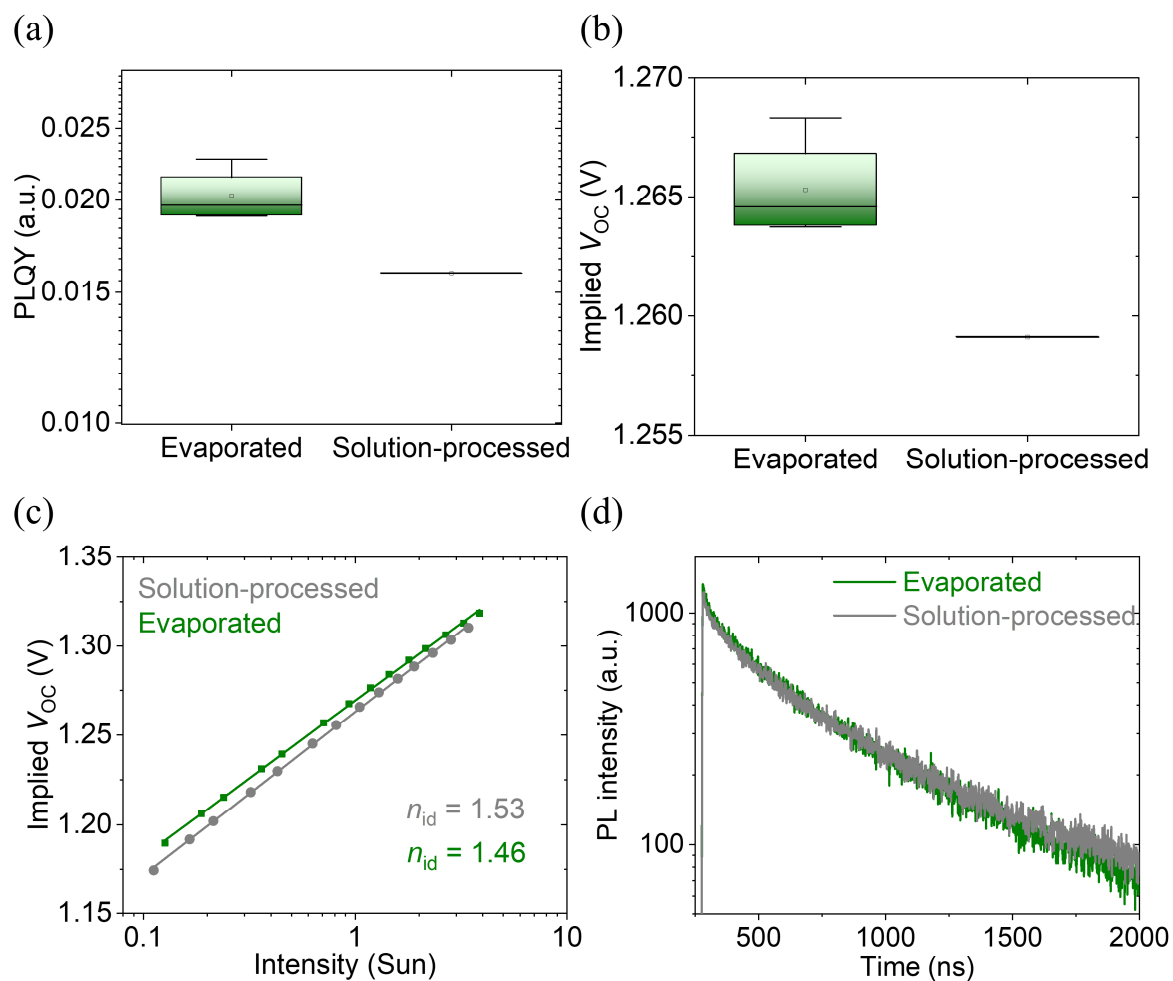


Figure A5.3. (a) PLQY comparison of the half-stacks ITO/HTL/perovskite, employing solution-processed and evaporated Me-4PACz. (b) The corresponding implied V_{oc} . (c) n_{id} extracted from a fit to the intensity-dependent implied V_{oc} . (d) TRPL comparison of the corresponding half-stacks. The TRPL data indicate a comparable decay trend for solution-processed and evaporated Me-4PACz. Reproduced from ref.⁶⁰ with permission from Wiley.

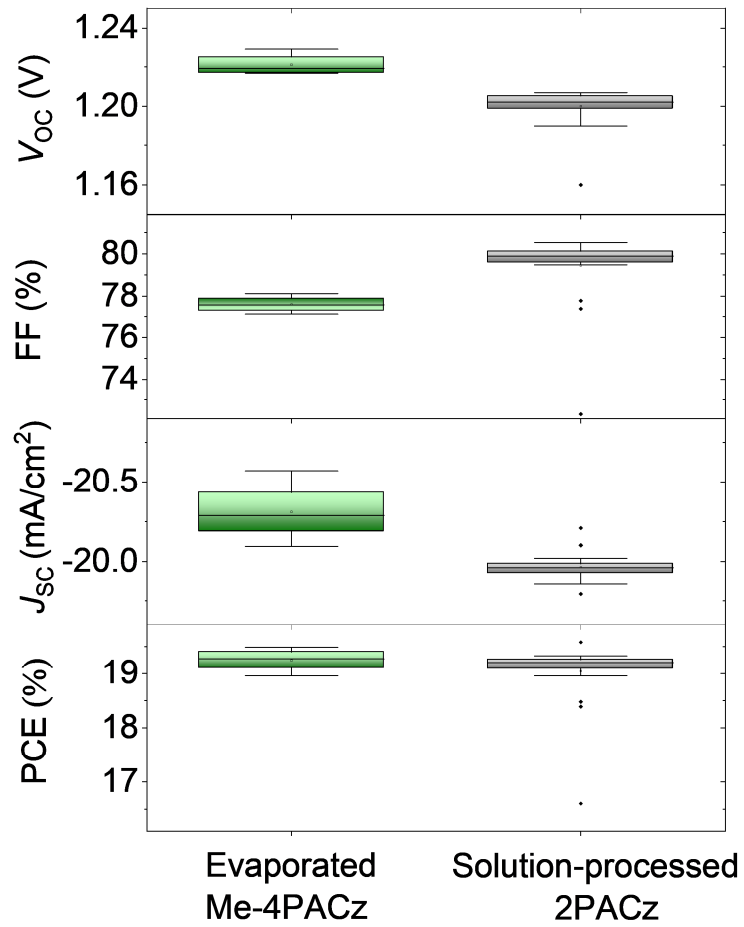


Figure A5.4. Statistical distribution of the photovoltaic (PV) parameters of perovskite solar cells (PSCs) employing a triple-cation perovskite composition $\text{Cs}_{0.17}\text{FA}_{0.83}\text{PbI}_{2.75}\text{Br}_{0.25}$ with a band gap of 1.68 eV. The employed HTLs are evaporated Me-4PACz and solution-processed 2PACz.

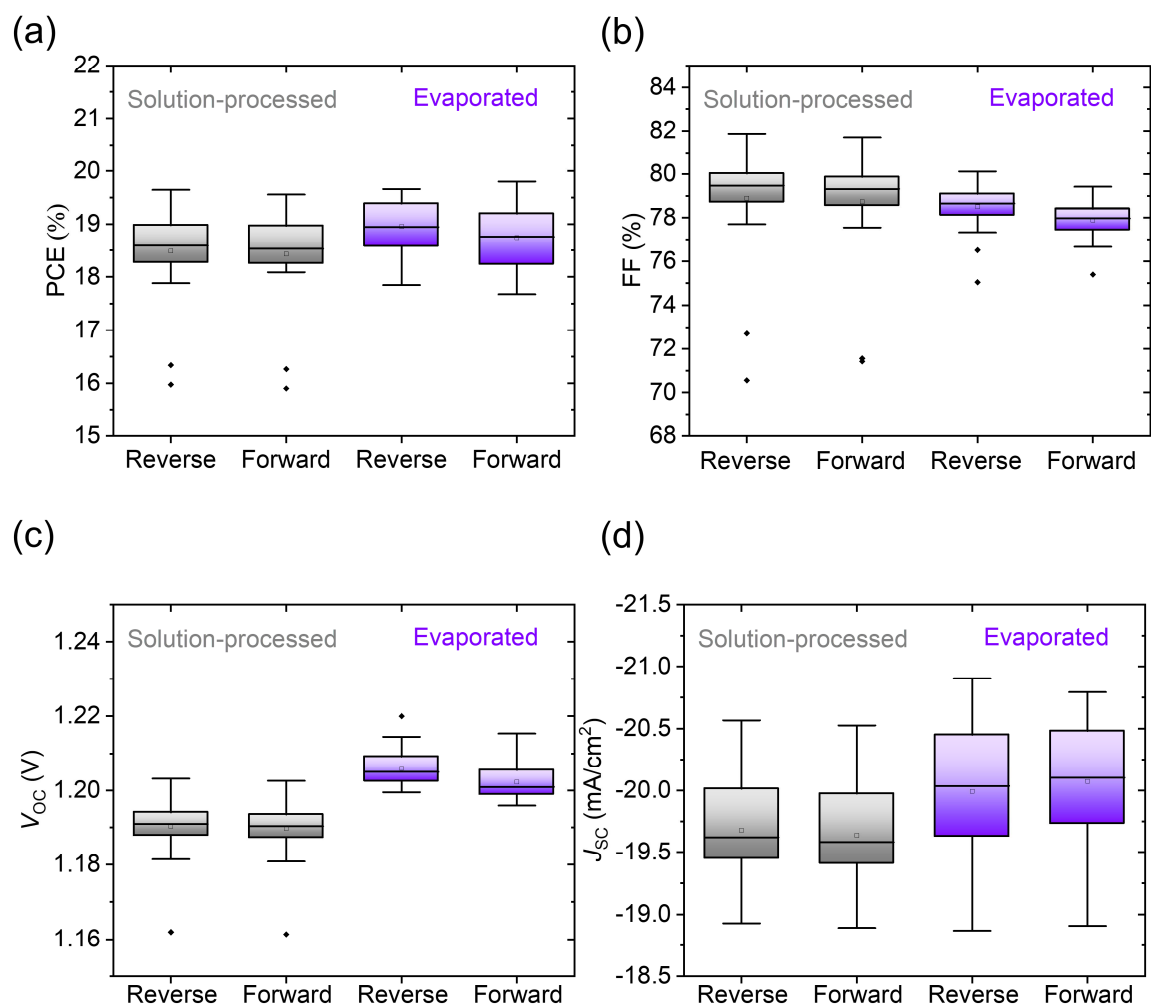


Figure A5.5. Comparison of the statistical distribution of the PV performance in forward and reverse scan for PSCs employing evaporated (~6 nm) and solution-processed 2PACz HTLs. Reproduced from ref.⁶⁰ with permission from Wiley.

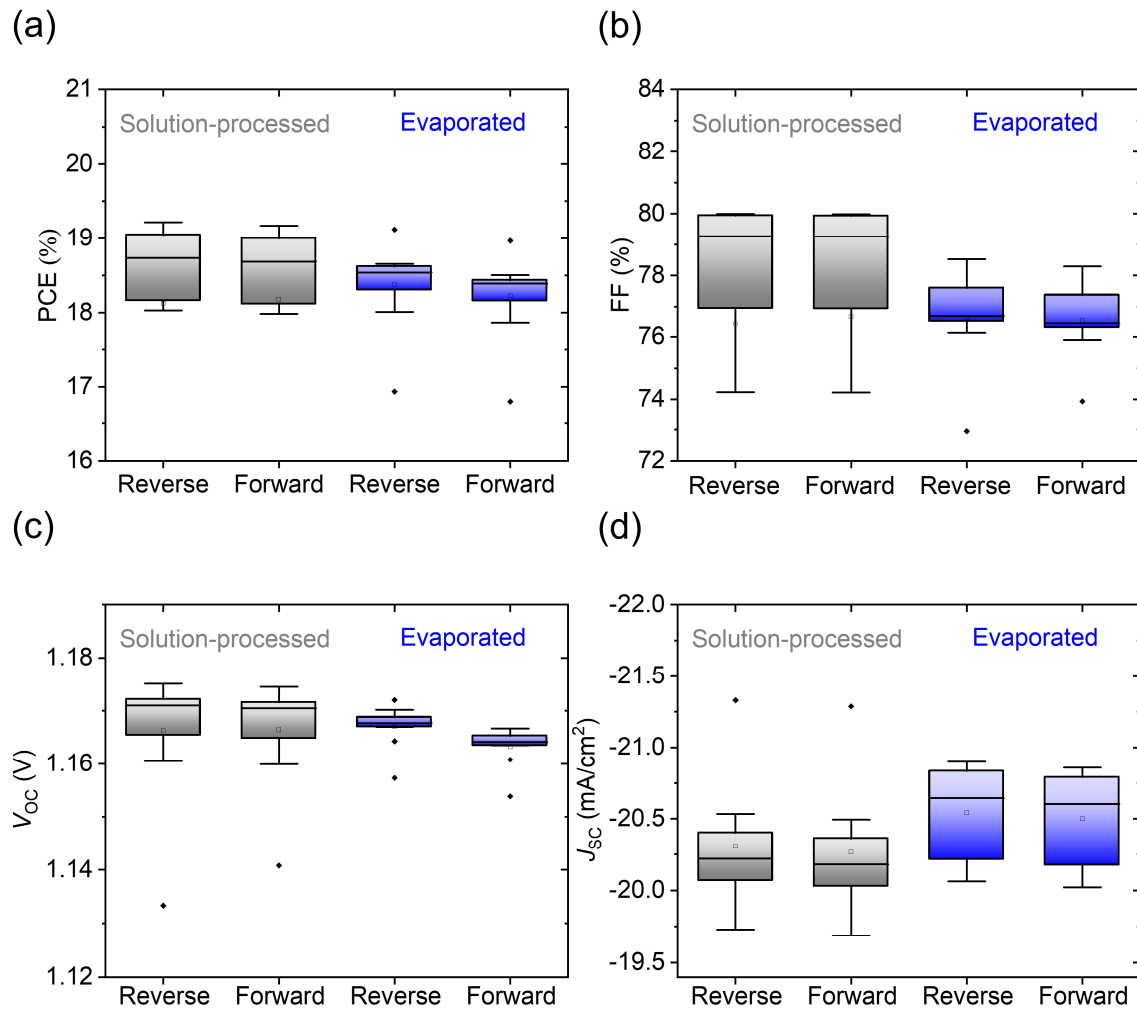


Figure A5.6. Comparison of the statistical distribution of the PV performance in forward and reverse scan for PSCs employing evaporated (~6 nm) and solution-processed MeO-2PACz HTLs. Reproduced from ref.⁶⁰ with permission from Wiley.

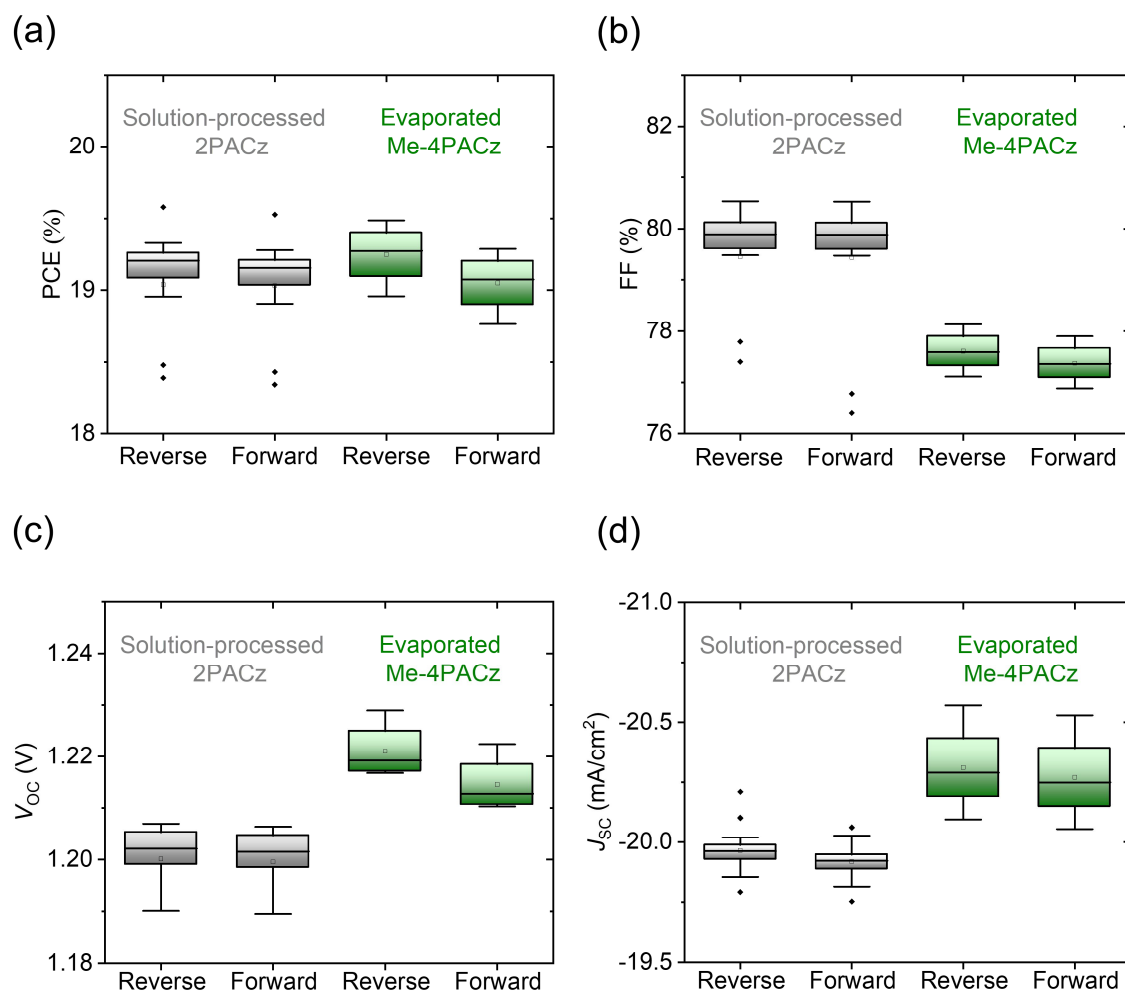


Figure A5.7. Comparison of the statistical distribution of the PV performance in forward and reverse scan for PSCs employing evaporated (~ 6 nm) Me-4PACz and solution-processed 2PACz HTLs. Reproduced from ref.⁶⁰ with permission from Wiley.

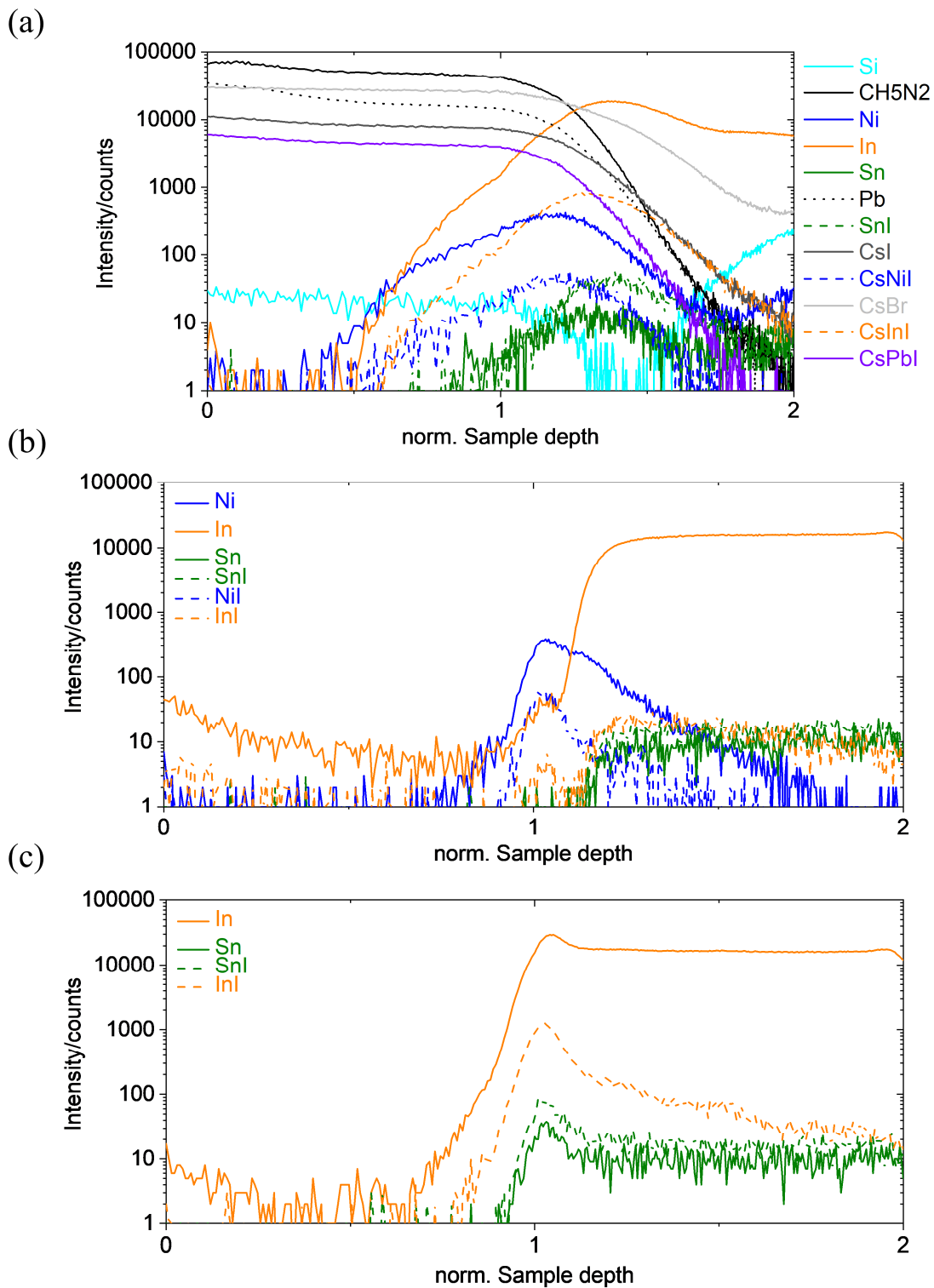


Figure A6.1. (a) Time of flight secondary ion mass spectroscopy (ToF-SIMS) depth profiling measurement of perovskite film processed over micrometer sized textured Si substrate. The hole transport layer (HTL) is ~ 15 nm NiO_x and the transparent conductive oxide (TCO) is ~ 135 nm of indium tin oxide (ITO). (b) ToF-SIMS depth profiling of perovskite thin film processed over planar Si substrate, indicating the interaction of HTL component (Nickel) and TCO components (tin and indium) with iodine, when the perovskite film is processed over planar Si substrate. The HTL is 15 nm NiO_x . (c) Similar to b with a different HTL (~ 10 nm evaporated 2PACz). Part of this figure is reproduced from ref.⁶¹ with permission from Wiley.

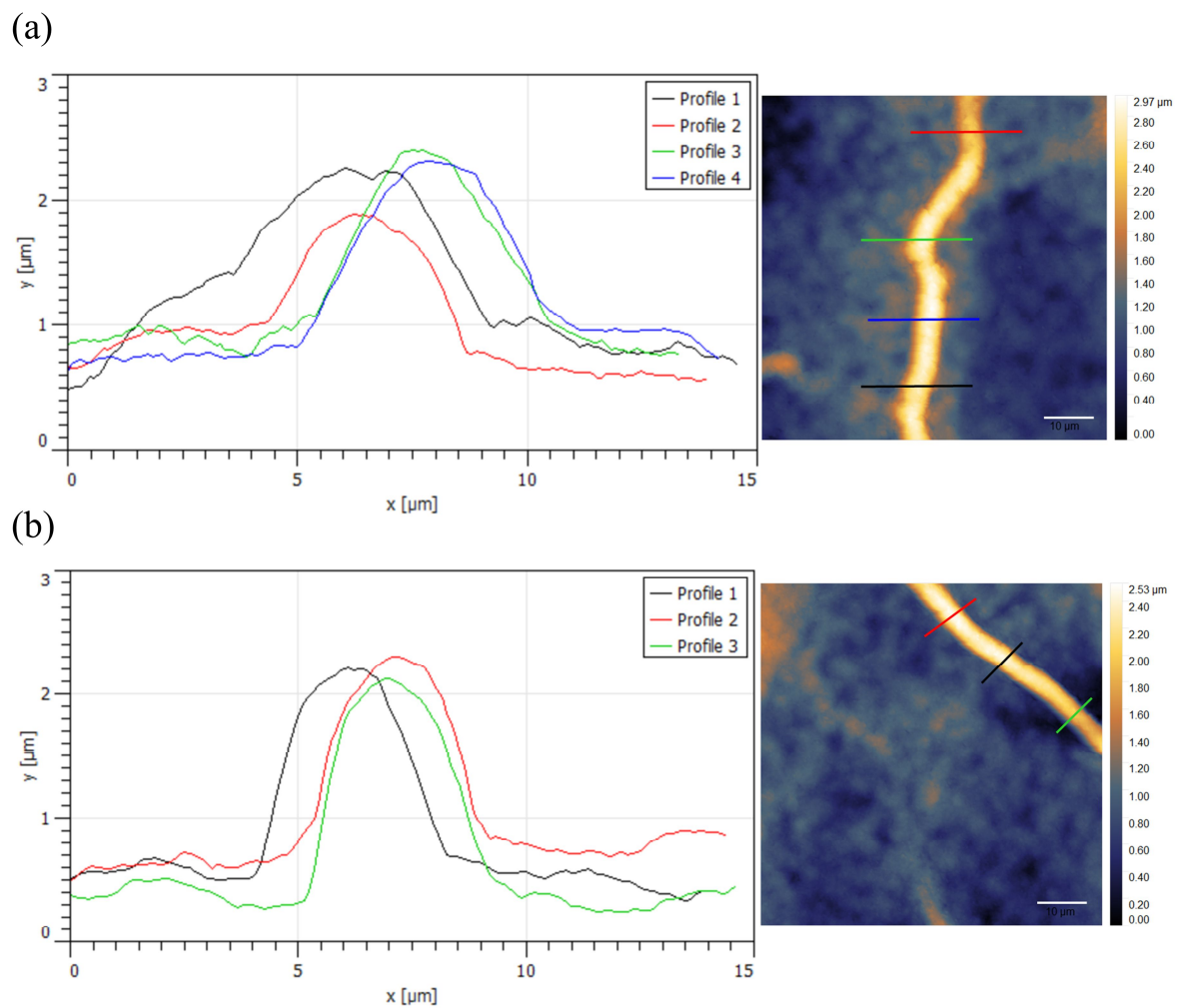


Figure A6.2. Atomic force microscopy (AFM) scan of a $50 \times 50 \mu\text{m}^2$ area with the corresponding profile width and height spectra for two perovskite thin films processed over micrometer-sized textured Si employing (a) 20% DMSO (b) 35% DMSO. Reproduced from ref.⁶¹ with permission from Wiley.

References

1. Heede, R. & Oreskes, N. Potential emissions of CO₂ and methane from proved reserves of fossil fuels: An alternative analysis. *Glob. Environ. Chang.* **36**, 12–20 (2016).
2. Oppenheimer, M. Global warming and the stability of the West Antarctic Ice Sheet. *Nat.* **393**, 325–332 (1998).
3. Dobson, A., Jolly, A. & Rubenstein, D. The greenhouse effect and biological diversity. *Trends Ecol. & Evol.* **4**, 64–68 (1989).
4. Unfccc. Report of the Conference of the Parties on its twenty-first session, held in Paris from 30 November to 11 December 2015. Part one: Proceedings.
5. Global Energy Outlook 2019: The Next Generation of Energy. <https://www.rff.org/publications/reports/global-energy-outlook-2019/>.
6. Energy Information Administration, U. International Energy Outlook 2019. (2019).
7. Study: Levelized Cost of Electricity - Renewable Energy Technologies - Fraunhofer ISE. <https://www.ise.fraunhofer.de/en/publications/studies/cost-of-electricity.html>.
8. Best Research-Cell Efficiency Chart | Photovoltaic Research | NREL. <https://www.nrel.gov/pv/cell-efficiency.html>.
9. Baiju, A. & Yarema, M. Status and challenges of multi-junction solar cell technology. *Front. Energy Res.* **10**, 1453 (2022).
10. Kurinec, S. K. Emerging Photovoltaic Materials : silicon & beyond. 826 (2018).
11. Howard, I. A. *et al.* Coated and Printed Perovskites for Photovoltaic Applications. *Adv. Mater.* **31**, 1806702 (2019).
12. Lee, S.-W. *et al.* Perovskites fabricated on textured silicon surfaces for tandem solar cells. *Commun. Chem.* **3**, 37 (2020).
13. Sahli, F. *et al.* Fully textured monolithic perovskite/silicon tandem solar cells with 25.2% power conversion efficiency. *Nat. Mater.* **17**, 820–826 (2018).
14. Gharibzadeh, S. *et al.* Two Birds with One Stones: Dual Grain-Boundary and Interface Passivation Enables > 22% Efficient Inverted Methylammonium-Free Perovskite Solar Cells. *Energy Environ. Sci.* (2021) doi:10.1039/D1EE01508G.
15. Hamada, K. *et al.* Vacuum deposition of CsPbI₃ layers on textured Si for Perovskite/Si tandem solar cells. *Jpn. J. Appl. Phys.* **58**, SBBF06 (2019).
16. Gil-Escrig, L. *et al.* Fully Vacuum-Processed Perovskite Solar Cells on Pyramidal Microtextures. *Sol. RRL* **5**, 2000553 (2021).
17. Ritzer, D. B. *et al.* Upscaling of perovskite solar modules: The synergy of fully evaporated layer fabrication and all-laser-scribed interconnections. *Prog. Photovoltaics Res. Appl.* **30**, 360–373 (2022).
18. Abzieher, T. *et al.* From Groundwork to Efficient Solar Cells: On the Importance of the Substrate Material in Co-Evaporated Perovskite Solar Cells. *Adv. Funct. Mater.* **31**, (2021).
19. Meloni, S., Palermo, G., Ashari-Astani, N., Grätzel, M. & Rothlisberger, U. Valence and conduction band tuning in halide perovskites for solar cell applications. *J. Mater. Chem. A* **4**, 15997–16002 (2016).
20. Prasanna, R. *et al.* Band Gap Tuning via Lattice Contraction and Octahedral Tilting in Perovskite Materials for Photovoltaics. *J. Am. Chem. Soc.* **139**, 11117–11124 (2017).
21. Jošt, M. *et al.* Perovskite/CIGS Tandem Solar Cells: From Certified 24.2% toward 30% and beyond. *ACS Energy Lett.* **7**, 1298–1307 (2022).
22. Chen, D. & Manley, P. Nanophotonic light management for perovskite–silicon tandem solar cells. *J. Photonics Energy* **8**, 1 (2018).

23. Jacobs, D. A. *et al.* Light Management: A Key Concept in High-Efficiency Perovskite/Silicon Tandem Photovoltaics. *J. Phys. Chem. Lett.* **10**, 3159–3170 (2019).
24. Jošt, M. *et al.* Textured interfaces in monolithic perovskite/silicon tandem solar cells: Advanced light management for improved efficiency and energy yield. *Energy Environ. Sci.* **11**, 3511–3523 (2018).
25. Gota, F. *et al.* Energy yield modelling of textured perovskite/silicon tandem photovoltaics with thick perovskite top cells. *Opt. Express, Vol. 30, Issue 9, pp. 14172-14188* **30**, 14172–14188 (2022).
26. De Bastiani, M. *et al.* Efficient bifacial monolithic perovskite/silicon tandem solar cells via bandgap engineering. *Nat. Energy* **2021 62 6**, 167–175 (2021).
27. Albrecht, S. *et al.* Monolithic perovskite/silicon-heterojunction tandem solar cells processed at low temperature. *Energy Environ. Sci.* **9**, 81–88 (2016).
28. Mailoa, J. P. *et al.* A 2-terminal perovskite/silicon multijunction solar cell enabled by a silicon tunnel junction. *Appl. Phys. Lett.* **106**, 121105 (2015).
29. Bush, K. A. *et al.* 23.6%-Efficient Monolithic Perovskite/Silicon Tandem Solar Cells With Improved Stability. *Nat. Energy* **2**, (2017).
30. Sahli, F. *et al.* Improved Optics in Monolithic Perovskite/Silicon Tandem Solar Cells with a Nanocrystalline Silicon Recombination Junction. *Adv. Energy Mater.* **8**, 1701609 (2018).
31. Nogay, G. *et al.* 25.1%-Efficient monolithic perovskite/silicon tandem solar cell based on a p-type monocrystalline textured silicon wafer and high-temperature passivating contacts. *ACS Energy Lett.* **4**, 844–845 (2019).
32. Chen, B. *et al.* Blade-Coated Perovskites on Textured Silicon for 26%-Efficient Monolithic Perovskite/Silicon Tandem Solar Cells. (2020) doi:10.1016/j.joule.2020.01.008.
33. Lehr, J. *et al.* Energy yield modelling of perovskite/silicon two-terminal tandem PV modules with flat and textured interfaces. *Sustain. Energy Fuels* **2**, 2754–2761 (2018).
34. Hörantner, M. T., Zhang, W., Saliba, M., Wojciechowski, K. & Snaith, H. J. Templated microstructural growth of perovskite thin films via colloidal monolayer lithography. *Energy Environ. Sci.* **8**, 2041–2047 (2015).
35. Pourdavoud, N. *et al.* Photonic Nanostructures Patterned by Thermal Nanoimprint Directly into Organo-Metal Halide Perovskites. *Adv. Mater.* **29**, 1605003 (2017).
36. Pascoe, A. R. *et al.* Enhancing the Optoelectronic Performance of Perovskite Solar Cells via a Textured CH₃NH₃PbI₃ Morphology. *Adv. Funct. Mater.* **26**, 1278–1285 (2016).
37. Tockhorn, P. *et al.* Improved Quantum Efficiency by Advanced Light Management in Nanotextured Solution-Processed Perovskite Solar Cells. *ACS Photonics* **7**, 2589–2600 (2020).
38. Sutter, J. *et al.* Tailored Nanostructures for Light Management in Silicon Heterojunction Solar Cells. *Sol. RRL* **4**, 1–8 (2020).
39. Zhong, S., Wang, W., Tan, M., Zhuang, Y. & Shen, W. Realization of Quasi-Omnidirectional Solar Cells with Superior Electrical Performance by All-Solution-Processed Si Nanopyramids. *Adv. Sci.* **4**, 1700200 (2017).
40. Zhu, J. *et al.* Optical absorption enhancement in amorphous silicon nanowire and nanocone arrays. *Nano Lett.* **9**, 279–282 (2009).
41. Schmager, R. *et al.* Texture of the Viola Flower for Light Harvesting in Photovoltaics. *ACS Photonics* **4**, 2687–2692 (2017).
42. Hünig, R. *et al.* Flower Power: Exploiting Plants' Epidermal Structures for Enhanced Light Harvesting in Thin-Film Solar Cells. *Adv. Opt. Mater.* **4**, 1487–1493 (2016).
43. Tockhorn, P. *et al.* Nano-optical designs for high-efficiency monolithic perovskite–silicon tandem solar cells. *Nat. Nanotechnol.* **2022 1–8** (2022) doi:10.1038/s41565-022-01228-8.

44. Filipič, M. *et al.* CH₃NH₃PbI₃ perovskite / silicon tandem solar cells: characterization based optical simulations. *Opt. Express* **23**, A263 (2015).
45. Xu, Q., Zhao, Y. & Zhang, X. Light Management in Monolithic Perovskite/Silicon Tandem Solar Cells. *Sol. RRL* **4**, 1–16 (2020).
46. Hua, X. S., Zhang, Y. J. & Wang, H. W. The effect of texture unit shape on silicon surface on the absorption properties. *Sol. Energy Mater. Sol. Cells* **94**, 258–262 (2010).
47. Fesquet, L. *et al.* Modification of textured silicon wafer surface morphology for fabrication of heterojunction solar cell with open circuit voltage over 700 mV. *Conf. Rec. IEEE Photovolt. Spec. Conf.* 000754–000758 (2009) doi:10.1109/PVSC.2009.5411173.
48. Yablonovitch, E. Statistical ray optics. *J. Opt. Soc. Am.* **72**, 899 (1982).
49. Jošt, M. *et al.* Textured interfaces in monolithic perovskite/silicon tandem solar cells: advanced light management for improved efficiency and energy yield. *Energy Environ. Sci.* **11**, 3511–3523 (2018).
50. Basu, P. K., Khanna, A. & Hameiri, Z. The effect of front pyramid heights on the efficiency of homogeneously textured inline-diffused screen-printed monocrystalline silicon wafer solar cells. *Renew. Energy* **78**, 590–598 (2015).
51. Basu, P. K., Sarangi, D., Shetty, K. D. & Boreland, M. B. Liquid silicate additive for alkaline texturing of mono-Si wafers to improve process bath lifetime and reduce IPA consumption. *Sol. Energy Mater. Sol. Cells* **113**, 37–43 (2013).
52. Baker-Finch, S. C. & McIntosh, K. R. Reflection distributions of textured monocrystalline silicon: Implications for silicon solar cells. *Prog. Photovoltaics Res. Appl.* **21**, 960–971 (2013).
53. Hou, Y. *et al.* Efficient tandem solar cells with solution-processed perovskite on textured crystalline silicon. *Science (80-.)*. **367**, 1135–1140 (2020).
54. Chen, B. *et al.* Blade-Coated Perovskites on Textured Silicon for 26%-Efficient Monolithic Perovskite/Silicon Tandem Solar Cells. *Joule* **4**, 850–864 (2020).
55. Alasfour, A., Yu, Z. J., Weigand, W., Quispe, D. & Holman, Z. C. Sub-micrometer random-pyramid texturing of silicon solar wafers with excellent surface passivation and low reflectance. *Sol. Energy Mater. Sol. Cells* **218**, 110761 (2020).
56. Subhan, F. E. *et al.* Optical optimization of double-side-textured monolithic perovskite–silicon tandem solar cells for improved light management. *RSC Adv.* **10**, 26631–26638 (2020).
57. Lee, E. M. Y. & Tisdale, W. A. Determination of exciton diffusion length by transient photoluminescence quenching and its application to quantum dot films. *J. Phys. Chem. C* **119**, 9005–9015 (2015).
58. Aydin, E. *et al.* Ligand-bridged charge extraction and enhanced quantum efficiency enable efficient n–i–p perovskite/silicon tandem solar cells. *Energy Environ. Sci.* (2021) doi:10.1039/D1EE01206A.
59. Wang, J. *et al.* Simple Solution-Processed Approach for Nanoscale Coverage of Perovskite on Textured Silicon Surface Enabling Highly Efficient Perovskite/Si Tandem Solar Cells. *Energy Technol.* **9**, 2000778 (2021).
60. Farag, A. *et al.* Evaporated Self-Assembled Monolayer Hole Transport Layers: Lossless Interfaces in p–i–n Perovskite Solar Cells. *Adv. Energy Mater.* 2203982 (2023) doi:10.1002/AENM.202203982.
61. Farag, A. *et al.* Mitigation of Open-Circuit Voltage Losses in Perovskite Solar Cells Processed over Micrometer-Sized-Textured Si Substrates. *Adv. Funct. Mater.* 2210758 (2022) doi:10.1002/ADFM.202210758.
62. Islam, M. B., Yanagida, M., Shirai, Y., Nabetani, Y. & Miyano, K. NiO_x Hole Transport Layer for Perovskite Solar Cells with Improved Stability and Reproducibility. *ACS Omega* **2**, 2291–2299 (2017).
63. Pant, N. *et al.* Investigating the Growth of CH₃NH₃PbI₃ Thin Films on RF-Sputtered NiO_x for Inverted Planar Perovskite Solar Cells: Effect of CH₃NH₃ + Halide Additives versus CH₃NH₃ +

- Halide Vapor Annealing. *Adv. Mater. Interfaces* **7**, 1901748 (2020).
64. Aydin, E. *et al.* Room-Temperature-Sputtered Nanocrystalline Nickel Oxide as Hole Transport Layer for p-i-n Perovskite Solar Cells. *ACS Appl. Energy Mater.* **1**, 6227–6233 (2018).
65. Abzieher, T. *et al.* Electron-Beam-Evaporated Nickel Oxide Hole Transport Layers for Perovskite-Based Photovoltaics. *Adv. Energy Mater.* **9**, 1802995 (2019).
66. Hasan, A. K. M. *et al.* Air-stable perovskite photovoltaic cells with low temperature deposited NiOx as an efficient hole-transporting material. *Opt. Mater. Express, Vol. 10, Issue 8, pp. 1801-1816* **10**, 1801–1816 (2020).
67. Di Girolamo, D. *et al.* Stability and Dark Hysteresis Correlate in NiO-Based Perovskite Solar Cells. *Adv. Energy Mater.* **9**, 1901642 (2019).
68. Hu, Y. *et al.* Construction of Charge Transport Channels at the NiOx/Perovskite Interface through Moderate Dipoles toward Highly Efficient Inverted Solar Cells. *ACS Appl. Mater. Interfaces* **14**, 13431–13439 (2022).
69. Boyd, C. C. *et al.* Overcoming Redox Reactions at Perovskite-Nickel Oxide Interfaces to Boost Voltages in Perovskite Solar Cells. *Joule* **4**, 1759–1775 (2020).
70. Zhumagali, S. *et al.* Linked Nickel Oxide/Perovskite Interface Passivation for High-Performance Textured Monolithic Tandem Solar Cells. *Adv. Energy Mater.* **11**, 2101662 (2021).
71. Zhang, J. *et al.* Obstructing interfacial reaction between NiOx and perovskite to enable efficient and stable inverted perovskite solar cells. *Chem. Eng. J.* **426**, 131357 (2021).
72. Al-Ashouri, A. *et al.* Supporting Information Conformal Monolayer Contacts with Lossless Interfaces for Perovskite Single Junction and Monolithic Tandem Solar Cells. (2019).
73. Liu, J. *et al.* Efficient and stable perovskite-silicon tandem solar cells through contact displacement by MgF₂. *Science (80-.)*. **8910**, 2003–2005 (2022).
74. Al-Ashouri, A. *et al.* Monolithic perovskite/silicon tandem solar cell with >29% efficiency by enhanced hole extraction. *Science (80-.)*. **370**, 1300–1309 (2020).
75. Isikgor, F. H. *et al.* Concurrent cationic and anionic perovskite defect passivation enables 27.4% perovskite/silicon tandems with suppression of halide segregation. *Joule* **5**, 1566–1586 (2021).
76. Stolterfoht, M. *et al.* Visualization and suppression of interfacial recombination for high-efficiency large-area pin perovskite solar cells. *Nat. Energy* **3**, 847–854 (2018).
77. Peña-Camargo, F. *et al.* Halide Segregation versus Interfacial Recombination in Bromide-Rich Wide-Gap Perovskite Solar Cells. *ACS Energy Lett.* **5**, 2728–2736 (2020).
78. Stolterfoht, M. *et al.* The impact of energy alignment and interfacial recombination on the internal and external open-circuit voltage of perovskite solar cells. *Energy Environ. Sci.* **12**, 2778–2788 (2019).
79. Gharibzadeh, S. *et al.* Two birds with one stone: dual grain-boundary and interface passivation enables >22% efficient inverted methylammonium-free perovskite solar cells. *Energy Environ. Sci.* (2021) doi:10.1039/D1EE01508G.
80. Mahmud, M. A. *et al.* Cation-Diffusion-Based Simultaneous Bulk and Surface Passivations for High Bandgap Inverted Perovskite Solar Cell Producing Record Fill Factor and Efficiency. *Adv. Energy Mater.* 2201672 (2022) doi:10.1002/AENM.202201672.
81. Sveinbjörnsson, K. *et al.* Ambient air-processed mixed-ion perovskites for high-efficiency solar cells. *J. Mater. Chem. A* **4**, 16536–16545 (2016).
82. Kim, S.-G. *et al.* How antisolvent miscibility affects perovskite film wrinkling and photovoltaic properties. *Nat. Commun.* **12**, 1554 (2021).
83. Zhao, J. *et al.* Strained hybrid perovskite thin films and their impact on the intrinsic stability of perovskite solar cells. *Sci. Adv.* **3**, eaao5616 (2017).

References

84. Mohan, M. Perovskite photovoltaics. *Perovskite Photovoltaics Basic to Adv. Concepts Implement.* 447–480 (2018) doi:10.1016/B978-0-12-812915-9.00014-9.
85. Tilley, R. J. D. Chapter 1 The ABX₃ Perovskite Structure. *Perovskites Struct. Relationships* (2016).
86. Li, C. *et al.* lity of ABX₃ (X = F, Cl, Br, I) halide perovskitesFormabi. *Acta Crystallogr. Sect. B Struct. Sci.* **64**, 702–707 (2008).
87. Liu, N. *et al.* Recent Progress in Developing Monolithic Perovskite/Si Tandem Solar Cells. *Front. Chem.* **8**, (2020).
88. Niu, T. *et al.* High performance ambient-air-stable FAPbI₃ perovskite solar cells with molecule-passivated Ruddlesden–Popper/3D heterostructured film. *Energy Environ. Sci.* **11**, 3358–3366 (2018).
89. Zhang, W. & Zhou, H. Perovskite intermediate phases fundamentally address the urgent stability issue. *Chem* **7**, 2862–2865 (2021).
90. Goldschmidt, V. M. Krystallbau und chemische Zusammensetzung. *Berichte der Dtsch. Chem. Gesellschaft (A B Ser.)* **60**, 1263–1296 (1927).
91. Xiao, Z., Yan, Y., Xiao, Z. & Yan, Y. Progress in Theoretical Study of Metal Halide Perovskite Solar Cell Materials. *Adv. Energy Mater.* **7**, 1701136 (2017).
92. Sarritzu, V. *et al.* Direct or Indirect Bandgap in Hybrid Lead Halide Perovskites? *Adv. Opt. Mater.* **6**, 1701254 (2018).
93. Galkowski, K. *et al.* Determination of the exciton binding energy and effective masses for methylammonium and formamidinium lead tri-halide perovskite semiconductors.
94. Chen, B. *et al.* Enhanced optical path and electron diffusion length enable high-efficiency perovskite tandems. *Nat. Commun.* **11**, 1–9 (2020).
95. Yin, W.-J. *et al.* Unique Properties of Halide Perovskites as Possible Origins of the Superior Solar Cell Performance. *Adv. Mater.* **26**, 4653–4658 (2014).
96. Subhan, F. E. *et al.* Optical optimization of double-side-textured monolithic perovskite-silicon tandem solar cells for improved light management. *RSC Adv.* **10**, 26631–26638 (2020).
97. Shen, H. *et al.* Monolithic Perovskite/Si Tandem Solar Cells: Pathways to Over 30% Efficiency. *Adv. Energy Mater.* **10**, 1902840 (2020).
98. Hu, Y., Song, L., Chen, Y. & Huang, W. Two-Terminal Perovskites Tandem Solar Cells: Recent Advances and Perspectives. *Sol. RRL* **3**, 1–21 (2019).
99. Qarony, W. *et al.* Influence of Perovskite Interface Morphology on the Photon Management in Perovskite/Silicon Tandem Solar Cells. *ACS Appl. Mater. Interfaces* **12**, 15080–15086 (2020).
100. Chen, B. *et al.* Grain Engineering for Perovskite/Silicon Monolithic Tandem Solar Cells with Efficiency of 25.4%. *Joule* **3**, 177–190 (2019).
101. Köhnen, E. *et al.* 27.9% Efficient Monolithic Perovskite/Silicon Tandem Solar Cells on Industry Compatible Bottom Cells. *Sol. RRL* 2100244 (2021) doi:10.1002/SOLR.202100244.
102. De Bastiani, M. *et al.* Efficient bifacial monolithic perovskite/silicon tandem solar cells via bandgap engineering. *Nat. Energy* **6**, 167–175 (2021).
103. Köhnen, E. *et al.* Highly efficient monolithic perovskite silicon tandem solar cells: Analyzing the influence of current mismatch on device performance. *Sustain. Energy Fuels* **3**, 1995–2005 (2019).
104. Xu, J. *et al.* Triple-halide wide-band gap perovskites with suppressed phase segregation for efficient tandems. *Science (80-.)*. **367**, 1097–1104 (2020).
105. Roß, M. *et al.* Co-Evaporated Formamidinium Lead Iodide Based Perovskites with 1000 h Constant Stability for Fully Textured Monolithic Perovskite/Silicon Tandem Solar Cells. (2021) doi:10.1002/aenm.202101460.

References

106. Hyun, J. Y. *et al.* Perovskite/Silicon Tandem Solar Cells with a V_{oc} of 1784 mV Based on an Industrially Feasible 25 cm² TOPCon Silicon Cell. *ACS Appl. Energy Mater.* **10**, 44 (2022).
107. Roger, J. *et al.* Laminated Monolithic Perovskite/Silicon Tandem Photovoltaics. *Adv. Energy Mater.* 2200961 (2022) doi:10.1002/AENM.202200961.
108. Kim, D. H. *et al.* Bimolecular Additives Improve Wide-Band-Gap Perovskites for Efficient Tandem Solar Cells with CIGS. *Joule* **3**, 1734–1745 (2019).
109. Gharibzadeh, S. *et al.* 2D/3D Heterostructure for Semitransparent Perovskite Solar Cells with Engineered Bandgap Enables Efficiencies Exceeding 25% in Four-Terminal Tandems with Silicon and CIGS. *Adv. Funct. Mater.* **30**, 1909919 (2020).
110. Al-Ashouri, A. *et al.* Conformal monolayer contacts with lossless interfaces for perovskite single junction and monolithic tandem solar cells. *Energy Environ. Sci.* **12**, 3356–3369 (2019).
111. Ruiz-Preciado, M. A. *et al.* Monolithic Two-Terminal Perovskite/CIS Tandem Solar Cells with Efficiency Approaching 25%. *ACS Energy Lett.* 2273–2281 (2022) doi:10.1021/ACSENERGYLETT.2C00707.
112. Datta, K. *et al.* Monolithic All-Perovskite Tandem Solar Cells with Minimized Optical and Energetic Losses. *Adv. Mater.* **34**, 2110053 (2022).
113. Abdollahi Nejang, B. *et al.* Scalable two-terminal all-perovskite tandem solar modules with a 19.1% efficiency. *Nat. Energy* 2022 1–11 (2022) doi:10.1038/s41560-022-01059-w.
114. Bisquert, J. The physics of solar cells: Perovskites, organics, and photovoltaic fundamentals. *Phys. Sol. Cells Perovskites, Org. Photovolt. Fundam.* 1–226 (2017) doi:10.1201/B22380/PHYSICS-SOLAR-CELLS-JUAN-BISQUERT.
115. How a Solar Cell Works - American Chemical Society. <https://www.acs.org/education/resources/highschool/chemmatters/past-issues/archive-2013-2014/how-a-solar-cell-works.html>.
116. Edri, E. *et al.* Elucidating the charge carrier separation and working mechanism of CH₃NH₃PbI₃-xCl_x perovskite solar cells. *Nat. Commun.* 2014 51 **5**, 1–8 (2014).
117. Shi, J. *et al.* From Ultrafast to Ultraslow: Charge-Carrier Dynamics of Perovskite Solar Cells. *Joule* **2**, 879–901 (2018).
118. Levine, I. *et al.* Charge transfer rates and electron trapping at buried interfaces of perovskite solar cells. *Joule* **5**, 2915–2933 (2021).
119. Courtier, N. E., Cave, J. M., Foster, J. M., Walker, A. B. & Richardson, G. How transport layer properties affect perovskite solar cell performance: insights from a coupled charge transport/ion migration model. *Energy Environ. Sci.* **12**, 396–409 (2019).
120. Wu, S. *et al.* Modulation of Defects and Interfaces through Alkylammonium Interlayer for Efficient Inverted Perovskite Solar Cells. *Joule* **4**, 1248–1262 (2020).
121. Le Corre, V. M. *et al.* Charge Transport Layers Limiting the Efficiency of Perovskite Solar Cells: How to Optimize Conductivity, Doping, and Thickness. *ACS Appl. Energy Mater.* **2**, 6280–6287 (2019).
122. Byeon, J. *et al.* Charge Transport Layer-Dependent Electronic Band Bending in Perovskite Solar Cells and Its Correlation to Light-Induced Device Degradation. *ACS Energy Lett.* **5**, 2580–2589 (2020).
123. Hellmann, T. *et al.* The Electronic Structure of MAPI-Based Perovskite Solar Cells: Detailed Band Diagram Determination by Photoemission Spectroscopy Comparing Classical and Inverted Device Stacks. *Adv. Energy Mater.* **10**, 2002129 (2020).
124. Kirchartz, T. Generalized detailed balance theory of solar cells.
125. Hellmann, T. Advanced Understanding of the Electronic Properties of Perovskite Solar Cells.
126. Caprioglio, P. *et al.* On the Origin of the Ideality Factor in Perovskite Solar Cells. *Adv. Energy Mater.* **10**, 2000502 (2020).

127. Satpathy, R. & Pamuru, V. Making of crystalline silicon solar cells. *Sol. PV Power* 71–134 (2021) doi:10.1016/B978-0-12-817626-9.00004-6.
128. Theristis, M., Venizelou, V., Makrides, G. & Georghiou, G. E. Energy yield in photovoltaic systems. *McEvoy's Handb. Photovoltaics Fundam. Appl.* 671–713 (2018) doi:10.1016/B978-0-12-809921-6.00017-3.
129. Green, M. A. Solar cell fill factors: General graph and empirical expressions. *Solid. State. Electron.* **24**, 788–789 (1981).
130. Green, M. A. Accuracy of analytical expressions for solar cell fill factors. *Sol. Cells* **7**, 337–340 (1982).
131. Nemnes, G. A. *et al.* How measurement protocols influence the dynamic J-V characteristics of perovskite solar cells: Theory and experiment. *Sol. Energy* **173**, 976–983 (2018).
132. Snaith, H. J. *et al.* Anomalous hysteresis in perovskite solar cells. *J. Phys. Chem. Lett.* **5**, 1511–1515 (2014).
133. Calado, P. *et al.* Evidence for ion migration in hybrid perovskite solar cells with minimal hysteresis. *Nat. Commun.* **2016 71 7**, 1–10 (2016).
134. Chen, B., Yang, M. & Wu, C. Impact of Capacitive Effect and Ion Migration on the Hysteretic Behavior of Perovskite Solar Cells Application of magnetoelectric composites in low and high frequency devices. View project Organic solar cells: energetics and disorder View project. *Artic. J. Phys. Chem. Lett.* (2015) doi:10.1021/acs.jpcllett.5b02229.
135. Tress, W. Metal Halide Perovskites as Mixed Electronic-Ionic Conductors: Challenges and Opportunities - From Hysteresis to Memristivity. *J. Phys. Chem. Lett.* **8**, 3106–3114 (2017).
136. Ding, C. *et al.* Effect of the conduction band offset on interfacial recombination behavior of the planar perovskite solar cells. *Nano Energy* **53**, 17–26 (2018).
137. Shockley, W. & Queisser, H. J. Detailed balance limit of efficiency of p-n junction solar cells. *J. Appl. Phys.* **32**, 510–519 (1961).
138. Schmager, R. Advanced light management concepts for perovskite photovoltaics. (2020).
139. Zhang, Z. G. *et al.* One-step low temperature hydrothermal synthesis of flexible TiO₂/PVDF@MoS₂ core-shell heterostructured fibers for visible-light-driven photocatalysis and self-cleaning. *Nanomaterials* **9**, (2019).
140. Gharibzadeh, S. *et al.* Record Open-Circuit Voltage Wide-Bandgap Perovskite Solar Cells Utilizing 2D/3D Perovskite Heterostructure. *Adv. Energy Mater.* **9**, 1803699 (2019).
141. Luo, D., Su, R., Zhang, W., Gong, Q. & Zhu, R. Minimizing non-radiative recombination losses in perovskite solar cells. *Nat. Rev. Mater.* **2019 51 5**, 44–60 (2019).
142. Chen, J. & Park, N. G. Causes and Solutions of Recombination in Perovskite Solar Cells. *Adv. Mater.* **31**, 1803019 (2019).
143. Comprehensive Characterization and Modelling of Operation Mechanisms in Third Generation Solar Cells.
144. Qin, J., Liu, X. K., Yin, C. & Gao, F. Carrier Dynamics and Evaluation of Lasing Actions in Halide Perovskites. *Trends Chem.* **3**, 34–46 (2021).
145. Stranks, S. D. Nonradiative Losses in Metal Halide Perovskites. *ACS Energy Lett.* **2**, 1515–1525 (2017).
146. Gerlach, W., Schlagenotto, H. & Maeder, H. On the radiative recombination rate in silicon. *Phys. status solidi* **13**, 277–283 (1972).
147. Davies, C. L. *et al.* Bimolecular recombination in methylammonium lead triiodide perovskite is an inverse absorption process. *Nat. Commun.* **2018 91 9**, 1–9 (2018).
148. Hidayat, R. *et al.* Revealing the charge carrier kinetics in perovskite solar cells affected by mesoscopic

- structures and defect states from simple transient photovoltage measurements. *Sci. Reports* 2020 101 **10**, 1–13 (2020).
149. Kepenekian, M. *et al.* Concept of Lattice Mismatch and Emergence of Surface States in Two-dimensional Hybrid Perovskite Quantum Wells. *Nano Lett.* **18**, 5603–5609 (2018).
150. Shockley, W. & Read, W. T. Statistics of the Recombinations of Holes and Electrons. *Phys. Rev.* **87**, 835 (1952).
151. Pratheek, M., Abhinav, T., Bhattacharya, S., Chandra, G. K. & Predeep, P. Recent progress on defect passivation in perovskites for solar cell application. *Mater. Sci. Energy Technol.* **4**, 282–289 (2021).
152. Ball, J. M. & Petrozza, A. Defects in perovskite-halides and their effects in solar cells. *Nat. Energy* 2016 111 **1**, 1–13 (2016).
153. Singh, S., Laxmi & Kabra, D. Defects in halide perovskite semiconductors: impact on photo-physics and solar cell performance. *J. Phys. D. Appl. Phys.* **53**, 503003 (2020).
154. Goudon, T., Miljanović, V. & Schmeiser, C. On the Shockley–Read–Hall Model: Generation-Recombination in Semiconductors. <https://doi.org/10.1137/060650751> **67**, 1183–1201 (2007).
155. Zhu, L. *et al.* Investigation on the role of Lewis bases in the ripening process of perovskite films for highly efficient perovskite solar cells. *J. Mater. Chem. A* **5**, 20874–20881 (2017).
156. Chen, J. *et al.* High-Performance Thickness Insensitive Perovskite Solar Cells with Enhanced Moisture Stability. *Adv. Energy Mater.* **8**, 1–10 (2018).
157. Stolterfoht, M. *et al.* How To Quantify the Efficiency Potential of Neat Perovskite Films: Perovskite Semiconductors with an Implied Efficiency Exceeding 28%. *Adv. Mater.* **32**, 2000080 (2020).
158. Liu, Y. *et al.* Surface-Tension-Controlled Crystallization for High-Quality 2D Perovskite Single Crystals for Ultrahigh Photodetection. *Matter* **1**, 465–480 (2019).
159. Gutierrez-Partida, E. *et al.* Large-Grain Double Cation Perovskites with 18 μ s Lifetime and High Luminescence Yield for Efficient Inverted Perovskite Solar Cells. *ACS Energy Lett.* **6**, 1045–1054 (2021).
160. Li, Z. *et al.* Cations Functionalized Carbon Nano-Dots Enabling Interfacial Passivation and Crystallization Control for Inverted Perovskite Solar Cells. *Sol. RRL* **4**, 1900369 (2020).
161. Seo, Y. H., Kim, E. C., Cho, S. P., Kim, S. S. & Na, S. I. High-performance planar perovskite solar cells: Influence of solvent upon performance. *Appl. Mater. Today* **9**, 598–604 (2017).
162. Wu, S. *et al.* Modulation of Defects and Interfaces through Alkylammonium Interlayer for Efficient Inverted Perovskite Solar Cells. *Joule* **4**, 1248–1262 (2020).
163. Yang, G. *et al.* Defect engineering in wide-bandgap perovskites for efficient perovskite–silicon tandem solar cells. *Nat. Photonics* 2022 168 **16**, 588–594 (2022).
164. Gaubas, E., Simoen, E. & Haugi, A. Auger recombination in direct-gap semiconductors: band-structure effects. *J. Phys. C Solid State Phys.* **16**, 4159 (1983).
165. Hou, X. *et al.* Engineering Auger recombination in colloidal quantum dots via dielectric screening. *Nat. Commun.* 2019 101 **10**, 1–11 (2019).
166. Tress, W. Perovskite Solar Cells on the Way to Their Radiative Efficiency Limit – Insights Into a Success Story of High Open-Circuit Voltage and Low Recombination. *Adv. Energy Mater.* **7**, 1602358 (2017).
167. Kirchartz, T., Mattheis, J. & Rau, U. Detailed balance theory of excitonic and bulk heterojunction solar cells. *Phys. Rev. B - Condens. Matter Mater. Phys.* **78**, 235320 (2008).
168. Wolff, C. M. *et al.* Reduced Interface-Mediated Recombination for High Open-Circuit Voltages in CH₃NH₃PbI₃ Solar Cells. *Adv. Mater.* **29**, 1700159 (2017).
169. Würfel, P. & Ruppel, W. The chemical potential of luminescent radiation. *J. Lumin.* **24–25**, 925–928

- (1981).
170. Krückemeier, L., Rau, U., Stolterfoht, M. & Kirchartz, T. How to Report Record Open-Circuit Voltages in Lead-Halide Perovskite Solar Cells. *Adv. Energy Mater.* **10**, 1902573 (2020).
171. Fassel, P. *et al.* Revealing the internal luminescence quantum efficiency of perovskite films via accurate quantification of photon recycling. *Matter* **4**, 1391–1412 (2021).
172. de Mello, J. C., Wittmann, H. F. & Friend, R. H. An improved experimental determination of external photoluminescence quantum efficiency. *Adv. Mater.* **9**, 230–232 (1997).
173. Stolterfoht, M. *et al.* How To Quantify the Efficiency Potential of Neat Perovskite Films: Perovskite Semiconductors with an Implied Efficiency Exceeding 28%. *Adv. Mater.* **32**, 2000080 (2020).
174. Fassel, P. *et al.* Revealing the internal luminescence quantum efficiency of perovskite films via accurate quantification of photon recycling. *Matter* **4**, 1391–1412 (2021).
175. Prakash, S. B., Singh, G. & Singh, S. Modeling and Performance Analysis of Simplified Two-Diode Model of Photovoltaic Cells. *Front. Phys.* **9**, 236 (2021).
176. Yadav, P., Pandey, K., Bhatt, V., Kumar, M. & Kim, J. Critical aspects of impedance spectroscopy in silicon solar cell characterization: A review. *Renew. Sustain. Energy Rev.* **76**, 1562–1578 (2017).
177. Jäger, K., Sutter, J., Hammerschmidt, M., Schneider, P. I. & Becker, C. Prospects of light management in perovskite/silicon tandem solar cells. *Nanophotonics* **1599**, (2021).
178. Eisenhauer, D., Trinh, C. T., Amkreutz, D. & Becker, C. Light management in crystalline silicon thin-film solar cells with imprint-textured glass superstrate. *Sol. Energy Mater. Sol. Cells* **200**, 109928 (2019).
179. Hossain, I. M. *et al.* Nanostructured front electrodes for perovskite/c-Si tandem photovoltaics. *Opt. Express* **28**, 8878 (2020).
180. Farag, A. *et al.* Efficient Light Harvesting in Thick Perovskite Solar Cells Processed on Industry-Applicable Random Pyramidal Textures. *ACS Appl. Energy Mater.* (2022) doi:10.1021/ACSAEM.1C04028.
181. Schultes, M. *et al.* Sputtered Transparent Electrodes (IO:H and IZO) with Low Parasitic Near-Infrared Absorption for Perovskite-Cu(In,Ga)Se₂ Tandem Solar Cells. *ACS Appl. Energy Mater.* **2**, 7823–7831 (2019).
182. Feeney, T. *et al.* Four-Terminal Perovskite/Copper Indium Gallium Selenide Tandem Solar Cells: Unveiling the Path to >27% in Power Conversion Efficiency. *Sol. RRL* **6**, 2200662 (2022).
183. Hossain, I. M. Semitransparent perovskite solar cells for perovskite-based tandem photovoltaics. (2020).
184. Moghadamzadeh, S. *et al.* In₂O₃:H-Based Hole-Transport-Layer-Free Tin/Lead Perovskite Solar Cells for Efficient Four-Terminal All-Perovskite Tandem Solar Cells. *ACS Appl. Mater. Interfaces* **13**, 46488–46498 (2021).
185. Aktas, E. *et al.* Understanding the perovskite/self-assembled selective contact interface for ultra-stable and highly efficient p–i–n perovskite solar cells. *Energy Environ. Sci.* **14**, 3976–3985 (2021).
186. Gota, F., Langenhorst, M., Schmager, R., Lehr, J. & Paetzold, U. W. Energy Yield Advantages of Three-Terminal Perovskite-Silicon Tandem Photovoltaics. *Joule* **4**, 2387–2403 (2020).
187. Roß, M. *et al.* Co-Evaporated Formamidinium Lead Iodide Based Perovskites with 1000 h Constant Stability for Fully Textured Monolithic Perovskite/Silicon Tandem Solar Cells. *Adv. Energy Mater.* **11**, (2021).
188. Mandel, S. Pyramid texturing on silicon solar cells traps light more efficiently. *Scilight* **2020**, 071106 (2020).
189. Dottermusch, S. *et al.* Micro-cone textures for improved light in-coupling and retroreflection-inspired light trapping at the front surface of solar modules. *Prog. Photovoltaics Res. Appl.* **27**, 3133 (2019).

References

190. Shockley, W. & Queisser, H. J. Detailed balance limit of efficiency of p-n junction solar cells. *J. Appl. Phys.* **32**, 510–519 (1961).
191. Tockhorn, P. *et al.* Three-Terminal Perovskite/Silicon Tandem Solar Cells with Top and Interdigitated Rear Contacts. *ACS Appl. Energy Mater.* **3**, 1381–1392 (2020).
192. Werner, J., Niesen, B. & Ballif, C. Perovskite/Silicon Tandem Solar Cells: Marriage of Convenience or True Love Story? - An Overview. *Adv. Mater. Interfaces* **5**, 1700731 (2018).
193. Liu, D., Gangishetty, M. K. & Kelly, T. L. Effect of CH₃NH₃PbI₃ thickness on device efficiency in planar heterojunction perovskite solar cells. *J. Mater. Chem. A* **2**, 19873–19881 (2014).
194. Wang, K. *et al.* Efficiencies of perovskite hybrid solar cells influenced by film thickness and morphology of CH₃NH₃PbI₃-xCl_x layer. *Org. Electron.* **21**, 19–26 (2015).
195. Sandberg, O. J. *et al.* On the Question of the Need for a Built-In Potential in Perovskite Solar Cells. *Adv. Mater. Interfaces* **7**, 2000041 (2020).
196. Bahrami, B. *et al.* Nanoscale spatial mapping of charge carrier dynamics in perovskite solar cells. *Nano Today* **33**, 100874 (2020).
197. Bercegol, A. *et al.* Quantitative optical assessment of photonic and electronic properties in halide perovskite. *Nat. Commun.* **10**, 1586 (2019).
198. Du, T. *et al.* Light-intensity and thickness dependent efficiency of planar perovskite solar cells: charge recombination versus extraction. *J. Mater. Chem. C* **8**, 12648–12655 (2020).
199. Eggers, H. *et al.* Inkjet-Printed Micrometer-Thick Perovskite Solar Cells with Large Columnar Grains. *Adv. Energy Mater.* **10**, 1903184 (2020).
200. Yuan, Z. *et al.* Approximately 800-nm-Thick Pinhole-Free Perovskite Films via Facile Solvent Retarding Process for Efficient Planar Solar Cells. *ACS Appl. Mater. Interfaces* **8**, 34446–34454 (2016).
201. Yan, K. *et al.* Achieving high-performance thick-film perovskite solar cells with electron transporting Bingel fullerenes. *J. Mater. Chem. A* **6**, 15495–15503 (2018).
202. Yang, D. *et al.* High efficiency planar-type perovskite solar cells with negligible hysteresis using EDTA-complexed SnO₂. *Nat. Commun.* **9**, 3239 (2018).
203. Hsieh, C. M. *et al.* Low-temperature, simple and efficient preparation of perovskite solar cells using Lewis bases urea and thiourea as additives: Stimulating large grain growth and providing a PCE up to 18.8%. *RSC Adv.* **8**, 19610–19615 (2018).
204. Han, L. *et al.* Environmental-Friendly Urea Additive Induced Large Perovskite Grains for High Performance Inverted Solar Cells. *Sol. RRL* **2**, 1800054 (2018).
205. Lv, Y. *et al.* All-in-One Deposition to Synergistically Manipulate Perovskite Growth for High-Performance Solar Cell. **2020**, (2020).
206. Lee, J. W., Kim, H. S. & Park, N. G. Lewis Acid-Base Adduct Approach for High Efficiency Perovskite Solar Cells. *Acc. Chem. Res.* **49**, 311–319 (2016).
207. Kruszyńska, J. *et al.* Effect of 1,3-Disubstituted Urea Derivatives as Additives on the Efficiency and Stability of Perovskite Solar Cells. *ACS Appl. Energy Mater.* **2022**, 13617–13626 (2022).
208. Hou, Y. *et al.* Supplementary Materials for Efficient tandem solar cells with solution-processed perovskite on textured crystalline silicon. doi:10.1126/science.aaz3691.
209. Rai, M., Wong, L. H. & Etgar, L. Effect of Perovskite Thickness on Electroluminescence and Solar Cell Conversion Efficiency. *J. Phys. Chem. Lett.* **11**, 8189–8194 (2020).
210. Patel, J. B. *et al.* Light Absorption and Recycling in Hybrid Metal Halide Perovskite Photovoltaic Devices. *Adv. Energy Mater.* **10**, 1903653 (2020).
211. Haque, M. A., Troughton, J. & Baran, D. Processing-Performance Evolution of Perovskite Solar Cells:

- From Large Grain Polycrystalline Films to Single Crystals. *Adv. Energy Mater.* **10**, 1–20 (2020).
212. Yao, K. *et al.* Plasmon-induced trap filling at grain boundaries in perovskite solar cells. *Light Sci. Appl.* **2021 101** **10**, 1–12 (2021).
213. Rahman, S. I. *et al.* Grain Boundary Defect Passivation of Triple Cation Mixed Halide Perovskite with Hydrazine-Based Aromatic Iodide for Efficiency Improvement. *ACS Appl. Mater. Interfaces* **12**, 41312–41322 (2020).
214. Peter Amalathas, A. *et al.* Controlled Growth of Large Grains in CH₃NH₃PbI₃ Perovskite Films Mediated by an Intermediate Liquid Phase without an Antisolvent for Efficient Solar Cells. *ACS Appl. Energy Mater.* **3**, 12484–12493 (2020).
215. Kim, M. *et al.* Methylammonium Chloride Induces Intermediate Phase Stabilization for Efficient Perovskite Solar Cells. *Joule* **3**, 2179–2192 (2019).
216. Wen, Y., Tang, Y.-G. & Yan, G.-Q. Large grain size CH₃NH₃PbI₃ film for perovskite solar cells with hydroic acid additive.
217. Li, Y. *et al.* Enhanced power conversion efficiency and preferential orientation of the MAPbI₃ perovskite solar cells by introduction of urea as additive. *Org. Electron.* **73**, 130–136 (2019).
218. Pylnev, M., Barbisan, A. M. & Wei, T. C. Effect of wettability of substrate on metal halide perovskite growth. *Appl. Surf. Sci.* **541**, (2021).
219. Bi, C. *et al.* Non-wetting surface-driven high-aspect-ratio crystalline grain growth for efficient hybrid perovskite solar cells. *Nat. Commun.* **2015 61** **6**, 1–7 (2015).
220. Pylnev, M., Barbisan, A. M. & Wei, T. C. Effect of wettability of substrate on metal halide perovskite growth. *Appl. Surf. Sci.* **541**, (2021).
221. Lee, J. W. *et al.* A Bifunctional Lewis Base Additive for Microscopic Homogeneity in Perovskite Solar Cells. *Chem* **3**, 290–302 (2017).
222. Merdasa, A. *et al.* Impact of Excess Lead Iodide on the Recombination Kinetics in Metal Halide Perovskites. *ACS Energy Lett.* **4**, 1370–1378 (2019).
223. Basumatary, P. & Agarwal, P. Photocurrent transient measurements in MAPbI₃ thin films. *J. Mater. Sci. Mater. Electron.* **31**, 10047–10054 (2020).
224. Wu, Z. Y., Jian, B. & Hsu, H. Photoluminescence characterizations of highly ambient-air-stable CH₃NH₃PbI₃/PbI₂ heterostructure. *Opt. Mater. Express* **9**, 1882 (2019).
225. Li, B. & Zhang, W. Improving the stability of inverted perovskite solar cells towards commercialization. *Commun. Mater.* **2022 31** **3**, 1–13 (2022).
226. Rong, Y. *et al.* Challenges for commercializing perovskite solar cells. *Science (80-.)*. **361**, (2018).
227. Mao, L. *et al.* Fully Textured, Production-Line Compatible Monolithic Perovskite/Silicon Tandem Solar Cells Approaching 29% Efficiency. *Adv. Mater.* **7**, 2206193 (2022).
228. Abzieher, T. *et al.* Electron-Beam-Evaporated Nickel Oxide Hole Transport Layers for Perovskite-Based Photovoltaics. *Adv. Energy Mater.* **9**, 1802995 (2019).
229. Lee, H. J. & Na, S. I. Investigation of PCBM/ZnO and C60/BCP-based electron transport layer for high-performance p-i-n perovskite solar cells. *J. Alloys Compd.* **921**, 166007 (2022).
230. De Bastiani, M. *et al.* Efficient bifacial monolithic perovskite/silicon tandem solar cells via bandgap engineering. *Nat. Energy* **2021 62** **6**, 167–175 (2021).
231. Yin, X. *et al.* Critical roles of potassium in charge-carrier balance and diffusion induced defect passivation for efficient inverted perovskite solar cells. *J. Mater. Chem. A* **7**, 5666–5676 (2019).
232. Park, I. J. *et al.* Highly Efficient and Uniform 1 cm² Perovskite Solar Cells with an Electrochemically Deposited NiO_x Hole-Extraction Layer. *ChemSusChem* **10**, 2660–2667 (2017).

References

233. Michalska, M. *et al.* Microfluidic Processing of Ligand-Engineered NiO Nanoparticles for Low-Temperature Hole-Transporting Layers in Perovskite Solar Cells. *Sol. RRL* **5**, 2100342 (2021).
234. Di Girolamo, D. *et al.* Progress, highlights and perspectives on NiO in perovskite photovoltaics. *Chem. Sci.* **11**, 7746–7759 (2020).
235. Rombach, F. M., Haque, S. A. & Macdonald, T. J. Lessons learned from spiro-OMeTAD and PTAA in perovskite solar cells. *Energy Environ. Sci.* **14**, 5161–5190 (2021).
236. Xu, X. *et al.* Improving Contact and Passivation of Buried Interface for High-Efficiency and Large-Area Inverted Perovskite Solar Cells. *Adv. Funct. Mater.* **32**, 2109968 (2022).
237. Chen, K. *et al.* Facile Physical Modifications of Polymer Hole Transporting Layers for Efficient and Reproducible Perovskite Solar Cells with Fill Factor Exceeding 80%. *Sol. RRL* (2020) doi:10.1002/SOLR.202000365.
238. Aydin, E., De Bastiani, M. & De Wolf, S. Defect and Contact Passivation for Perovskite Solar Cells. *Adv. Mater.* **31**, 1900428 (2019).
239. Li, B. *et al.* Reduced bilateral recombination by functional molecular interface engineering for efficient inverted perovskite solar cells. *Nano Energy* **78**, 105249 (2020).
240. You, J. *et al.* The fabrication of homogeneous perovskite films on non-wetting interfaces enabled by physical modification. *J. Energy Chem.* **38**, 192–198 (2019).
241. Phung, N. *et al.* Enhanced Self-Assembled Monolayer Surface Coverage by ALD NiO in p-i-n Perovskite Solar Cells. *ACS Appl. Mater. Interfaces* **14**, 2166–2176 (2022).
242. Halik, M., Hirsch, A., Halik, M. & Hirsch, A. The Potential of Molecular Self-Assembled Monolayers in Organic Electronic Devices. *Adv. Mater.* **23**, 2689–2695 (2011).
243. Yalcin, E. *et al.* Semiconductor self-assembled monolayers as selective contacts for efficient PiN perovskite solar cells. *Energy Environ. Sci.* **12**, 230–237 (2019).
244. Schreiber, F. Structure and growth of self-assembling monolayers. *Prog. Surf. Sci.* **65**, 151–257 (2000).
245. Magomedov, A. *et al.* Self-Assembled Hole Transporting Monolayer for Highly Efficient Perovskite Solar Cells. *Adv. Energy Mater.* **8**, 1801892 (2018).
246. Paniagua, S. A. *et al.* Phosphonic Acids for Interfacial Engineering of Transparent Conductive Oxides. *Chem. Rev.* **116**, 7117–7158 (2016).
247. Liu, L. *et al.* Fully printable mesoscopic perovskite solar cells with organic silane self-assembled monolayer. *J. Am. Chem. Soc.* **137**, 1790–1793 (2015).
248. Hubmann, A. H., Dietz, D., Brötz, J. & Klein, A. Interface Behaviour and Work Function Modification of Self-Assembled Monolayers on Sn-Doped In₂O₃. (2019) doi:10.3390/surfaces2020019.
249. Song, D., Narra, S., Li, M. Y., Lin, J. S. & Diau, E. W. G. Interfacial Engineering with a Hole-Selective Self-Assembled Monolayer for Tin Perovskite Solar Cells via a Two-Step Fabrication. *ACS Energy Lett.* **6**, 4179–4186 (2021).
250. Subbiah, A. S. *et al.* High-performance perovskite single-junction and textured perovskite/silicon tandem solar cells via slot-die-coating. *ACS Energy Lett.* **5**, 3034–3040 (2020).
251. Liu, J. *et al.* Efficient and stable perovskite-silicon tandem solar cells through contact displacement by MgFx. *Science (80-)*. (2022) doi:10.1126/SCIENCE.ABN8910.
252. Zheng, X. *et al.* Photoactivated p-Doping of Organic Interlayer Enables Efficient Perovskite/Silicon Tandem Solar Cells. *ACS Energy Lett.* **2022**, 1987–1993 (2022).
253. Biesinger, M. C. Accessing the robustness of adventitious carbon for charge referencing (correction) purposes in XPS analysis: Insights from a multi-user facility data review. *Appl. Surf. Sci.* **597**, 153681 (2022).
254. Larrude, D. G., Maia Da Costa, M. E. H., Monteiro, F. H., Pinto, A. L. & Freire, F. L. Characterization

- of phosphorus-doped multiwalled carbon nanotubes. *Cit. J. Appl. Phys* **111**, 64315 (2012).
255. Furlan, A. *et al.* Synthesis of phosphorus-carbide thin films by magnetron sputtering. *Phys. status solidi – Rapid Res. Lett.* **2**, 191–193 (2008).
256. Bulusheva, L. G. *et al.* Electronic Structure of Nitrogen- and Phosphorus-Doped Graphenes Grown by Chemical Vapor Deposition Method. *Materials (Basel)*. **13**, (2020).
257. Puziy, A. M., Poddubnaya, O. I., Socha, R. P., Gurgul, J. & Wisniewski, M. XPS and NMR studies of phosphoric acid activated carbons. *Carbon N. Y.* **46**, 2113–2123 (2008).
258. Tan, Y. *et al.* Chemical linkage and passivation at buried interface for thermally-stable inverted perovskite solar cells with efficiency over 22%. *CCS Chem.* 1–28 (2022) doi:10.31635/CCSCHEM.022.202202154.
259. Taddei, M. *et al.* Ethylenediamine Addition Improves Performance and Suppresses Phase Instabilities in Mixed-Halide Perovskites.
260. Bin, H. *et al.* Finetuning Hole-Extracting Monolayers for Efficient Organic Solar Cells. *ACS Appl. Mater. Interfaces* **14**, 16497–16504 (2022).
261. Tockhorn, P. *et al.* Nano-optical designs enhance monolithic perovskite/silicon tandem solar cells toward 29.8% efficiency. (2022) doi:10.21203/RS.3.RS-1439562/V1.
262. Cassie, A. B. D. & Baxter, S. Wettability of porous surfaces. *Trans. Faraday Soc.* **40**, 546–551 (1944).
263. Adam, N. K. & Cassie, B. D. Contact angles. *Discuss. Faraday Soc.* **3**, 11–16 (1948).
264. Wenzel, R. N. Resistance of solid surfaces to wetting by water. *Ind. Eng. Chem.* **28**, 988–994 (1936).
265. Kim, S., Quy, H. Van, Choi, H. W. & Bark, C. W. Effect of UV-Light Treatment on Efficiency of Perovskite Solar Cells (PSCs). *Energies 2020, Vol. 13, Page 1069* **13**, 1069 (2020).
266. Kwok, D. Y. & Neumann, A. W. Contact angle measurement and contact angle interpretation. *Adv. Colloid Interface Sci.* **81**, 167–249 (1999).
267. Owens, D. K. & Wendt, R. C. Estimation of the surface free energy of polymers. *J. Appl. Polym. Sci.* **13**, 1741–1747 (1969).
268. Wang, Y. *et al.* Patterned Wettability Surface for Competition-Driving Large-Grained Perovskite Solar Cells. *Adv. Energy Mater.* **9**, 1900838 (2019).
269. Gidey, A. T., Assayehegn, E. & Kim, J. Y. Hydrophilic Surface-Driven Crystalline Grain Growth of Perovskites on Metal Oxides. *ACS Appl. Energy Mater.* **4**, 6923–6932 (2021).
270. Kim, H. *et al.* Impact of Hydroxyl Groups Boosting Heterogeneous Nucleation on Perovskite Grains and Photovoltaic Performances. *J. Phys. Chem. C* **122**, 16630–16638 (2018).
271. Gebremichael, Z. T. *et al.* How varying surface wettability of different PEDOT:PSS formulations and their mixtures affects perovskite crystallization and the efficiency of inverted perovskite solar cells. *RSC Adv.* **12**, 25593–25604 (2022).
272. Othman, M. *et al.* Structural and Photophysical Properties of Guanidinium–Iodide-Treated Perovskite Solar Cells. *Sol. RRL* 2200852 (2022) doi:10.1002/SOLR.202200852.
273. Hsieh, C. M. *et al.* Low-temperature, simple and efficient preparation of perovskite solar cells using Lewis bases urea and thiourea as additives: Stimulating large grain growth and providing a PCE up to 18.8%. *RSC Adv.* **8**, 19610–19615 (2018).
274. Xu, K. *et al.* Slot-Die Coated Triple-Halide Perovskites for Efficient and Scalable Perovskite/Silicon Tandem Solar Cells. *ACS Energy Lett.* **29**, 3600–3611 (2022).
275. Aydin, E. *et al.* Ligand-bridged charge extraction and enhanced quantum efficiency enable efficient n–i–p perovskite/silicon tandem solar cells. *Energy Environ. Sci.* (2021) doi:10.1039/D1EE01206A.
276. Bush, K. A. *et al.* 23.6%-efficient monolithic perovskite/silicon tandem solar cells with improved

- stability. *Nat. Energy* **2**, 1–7 (2017).
277. Ebert, M., Stascheit, H., Hädrich, I. & Eitner, U. *THE IMPACT OF ANGULAR DEPENDENT LOSS MEASUREMENT ON PV MODULE ENERGY YIELD PREDICTION*.
278. Alghamdi, A. R. M., Yanagida, M., Shirai, Y., Andersson, G. G. & Miyano, K. Surface Passivation of Sputtered NiOx Using a SAM Interface Layer to Enhance the Performance of Perovskite Solar Cells. *ACS Omega* **7**, 12147–12157 (2022).
279. Mao, L. *et al.* Fully Textured, Production-Line Compatible Monolithic Perovskite/Silicon Tandem Solar Cells Approaching 29% Efficiency. *Adv. Mater.* **34**, 2206193 (2022).
280. Liu, J. *et al.* Efficient and stable perovskite-silicon tandem solar cells through contact displacement by MgFx. *Science (80-.)*. (2022) doi:10.1126/SCIENCE.ABN8910.
281. Lee, S. W. *et al.* Perovskites fabricated on textured silicon surfaces for tandem solar cells. *Commun. Chem.* **3**, 1–11 (2020).
282. Gil-Escrig, L. *et al.* Fully Vacuum-Processed Perovskite Solar Cells on Pyramidal Microtextures. *Sol. RRL* **5**, 1–9 (2021).
283. Chen, B. *et al.* Blade-Coated Perovskites on Textured Silicon for 26%-Efficient Monolithic Perovskite/Silicon Tandem Solar Cells. *Joule* **4**, 850–864 (2020).
284. Saliba, M. *et al.* How to Make over 20% Efficient Perovskite Solar Cells in Regular (n-i-p) and Inverted (p-i-n) Architectures. *Chem. Mater.* **30**, 4193–4201 (2018).
285. Saliba, M. *et al.* Cesium-containing triple cation perovskite solar cells: improved stability, reproducibility and high efficiency. *Energy Environ. Sci.* **9**, 1989–1997 (2016).
286. Wang, H. *et al.* Ligand-Modulated Excess PbI2 Nanosheets for Highly Efficient and Stable Perovskite Solar Cells. *Adv. Mater.* **32**, 2000865 (2020).
287. Jacobsson, T. J. *et al.* Unreacted PbI2 as a Double-Edged Sword for Enhancing the Performance of Perovskite Solar Cells. *J. Am. Chem. Soc.* **138**, 10331–10343 (2016).
288. Park, B. wook *et al.* Understanding how excess lead iodide precursor improves halide perovskite solar cell performance. *Nat. Commun.* **2018** *9* 1, 1–8 (2018).
289. Liu, F. *et al.* Is excess PbI2 beneficial for perovskite solar cell performance? *Adv. Energy Mater.* **6**, 1502206 (2016).
290. Kim, Y. C. *et al.* Beneficial effects of PbI2 incorporated in organo-lead halide perovskite solar cells. *Adv. Energy Mater.* **6**, 1502104 (2016).
291. Tumen-Ulzii, G. *et al.* Detrimental Effect of Unreacted PbI2 on the Long-Term Stability of Perovskite Solar Cells. *Adv. Mater.* **32**, 1905035 (2020).
292. Hu, Z. *et al.* Enhancing the Efficiency and Stability of Triple-Cation Perovskite Solar Cells by Eliminating Excess PbI2 from the Perovskite/Hole Transport Layer Interface. *ACS Appl. Mater. Interfaces* **12**, 54824–54832 (2020).
293. Meier, T. *et al.* Impact of excess PbI2 on the structure and the temperature dependent optical properties of methylammonium lead iodide perovskites. *J. Mater. Chem. C* **6**, 7512–7519 (2018).
294. Barbé, J. *et al.* Localized effect of PbI2 excess in perovskite solar cells probed by high-resolution chemical–optoelectronic mapping. *J. Mater. Chem. A* **6**, 23010–23018 (2018).
295. Cao, D. H. *et al.* Remnant PbI2, an unforeseen necessity in high-efficiency hybrid perovskite-based solar cells? *APL Mater.* **2**, 091101 (2014).
296. Roose, B., Dey, K., Chiang, Y. H., Friend, R. H. & Stranks, S. D. Critical Assessment of the Use of Excess Lead Iodide in Lead Halide Perovskite Solar Cells. *J. Phys. Chem. Lett.* **11**, 6505–6512 (2020).
297. Jiang, M., Wu, Y., Zhou, Y. & Wang, Z. Observation of lower defect density brought by excess PbI2 in CH3NH3PbI3 solar cells. *AIP Adv.* **9**, 085301 (2019).

References

298. Bi, D. *et al.* Efficient luminescent solar cells based on tailored mixed-cation perovskites. *Sci. Adv.* **2**, (2016).
299. Thampy, S., Xu, W. & Hsu, J. W. P. Metal Oxide-Induced Instability and Its Mitigation in Halide Perovskite Solar Cells. *J. Phys. Chem. Lett.* **12**, 8495–8506 (2021).
300. Thampy, S., Zhang, B., Hong, K. H., Cho, K. & Hsu, J. W. P. Altered Stability and Degradation Pathway of CH₃NH₃PbI₃ in Contact with Metal Oxide. *ACS Energy Lett.* **5**, 1147–1152 (2020).
301. Bonomo, M., Dini, D. & Marrani, A. G. Adsorption Behavior of I³⁻ and I⁻ Ions at a Nanoporous NiO/Acetonitrile Interface Studied by X-ray Photoelectron Spectroscopy. *Langmuir* **32**, 11540–11550 (2016).
302. Głowienka, D. *et al.* Role of surface recombination in perovskite solar cells at the interface of HTL/CH₃NH₃PbI₃. *Nano Energy* **67**, 104186 (2020).
303. Braunger, S. *et al.* Cs_xFA_{1-x}Pb(I_{1-y}Br_y)₃ Perovskite Compositions: The Appearance of Wrinkled Morphology and its Impact on Solar Cell Performance. *J. Phys. Chem. C* **122**, 17123–17135 (2018).
304. Bush, K. A. *et al.* Controlling Thin-Film Stress and Wrinkling during Perovskite Film Formation. *ACS Energy Lett.* **3**, 1225–1232 (2018).
305. Dailey, M., Li, Y. & Printz, A. D. Residual Film Stresses in Perovskite Solar Cells: Origins, Effects, and Mitigation Strategies. *ACS Omega* **6**, 30214–30223 (2021).
306. Menda, U. D. *et al.* High-performance wide bandgap perovskite solar cells fabricated in ambient high-humidity conditions. *Mater. Adv.* **2**, 6344–6355 (2021).
307. Bercegol, A. *et al.* Spatial Inhomogeneity Analysis of Cesium-Rich Wrinkles in Triple-Cation Perovskite. *J. Phys. Chem. C* **122**, 23345–23351 (2018).
308. Kim, S. G. *et al.* How antisolvent miscibility affects perovskite film wrinkling and photovoltaic properties. *Nat. Commun.* **2021 121** **12**, 1–10 (2021).
309. Sveinbjörnsson, K. *et al.* Ambient air-processed mixed-ion perovskites for high-efficiency solar cells. *J. Mater. Chem. A* **4**, 16536–16545 (2016).
310. Zhao, J. *et al.* Strained hybrid perovskite thin films and their impact on the intrinsic stability of perovskite solar cells. *Sci. Adv.* **3**, (2017).
311. Ye, J. *et al.* Crack-free perovskite layers for high performance and reproducible devices via improved control of ambient conditions during fabrication. *Appl. Surf. Sci.* **407**, 427–433 (2017).
312. Zhu, C. *et al.* Strain engineering in perovskite solar cells and its impacts on carrier dynamics. *Nat. Commun.* **2019 101** **10**, 1–11 (2019).
313. Liu, C., Cheng, Y. B. & Ge, Z. Understanding of perovskite crystal growth and film formation in scalable deposition processes. *Chem. Soc. Rev.* **49**, 1653–1687 (2020).
314. Chen, S. *et al.* Crystallization in one-step solution deposition of perovskite films: Upward or downward? *Sci. Adv.* **7**, (2021).
315. Chen, S. *et al.* Stabilizing perovskite-substrate interfaces for high-performance perovskite modules. *Science (80-.)*. **373**, 902–907 (2021).
316. Liu, C., Cheng, Y.-B. & Ge, Z. Understanding of perovskite crystal growth and film formation in scalable deposition processes. *Chem. Soc. Rev.* **49**, 1653–1687 (2020).
317. Seo, G. *et al.* Microscopic Analysis of Inherent Void Passivation in Perovskite Solar Cells. *ACS Energy Lett.* **2**, 1705–1710 (2017).
318. Fu, F. *et al.* I₂ vapor-induced degradation of formamidinium lead iodide based perovskite solar cells under heat–light soaking conditions. *Energy Environ. Sci.* **12**, 3074–3088 (2019).
319. Thampy, S., Zhang, B., Hong, K.-H., Cho, K. & Hsu, J. W. P. Altered Stability and Degradation Pathway of CH₃NH₃PbI₃ in Contact with Metal Oxide. *ACS Energy Lett.* **5**, 1147–1152 (2020).

References

320. Park, K. S., Choi, Y. J., Kang, J. G., Sung, Y. M. & Park, J. G. The effect of the concentration and oxidation state of Sn on the structural and electrical properties of indium tin oxide nanowires. *Nanotechnology* **22**, 285712 (2011).
321. Tuck, D. G. The Lower Oxidation States of Indium.
322. Payling, R. Glow discharge optical emission spectrometry. *Met. forum* **18**, 195–213 (1994).
323. Kodalle, T. *et al.* Glow discharge optical emission spectrometry for quantitative depth profiling of CIGS thin-films. *J. Anal. At. Spectrom.* **34**, 1233–1241 (2019).
324. Salomé, P. M. P. *et al.* CdS and Zn_{1-x}Sn_xO_y buffer layers for CIGS solar cells. *Sol. Energy Mater. Sol. Cells* **159**, 272–281 (2017).
325. Zheng, D. & Pauporté, T. Control of the quality and homogeneity of halide perovskites by mixed-chloride additives upon the film formation process. *J. Mater. Chem. A* **9**, 17801–17811 (2021).
326. Dally, P. *et al.* Probing the chemistry of perovskite systems by XPS and GD-OES depth-profiling: Potentials and limitations. *Conf. Rec. IEEE Photovolt. Spec. Conf.* 931–934 (2021) doi:10.1109/PVSC43889.2021.9518696.
327. Harvey, S. P. *et al.* Mitigating Measurement Artifacts in TOF-SIMS Analysis of Perovskite Solar Cells. *ACS Appl. Mater. Interfaces* **11**, 30911–30918 (2019).
328. Rombach, F. M., Haque, S. A. & Macdonald, T. J. Lessons learned from spiro-OMeTAD and PTAA in perovskite solar cells. *Energy Environ. Sci.* (2021) doi:10.1039/D1EE02095A.
329. Fu, F. *et al.* I₂ vapor-induced degradation of formamidinium lead iodide based perovskite solar cells under heat–light soaking conditions. *Energy Environ. Sci.* **12**, 3074–3088 (2019).
330. Wang, R. *et al.* Unraveling the surface state of photovoltaic perovskite thin film. *Matter* **4**, 2417–2428 (2021).
331. Yang, G. *et al.* Stable and low-photovoltage-loss perovskite solar cells by multifunctional passivation. *Nat. Photonics* **15**, 681–689 (2021).
332. Domanski, K. *et al.* Not All That Glitters Is Gold: Metal-Migration-Induced Degradation in Perovskite Solar Cells. *ACS Nano* **10**, 6306–6314 (2016).
333. Menda, U. D. *et al.* High-performance wide bandgap perovskite solar cells fabricated in ambient high-humidity conditions. *Mater. Adv.* **2**, 6344–6355 (2021).
334. Bercegol, A. *et al.* Spatial Inhomogeneity Analysis of Cesium-Rich Wrinkles in Triple-Cation Perovskite. *J. Phys. Chem. C* **122**, 23345–23351 (2018).
335. Chao, L. *et al.* Solvent Engineering of the Precursor Solution toward Large-Area Production of Perovskite Solar Cells. *Adv. Mater.* **33**, 2005410 (2021).
336. Cai, B., Zhang, W. H. & Qiu, J. Solvent engineering of spin-coating solutions for planar-structured high-efficiency perovskite solar cells. *Chinese J. Catal.* **36**, 1183–1190 (2015).
337. Li, J. *et al.* 20.8% Slot-Die Coated MAPbI₃ Perovskite Solar Cells by Optimal DMSO-Content and Age of 2-ME Based Precursor Inks. *Adv. Energy Mater.* **11**, 2003460 (2021).
338. Warby, J. *et al.* Understanding Performance Limiting Interfacial Recombination in pin Perovskite Solar Cells. *Adv. Energy Mater.* **12**, 2103567 (2022).
339. Melikhova, O. *et al.* Defects in nanocrystalline Nb films: Effect of sputtering temperature. (2005) doi:10.1016/j.apsusc.2005.08.083.
340. Jamnig, A., Sangiovanni, D. G., Abadias, G. & Sarakinos, K. Atomic-scale diffusion rates during growth of thin metal films on weakly-interacting substrates. *Sci. Reports* **9**, 1–11 (2019).
341. Schou, J. Slowing-down processes, energy deposition, sputtering and desorption in ion and electron interactions with solids.

342. Bou, A. *et al.* Extracting in Situ Charge Carrier Diffusion Parameters in Perovskite Solar Cells with Light Modulated Techniques. *ACS Energy Lett.* **6**, 2248–2255 (2021).
343. Chen, Y. *et al.* Extended carrier lifetimes and diffusion in hybrid perovskites revealed by Hall effect and photoconductivity measurements. *Nat. Commun.* **2016** *7* **1**, 1–9 (2016).
344. Chu, T. L. & Stokes, E. D. Minority Carrier Diffusion Lengths in Silicon Slices and Shallow Junction Devices. *J. Electron. Mater.* **7**, 173–182 (1978).
345. Hodes, G. & Kamat, P. V. Understanding the Implication of Carrier Diffusion Length in Photovoltaic Cells. *J. Phys. Chem. Lett.* **6**, 4090–4092 (2015).
346. Rajagopal, A., Stoddard, R. J., Jo, S. B., Hillhouse, H. W. & Jen, A. K. Y. Overcoming the Photovoltage Plateau in Large Bandgap Perovskite Photovoltaics. *Nano Lett.* **18**, 3985–3993 (2018).
347. Yang, T. C. J., Fiala, P., Jeangros, Q. & Ballif, C. High-Bandgap Perovskite Materials for Multijunction Solar Cells. *Joule* vol. 2 1421–1436 (2018).
348. Liu, X. *et al.* Stable Pure Iodide MA_{0.95}Cs_{0.05}PbI₃ Perovskite toward Efficient 1.6 eV Bandgap Photovoltaics. *J. Phys. Chem. Lett.* **13**, 5088–5093 (2022).
349. Chen, Z. *et al.* Thin single crystal perovskite solar cells to harvest below-bandgap light absorption. *Nat. Commun.* **2017** *8* **1**, 1–7 (2017).
350. Schmid, M., Ludescher, D. & Giessen, H. Optical properties of photoresists for femtosecond 3D printing: refractive index, extinction, luminescence-dose dependence, aging, heat treatment and comparison between 1-photon and 2-photon exposure. *Opt. Mater. Express* **9**, (2019).
351. Yuanjian Jiang, Xiaodan Zhang, Fengyou Wang & Ying Zhao. Optimization of a silicon wafer texturing process by modifying the texturing temperature for heterojunction solar cell applications. *RSC Adv.* **5**, 69629–69635 (2015).
352. Sjerps-Koomen, E. A., Alsema, E. A. & Turkenburg, W. C. A SIMPLE MODEL FOR PV MODULE REFLECTION LOSSES UNDER FIELD CONDITIONS. *Solar Energy* vol. 57 (1996).
353. Martin, N. & Ruiz, J. M. Calculation of the PV modules angular losses under field conditions by means of an analytical model. *Sol. Energy Mater. Sol. Cells* **70**, 25–38 (2001).
354. Gota, F., Schmager, R., Farag, A. & Paetzold, U. W. Energy yield modelling of textured perovskite/silicon tandem photovoltaics with thick perovskite top cells. *Opt. Express* **30**, 14172 (2022).
355. Singh, M. *et al.* Comparing optical performance of a wide range of perovskite/silicon tandem architectures under real-world conditions. *Nanophotonics* **10**, 2043–2057 (2021).
356. Park, J. *et al.* Controlled growth of perovskite layers with volatile alkylammonium chlorides. *Nat.* **2023** 1–3 (2023) doi:10.1038/s41586-023-05825-y.
357. Borriello, I., Cantele, G. & Ninno, D. Ab initio investigation of hybrid organic-inorganic perovskites based on tin halides. *Phys. Rev. B - Condens. Matter Mater. Phys.* **77**, 235214 (2008).
358. GitHub - marcus-cmc/Shockley-Queisser-limit: Calculation and visualization tools for theoretical solar cell efficiencies based on the Shockley Queisser limit with options to change temperature, light intensity, and radiative efficiency. <https://github.com/marcus-cmc/Shockley-Queisser-limit>.

List of publications and conference contributions

Peer-reviewed publications

Ahmed Farag,* Raphael Schmager, Paul Fassel, Philipp Noack, Bianca Wattenberg, Torsten Dippell, and Ulrich W. Paetzold, Efficient Light Harvesting in Thick Perovskite Solar Cells Processed on Industry-Applicable Random Pyramidal Textures, *ACS Applied Energy Materials*, **5**, 6700, 2022.

Ahmed Farag,* Paul Fassel, Hang Hu, Thomas Feeney, Aina Quintilla, Marco A. Ruiz-Preciado, Wolfram Hempel, Dominik Bagrowski, Philipp Noack, Bianca Wattenberg, Torsten Dippell, and Ulrich W. Paetzold, Mitigation of Open-Circuit Voltage Losses in Perovskite Solar Cells Processed over Micrometer-Sized-Textured Si Substrates, *Advanced Functional Materials*, 2210758, 2022.

Ahmed Farag,* Thomas Feeney,* Ihteaz M. Hossain, Fabian Schackmar, Paul Fassel, Kathrin Küster, Rainer Bäuerle, Marco A. Ruiz-Preciado, Mario Hentschel, David B. Ritzer, Alexander Diercks, Yang Li, Bahram Abdollahi Nejand, Felix Laufer, Roja Singh, Ulrich Starke, and Ulrich W. Paetzold, Evaporated Self-Assembled Monolayer Hole Transport Layers: Lossless Interfaces in p-i-n Perovskite Solar Cells, *Advanced Energy Materials*, **13**, 2203982, 2023.

Thomas Feeney,* Ihteaz M. Hossain, Saba Gharibzadeh, Fabrizio Gota, Roja Singh, Paul Fassel, Adrian Mertens, **Ahmed Farag**, Jan-Philipp Becker, Stefan Paetel, Erik Ahlswede, Ulrich W. Paetzold, Four-Terminal Perovskite/Copper Indium Gallium Selenide Tandem Solar Cells: Unveiling the Path to >27% in Power Conversion Efficiency, *Solar RRL*, **6**, 2200662, 2022.

Julie Roger,* Luisa K. Schorn, Minasadat Heydarian, **Ahmed Farag**, Thomas Feeney, Daniel Baumann, Hang Hu, Felix Laufer, Weyuan Duan, Kaining Ding, Andreas Lambertz, Paul Fassel, Matthias Worgull, and Ulrich W. Paetzold, Laminated Monolithic Perovskite/Silicon Tandem Photovoltaics, *Advanced Energy Materials*, **12**, 2200961, 2022.

Fabrizio Gota,* Raphael Schmager, **Ahmed Farag**, and Ulrich W. Paetzold, Energy yield modelling of textured perovskite/silicon tandem photovoltaics with thick perovskite top cells, *Optics Express*, **30**, 14172, 2022.

Marco A. Ruiz-Preciado,* Fabrizio Gota, Paul Fassel, Ihteaz M. Hossain, Roja Singh, Felix Laufer, Fabian Schackmar, Thomas Feeney, **Ahmed Farag**, Isabel Allegro, Hang Hu, Saba Gharibzadeh, Bahram Abdollahi Nejand, Veronique S. Gevaerts, Marcel Simor, Pieter J. Bolt, and Ulrich W. Paetzold, Monolithic Two-Terminal Perovskite/CIS Tandem Solar Cells with Efficiency Approaching 25%, *ACS Energy Letters*, **7**, 2273, 2022.

Fabian Schackmar,* Felix Laufer, Roja Singh, **Ahmed Farag**, Helge Eggers, Saba Gharibzadeh, Bahram Abdollahi Nejand, Uli Lemmer, Gerardo Hernandez-Sosa, and Ulrich W. Paetzold, In Situ Process Monitoring and Multichannel Imaging for Vacuum-Assisted Growth Control of Inkjet-Printed and Blade-Coated Perovskite Thin-Films, *Advanced Materials Technologies*, 2201331, 2022.

Yang Li,* Hang Hu, **Ahmed Farag**, Thomas Feeney, Isabel Allegro, Uli Lemmer, Ulrich W. Paetzold, and Ian A. Howard, Enhancement of Amplified Spontaneous Emission by Electric Field in CsPbBr₃ Perovskites, *Nano Letters*, 2023.

Benjamin Hacene,* Felix Laufer, Simon Ternes, **Ahmed Farag**, Ronja Pappenberger, Paul Faßl, Somayeh Moghadamzadeh, Bahram Abdollahi, Ian Howard, and Ulrich W. Paetzold, Intensity dependent photoluminescence imaging for in-line quality control of perovskite thin film processing, (submitted).

Mohamed Hussein,* Fabrizio Gota, **Ahmed Farag**, Ulrich W. Paetzold, and Uli Lemmer, Energy yield modelling of triple-junction all perovskite tandem photovoltaics, (in preparation).

Conference contributions

Ahmed Farag,* Raphael Schmagel, Paul Fassel, Bianca Wattenberg, Torsten Dippell, and Ulrich W. Paetzold, Micrometer-Thick Solution Processed Perovskite Solar Cells on Industrial-Like Textured Si Substrates for Efficient Light Harvesting, , *Material Research Society (MRS) fall meeting* (2021).

Julie Roger,* Luisa K. Schorn, Minasadat Heydarian, **Ahmed Farag**, Thomas Feeney, Daniel Baumann, Hang Hu, Felix Laufer, Weiyuan Duan, Kaining Ding, Andreas Lambertz, Paul Fassel, Matthias Worgull, and Ulrich W. Paetzold, Novel lamination approach for fabrication of monolithic perovskite/silicon tandem photovoltaics, *PVSEC-33* (2022).

Julie Roger,* Luisa K. Schorn, Minasadat Heydarian, **Ahmed Farag**, Thomas Feeney, Daniel Baumann, Hang Hu, Felix Laufer, Weiyuan Duan, Kaining Ding, Andreas Lambertz, Paul Fassel, Matthias Worgull, and Ulrich W. Paetzold, Novel lamination approach for fabrication of monolithic perovskite/silicon tandem photovoltaics, *Tandem PV Workshop* (2022).

Ronja Pappenberger,* Paul Fassel, Alexander Diercks, Somayeh Moghadamzadeh, **Ahmed Farag**, and Ulrich W. Paetzold, Bandgap engineering of two-step processed perovskite top cells for application in perovskite-based tandem photovoltaics, *Tandem PV Workshop* (2023).

Marco A. Ruiz-Preciado,* Ihtez M. Hossain, Thomas Feeney, **Ahmed Farag**, Hang Hu, Saba Gharibzadeh, Fabrizio Gota, Roja Singh, Marcel Simor, Pieter J. Bolt, Ulrich W. Paetzold. Highly Efficient Perovskite-CIS Monolithic Tandem Solar Cells, *Material Research Society* (2022).

Fabian Schackmar,* Felix Laufer, Roja Singh, **Ahmed Farag**, Helge Eggers, Saba Gharibzadeh, Bahram Abdollahi Nejand, Gerardo Hernandez-Sosa, Uli Lemmer and Ulrich W. Paetzold, Multichannel Imaging and In-Situ Process Monitoring for Vacuum-Assisted Drying for Inkjet-Printed and Blade-Coated Perovskite Thin-Films, *Material Research Society* (2022).

Ahmed Farag,* Thomas Feeney,* Ihtez M. Hossain, Fabian Schackmar, Paul Fassel, Kathrin Küster, Rainer Bäuerle, Marco A. Ruiz-Preciado, Mario Hentschel, David B. Ritzer, Alexander Diercks, Yang Li, Bahram Abdollahi Nejand, Felix Laufer, Roja Singh, Ulrich

Starke, and Ulrich W. Paetzold, Thermal Evaporation: an Alternative Deposition Method of Self-Assembled Monolayers for Lossless Interfaces in p-i-n Perovskite Solar Cells, HOPV (2023).

Acknowledgments

It started in April 2020, after successfully finishing my master's degree at the University of Stuttgart. Back then, it was the very first corona wave when many people thought life on planet earth is under real threat (this is a precise description without a tiny bit of exaggeration!). Curfew after normal working hours, police controlling that no more than two people are walking together if they are not from the same household, in addition to a completely empty train when I was moving from Stuttgart to Karlsruhe. Restrictions have reached the labs as well, including limited numbers, keeping distance, and wearing masks all the time (for more than 12 h in some days). Moving to a new group and conducting research in a completely new topic under such circumstances made a smooth start to be far from reach. However, with some faith, hard work, and support, nothing is far from reach. Therefore, I would like to thank:

- Tenure-Track-Prof. Dr. Ulrich W. Paetzold for giving me the chance to conduct scientific research in his group, for his supervision, guidance, patience, and wisdom during the challenging situations.
- Prof. Dr. Jan Philipp Hofmann for spending the time and effort as the second supervisor.
- Dr. Saba Gharibzadeh for guiding me through my very first days in the lab.
- Dr. Paul Faßl for proof reading my manuscripts and his advices for enhancing their quality.
- Dr. Bahram A. Nejang for being around in the lab whenever needed, particularly at the starting phase when I had lack of experience and knowledge.
- Our collaborators from Singulus Technologies AG, Max Planck Institute for Solid State Research, InnovationLab, and Zentrum für Sonnenenergie- und Wasserstoff for their valuable contribution and the fruitful discussions.
- My colleagues Thomas, Sara, Marco, Felix, and Paul for proofreading parts of this thesis.
- The colleagues of the taskforce for their support and cooperation.
- And last but not least, my parents for their continuous support and magical prayers.

وكان فضل الله عليك عظيما